Fluid Mechanics and Its Applications

Yasushi Takeda *Editor*

Ultrasonic Doppler Velocity Profiler for Fluid Flow

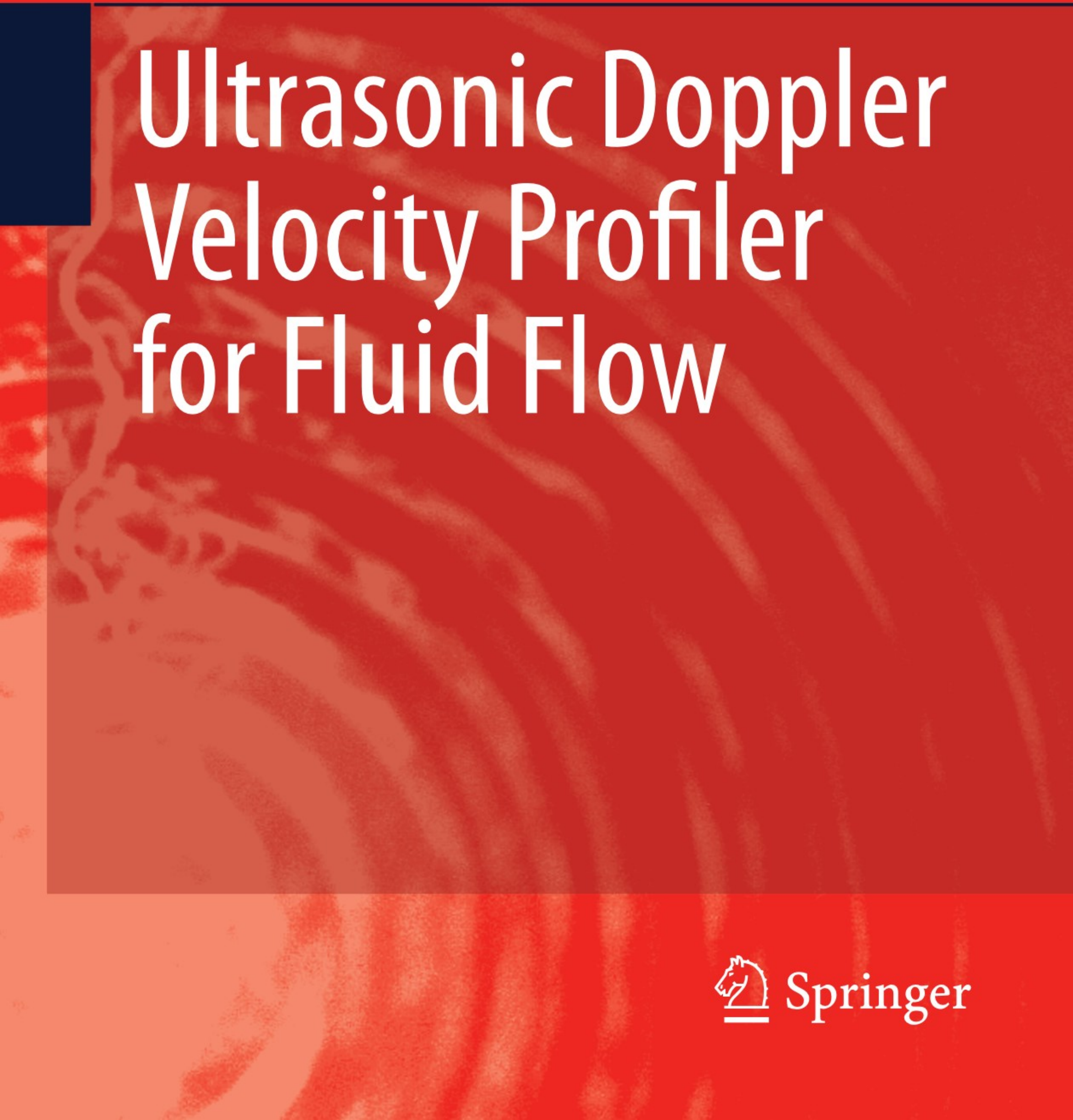

Springer

Ultrasonic Doppler Velocity Profiler for Fluid Flow

FLUID MECHANICS AND ITS APPLICATIONS
Volume 101

Aims and Scope of the Series

The purpose of this series is to focus on subjects in which fluid mechanics plays a fundamental role.

As well as the more traditional applications of aeronautics, hydraulics, heat and mass transfer etc., books will be published dealing with topics which are currently in a state of rapid development, such as turbulence, suspensions and multiphase fluids, super and hypersonic flows and numerical modeling techniques.

It is a widely held view that it is the interdisciplinary subjects that will receive intense scientific attention, bringing them to the forefront of technological advancement. Fluids have the ability to transport matter and its properties as well as to transmit force, therefore fluid mechanics is a subject that is particularly open to cross fertilization with other sciences and disciplines of engineering. The subject of fluid mechanics will be highly relevant in domains such as chemical, metallurgical, biological and ecological engineering. This series is particularly open to such new multidisciplinary domains.

The median level of presentation is the first year graduate student. Some texts are monographs defining the current state of a field; others are accessible to final year undergraduates; but essentially the emphasis is on readability and clarity.

For further volumes:
http://www.springer.com/series/5980

Yasushi Takeda
Editor

Ultrasonic Doppler Velocity Profiler for Fluid Flow

Springer

Editor
Yasushi Takeda
Hokkaido University, Sapporo, Japan

Tokyo Institute of Technology, Tokyo, Japan

ISSN 0926-5112
ISBN 978-4-431-54025-0 ISBN 978-4-431-54026-7 (eBook)
DOI 10.1007/978-4-431-54026-7
Springer Tokyo Heidelberg New York Dordrecht London

Library of Congress Control Number: 2012946915

© Springer Japan 2012
This work is subject to copyright. All rights are reserved by the Publisher, whether the whole or part of the material is concerned, specifically the rights of translation, reprinting, reuse of illustrations, recitation, broadcasting, reproduction on microfilms or in any other physical way, and transmission or information storage and retrieval, electronic adaptation, computer software, or by similar or dissimilar methodology now known or hereafter developed. Exempted from this legal reservation are brief excerpts in connection with reviews or scholarly analysis or material supplied specifically for the purpose of being entered and executed on a computer system, for exclusive use by the purchaser of the work. Duplication of this publication or parts thereof is permitted only under the provisions of the Copyright Law of the Publisher's location, in its current version, and permission for use must always be obtained from Springer. Permissions for use may be obtained through RightsLink at the Copyright Clearance Center. Violations are liable to prosecution under the respective Copyright Law.
The use of general descriptive names, registered names, trademarks, service marks, etc. in this publication does not imply, even in the absence of a specific statement, that such names are exempt from the relevant protective laws and regulations and therefore free for general use.
While the advice and information in this book are believed to be true and accurate at the date of publication, neither the authors nor the editors nor the publisher can accept any legal responsibility for any errors or omissions that may be made. The publisher makes no warranty, express or implied, with respect to the material contained herein.

Printed on acid-free paper

Springer is part of Springer Science+Business Media (www.springer.com)

Preface

The ultrasonic velocity profile (UVP) method was originally developed for cardiovascular measurements in the human body by Japanese researchers in medical engineering almost 50 years ago, but it has not been extensively used until recently. This long delay was presumably because the research team lacked expertise in fluid dynamics and thus was unable to achieve an adequate understanding and interpretation of the results.

Roughly 30 years ago, I was looking for a technique that could be used to measure the flow of opaque liquid metal when a colleague in medical engineering told me about the ultrasonic velocity method. I modified an existing instrument and demonstrated that the ultrasonic method could indeed measure the flow in a liquid metal. This success stimulated me to extend the ultrasonic method so that it could be used to measure many kinds of fluid flows. In the course of time, diverse flow configurations were tested to verify and validate the method. The results of this testing and validation demonstrated that the ultrasonic velocity method, referred to simply as UVP, was a powerful new tool in experimental fluid mechanics (EFD).

After using the UVP method for physics studies of fluid flow, I realized that it might bring us a revolutionary change in EFD—namely, a change of emphasis from measuring average velocity profiles in space, or velocity time series at a fixed position in space, to one where the objective was to measure the instantaneous velocity distribution (i.e., the instantaneous velocity as a function of both space and time).

All the early developmental work was designed to confirm and emphasize this change in perspective. Many researchers in Europe and Japan were involved in the effort, and this book is a compilation of that research.

Originally this book was planned as a textbook for current users of the UVP method. Its purpose was later extended both to show the capability of the method for various types of applications and to encourage more use of the method. Publication of the book is the result of teamwork by the many researchers whose names appear in the following pages. I deeply appreciate their extensive and energetic work.

I would like to point out that a Users and Researchers Community has been formed, referred to as ISUD (International Symposium on Ultrasonic Doppler method in fluid flow). A symposium is held every 2 years, and the reader is encouraged to visit their website for more details. Finally, I would like to acknowledge that we have received constant support from Mr. G. Gogniat of Met-Flow S.A. (Lausanne)[†]. I am grateful to him for his support, without which the ultrasonic velocity method would not have been developed to the extent that we now enjoy. I am also grateful to all the people who worked to make this book possible.

Tokyo, Japan Yasushi Takeda

[†] Mr. G. Gogniat passed away on 19. April 2012 before a completion of this book.

Contents

Part I Fundamentals

Part II Applications

Contributors

Editors

Yasushi Takeda, Chief Editor

Yuji Tasaka, Co-Editor

Hideki Murakawa, Co-Editor

Authors

Beat Birkhofer (Sect. 5.3.1, 5.4, 6.2) Sika Services AG, Zürich, Switzerland

Noriyuki Furuichi (Sect. 4.2.6, 5.1, 6.1) National Metrology Institute of Japan, National Institute of Advanced Industrial Science and Technology (AIST), Tsukuba, Japan

Tatsuya Kawaguchi (Sect. 7.5) Tokyo Institute of Technology, Tokyo, Japan

Hiroshige Kikura (Sect. 5.5) Tokyo Institute of Technology, Tokyo, Japan

Hisato Minagawa (Sect. 5.6) The University of Shiga Prefecture, Shiga, Japan

Michitsugu Mori (Sect. 3.2) Hokkaido University, Sapporo, Japan

Yuichi Murai (Sect. 4.2, 5.3.2, 5.6, 6.3, 7.2, 7.3) Faculty of Engineering, Hokkaido University, Sapporo, Japan

Hideki Murakawa (Sect. 3.1, 3.3, 5.6, 7.1) Graduate School of Engineering, Kobe University, Kobe, Japan

Masaaki Motozawa (Sect. 5.5) Tokyo University of Science, Chiba, Japan

Samsun Nahar (Sect. 5.8) Swiss Federal Institute of Technology Zürich (ETH-Zürich), Zürich, Switzerland

Hironari Obayashi (Sect. 5.2.3, 7.4) Japan Atomic Energy Agency (JAEA), Ibaraki, Japan

Tatsuo Sawada (Sect. 5.5) Keio University, Yokohama, Japan

A.K. Jeelani Shaik (Sect. 5.3.1, 5.4, 5.8, 6.2) Institute of Food, Nutrition and Health, Swiss Federal Institute of Technology Zürich (ETH-Zürich), Zürich, Switzerland

Yasushi Takeda (Chapter 1, Sect. 2.7, 3.1, 3.2, 4.1.4, 5.8) Hokkaido University, Sapporo, Japan

Tokyo Institute of Technology Tokyo, Japan

Yuji Tasaka (Chapter 2, Sect. 4.1, 5.1, 7.2, & Appendix) Faculty of Engineering, Hokkaido University, Sapporo, Japan

Kenichi Tezuka (Sect. 5.7) Tokyo Electric Power Company, Yokohama, Japan

Yoshiyuki Tsuji (Sect. 5.2.1) Nagoya University, Nagoya, Japan

Sanehiro Wada (Sect. 5.2.2) Tokyo Electric Power Company, Yokohama, Japan

Johan Wiklund (Sect. 5.3.1, 5.4, 6.2) The Swedish Institute for Food and Biotechnology (SIK), Göteborg, Sweden

Erich J. Windhab (Sect. 5.3.1, 5.4, 5.8, 6.2) Institute of Food, Nutrition and Health, Swiss Federal Institute of Technology Zürich (ETH-Zürich), Zürich, Switzerland

Takatoshi Yanagisawa (Sect. 5.7) Japan Agency for Marine-Earth Science and Technology (JAMSTEC), Yokosuka, Japan

Chapter 1
Introduction

Yasushi Takeda

Abstract The ultrasonic Doppler velocity profiler (UVP) method is now an accepted and established tool in modern experimental fluid mechanics and fluid engineering. I presented my first set of results illustrating the versatility and power of UVP at the conference in 1985 [Takeda, Velocity profile measurement by ultrasound Doppler shift method. In: Harada M, Pergamon (eds) Fluid control and measurement, FLUCOME TOKYO '85, Tokyo, 1985, p 851]. The span of almost two decades from introduction to acceptance is remarkably in accord with the remarks made by Leibovich (Annu Rev Fluid Mech 35, 2003) on the time it takes for novel theoretical ideas to gain acceptance in fluid mechanics. In the 1985 conference I presented the results of UVP measurement in several flow configurations and emphasized the importance of this development because it is a line measurement and different from point measurement. In the meeting I recall discussing the future of flow measurement with R.J. Adrian, who admitted that line or areal measurement of flow field is important. [Adrian extended the laser speckle method to a development of PTV/PIV, which is also a key technology of current flow measurements (Exp Fluids 39:159–169, 2005).]

In this review I give a brief history of the development of the ultrasonic Doppler velocity profiler (UVP) and describe several examples of its diversity and use in fluid mechanics and engineering.

Y. Takeda (✉)
Hokkaido University, Sapporo, Japan

Tokyo Institute of Technology, Tokyo, Japan
e-mail: yft@eng.hokudai.ac.jp

Y. Takeda (ed.), *Ultrasonic Doppler Velocity Profiler for Fluid Flow*,
Fluid Mechanics and Its Applications 101, DOI 10.1007/978-4-431-54026-7_1,

1.1 Introduction

1.1.1 Principle

Although much weaker than a laser, ultrasound has the characteristics of a beam if the basic frequency and transducer size (or initial beam size) are carefully selected. An ultrasonic pulse is emitted from the transducer, and the same transducer receives the echo from tracer particles suspended in the fluid. The position information is obtained from the time lapse between the pulse emission and echo reception: an echo relationship; namely from where it is reflected. The velocity at the position can be obtained from the instantaneous Doppler shift frequency of the echo. The echo signal is treated so as to derive a series of Doppler shift frequency of the echo, to form a velocity distribution–velocity profile. As the sound speed is fairly moderate and the attenuation is relatively small in liquid, very fast electronics are not necessary to process the signals. This enables two simple principles—echo relationship and Doppler shift—to be successfully combined to produce a velocity profile at high time resolution.

1.1.2 Historical

The ultrasound Doppler method had been used in earlier works, but all of them were for a small-diameter pipe flow, and the velocity was a space-averaged value. The development was targeted for cardiovascular flow, and medical electronics engineers were the main developers. At that time the concept of measuring the velocity profile in the flow was not considered. The first appearance of this technique in general fluid mechanics was a work by Fox [1], who reported theoretical and experimental work on range-gated Doppler detection to form a velocity profile. In the field of experimental fluid mechanics, there were some other works, such as papers by Garbini et al. [2, 3], but the focus was on evaluation of turbulent intensity, and velocity profiling was not considered. Similar works using the ultrasonic Doppler principle often appeared but few systematic studies were published.

I began a program of methodical development and investigation starting with a paper in 1986 [4]. At the time Laser Doppler Anemometry (LDA) was the main tool for velocity measurements in experimental fluid dynamics (EFD) and thus comparison was made with LDA measurement in a pipe [5]. However, the importance and capability of obtaining a velocity profile or velocity distribution instantaneously was still not fully appreciated.

1.1.3 Advantages

The UVP method has three main advantages over conventional measurement techniques used in fluid mechanics and fluid engineering:

1. UVP obtains high-resolution *spatiotemporal information* on the flow field. By conventional techniques, most of the differential measurements such as hot-wire or LDA were possible only at one position in space, although with very high time resolution. Visualized images—photographs—could give information on spatial distribution of velocity or other quantities but only at one instant. Because an instantaneous velocity distribution can be obtained and recorded in a time series, it is like a “snapshot” of the flow. The time between snapshots is short and thus they can be played back in movie form, although it is basically a single spatial dimension.
2. UVP can be applied to *opaque fluids* such as liquid metals, chemical and pharmaceutical substances, and organic fluids such as blood and food materials. These opaque fluids are often used not only in fluid engineering but also for fundamental physics studies such as magnetohydrodynamics (MHD), geosciences, and astronomy. Even if the fluid is transparent, such as water or petroleum, the walls of containers or conduits are usually opaque. The transducers can be placed behind these walls without disturbing the flow.
3. UVP is a *line measurement*. The number of spatial points along the line range from about 30 to around 500 (depending on the system and development) so that UVP is very efficient for flow mapping. Flow mapping is necessary to know velocity profile and flow structure and is an important task for fluid engineers designing fluid machinery or devices: for example, flow channels in cooling circuits for combustion engines, chemical plants, power generation plants, and land structures in civil engineering. Flow mapping is also important for comparison with the results of numerical simulation.

1.1.4 Paradigm Shift

The characteristics of the UVP method requires us to change the way we think about a flow problem, its observation, and the interpretation of the measured results. For a long time there has been a discrepancy in the path of information flow in fluid mechanical studies. In theoretical and numerical studies, the work is started to obtain the field quantity or characteristics of solutions, which are used for physics studies by using manipulation of images. In contrast, in the conventional experimental study flow visualization has been extensively used as a first step to gain information about the flow before proceeding to quantitative measurements (formerly only point measurements) for studying physics. By inventing the UVP [as well as particle image velocimetry (PIV) these days], the work is started by first generating/obtaining the data on the field first and working on its physics using various techniques of imaging of such data sets. It is hoped that barriers between branches of theoretical/numerical and experimental fluid mechanics can be lowered and it can work more smoothly in a collaborative manner (Fig. 1.1).

The UVP method has helped give rise to a paradigm shift—a fundamental change in the design, performance, and analysis of laboratory and field experiments and of industrial applications. For example, one should know that the well-known parabolic

Fig. 1.1 Information flow in studying fluid mechanics

	Theoretical	*Numerical*	*Experimental*	
			Conventional	*UVP*
Image	⇑	⇑	●	⇑
Field	●	●	⇓	●
Physics	⇓	⇓	⇓	⇓

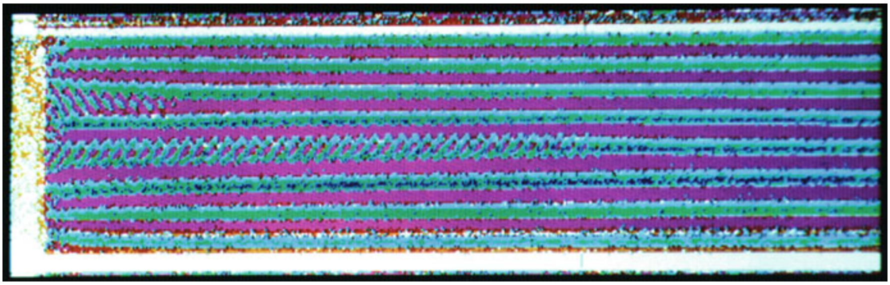

Fig. 1.2 Flow development of Taylor vortices after a sudden start of the inner cylinder [6] (with kind permission from Springer Science+Business Media)

velocity profile in a pipe can never appear in a laboratory experiment without time-averaging. An instantaneous velocity profile reflects the out-of-equilibrium dynamics that cause the profile to deviate from the parabolic distribution.

Instantaneous velocity distribution is a part of the full solution of the equation governing fluid motion. As such it is possible to make direct comparison with theoretical and numerical results, just as is now done in meteorology using satellite-measured velocity fields. Moreover, the various principles for measurement of flow characteristics based on theoretical integral values need to be revised.

Recent development of the measurement techniques of UVP, together with the PIV method, requires a paradigm shift for working with fluid flow, not only in fluid mechanics and fluid engineering but also in all disciplines involving flow.

In this review article, many works are introduced, being classified according to these advantages to the study of fluid motion made possible by UVP.

1.2 Spatiotemporal Flow Field

During and after the initial phase of development and establishment of the method, several new and challenging observations were reported: these were the observation of transient behavior of the flow field in a rotating Taylor–Couette system (Fig. 1.2) [6], spatial characteristics of dynamic properties in Taylor Couette Flow (TCF) [7, 8], evolution of the flow pattern in a Czokralski puller configuration (Fig. 1.3) [9], and

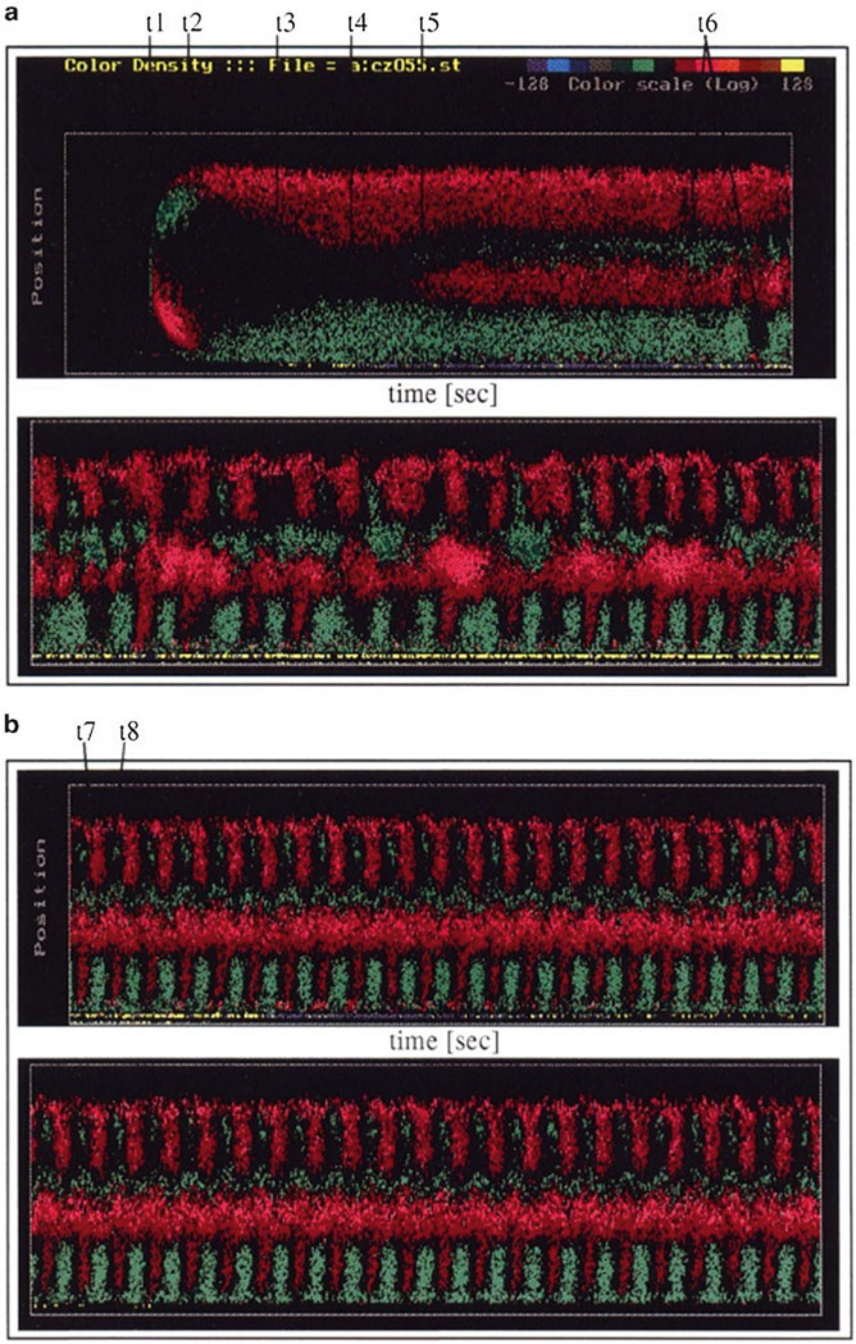

Fig. 1.3 Evolution of the flow pattern in a Czokralski puller configuration (reprinted from [9] with permission from Elsevier). Each marked timing (t1 to t8) indicates a change of flow structure due to flow instability. (a) transient state, (b) steady state. Detail be referred to the original paper

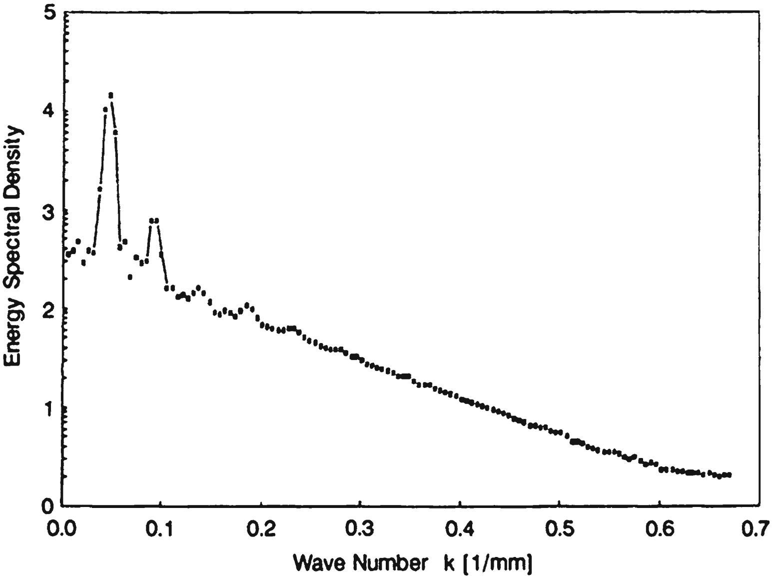

Fig. 1.4 Measured energy spectral density (ESD) [10] (Copyright (1993) by The American Physical Society)

measurement of energy spectral density (Fig. 1.4) [10]. Soon after these reports, it was shown that the velocity field can be obtained in the form of a spatiotemporal function and decomposed into fundamental modes using orthogonal functions. These spatiotemporal modes were then used to characterize the flow field (Fig. 1.5) [11]. The energy spectrum or field decomposition is a fundamental methodology in physics studies. It was a significant step forward in experimental fluid mechanics to be able to obtain such information directly from the flow field, rather than to rely on the Taylor frozen-flow hypothesis to convert frequency to wave number.

Quite often, the first appearance of a hydrodynamic instability, for example, departing from laminar flow, is a change in the spatial distribution of the velocity field. The UVP method can capture this behavior quite well. Typical examples of the use of UVP in this type of investigation are found in the works by Aider and Wesfried [12] on Göertler vortices, by Le Gal et al. [13] on multiple wakes, by Schouveiler et al. [14] on a rotating disk (Fig. 1.6), and by Peschard et al. [15] on the cylinder wake.

In the physics study of fluid flow, two types of investigations have been carried out that took advantage of spatiotemporal field measurements by UVP. One type is the study of turbulent flow and its statistical characterization. Alfonsi et al. measured streamwise velocity fluctuations and velocity profiles in turbulent pipe flow [16, 17]. However, their measurement system had insufficient space and time resolution for investigating the characteristics of the flow structure, and only average velocity profiles and various statistical characteristics were obtained. Le Guer et al. [18] investigated probability distribution functions (PDFs) of velocity of a buoyant particle dispersion

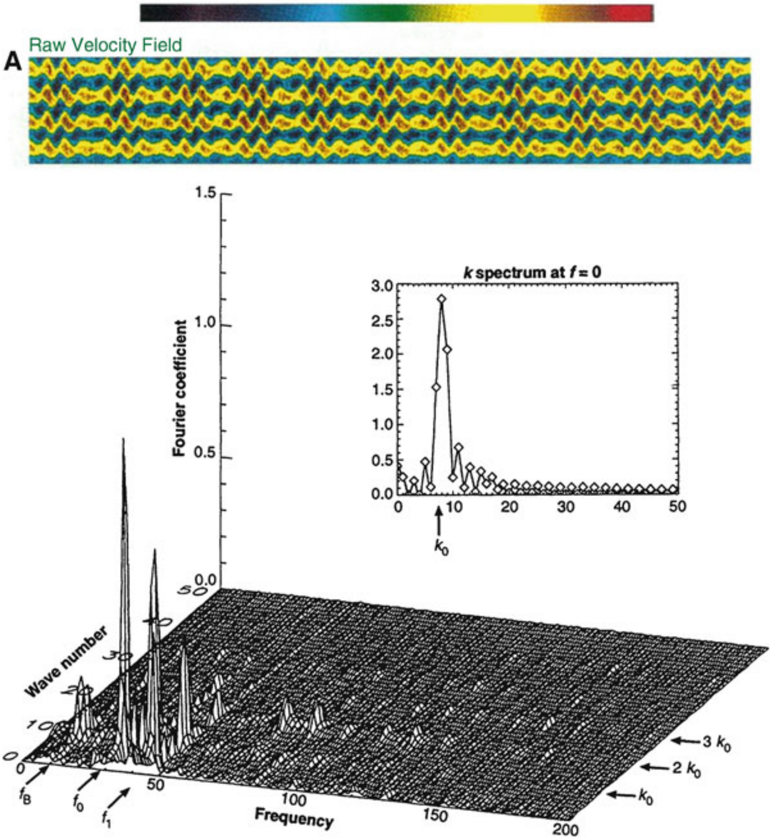

Fig. 1.5 Spatio-temporal velocity field (*top*) and its two dimensional Fourier spectrum (*bottom*) (from [11]. Reprinted with permission from AAAS.)

in a pipe flow. Mordant et al. [19] measured Lagrangian velocity in turbulent flow between two rotating disks. Although both Le Guer and Mordant applied the UVP method, neither took full advantage of spatiotemporal measurement.

The second type of investigations are those in which the velocity field was decomposed using fast Fourier transform (FFT) or orthogonal decomposition (POD) and thus make full use of the UVP measurement. In addition to those described earlier, Inoue et al. [20] investigated the flow field of wake behind the torus. Space-dependent power spectrum is a good methodology for this kind of investigation. Ern and Wesfried [21] investigated the effect of time-periodic forcing in the flow between corotating cylinders. Lusseyran et al. [22] studied a stratified shear layer, and Inoue et al. [23] investigated flow structure in the near field of a square free jet. Inoue et al. [23] also made a POD analysis of the flow field, after discussing the space-dependent power spectra. Furuichi et al. [24] investigated flow transition in a backward-facing step flow using POD analysis and global

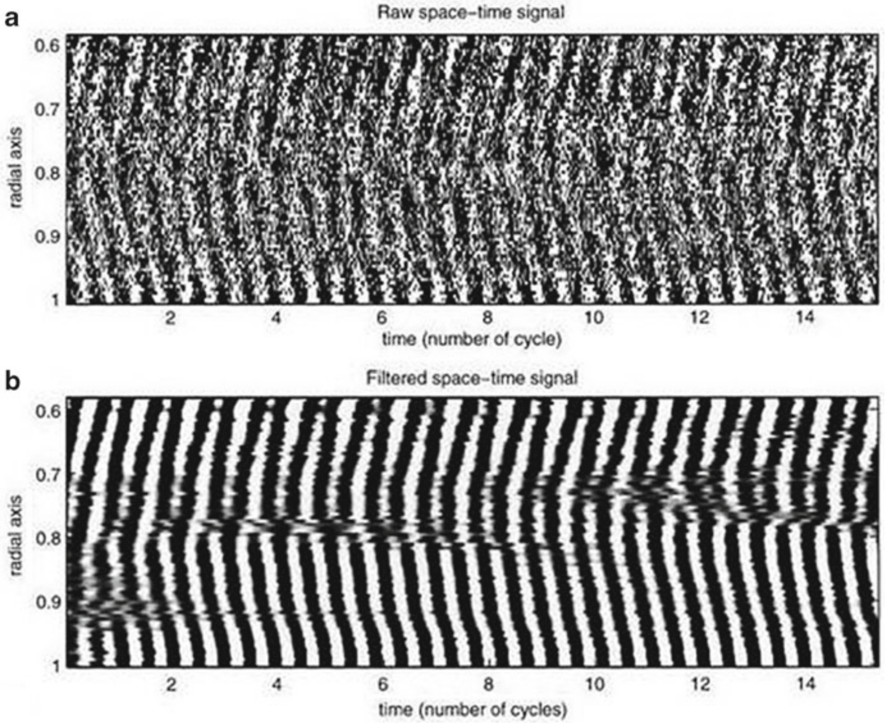

Fig. 1.6 Spatio-temporal velocity field showing a characteristic change of its structure on a rotating disk (a) raw data, (b) filtered data [14] (with kind permission from Springer Science+ Business Media)

entropy. Mashiko et al. [25] studied the thermal convection of mercury flow in a container and calculated the energy spectral density, and Tsuji et al. [26] studied the mean wind in convective turbulence.

It should be pointed out that these physics investigations are a realization of the call made by Frisch and Orszag [27]—before the establishment of UVP and PIV—that "A high priority should be the development of data acquisition and visualization techniques that will give spatio-temporal information across a broad range of scales."

1.3 Opaque Liquids

It has been known for a long time that ultrasonic waves had the characteristics necessary to investigate the flow behavior of liquid metals. It has also been known that the ultrasonic wave is the only possible wave to be used for flow investigation of other opaque liquids such as food materials, chemical and pharmaceutical reagents, and magnetic fluids such as ferrofluid. Fowlis [28] was possibly the first to take up the challenge of using the ultrasonic Doppler method for liquid metal study, but his

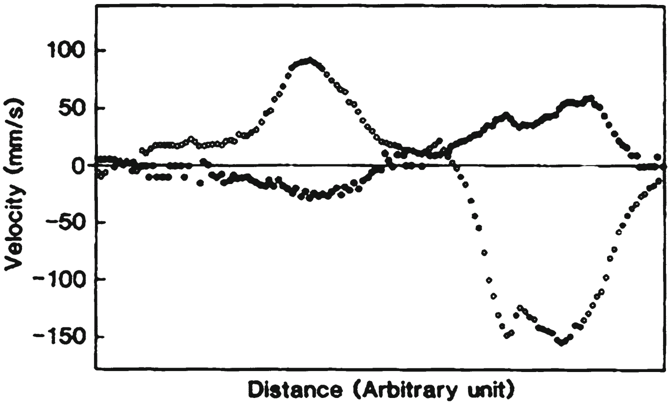

Fig. 1.7 Measured average velocity profile of mercury flow

instrument was only able to measure the average velocity at a single point in a pipe. The original driving force for my development of the UVP was to invent a new measurement technology to study a liquid metal flow to be used in the production of a neutron beam. I applied the method immediately after a successful measurement in water (Fig. 1.7) [29]. It was very difficult to judge if the measurement was correct because no visual observation was possible. Judgment was made based on observation of positive and negative flow direction and the temporal change of the velocity profile by controlling the flow in a pipe. The velocity profile changed its shape in response to the manual manipulation of the flow controller.

Magnetic fluids is one of the most important applications of UVP in engineering research. Kikura et al. [30, 31] checked its applicability using the Taylor–Couette configuration, and Sawada et al. [32] investigated its use to study the sloshing of magnetic fluids in an oscillating container. Brito et al. measured the vortex flow of gallium in a cylindrical container agitated by a propeller (Fig. 1.8) [33]. Thereafter, Brito's group used this method extensively for investigating the flow in various configurations using liquid metals [34]. Eckert and co-workers have reported using UVP to investigate liquid metals in a series of papers. Their first study was of flowing liquid sodium [35], followed by a study of the flow behavior in a casting model using mercury and InGaSn [36] in the spin-up of a flow driven by a rotating magnet [37]. Eckert's group has extended application of the method to a high-temperature environment by using a special sound guide system [38], single bubble motion in liquid metal [39], and bubble-driven jet flow [40].

Liquid metal flows are of scientific importance in physics and geosciences. Researchers at the University of Tokyo use mercury for their study of natural convection in a barrel [25, 26], of Ga [41], and the effect of magnetic fields [42, 43]. Brawn et al. obtained chaotic flow motion of Na in spherical Couette flow (Fig. 1.9) [44]. Chaves et al. [45] investigated a bulk flow of a ferrofluid in a uniform rotating magnetic field. The direct velocity measurement in those configurations is now an essential methodology for experimental testing of various theories.

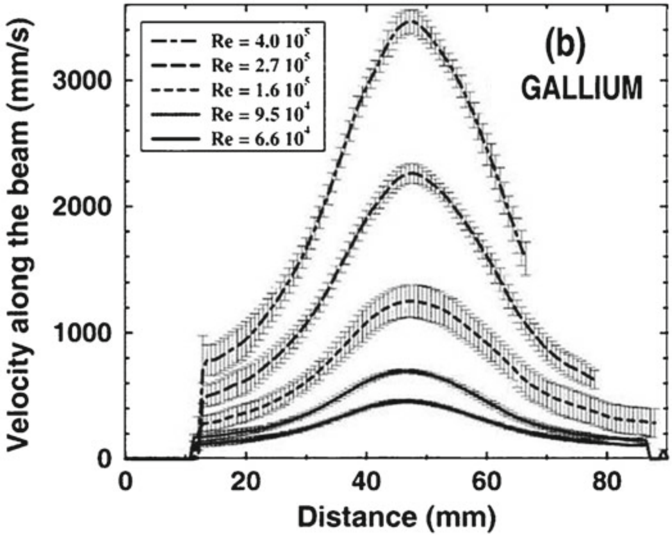

Fig. 1.8 Velocity profile of gallium flow [33] (with kind permission from Springer Science+Business Media)

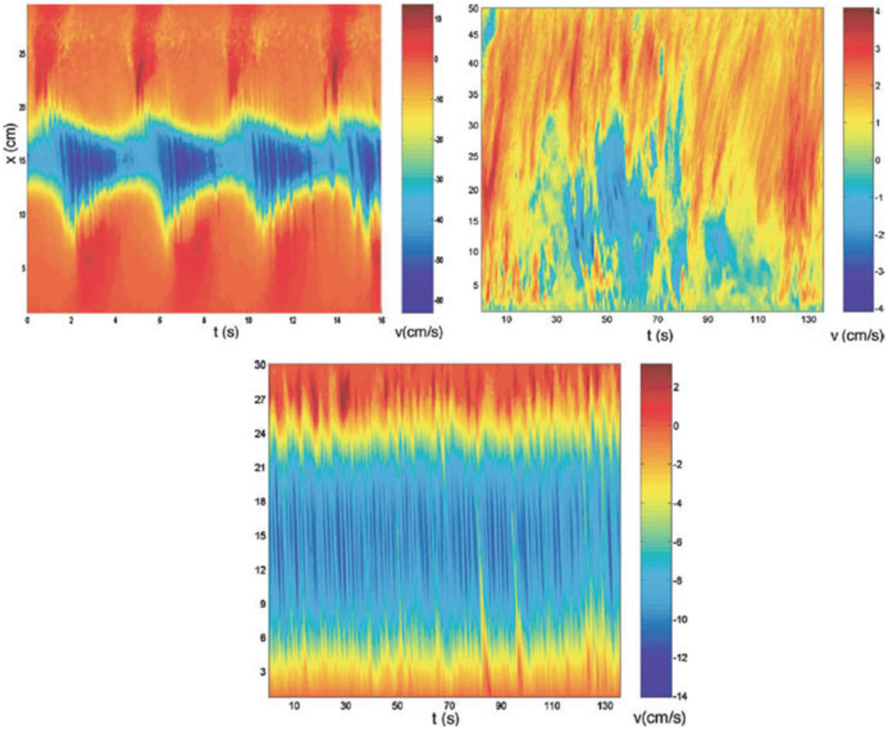

Fig. 1.9 Spatio-temporal velocity field of Na flow (reprinted with permission from [44]. Copyright (2005), American Institute of Physics.)

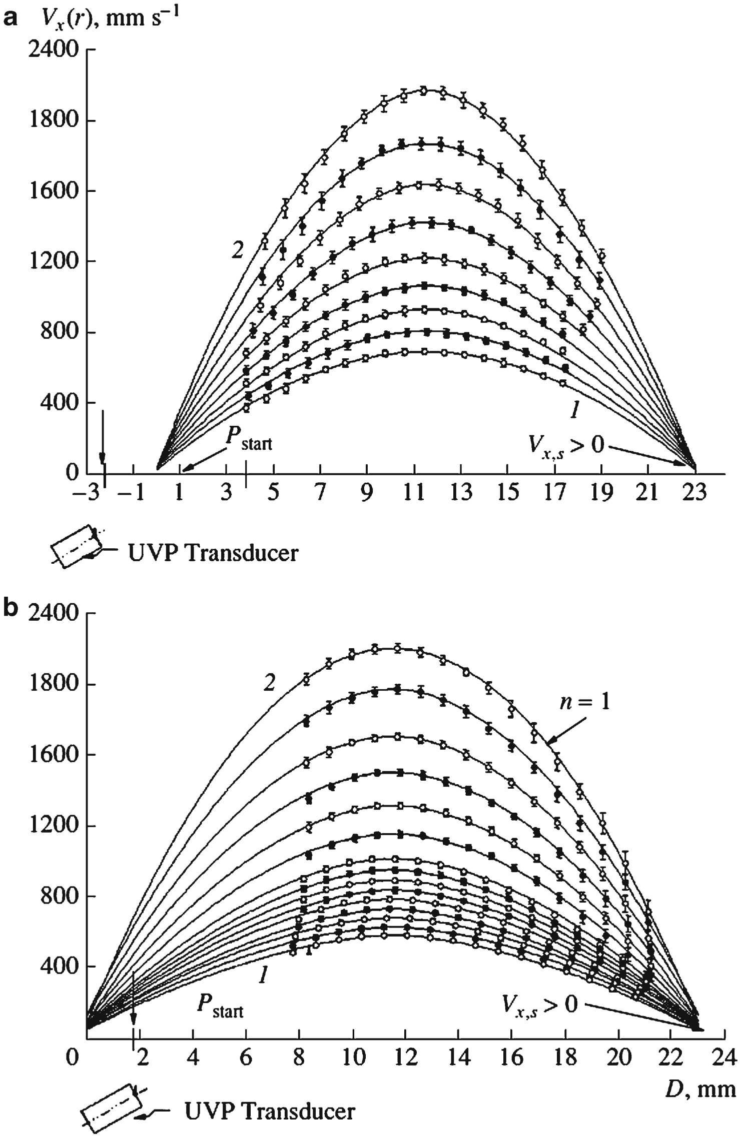

Fig. 1.10 Velocity profile of starch flow in a pipe (a) lower concentration and (b) higher concentration [46] (with kind permission from Springer Science+Business Media)

Opaque liquids other than liquid metals include various industrial substances such as foods and chemical agents. Ouriev [46] applied UVP to a pipe flow of dilatant suspensions of starch, which shows a strongly shear-thickening velocity profile (Fig. 1.10). This work suggested the possibility of setting up an in-line shear viscosity monitoring in combination with pressure drop measurement. They made a flow mapping of food flow in an extruder geometry and demonstrated the high potential of UVP to food flow research, as well as rheological study [47, 48].

A flow with a fiber suspension was investigated by Bergstrom and Vomhoff [49] in a cylindrical hydrocyclone and Xu and Aidun [50] in a rectangular channel. Both studies concluded the high potential of UVP for these substances and indicated that the theoretical models can be validated by measuring the velocity profile for comparison.

Flows of other substances, such as slurry (glass beads) in an air lift reactor [51], and oscillatory flow of sand mixture [52], were also attempted.

There are many more examples for this kind of application, all of which indicate that the use of ultrasound is powerful in flow studies of such substances, especially unique in the methodology of modern EFD.

It should be added that even for transparent liquids such as water, the container walls are often opaque. Because the ultrasonic wave does not need the installation of a special observation window, the investigator is free to choose the measurement position along the channel [53, 54].

1.4 Flow Metering

The capability of measuring the instantaneous velocity distribution in a pipe is changing the paradigm of flow metering. The old paradigm is based on a principle of Heron and is said to be 2,000 years old [55]. Heron's principle states: "… it does not suffice to determine the section of flow, to know the quantity of water ..... It is necessary to find the velocity of the current…". Namely, the volume flow rate was and still is estimated as an average flow velocity times cross-sectional area: $Q = Av$. A paradigm shift has occurred to use the first principle of flow rate as an integral of the total volume or mass flux passing a cross section of the pipe, which corresponds to the integral of velocity distribution over an area [56]:

$$Q(t) = \iint v(r,\theta,t)\, r\, dr\, d\theta \tag{1.1}$$

by assuming an axial symmetry, it is reduced to a simple one-dimensional form as

$$Q(t) = 2\pi \int_0^R v(r,t)\, r\, dr \tag{1.2}$$

It should be noted that the flowrate so obtained is a time-dependent quantity, and this implies the flow meter adopting this principle gives a transient flowrate with high accuracy, which conventional flow meters are unable to measure.

Japanese companies are the main players for the industrial flow metering business. Tokyo Electric Power developed a system called UDFlow to measure the instantaneous flowrate with high accuracy [56]. Because the objective was to use this flow meter in nuclear, fossil, and hydropower plants, validation experiments have been performed at various national standards institutes, such as NIST, NMIJ, NMI, and CENAM [57]. Results of all tests give an extended uncertainty as low as 0.2%, which is a significant improvement over the measurement of flowrate accuracy achieved by conventional devices. Fuji Electric developed and marketed a device called Duosonics, which is a hybrid system of UVP and conventional TOF (time of flight) methods [58]. The device can measure the flowrate of liquids containing bubbles or particles, which cannot be achieved using only the TOF principle.

The combined UVP-TOF methodology has been extended to different flow configurations. Murai et al. [59, 60] developed a multiphase flow metering system where the flowrates of gas and liquid flow were measured obtained separately in the pipe flow configuration. They modified Eq. (1.2) to include the phase distribution

$$Q_L(t) = \iint v(r,\theta,t) f_L(r,\theta,t)\,dr\,d\theta \tag{1.3}$$

for the liquid flowrate. Phase distribution f_{L} is obtained by analyzing the echo signals from multiple transducers or using optical methods.

An environmental flow monitoring system has been developed using the same principle. Velocity distribution of small rivers or channels is measured and integrated over the flowing area. The system is being developed for use in the field by Abda et al. [61] and Yokoyama et al. [62, 63].

1.5 Rheology

The instantaneous velocity distribution is a solution of the governing equations describing the motion of fluid materials. Conventionally, it is said that rheological study does not include the subject of hydrodynamics in itself [64], but fluid dynamicists are now active in this field as well. In addition to those given before in the section (opaque fluids), experiments attempt to determine the model parameters used in the various rheological models describing the dependence of viscosity or viscoelasticity on characteristics of the flow. Mueller and Wunderlich [65] measured velocity distributions for flow in a pipe of Newtonian and non-Newtonian fluids, such as polyacrylamide. From the time-averaged velocity distributions the velocity gradient distribution was calculated, and from that the viscosity function was determined. Ouriev [46] investigated the rheological behavior of non-Newtonian fluids in a pressure-driven shear flow and found a transition between strongly non-Newtonian and Newtonian velocity profiles with increasing flow velocity, and an abrupt reduction of wall slip velocity. This investigation uses theoretical velocity profiles in combination with several viscosity models and comparison was made with the measured profiles to determine model parameters.

Wunderlich and Brunn [66, 67] showed a possible development of a viscometer for process monitoring using UVP. Wiklund et al. [68] applied UVP to various complex model fluids to measure rheological characteristics. Corvisier et al.

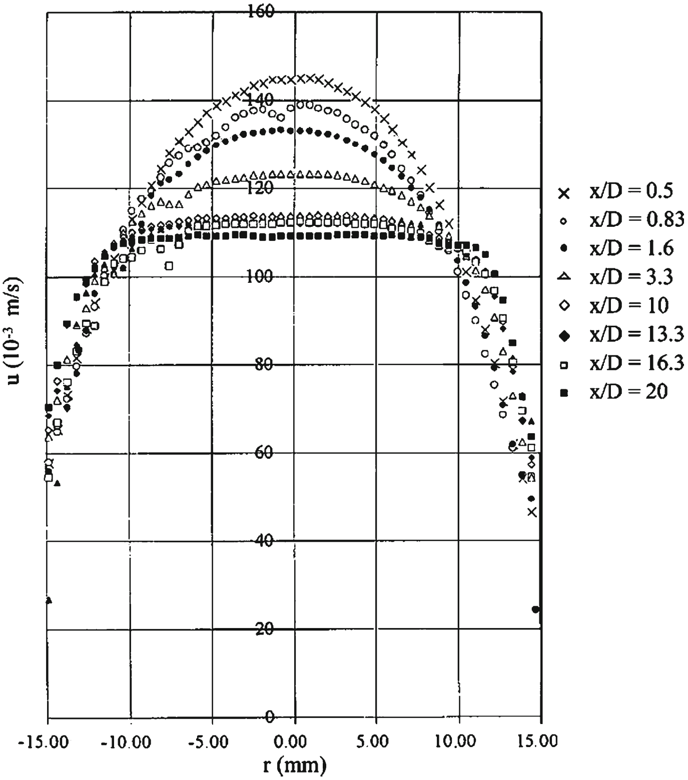

Fig. 1.11 Evolution of axial velocity profile for the Veegum suspension: $U_d = 0.1$ m/s [69] (with kind permission from Springer Science+Business Media)

[69] studied the development of a thixotropic fluid flow in a pipe and used the capability of UVP to record a time series of instantaneous velocity distributions (Fig. 1.11). Dogan et al. constructed a measurement system using UVP to investigate rheological characteristics of tomato concentrate and other polymer melts [70, 71]. The possibility to develop an in-line rheometer using the UVP principle is indicated by these and other investigators [72]. Following publication of the foregoing papers, various rheological materials have been investigated using UVP. Brunn et al. [73] investigated the characteristics of body lotion, which shows a Newtonian behavior up to a yielding point of shear rate where a phase change occurs. Bachelet et al. [74, 75] used the UVP method to validate their indirect determination of a power law viscosity function for a Newtonian fluid. Xu et al. [50] investigated characteristics of fiber suspension flow for different fiber concentrations and included the effect in the normalized velocity profile. Many other groups have carried out studies of the rheological behavior of various industrial substances [76–82].

1.6 Summary

The data obtained by UVP are the instantaneous velocity distribution in differential form. This substantial change of data format from the conventional point measurements has led to a change of methodology in experimental fluid mechanics. Many of the well-known flow configurations might be revisited to obtain new insight into the flow structure and its dynamic behavior.

The development of the UVP technique during its earliest stages was mainly undertaken by medical engineers. We are far from this field, and thus the work related to medical application is not reviewed here. Many investigations of multiphase flow, environmental flow, and in the field of civil engineering are now using the same principle of velocity profiling. Reviewing the work in those fields is out of the author's reach.

One last thing to note is that there is a forum, meeting biannually, where scientists and engineers gather to present progress in their investigations. The name of this forum is ISUD (International Symposium on Ultrasonic Doppler method for Fluid Mechanics and Fluid Engineering). Efforts made by the members of this forum for the development and establishment of the UVP technique are highly acknowledged.

In preparing this review, I am grateful to Dr. G.P. King at University of Lisbon, who worked with me quite often from the early stages of the development work, and Prof. E. Windhab at ETH Zürich for his constant support and collaboration. Many Japanese researchers are also highly appreciated for their contributions to the ongoing development of this method.

References

1. Fox TF (1981) A theoretical and experimental investigation of a range-gated ultrasonic Doppler flow detector. J Phys E Sci Instrum 14:330–334
2. Garbini J, Forster FK, Jorgensen JE (1982) Measurement of fluid turbulence based on pulsed ultrasound techniques. Part 1. Analysis. J Fluid Mech 118:445–470
3. Garbini J, Forster FK, Jorgensen JE (1982) Measurement of fluid turbulence based on pulsed ultrasound techniques. Part 2. Experimental investigation. J Fluid Mech 118:471–505
4. Takeda Y (1986) Velocity profile measurement by ultrasound Doppler shift method. Int J Heat Fluid Flow 7(4):313–318
5. Teufel M, Trimis D, Lohmueller A, Takeda Y, Durst F (1992) Determination of velocity profiles in oscillating pipe-flows by using laser Doppler velocimetry and ultrasonic measuring devices. Flow Meas Instrum 3(2):95–101
6. Takeda Y, Kobashi K, Fischer WE (1990) Observation of the transient behavior of Taylor vortex flow between rotating concentric cylinders after sudden start. Exp Fluids 9:317–319
7. Takeda Y, Fischer WE, Kobashi K, Takada T (1992) Spatial characteristics of dynamic properties of modulated wavy vortex flow in a rotating Couette system. Exp Fluids 13:199–207
8. Takeda Y, Fischer WE, Sakakibara J, Ohmura K (1993) Experimental observation of the quasiperiodic modes in a rotating Couette system. Phys Rev E 47:4130–4134
9. Tokuhiro A, Takeda Y (1993) Measurement of flow phenomena using the ultrasonic velocity profile method in a simulated Czochralski crystal puller. J Cryst Growth 130:421–432

10. Takeda Y, Fischer WE, Sakakibara J (1993) Measurement of energy spectral density of a flow in a rotating Couette system. Phys Rev Lett 70:3569–3571
11. Takeda Y, Fischer WE, Sakakibara J (1994) Decomposition of the modulated waves in a rotating Couette system. Science 263:502–505
12. Aider JL, Wesfried JE (1996) Characterization of longitudinal Göertler vortices in a curved channel using ultrasonic Doppler velocimetry and visualizations. J Phys III Fr 6:893–906
13. Le Gal P, Peschard I, Chauve MP, Takeda Y (1996) Collective behavior of wakes downstream a row of cylinders. Phys Fluids 8:2098–2106
14. Schouveiler L, Le Gal P, Chauve MP, Takeda Y (1999) Spiral and circular waves in the flow between a rotating and a stationary disk. Exp Fluids 26:179–187
15. Peschard I, Le Gal P, Takeda Y (1999) On the spatio-temporal structure of cylinder wakes. Exp Fluids 26:188–196
16. Alfonsi G (2001) Analysis of streamwise velocity fluctuations in turbulent pipe flow with the use of an ultrasonic Doppler flowmeter. Flow Turbulence Combust 67:137–142
17. Alfonsi G, Brambilla S, Chiuch D (2003) The use of an ultrasonic Doppler velocimeter in turbulent pipe flow. Exp Fluids 35:553–559
18. Le Guer Y, Reghem P, Petit I, Stutz B (2003) Experimental study of a buoyant particle dispersion in pipe flow. Trans I Chem Eng 81(Part A):1136–1143
19. Mordant N, Metz P, Michel O, Pinton JF (2001) Measurement of Lagrangian velocity in fully developed turbulence. Phys Rev Lett 87:214501
20. Inoue Y, Yamashita S, Kumada M (1999) An experimental study on a wake behind a torus using the UVP monitor. Exp Fluids 26:197–207
21. Ern P, Wesfried JE (2002) Time behavior of the secondary flow between time-periodically corotating cylinders: a two-frequency forcing case. Phys Rev E 65:047301
22. Lusseyran F, Izrar B, Audemar C, Skali-lami S (2003) Time–space characteristics of stratified shear layer from UVP measurements. Exp Fluids 35:32–40
23. Inoue Y, Yamashita S, Kondo K (2002) The ultrasonic velocity profile measurement of flow structure in the near field of a square free jet. Exp Fluids 32:170–178
24. Furuichi N, Takeda Y, Kumada M (2003) Spatial structure of the flow through an axisymmetric sudden expansion. Exp Fluids 34:643–650
25. Mashiko T, Tsuji Y, Mizuno T, Sano M (2004) Instantaneous measurement of velocity fields in developed thermal turbulence in mercury. Phys Rev E 69:036306
26. Tsuji Y, Mizuno T, Mashiko T, Sano M (2005) Mean wind in convective turbulence of mercury. Phys Rev Lett 94:034501
27. Frisch U, Orszag SA (1990) Turbulence: challenges for theory and experiment. Phys Today 43:24–32
28. Fowlis WW (1973) Liquid metal flow measurements using an ultrasonic Doppler velocimeter. Nat Phys Sci 242:12–13
29. Takeda Y (1987) Measurement of velocity profile of mercury flow by ultrasound Doppler-shift method. Nucl Technol 79:120–124
30. Kikura H, Takeda Y, Durst F (1999) Velocity profile measurement of the Taylor vortex flow of a magnetic fluid using the ultrasonic Doppler method. Exp Fluids 26:208–214
31. Kikura H, Takeda Y, Sawada T (1999) Velocity profile measurements of magnetic fluid flow using ultrasonic Doppler method. J Magn Magn Mater 201:276–280
32. Sawada T, Kikura H, Tanahashi T (1999) Kinematic characteristics of magnetic fluid sloshing in a rectangular container. Exp Fluids 26:215–221
33. Brito D, Nataf HC, Carddin P, Aubert J, Masson JP (2001) Ultrasonic Doppler velocimetry in liquid gallium. Exp Fluids 31:653–663
34. Aubert J, Brito D, Nataf HC, Cardin P, Masson JP (2001) A systematic experimental study of rapidly rotating spherical convection in water and liquid gallium. Phys Earth Planet In 128:51–74
35. Eckert S, Gerbeth G (2002) Velocity measurements in liquid sodium by means of ultrasound Doppler velocimetry. Exp Fluids 32:542–546
36. Cramer A, Eckert S, Galindo V, Gerbeth Gm Willers B, Witke W (2004) Liquid metal model experiments on casting and solidification processes. J Mater Sci 39:7285–7294

37. Raebiger D, Eckert S, Gerbeth G (2010) Measurements of an unsteady liquid metal flow during spin-up driven by a rotating magnetic field. Exp Fluids 48:233–244
38. Eckert S, Gerbeth G, Melnikov VI (2003) Velocity measurements at high temperatures by ultrasound Doppler velocimetry using an acoustic wave guide. Exp Fluids 35:381–388
39. Zhang C, Eckert S, Gerbeth G (2005) Experimental study of single bubble motion in a liquid metal column exposed to a DC magnetic field. Int J Multiphase Flow 31:824–842
40. Zhang C, Eckert S, Gerbeth G (2007) The flow structure of a bubble-driven liquid-metal jet in a horizontal magnetic field. J Fluid Mech 575:57–82
41. Yanagisawa T, Yamagishi Y, Hamano Y, Tasaka Y, Yoshida M, Yano K, Takeda Y (2010) Structure of large-scale flows and their oscillation in the thermal convection of liquid gallium. Phys Rev E 82:016320
42. Yanagisawa T, Yamagishi Y, Hamano Y, Tasaka Y, Yano K, Takahashi J, Takeda Y (2010) Detailed investigation of thermal convection in a liquid metal under a horizontal magnetic field: suppression of oscillatory flow observed by velocity profiles. Phys Rev E 82:56306
43. Yanagisawa T, Yamagishi Y, Hamano Y, Tasaka Y, Takeda Y (2011) Spontaneous flow reversals in Rayleigh-Bénard convection of a liquid metal. Phys Rev E 83:036307
44. Brawn B, Joshi K, Lathrop DP, Mujica N, Sisan DR (2005) Visualizing the invisible: ultrasound velocimetry in liquid sodium. Chaos 15:041104
45. Chaves A, Rinaldi C, Elborai S, He X, Zahn M (2006) Bulk flow in ferrofluids in a uniform rotating magnetic field. Phys Rev Lett 96:194501
46. Ouriev NB (2002) Investigation of the wall slip effect in highly concentrated disperse systems by means of non-invasive UVP-PD method in the pressure-driven shear flow. Colloid J 64:740–745
47. Ouriev B, Windhab E (2003) Novel ultrasound based time averaged flow mapping method for die entry visualization in flow of highly concentrated shear-thinning and shear-thickening suspensions. Meas Sci Technol 14:140–147
48. Ouriev B, Windhab E (2003) Transient flow of highly concentrated suspensions investigated using the ultrasound velocity profiler–pressure difference method. Meas Sci Technol 14:1963–1972
49. Bergstrom J, Vomhoff H (2004) Velocity measurements in a cylindrical hydrocyclone operated with an opaque fiber suspension. Miner Eng 17:599–604
50. Xu H, Aidun CK (2005) Characteristics of fiber suspension flow in a rectangular channel. Int J Multiphase Flow 31:318–336
51. Wang T, Wang J, Zhao B, Ren F, Jun Y (2004) Local hydrodynamics in an external loop airlift slurry reactor with and without a resistance-regulating element. Chem Eng Commun 191:1024–1042
52. O'Donoghue T, Wright S (2004) Flow tunnel measurements of velocities and sand flux in oscillatory sheet flow for well-sorted and graded sands. Coastal Eng 51:1163–1184
53. Taishi T, Kikura H, Aritomi M (2002) Effect of control volume of UVP method on the turbulent pipe flow measurement. Exp Fluids 32:188–196
54. Wada S, Kikura H, Aritomi M, Mori M, Takeda Y (2004) Development of pulsed ultrasonic Doppler method for flow rate measurement in power plant; multilines flow rate measurement on metal pipe. J Nucl Sci Technol 41:339–346
55. Bud R, Warner DJ (1998) Instruments of science: an historical encyclopedia. Science Museum, London, p 245
56. Mori M, Takeda Y, Taishi T, Furuichi N, Aritomi M, Kikura H (2002) Development of a novel flow metering system using ultrasonic velocity profile measurement. Exp Fluids 32:153–160
57. Mori M (2006) Calibration tests of new type flow metering system by ultrasonic pulse Doppler velocimetry at national standards loops. In: ICONE 14, Miami, 17–20 July 2006
58. Yao H (2004) Advanced hybrid type ultrasonic flow meter utilizing state-of-the-art pulsed Doppler method along with traditional transit time method. In: Proceedings ISUD 4, Sapporo, Japan, 6–8 September 2004
59. Gonzalez SR, Murai Y, Takeda Y (2009) Ultrasound-based gas–liquid interface detection in gas–liquid two-phase flows. In: Li J (ed) Advances in chemical engineering, vol 23. Elsevier, Amsterdam

60. Murai Y, Tasaka Y, Nambu Y, Takeda Y, Gonzalez SR (2010) Ultrasonic detection of moving interfaces in gas–liquid two-phase flow. Flow Meas Inst 21:356–366
61. Abda F, Azbaid A, Ensminger D, Fischer S, Francois P, Schmitt P, Pallares A (2009) Ultrasonic device for real-time sewage velocity and suspended particles concentration measurements. Water Sci Technol 60:117–125
62. Yokoyama K, Kashiwaguma N, Okubo T, Takeda Y (2004) Flow measurement in an open channel by UVP. In: Proceedings, ISUD 4, Sapporo, Japan, 6–8 September 2004
63. Tasaka Y, Takeda Y, Yokoyama Y, Kojima S (2007) Environmental flow field measurement by ultrasonic velocity profiling. In: Proceedings of the 5th joint ASME/JSME fluids engineering conference, 15th forum on industrial and environmental application of fluid mechanics, FEDSM2007-37071
64. Tanner RI (2000) Engineering rheology, 2nd edn. Oxford University Press, Oxford
65. Mueller M, Wunderlich T (1997) New rheometric technique: the gradient-ultrasound pulse Doppler method. Appl Rheol 7(5):204–210
66. Wunderlich T, Brunn PO (1999) Ultrasound pulse Doppler method as a viscometer for process monitoring. Flow Meas Instrum 10:201–205
67. Wunderlich T, Brunn PO (2000) A wall layer correction for ultrasound measurement in tube flow: comparison between theory and experiment. Flow Meas Instrum 11:63–69
68. Wiklund J, Johansson M, Shaik J, Fischer P, Stading M, Hermanson AM (2001) In-line rheological measurement of complex model fluids using ultrasound UVP-PD based method. Ann Trans Nordic Rheol Soc 8(9):128–130
69. Corvisier P, Nouar C, Devienne R, Lebouche M (2001) Development of a thixotropic fluid flow in a pipe. Exp Fluids 31:579–587
70. Dogan H, McCarthy MJ, Powell RL (2002) Comparison of in-line consistency measurement of tomato concentrates using ultrasonic and capillary methods. J Food Process Eng 25:571–587
71. Dogan H, McCarthy MJ, Powell RL (2005) Measurement of polymer melt rheology using ultrasonic-based in-line rheometry. Meas Sci Technol 16:1684–1690
72. Hou YY, Kassim HO (2005) Instrument techniques for rheometry. Rev Sci Instrum 76:101101
73. Brunn PO, Wunderlich T, Mueller M (2004) Ultrasonic rheological studies of a body lotion. Flow Meas Instrum 15:139–144
74. Bachelet C, Dantan P, Flaud P (2003) Indirect on-line determination of Newtonian fluid viscosity based on numerical flow simulations. Eur Phys J Appl Phys 21:67–73
75. Bachelet C, Dantan P, Flaud P (2004) Indirect on-line determination of rheological behavior of a power law fluid based on numerical flow simulations. Eur Phys J Appl Phys 25:209–217
76. Basaran T, McClements DJ (1999) Nondestructive monitoring of sucrose diffusion in oil-in-water emulsions by ultrasonic velocity profiling. J Colloid Interface Sci 220:429–435
77. Ein-Mozaffari F, Bennington CPJ, Dumont GA, Buckingham D (2007) Measuring flow velocity in pulp suspension mixing using ultrasonic Doppler velocimetry. Chem Eng Res Design Trans I Chem Eng Part A 85:591–597
78. Ein-Mozaffari F, Upreti SR (2009) Using ultrasonic Doppler velocimetry and CFD modeling to investigate the mixing of non-Newtonian fluids possessing yield stress. Chem Eng Res Design 87:515–523
79. Pakzad L, Ein-Mozaffari F, Chan P (2008) Using computational fluid dynamics modeling to study the mixing of pseudoplastic fluids with a Scaba 6SRGT impeller. Chem Eng Processing 47:2219–2227
80. Young NWG, Wassell P, Wiklund J, Stading M (2008) Monitoring struturants of fat blends with ultrasound based in-line rheometry. Intl J Food Sci Technol 43:2083–2089
81. Wassell P, Wiklund J, Stading M, Bonwick G, Smith C, Almiron-Roig E, Young NWG (2010) Ultrasound Doppler based in-line viscosity and solid fat profile measurement of fat blends. Int J Food Sci Technol 45:877–883
82. Wiklund J, Stading M, Tragardh C (2010) Monitoring liquid displacement of model and industrial fluids in pipes by in-line ultrasonic rheometry. J Food Eng 99:330–337

Part I
Fundamentals

Chapter 2
Ultrasonic Wave for Fluid Flow

Yasushi Takeda and Yuji Tasaka

Abstract Ultrasonic velocity profilers (UVP) utilize a pulsed ultrasonic beam and the scattering of ultrasonic waves on tracer particles to obtain instantaneous velocity profiles. This chapter summarizes (1) basic characteristics of ultrasonic waves, their propagation, diffraction, inflection, reflection, transmission, interference, and scattering (Sect. 2.3); (2) the formation of pulsed ultrasonic beams (Sects. 2.4 and 2.5); (3) mode transformations between longitudinal and transversal (shear) waves used in flow measurements in pipes with thicker walls (Sect. 2.6); and (4) basics of ultrasonic transducers that generate ultrasonic beams are also explained (Sect. 2.7). All the explanations about ultrasonic waves given here help to understand the principles and configurations of UVP measurements and to distinguish the content that is further highlighted in comparison with other textbooks of ultrasonic physics or ultrasonic techniques.

Keywords Beam formation • Pulsed ultrasonic beam • Ultrasonic transducer • Ultrasonic wave

2.1 Acoustic and Ultrasonic Waves

The ultrasonic waves used in UVP measurements are waves resembling the laser light used for laser Doppler anemometry (LDA), but they have different characteristics. Because ultrasonic waves are invisible, great care must be shown by the user

---

Y. Takeda
Hokkaido University, Sapporo, Japan

Tokyo Institute of Technology, Tokyo, Japan

Y. Tasaka (✉)
Faculty of Engineering, Hokkaido University, Sapporo, Japan
e-mail: tasaka@eng.hokudai.ac.jp

Y. Takeda (ed.), *Ultrasonic Doppler Velocity Profiler for Fluid Flow*,
Fluid Mechanics and Its Applications 101, DOI 10.1007/978-4-431-54026-7_2,

of ultrasonic waves as careless use of ultrasonic waves in measurements may result in erroneous results. This chapter details the basic characteristics of ultrasonic waves, the formation of ultrasonic beams, and the evaluation of the qualities of such beams to enable a detailed understanding of the measurement principles and configurations of UVP.

Acoustic waves are defined as longitudinal and transversal waves of elastic vibration propagating in elastic media. Ultrasonic waves are acoustic waves that have frequencies higher than the audible limit of the human range. There is no exact definition of what constitutes “higher frequencies,” but these are generally assumed to be frequencies of 20 kHz or higher. Because of their short wavelength, ultrasonic waves achieve high directional coherence. The general characteristics of ultrasonic waves are similar to those of acoustic waves and may be explained by the mathematical description of acoustic waves (Sect. 2.2), the basics of the characteristics of the propagation of acoustic waves (Sect. 2.3), the formation of pulsed ultrasonic beams (Sects. 2.4 and 2.5), and mode transformations between longitudinal and transversal (shear) waves that are used in flow measurements in pipes with a thicker wall (Sect. 2.6). This chapter also provides details of the fundamentals of the ultrasonic transducers that generate ultrasonic beams (Sect. 2.7). The explanation of acoustic and ultrasonic waves is provided to ensure an understanding of the principles of UVP measurement, and details of the derivation of equations, etc., are omitted. For readers who require more theoretical information about ultrasonic waves, the works by Povey [1] and Krautkrämer [2] are recommended.

2.2 Mathematical Description of Acoustic Waves

Longitudinal and transversal waves propagating in media as acoustic waves are waves of small volume changes (*longitudinal sound wave*) and deformation waves without volume changes (*shear wave*), respectively. Fluid media, excluding viscoelastic fluids, do not support strains, and as a result shear waves do not propagate in the media. The speed of propagation of the acoustic waves (speed of sound) depends on whether the waves are longitudinal or shear waves, and not only on the medium.

For acoustic waves propagating in fluid media, that is, longitudinal sound waves, the volume changes induced by the propagation of the longitudinal waves are represented as a pressure variation in medium. If the speed of flow of a fluid is sufficiently much slower than the speed of sound in the medium, propagation of acoustic waves is described as fluctuation in pressure P versus the static pressure (pressure without acoustic wave propagation, P_s). Variation in the pressure resulting from wave propagation at a point is defined as the sound pressure:

$$p(x,t) = P - P_s \tag{2.1}$$

The magnitude of the sound pressure is represented by the effective sound pressure:

$$P_{\mathrm{e}} = \sqrt{\frac{1}{T}\int_0^T p^2(t)\mathrm{d}t} \tag{2.2}$$

Usually the sound pressure is very much smaller than the static pressure, and the variations in the physical variables related to the sound pressure are also small, resulting in their squared and higher-order terms becoming negligible in the equations. Acoustic waves caused by volume changes are described by the displacement $\boldsymbol{d}$ of a small volume of the medium at a point $\boldsymbol{x}$ (x, y, z) as

$$p = -K\nabla \boldsymbol{d}, \quad \nabla = \left(\frac{\partial}{\partial x}, \frac{\partial}{\partial y}, \frac{\partial}{\partial z}\right), \tag{2.3}$$

where $\boldsymbol{d}=(\xi, \eta, \zeta)$ is the displacement vector and K is the bulk modulus of the medium. By substituting this into the Eular equations, which are equations of motion for inviscid (nonviscous) fluids, and utilizing the relationship $\partial(\nabla \mathrm{d})/\partial \mathrm{t} = \nabla u(u$ the velocity vector of the fluid particle motion from the propagation of the acoustic wave), the differential equation for p is derived as

$$\frac{\partial p}{\partial t} = \frac{K}{\rho}\Delta p, \quad \Delta = \nabla \cdot \nabla. \tag{2.4}$$

This equation is termed the *wave equation* and indicates that p propagates with the speed of waves traveling in the medium as a wave:

$$c = \sqrt{\frac{K}{\rho}} \tag{2.5}$$

The traveling speed c is the *speed of sound.*

For one-dimensional waves propagating in the x direction [*one-dimensional* (*1D) plane waves*], Eq. (2.4) has a general solution:

$$p(x,t) = F(t - x/c) + G(t + x/c) \tag{2.6}$$

The first and the second terms of Eq. (2.6) represent the progressing wave and the backward-moving wave, respectively. A progressing sinusoidal wave with amplitude A_+ and initial phase φ_{0+} is represented as

$$p_+(x,t) = A_+\sin(2\pi ft - kx + \varphi_{0+}) \tag{2.7}$$

where f and k are the *frequency* (number of oscillations per unit time; $\omega = 2\pi f$ is the *angular frequency*) and the *wave number* (number of oscillations per unit length). The relationship between f, k, and c is expressed by

$$c = \frac{\omega}{k}. \tag{2.8}$$

Further, $\varphi = \omega t - kx + \varphi_0$ is termed the *phase*, and a wave provides the same value for the same phase even for different moments t and different positions x. The distance of propagation of waves for one cycle ($T = 1/f$)

$$\lambda = cT = \frac{c}{f} \tag{2.9}$$

is called the *wavelength*.

By describing the displacement of the fluid particle motion resulting from the wave propagation for 1D plane waves as

$$\xi(x,t) = \xi(t - x/c) \tag{2.10}$$

the velocity of the fluid particle is expressed as

$$u(x,t) = \frac{\partial \xi}{\partial t} = \frac{\mathrm{d}\xi}{\mathrm{d}(t - x/c)}. \tag{2.11}$$

Then, Eq. (2.3) provides the sound pressure:

$$p(x,t) = -K\frac{\partial \xi}{\partial x} = \frac{K}{c}\frac{\mathrm{d}\xi}{\mathrm{d}(t - x/c)} \tag{2.12}$$

As in the foregoing equation, the sound pressure and the velocity of the fluid particle observed at a point are always a proportional relationship and in the same phase for 1D plane waves. The ratio of the pressure to the velocity of fluid particles, $Z = p/u$, is called the *acoustic impedance* and becomes

$$Z = \frac{p}{u} = \rho c \tag{2.13}$$

for 1D plane waves (according to Eq. (2.5), $K = \rho c^2$). With Eq. (2.13), Z is a specific constant for a medium, and it is also called the *characteristic acoustic resistance*. This value has great importance with more than one medium.

2.3 Fundamentals of Propagation

The propagation characteristics of acoustic wave are as those for other waves; for example, there are diffraction, inflection, reflection, transmission, and interference. Consideration of these characteristics is important in designing measurement systems and particulars of the formation of ultrasonic beams.

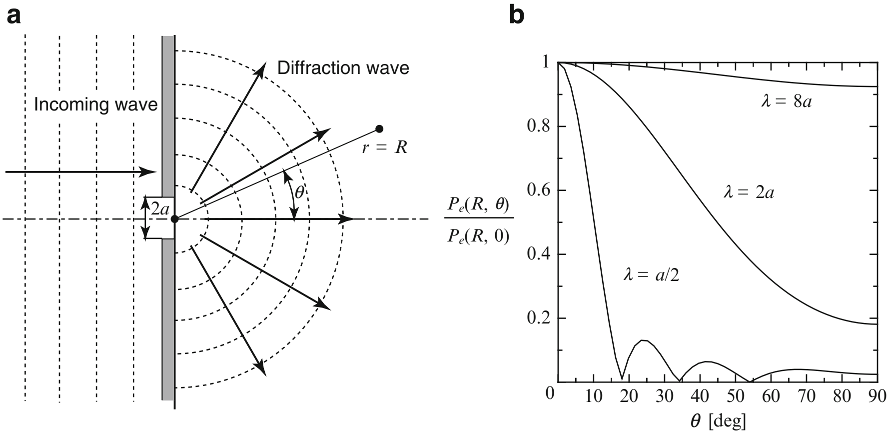

Fig. 2.1 (**a**) Diffraction of a plane wave passing through a gap. (**b**) Broadening of waves as a result of diffraction versus wavelength

2.3.1 *Diffraction*

Diffraction is the phenomenon in which waves encountering an obstacle move around it and continue movement beyond the obstacle. Figure 2.1a is an example of diffraction, where a plane wave moves perpendicularly into a plate with a gap $2a$. In this situation a part of the wave passes through this gap and propagates behind the plate as if emitted by a point source at the center of the gap. The further propagation and broadening of the wave depend on the wavelength of the incident wave, λ, relative to the size of the gap. The sound pressure $P_\mathrm{e}(r, \theta)$, relative to that at the axis of the gap, $P_\mathrm{e}(r, 0)$, varies with the propagation angle θ. The variation of P_e at the distance from the gap, $r = R$, is shown in Fig. 2.1b, where the position $r = R$ is assumed to be far enough from the gap. The influence of the diffraction becomes negligibly small when the gap size is large compared to the wavelength.

2.3.2 *Reflection, Transmission, and Inflection at an Interface*

The interface considered here is defined as the boundary between two media that have different acoustic impedances (Eq. (2.13)), as suggested in Fig. 2.2. When an acoustic wave reaches an interface at an angle θ_1, the amplitudes of the sound pressures of the incident wave, p_i, the reflected wave, p_r, and the transmitted wave, p_t, are related as

$$p_\mathrm{r} = \frac{Z_2 \cos\theta_1 - Z_1 \cos\theta_2}{Z_2 \cos\theta_1 + Z_1 \cos\theta_2} p_\mathrm{i}, \tag{2.14}$$

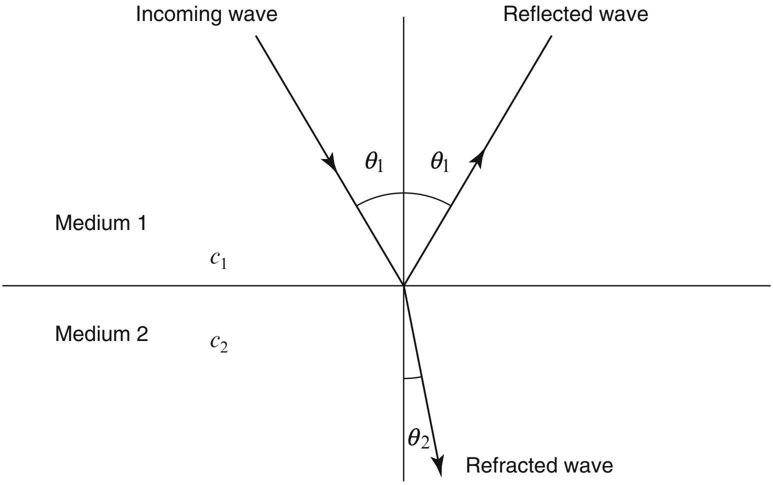

Fig. 2.2 Reflection, transmission, and inflection at an interface between two different media

$$p_t = p_i + p_r. \tag{2.15}$$

The reflection coefficient R is defined as the ratio of the amplitude of the acoustic pressure of the reflected wave to that of the incident wave,[1] and Eq. (2.14) becomes

$$R = \frac{p_r}{p_i} = \frac{Z_2\cos\theta_1 - Z_1\cos\theta_2}{Z_2\cos\theta_1 + Z_1\cos\theta_2}. \tag{2.16}$$

The transmission coefficient T is the ratio of the acoustic pressure amplitude of the transmitted wave to that of the incident wave, and with Eqs. (2.15) and (2.16)

$$T = \frac{p_t}{p_i} = 1 - R = \frac{2Z_1\cos\theta_2}{Z_2\cos\theta_1 + Z_1\cos\theta_2}. \tag{2.17}$$

Equations (2.16) and (2.17) indicate that the incident wave and the transmitted wave are in phase, but that the reflected wave is the phase opposite to the incident wave when $Z_1 > Z_2$. With incident waves crossing from a liquid medium to a gas medium, $Z_1 \gg Z_2$, T may be assumed zero, and the reflected wave is in the phase opposite to the incident wave.

The inflection of the wave at the interface follows Snell's law, which represents the incident angle θ_1 and inflected angle θ_2 as

---

[1] R is sometime expressed using square of p as an energy ratio.

$$\frac{\sin\theta_1}{\sin\theta_2} = \frac{c_1}{c_2} \tag{2.18}$$

where c_1 and c_2 represent the speed of sound in the respective media. With this equation, $\theta_2 = 90°$ suggests that all the incident waves are reflected at the interface and θ_1 in this condition is termed the *critical angle* ($\theta_1 = \sin^{-1}(c_1/c_2)$): acoustic waves cannot penetrate an interface with incident angles that are larger than this critical angle. When ultrasonic transducers are mounted on the outside walls of a flow channel, the angle of attachment of transducers must be smaller than this critical angle. Where there are extremely small differences in the acoustic impedance between two media, the transmission coefficient also becomes extremely small even though the incident angle is larger than the critical angle; this makes it critical to show great care in the selection of the material of the wall. If there is no possibility of choosing a suitable material, impedance matching becomes necessary. Impedance matching is achieved by putting a material with intermediate acoustic impedance between the fluid and the channel wall material on the wall. In the selection of tracer particles, large differences in the acoustic impedance of fluid and particles must be considered together with the traceability of the flows (see Sects. 3.2.3 and 3.3.5).

2.3.3 Interference

The wave equation is linear, and solutions can be superimposed; for instance, the interference of two plane waves expressed by Eq. (2.7), p_{+1} and p_{+2}, which have the same frequency and the same wave number, provides a wave (a *synthetic wave*) expressed by

$$p_+(x,t) = p_{+1} + p_{+2} = A_{+1}\sin(\varphi_1) + A_{+2}\sin(\varphi_2) = A_+\sin(\varphi) \tag{2.19}$$

where $\varphi_n = \omega t - kx + \varphi_{0n}$ ($n = 1$ or 2), $\varphi = \omega t - kx + \varphi_0$, and A_+ and φ_0 are, respectively,

$$A_+ = \sqrt{A_{+1}^2 + A_{+2}^2 + 2A_{+1}A_{+2}\cos(\varphi_{01} - \varphi_{02})}\,, \tag{2.20}$$

$$\tan\varphi_0 = \frac{A_{+1}\sin\varphi_{01} + A_{+2}\sin\varphi_{02}}{A_{+1}\cos\varphi_{01} + A_{+2}\cos\varphi_{02}}\,. \tag{2.21}$$

These equations indicate that interference increases the amplitude of synthetic waves with the same phase and reduces the amplitude for phase differences of a half cycle.

Next, the interference between an incoming wave perpendicular to an interface and its reflected wave is considered. Describing the sound pressure of the incident wave p_i and the reflected wave p_r as

$$p_{\mathrm{i}}(x,t) = A_{\mathrm{i}} \sin(\omega t - kx + \varphi_{0i}), \tag{2.22}$$

$$p_{\mathrm{r}}(x,t) = A_{\mathrm{r}} \sin(\omega t + kx + \varphi_{0r}), \tag{2.23}$$

the synthetic wave becomes

$$p(x,t) = p_{\mathrm{i}} + p_{\mathrm{r}} = A(x)\sin(\omega t + \varphi(x)). \tag{2.24}$$

The amplitude and phase of the synthetic wave are expressed as

$$A(x) = \sqrt{A_{\mathrm{i}}^2 + A_{\mathrm{r}}^2 + 2A_{\mathrm{i}}A_{\mathrm{r}}\cos[2kx - (\varphi_{0i} - \varphi_{0r})]} \tag{2.25}$$

$$\tan\varphi(x) = \frac{-A_{\mathrm{i}}\sin(kx - \varphi_{0i}) + A_r\sin(kx + \varphi_{0r})}{A_i\cos(kx - \varphi_{0i}) + A_r\cos(kx + \varphi_{0r})} \tag{2.26}$$

In the foregoing equation, the amplitude of the wave is a function of *x* and reaches a maximum, $A_{\mathrm{max}} = A_{\mathrm{i}} + A_{\mathrm{r}}$, at

$$x = -m\frac{\lambda}{2} + \frac{\varphi_{0i} - \varphi_{0r}}{2\pi}\frac{\lambda}{2} \quad (m = 0,1,2,\ldots) \tag{2.27}$$

(λ is the wavelength) and a minimum value, $A_{\mathrm{min}} = A_{\mathrm{i}} - A_{\mathrm{r}}$, at

$$x = -m\frac{\lambda}{2} - \frac{\lambda}{4} + \frac{\varphi_{0i} - \varphi_{0r}}{2\pi}\frac{\lambda}{2} \quad (m = 0,1,2,\ldots). \tag{2.28}$$

The variation in the amplitude in the *x* direction takes the maximum and minimum values alternating with a period of $\lambda/4$, and the wave motion appears to be stable (unchanging). Such synthetic waves are termed *standing waves*.

2.3.4 Scattering

When acoustic waves are reflected at a finite interface, the reflected wave is generated with infraction, and this has a distribution of sound pressure intensities in the angular direction: this is called *scattering*. At the *long wavelength limit* (the *Rayleigh limit*), where the wavelength of the incident ultrasonic wave, λ, is greater than the diameter of the particle, *d*, causing the scattering, the situation of the scattering becomes simplified. For spherical interfaces the reflected wave has the typical lobe-shaped characteristic, where the intensity becomes large in the direction of the propagation of the incident wave as well as in the opposite direction (Fig. 2.3): these are called *front- and back-scattering*. UVP utilizes this back-scattering to obtain ultrasonic echo information from tracer particles. The distribution of the intensity is the result of visco-inertia scattering of the ultrasonic wave, and particles that have larger

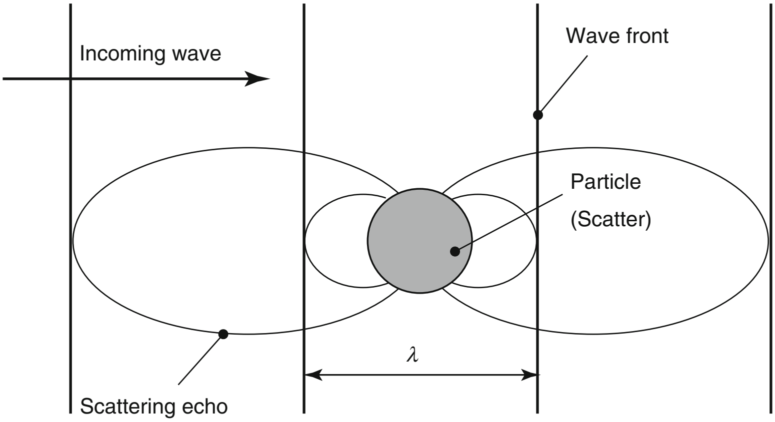

Fig. 2.3 Schematic illustration of ultrasonic scattering from a particle that is smaller than the wavelength of the ultrasonic wave

differences in the densities relative to the fluid provide larger scattering echo intensities. Microbubbles, therefore, would be good scatters, but it is also necessary to consider flow traceability (see Sect. 3.3.5).

2.3.5 Reflection and Transmission at Multiple Interfaces

So far the discussion has considered a single interface and its reflection, transmission, and diffraction. In actual situations, however, it is often necessary to take account of multiple interfaces. This section considers a situation with two layers of the same material (material 1) on both sides of a plate of a different material (material 2) with a finite thickness, *d* (Fig. 2.4). When an acoustic wave propagates perpendicularly to the interface, reflection and transmission occur at the boundaries between material 1 and plate (material 2), and again at plate and material 1. Describing the impedance ratio between the materials as

$$m = \frac{Z_1}{Z_2}. \tag{2.29}$$

The overall transmission coefficient and reflection coefficient including the two boundaries are expressed as

$$T_{plate} = \frac{1}{\sqrt{1 + \frac{1}{4}\left(m - \frac{1}{m}\right)^2 \sin^2 \frac{2\pi d}{\lambda}}} \tag{2.30}$$

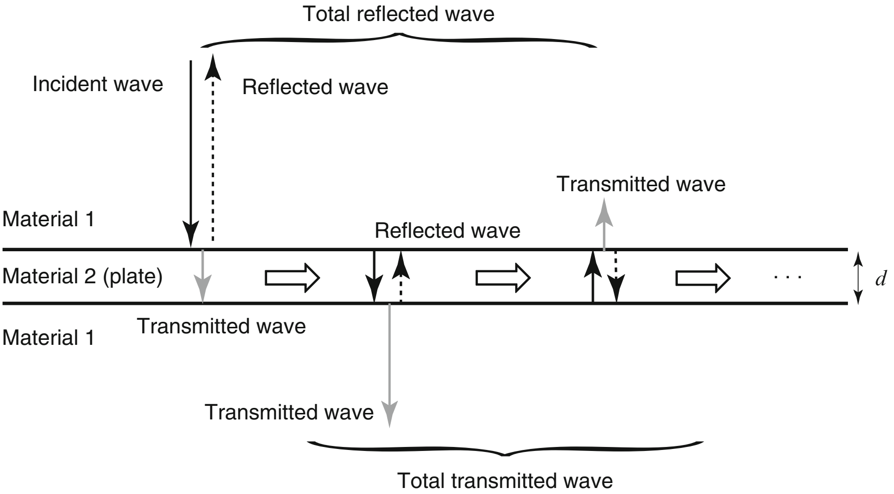

Fig. 2.4 Schematic diagram of multiple reflections and transmission

$$R_{plate} = \sqrt{\frac{\frac{1}{4}\left(m-\frac{1}{m}\right)^2 \sin^2 \frac{2\pi d}{\lambda}}{1+\frac{1}{4}\left(m-\frac{1}{m}\right)^2 \sin^2 \frac{2\pi d}{\lambda}}} \tag{2.31}$$

where λ is the wavelength in the plate (material 2). From the foregoing equations the transmission and reflection coefficients vary periodically depending on the d to λ ratio. The reflection coefficient becomes the minimum (the transmission coefficient becomes the maximum) at $d/\lambda = n/2$ ($n = 0, 1, 2, \ldots$) and becomes the maximum (transmission rate becomes the minimum) at $d/\lambda = (2n+1)/4$ ($n = 0, 1, 2, \ldots$). Therefore, the optimum thickness of the plate for transmitting acoustic waves would be half the wavelength in the plate.

2.4 Formation and Characteristics of Ultrasonic Beams

The previous sections considered plane or spherical waves. In UVP measurements, however, ultrasonic beams that have high directional coherence are utilized. The width of the beams determines the size of the measurement volume in UVP measurements, and the width should be kept small to enable high spatial resolution. The following section considers the formation of ultrasonic beams and the characteristic properties of the beams.

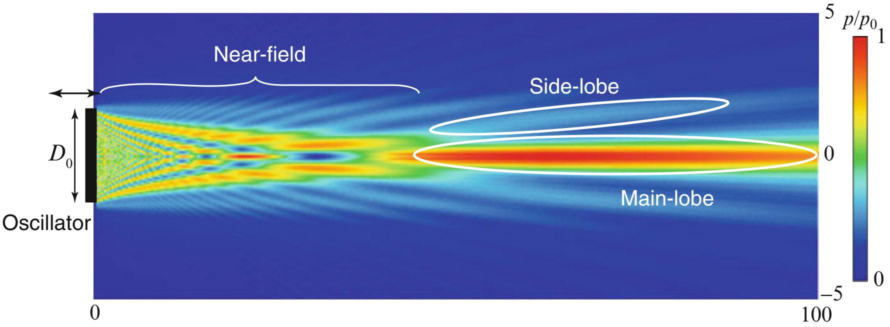

Fig. 2.5 Shape of an ultrasonic beam from an oscillator (sound pressure field) by numerical simulation of the wave equation (Eq. (2.4)) under the conditions diameter of oscillator $D = 7$ mm, frequency $f = 8$ MHz, in water)

Fig. 2.6 Schematic representation of group of spherical waves formed on an oscillator

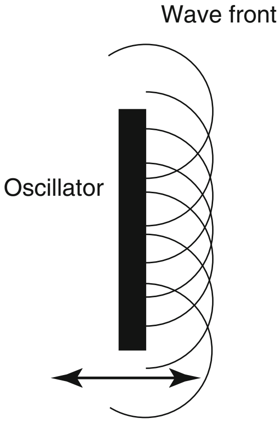

2.4.1 *Formation of Ultrasonic Beams*

Figure 2.5 shows an ultrasonic beam formed by periodic oscillations of a disk-like oscillator with diameter D_0. The sound pressure field displayed here is the numerical solution of the wave equation (Eq. (2.4)) normalized by its maximum value. The conditions for the calculation are the medium is water (speed of sound $c = 1{,}480$ m/s), $D_0 = 7$ mm, and frequency $f = 8$ MHz. The acoustic waves generated by the oscillation of a finite plate can be considered as a group of spherical waves generated by multiple sound sources across the plate (Fig. 2.6). Near the oscillator, the area called the *near-field*, a complex sound field is formed as a result of the interference of the waves: this area is not suitable for UVP measurements because of the nonuniform sound pressures. Further from the oscillator, the sound pressure gradually becomes stable and creates a beam-like distribution with higher directional coherence; this beam-like distribution of the sound pressure is termed the *main lobe*. Away from the

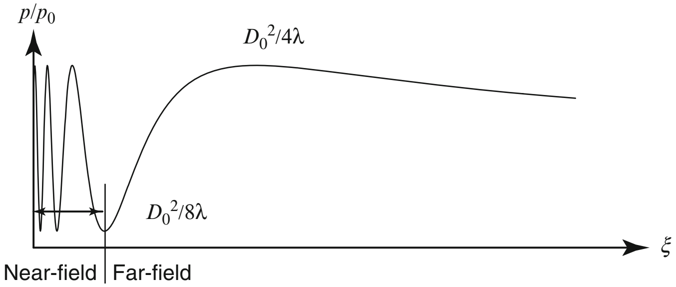

Fig. 2.7 Variations in the sound pressure on the central axis of an ultrasonic beam

main lobe, relatively higher sound pressure regions are also formed; these are termed *side lobes* and may be a source of erroneous results in UVP measurements.

2.4.2 Near-Field and Far-Field

The sound pressure distribution in ultrasonic beams formed by an oscillator along the central axis of the propagation, ξ, is given as

$$p / p_0 = 2\sin\left\{\frac{\pi}{\lambda}\left[\sqrt{\left(\frac{D_0}{2}\right)^2 + \xi^2} - \xi\right]\right\}. \tag{2.32}$$

The equation shows that the variation of the sound pressure depends on the wavelength λ and the diameter of the oscillator D_0, and Fig. 2.7 shows the variation of the sound pressure along the axis. As was also shown in Fig. 2.4, the sound pressure changes intricately near the oscillator and has many extreme values, but the variations become monotonic after the minimal point at $\xi = D_0^2/(8\lambda)$ and decrease gradually after the maximal point at $\xi = D_0^2/(4\lambda)$. The region of $\xi < D_0^2/(8\lambda)$ in an ultrasonic wave is defined as the *near-field* (NF) and the region beyond this point is defined as the *far-field*. The length of the near-field is

$$\xi_{NF} = \frac{D_0^2}{8\lambda} \tag{2.33}$$

and smaller oscillators and longer wavelengths result in shorter near-fields.

2.4.3 Divergence and Attenuation of Ultrasonic Waves

To quantify the variation in the intensity of ultrasonic waves, the *sound pressure level* (SPL) concept is introduced: this expresses the intensity of the sound pressure in dB and is given by

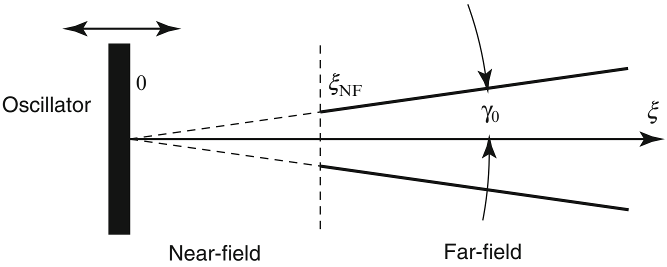

Fig. 2.8 Divergence of an ultrasonic beam formed by a circular oscillator

$$L_p = 20\log_{10}\frac{P_e}{P_{e0}}[dB]. \tag{2.34}$$

Attenuation of an ultrasonic beam is the result of divergence of the circular beam (as suggested in Fig. 2.8) and also of absorption of energy by the media the beam penetrates. In the far-field the maximum pressure is always at the center line of the beam. Defining a divergence angle of the beam, γ_0, as the half-width of the sound pressure (−6 dB), the angle is given by the wavelength, λ, and diameter of the oscillator, D_0, as

$$\gamma_0 = \sin^{-1}\left(0.70\frac{\xi}{D_0}\right). \tag{2.35}$$

Figure 2.9 shows a simple estimate of the beam divergence for different oscillator sizes, D_0, where D represents the beam diameter of the half-width of the sound pressure. The conditions for the estimates in Fig. 2.9 are the frequency, $f_0 = 2$ MHz; the speed of sound, $c = 1{,}480$ m/s (water); and $D_0 = 5$ mm and 10 mm. Depending on the initial diameter of the beam, the ultrasonic beam for $D_0 = 5$ mm has a smaller diameter than that of $D_0 = 10$ mm until $\xi \sim 50$ mm. However, the initial advantage disappears at $\xi > 50$ mm, and thus the oscillator with $D_0 = 10$ achieves a finer ultrasonic beam at $\xi > 50$ mm.

Absorption of ultrasonic energy is classified by the viscosity, thermal conduction, and molecular absorption of the media. The acoustic pressure at counting for the absorption for plane waves that propagate to the ξ direction is expressed as

$$P_e = P_{e0}\exp(-\alpha\xi). \tag{2.36}$$

Here α is the attenuation coefficient, and the viscosity and thermal conduction are given as

$$\alpha = \frac{\omega^2}{2\rho c^3}\left(\frac{4\mu}{3} + \frac{\kappa(\gamma - 1)}{c_p}\right). \tag{2.37}$$

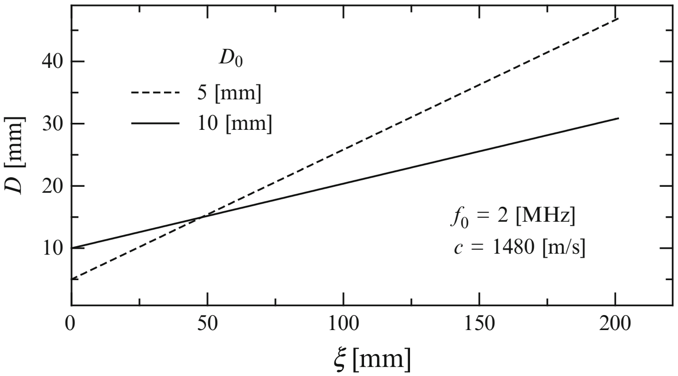

Fig. 2.9 Influence of diameter of the oscillators on the divergence of ultrasonic beams, for oscillator diameters of 5 and 10 mm

where μ, c_p, κ, and γ are the viscosity, specific heat, thermal diffusivity, and specific heat ratio of fluids, respectively. According to the foregoing equation, α increases in proportion to the square of the frequency of the ultrasonic wave (angular frequency, ω). The molecular absorption is attenuated by oscillation of the molecules constituting the fluid medium, resulting from the propagation of ultrasonic waves. The oscillation depends on the wavelength λ as well as the size of molecules and their structure, resulting in estimates of the absorption characteristics becoming difficult for complex molecules such as polymers.

2.5 Continuous and Pulsed Waves

The formation of ultrasonic beams in Figs. 2.5 and 2.7 is for continuous waves that are generated by continuous oscillations of an oscillator. Ultrasonic waves used in UVP measurements are pulsed waves, and the pulse length determines the size (axial extent) of the measurement volume; to keep the measurement volume small, pulse lengths should be as small as possible. However, a small number of cycles in the pulse do not provide clear beams because of a lack of interference in the near-field; for example, a one-cycle pulse forms spherical waves (Fig. 2.10a) with the divergence angle of the beam extremely wide, and a four-cycle pulse (Fig. 2.10b) achieves packet-like beams with high directional coherence. In practice, pulsed waves with four or more cycles are conventionally regarded as continuous waves and have propagation characteristics equivalent to continuous waves. The number of cycles required to form a pulsed ultrasonic beam was evaluated by numerical simulations of the wave equation; the four-cycle case is shown in Fig. 2.11.

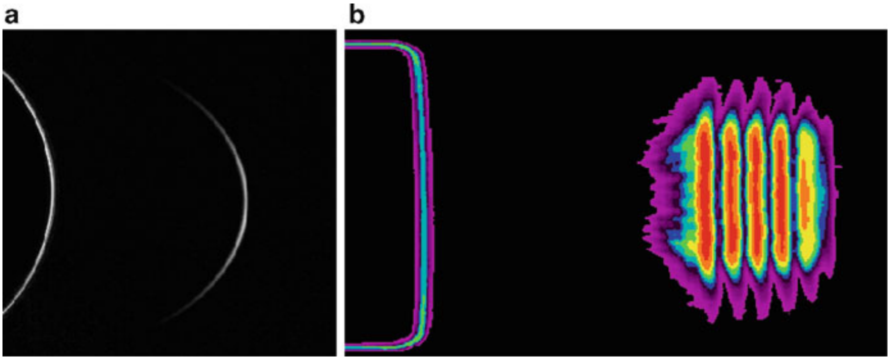

Fig. 2.10 Ultrasonic wave formed by a one-cycle pulse (**a**) and a four-cycle pulse (**b**)

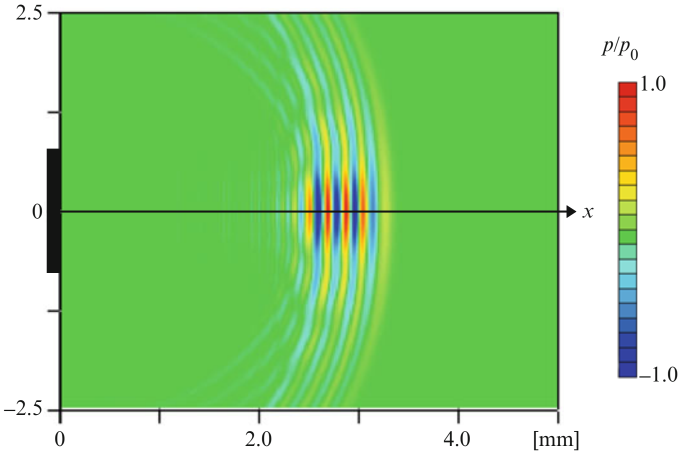

Fig. 2.11 Sound pressure field for a pulsed ultrasonic beam with four-cycles (numerical simulation)

2.6 Mode Transformation

2.6.1 Acoustic Wave and Speed of Sound in Solid Media

In solid media, there are both longitudinal waves resulting from volumetric changes and transverse shear waves from deformations without volumetric changes, a situation that does not occur in liquid media. The speed of propagation of longitudinal waves in a solid medium is given as

$$c_l = \sqrt{\frac{E}{\rho}\frac{1-\mu}{(1+\mu)(1-2\mu)}}\,. \tag{2.38}$$

The speed of the shear waves is

$$c_s = \sqrt{\frac{E}{\rho}\frac{1}{2(1+\mu)}} = \sqrt{\frac{G}{\rho}}\,, \tag{2.39}$$

where E, ρ, G, and μ are the Young's modulus, density, modulus of shear, and Poisson's ratio, respectively, and the two kinds of sound speeds, c_l and c_s, are related in the following equation:

$$c_s = c_l\sqrt{\frac{1-2\mu}{2(1-\mu)}} \equiv c_l\Gamma \tag{2.40}$$

μ takes a value from 0 to 0.5, and Γ in the above equation has a value from 0 to 0.707. Thus, the speed of propagation of the shear wave is slower than that of the longitudinal wave, and the maximum is about 70% of the longitudinal wave.

2.6.2 Mode Transformation between Longitudinal and Shear Waves

When an acoustic wave crosses a liquid–solid interface obliquely (Fig. 2.12), the incident wave does not generally keep its original mode (longitudinal and shear modes) and the wave becomes divided into several reflected and transmitted waves with different modes (a *mode transformation*). The following considers the mode transformation of these cases: (a) a longitudinal wave propagating in a liquid medium entering a solid medium; (b) a longitudinal wave propagating in a solid medium entering a liquid medium; and (c) a shear wave propagating in a solid medium crossing a solid–liquid interface (Fig. 2.12).

As above, acoustic waves propagating in liquid media are only longitudinal waves. However, as shown in Fig. 2.12a, a shear wave is generated as the result of the mode transformation at the transmission into the solid medium, when the longitudinal wave in a liquid medium crosses the liquid–solid interface at an angle α. The angle of propagation of the shear wave is determined by Snell's law as $\sin\alpha_t/\sin\alpha = c_s/c$, where c and c_s are the speed of sound in liquid media (Eq. (2.5)) and the speed of the shear wave propagating in the solid medium (Eq. (2.39)). The reflection coefficient in this case is determined by the speeds of sound (c_l is the speed of sound for the longitudinal wave propagating in the solid medium) and density (ρ is for the liquid and ρ_s is for the solid media) in the two media, and also the angles of propagation of the waves (α_l is the inflection angle of the longitudinal wave in the solid medium) as

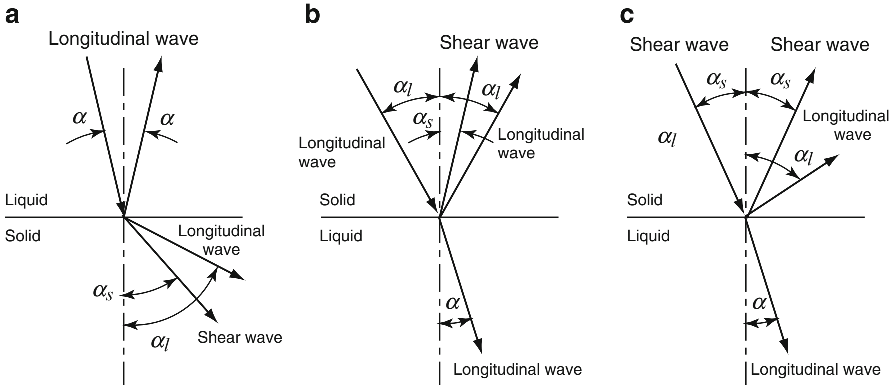

Fig. 2.12 Mode transformations between longitudinal and shear waves. (**a**) Incident longitudinal wave crossing liquid–solid interface. (**b**) Incident longitudinal wave crossing solid–liquid interface. (**c**) Incident shear wave crossing solid–liquid interface

$$R = \frac{1}{N}\left[\left(\frac{c_s}{c_l}\right)^2 \sin 2\alpha_l \sin 2\alpha_s + \cos^2 2\alpha_s - \frac{\rho c}{\rho_s c_l}\frac{\cos\alpha_l}{\cos\alpha}\right],$$
$$N = \left(\frac{c_s}{c_l}\right)^2 \sin 2\alpha_l \sin 2\alpha_s + \cos^2 2\alpha_s + \frac{\rho c}{\rho_s c_l}\frac{\cos\alpha_l}{\cos\alpha}. \tag{2.41}$$

The transmission coefficient for the longitudinal wave is given as

$$T_{ll} = \frac{2}{N}\cos 2\alpha_s \tag{2.42}$$

and that of the shear wave is

$$T_{sl} = -\frac{2}{N}\left(\frac{c_s}{c_l}\right)^2 \sin 2\alpha_l. \tag{2.43}$$

There are two cases of the mode transformation at solid–liquid interfaces: whether the incident wave reaching the interface is a longitudinal wave or a shear wave. For longitudinal waves (Fig. 2.12b), the reflection coefficient for reflected longitudinal waves is

$$R_{ll} = \frac{1}{N}\left[\left(\frac{c_s}{c_l}\right)^2 \sin 2\alpha_l \sin 2\alpha_s - \cos^2 2\alpha_s + \frac{\rho c}{\rho_s c_l}\frac{\cos\alpha_l}{\cos\alpha}\right] \tag{2.44}$$

and the reflection coefficient for the reflected shear waves caused by the mode transformation is

$$R_{\mathrm{sl}} = \frac{2}{N}\left(\frac{c_{\mathrm{s}}}{c_{\mathrm{l}}}\right)^2 \sin 2\alpha_{\mathrm{l}} \sin 2\alpha_{\mathrm{s}} \,. \tag{2.45}$$

Because only the longitudinal waves propagate in liquid media, the transmission coefficient becomes

$$T_{\mathrm{ll}} = \frac{2}{N}\frac{\rho c}{\rho_{\mathrm{s}} c_{\mathrm{l}}}\frac{\cos\alpha_{\mathrm{l}} \cos 2\alpha_{\mathrm{s}}}{\cos\alpha} \,. \tag{2.46}$$

For the shear wave (Fig. 2.12c), the reflection coefficient for the reflected shear waves is

$$R_{\mathrm{ss}} = \frac{1}{N}\left[\left(\frac{c_{\mathrm{s}}}{c_{\mathrm{l}}}\right)^2 \sin 2\alpha_{\mathrm{l}} \sin 2\alpha_{\mathrm{s}} - \cos^2 2\alpha_{\mathrm{s}} - \frac{\rho c}{\rho_{\mathrm{s}} c_{\mathrm{l}}}\frac{\cos\alpha_{\mathrm{l}}}{\cos\alpha}\right] \tag{2.47}$$

and the reflection rate for the reflected longitudinal waves caused by the mode transformation is

$$R_{\mathrm{ls}} = -\frac{1}{N}\sin 4\alpha_{\mathrm{s}} \,. \tag{2.48}$$

Because the longitudinal wave generated by mode transformation at the solid–liquid interface can propagate in the liquid medium, the transmission coefficient for the longitudinal waves is given as

$$T_{\mathrm{ls}} = \frac{2}{N}\frac{\rho c}{\rho_{\mathrm{s}} c_{\mathrm{l}}}\frac{\cos\alpha_{\mathrm{l}} \cos 2\alpha_{\mathrm{s}}}{\cos\alpha} \,. \tag{2.49}$$

2.6.3 Wave Propagating on Solid Surfaces

The UVP measurements utilize ultrasonic beams with a finite width (as described in Sect. 2.4): when such a beam crosses a liquid–solid interface with an incident angle, these will be other modes of the wave that propagate on the solid surface in addition to the longitudinal and shear wave modes detailed in the previous section (Sect. 2.6.2).

For longitudinal waves crossing a liquid–solid interface, and if the incident angle is close to the critical angle for the longitudinal wave, the mode transformation may result in a *creeping wave*, which propagates on the solid surface (Fig. 2.13a). This wave propagates with the same speed as the longitudinal wave and gives rise to continuous mode transformations into shear waves; the wave decays relatively quickly.

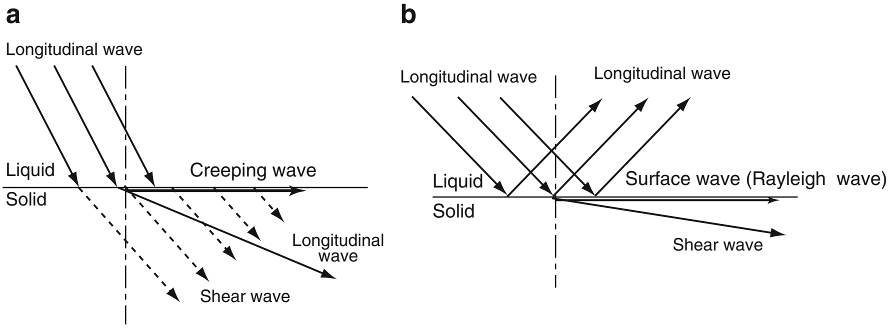

Fig. 2.13 Acoustic waves propagating on solid surfaces. (**a**) Creeping wave. (**b**) Surface wave (Rayleigh wave)

For larger incident angles, still around the critical angle for shear waves, a *surface wave* (*Rayleigh wave*) that is a shear wave propagating on the solid surface is generated (Fig. 2.13b). The speed of propagation of this wave is somewhat slower than that of the shear wave in a solid medium. For thin solid layers, displacements of small elements in the solid medium caused by the surface wave are restricted in the direction parallel to the interface; this is a so-called *lamb wave*, and all surface waves propagating in thin solid layers are classified as *plate waves*. Because plate waves do not cause mode transformations at the interfaces with adjacent liquid layers, this kind of wave can propagate for relatively long distances. Overall, an evaluation of the influence of plate waves is important in the measurement of flows in thin-walled pipes, in addition to an understanding of the mode transformations of the incident wave.

2.7 Ultrasonic Transducers and Ultrasonic Beam

The transducer is a key element of the UVP measurements. A transducer emits and receives ultrasonic pulse waves (*A-scan*), and the performance of the measurement equipment is determined by the transducer that is used. Among several different principles of electroacoustic transduction for generating ultrasonic waves as well as for detecting echo, the piezoelectric effect is recently the most often used for a variety of applications of ultrasonic wave such as in flaw detection, level metering, and general nondestructive testing. The piezoelectric effect arises from energy conversion of electric and mechanical signals and is seen in single crystals of some insulators, such as quartz and lithium sulfate. It is also observed in ceramics that are specially prepared to enhance this effect, such as barium titanate and lead zirconate titanate. The latter is frequently used and is termed PZT; the composition rate varies. These ceramics originally have no piezoelectric characteristics, but the piezoelectric

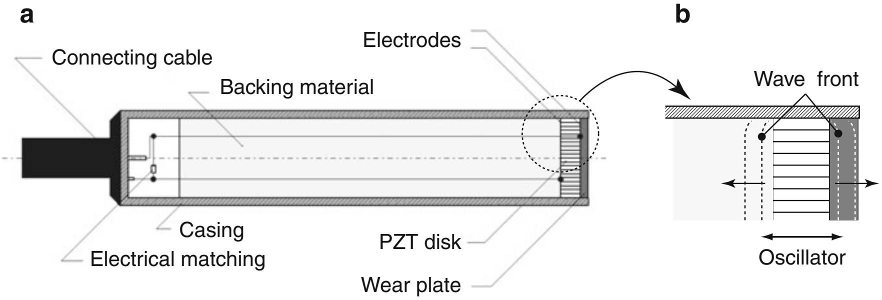

Fig. 2.14 (**a**) Elements of an ultrasonic transducer manufactured from a piezoceramic compound. (**b**) Schematic illustration of enlarged view of transducer head indicated by a *circle* in (**a**)

characteristics are coated when an appropriate porlarization is applied. A more detailed explanation can be found in Blitz and Simpson [3]. The advantages of using the ceramic materials are flexibility in shape formation in frequency selection, as well as the relatively low acoustic impedance.

A common structure of a conventional piezoelectric transducer is designed for using a ceramic disc as an oscillator, where the thickness of the disc determines its resonance frequency. Piezoelectric composite transducers are a recent development. A PZT material, in the shape of a rod or sphere, is embedded in a polymer resin and shaped to a required size. Such composite transducers possess higher efficiencies in the piezoelectric effect, and the intrinsic acoustic impedance is relatively low. As illustrated in Fig. 2.14a, the piezoelectric element is excited by an electric oscillator through the electrodes that are provided on the both sides of the element. A mechanical pressure is generated inside the element and the resonant oscillation of the element generates and emits the ultrasonic wave to the adjacent medium. Waves are emitted on both sides of the element (Fig. 2.14b). When the wave is not absorbed or attenuated on the back side, it is reflected at the boundary and propagates back to the other side inside the element, which may result in a deterioration of the waveform. In the actual transducer, therefore, a damping block is used to absorb the waves on the back.

The structure of the transducer is very important because the ultrasonic beam is invisible and determination of the beam line has to rely on the outer shape of the transducer. The front surface of the transducer should be flat, and the beam line must be precisely normal to this surface. Otherwise, the line of the measurement will not be at the place intended for measurements. It should be noticed that the measurement by UVP is a line measurement and that small errors in the beam alignment would result in larger errors of the position of the measurement volume at the far side from the origin of the beam.

Other types of transducer materials are also commonly used. For instance, single crystals of lithium niobate are used in high-temperature applications. It must be noted, however, that a transducer in the UVP method is used for emitting high-intensity ultrasonic waves and receiving the very weak echo waves by the same transducer, so its conversion efficiency must be high. Usually, the voltage applied to a transducer is of the order of 100 V and the received echo generates a very low piezoelectric voltage of the order of millivolts (mV). For this reason, composite transducers are preferably employed, because the conversion efficiency is much higher than that of a simple piezoceramic by one or two orders of magnitude.

References

1. Povey MJW (1997) Ultrasonic techniques for fluids characterization. Academic, London
2. Krautkrämer J, Krautkrämer H (1990) Ultrasonic testing of materials, 4th edn, fully revised. Springer, Berlin
3. Blitz J, Simpson G (1996) Ultrasonic methods of non-destructive testing. Chapman & Hall, London

Chapter 3
Ultrasonic Doppler Method

Hideki Murakawa, Michitsugu Mori, and Yasushi Takeda

Abstract The ultrasonic velocity profiler (UVP) mainly employs the ultrasonic Doppler method to obtain a one-dimensional velocity profile. The measurement position is a function of time-of-flight of the ultrasonic pulses, and the velocity is obtained from the Doppler shift frequency. The principle and the method to detect the Doppler shift frequency are described in Sect. 3.1. When we use UVP for measuring velocity profiles in real situation, selections of the ultrasonic basic frequency, transducer setting, and ultrasonic reflectors are important, as shown in Sect. 3.2. Attention to be paid for measuring velocity is described in Sect. 3.3. Velocity aliasing appears if the velocity is over the maximum velocity defined by the Nyquist sampling theorem. We have to set a transducer carefully to avoid multiple reflections from surroundings. Temperature directly affects the measurement accuracy because measurement positions and velocities are functions of sound speed, and we also have to pay attention to the effects of solid boundary and measurement volume.

Keywords Doppler shift frequency • Maximum depth • Maximum velocity • Seeding

---

H. Murakawa (✉)
Graduate School of Engineering, Kobe University,
1-1 Rokkodai, Nada, Kobe 657-8501, Japan
e-mail: murakawa@mech.kobe-u.ac.jp

M. Mori
Hokkaido University, Sapporo, Japan

Y. Takeda
Hokkaido University, Sapporo, Japan

Tokyo Institute of Technology, Tokyo, Japan

Y. Takeda (ed.), *Ultrasonic Doppler Velocity Profiler for Fluid Flow*,
Fluid Mechanics and Its Applications 101, DOI 10.1007/978-4-431-54026-7_3,

3.1 Basics

The ultrasonic Doppler method utilizes the Doppler shift frequency of the echo caused by reflected signals on moving tracer particles to obtain instantaneous velocity profiles in a flow field. It is difficult to obtain the Doppler shift frequency from a reflected signal directly because the ultrasonic signal is wide spectrum, and the shift frequency is much smaller than the basic frequency. Phase changes of consecutive echo signals are calculated to obtain the Doppler shift frequency in real systems using quadrature-phase detection.

3.1.1 Basic Principle [1, 2]

The velocity profile of the flow field to be measured is expressed as a data set of velocity values at various spatial locations at an instant, $V(x, t)$. In the ultrasonic Doppler method, this means that velocity as a distribution is obtained as a function of time. Figure 3.1 shows a schematic of the principle of the method.

A position information is obtained from a time lapse of echo reception after the pulse emission, τ; this corresponds to a time-of-flight of the ultrasonic pulse. Note that the path length on which the pulse flies is for both the ongoing and the returning path. The echography is used to determine a position x using sound speed c as

$$x = \frac{c\tau}{2}. \tag{3.1}$$

A Doppler shift frequency f_D at the instant gives us velocity information at that location as the following relationship:

$$V = \frac{cf_D}{2f_0}, \tag{3.2}$$

where f_0 is the basic frequency of the ultrasonic. In short, measurement of instantaneous velocity distribution is to measure instantaneous frequency as a function of time after the pulse emission.

3.1.2 Pulse Doppler Principle [3]

The echo signal includes all necessary information about the instantaneous velocity distribution. A single shot of the ultrasonic pulse and its echo reception might be used. Theoretically, there are various methods to derive instantaneous frequency

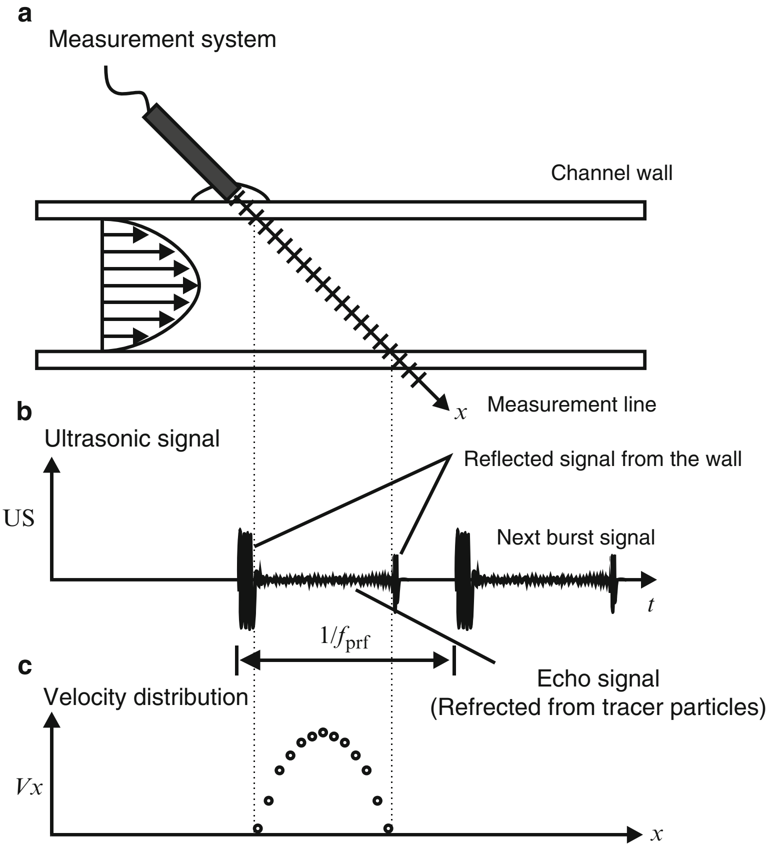

Fig. 3.1 Schematic of the measurement principle. (**a**) Measurement system. (**b**) Ultrasonic echo signal. (**c**) Measured velocity distribution

from the time series of the echo signal. In practice, however, because of various limitations by the speed of electronics, algorithms, and others arising from discrete characteristics of the digital data, repetition of pulse emission and echo reception is used to overcome those difficulties. This practice is indeed historical. The method had been developed in medical applications several decades ago, when fast electronics, especially the modern PC, were not available. This consideration is still valid even now when very fast electronics is available.

The algorithm generally adopted is illustrated in Fig. 3.2. An ultrasonic pulse is emitted. An emitted ultrasonic pulse should have a pulse width longer than a few cycles of the basic oscillation. In the figure, the pulse flies from the left. The right side is a time trace of the echo signal. The pulse is reflected from a reflector (seeding particle), and the echo is received by the same transducer at a time corresponding to a distance between the reflector and the transducer. In the following frame of the

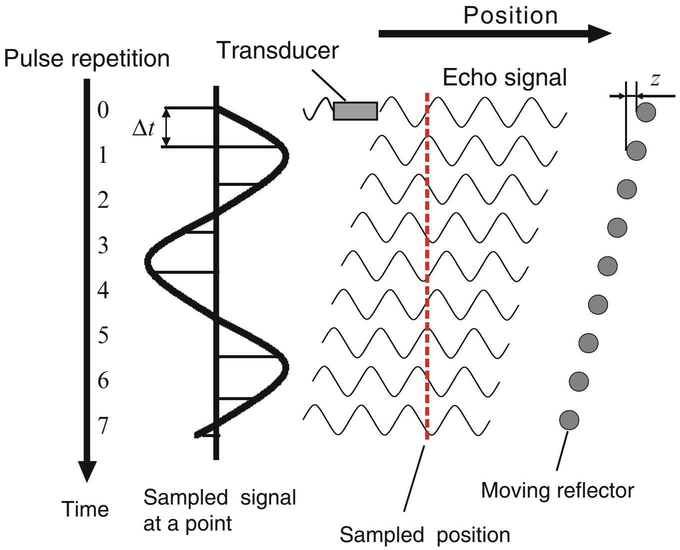

Fig. 3.2 Detection of Doppler shift frequency

echo, which is of the following pulse emission, an echo is detected in the same way with a very small time shift of the reflected echo: this is because a reflector is moving and the distance changes during this period between the first and the second repetition. At one fixed time after the pulse emission, there is a difference in the phase of the detected signals. This phase difference is used to detect an instantaneous Doppler shift frequency.

The phase difference φ between two successive frames of pulse echo can be expressed as follows:

$$\varphi = f_0 \Delta t. \tag{3.3}$$

Differentiating the above equation with time is

$$\frac{\mathrm{d}\varphi}{\mathrm{d}t} = f_0 \frac{\mathrm{d}(\Delta t)}{\mathrm{d}t}. \tag{3.4}$$

The time difference between two frames Δt is determined by the moving distance of a reflector z as

$$\Delta t = \frac{2z}{c}. \tag{3.5}$$

Differentiating this equation with time gives

$$\frac{\mathrm{d}(\Delta t)}{\mathrm{d}t} = \frac{2}{c} \cdot \frac{\mathrm{d}z}{\mathrm{d}t} = \frac{2V}{c}. \tag{3.6}$$

Substituting this into Eq. (3.4) and using Eq. (3.2), we obtain

$$\frac{\mathrm{d}\varphi}{\mathrm{d}t} = \frac{2Vf_0}{c} = f_{\mathrm{D}}. \tag{3.7}$$

In a practical algorithm, a number of repetitions of the echo reception are used to compute the phase. The procedure is applied to a number of times instant, various Δt, to form an instantaneous velocity profile.

3.1.3 Velocity Limitation and Constraint

Looking at such a signal analysis at a single spatial position, a pulse repetition frequency f_{prf}, corresponds to a sampling frequency. The maximum detectable frequency, namely, maximum velocity $V_{\max}$, is limited by the Nyquist sampling theorem, which states:

$$f_{\mathrm{D}\max} = \frac{f_{\mathrm{prf}}}{2} \Rightarrow V_{\max} = \frac{cf_{\mathrm{prf}}}{4f_0}. \tag{3.8}$$

The maximum depth to be covered is determined by a time for the pulse to travel back and forth from a transducer as

$$P_{\max} = \frac{c}{2f_{\mathrm{prf}}}. \tag{3.9}$$

A measurement constraint for this method is given from the foregoing two limiting equations as

$$V_{\max} \cdot P_{\max} = \frac{c^2}{8f_0}. \tag{3.10}$$

Using a fixed basic frequency, the maximum velocity to be detected is determined by the maximum depth of the ultrasonic beam path. Thus, if the measured maximum velocity of the flow is large, a small depth has to be set. For a wide area to be covered, only the smaller velocity can be detected.

It should, however, be noted that the velocity overflow occurs in the form of velocity aliasing (see Sect. 3.3.1), which can be compensated, in some cases, by a post-processing of the results.

3.1.4 Position and Velocity Uncertainty and Resolution

In the pulse Doppler method, the echo signal to be analyzed for velocity estimation comes from all parts of the transmitted pulse. As this pulse has a finite time width, both uncertainties of position and velocity are caused by this pulse width; that is, the wider pulse width gives a larger uncertainty of the position determination. This consideration gives us an estimate of position resolution Δz (a thickness of the measurement volume):

$$\Delta z = \frac{N\lambda_0}{2} = \frac{Nc}{2f_0} \tag{3.11}$$

where N is the number of cycles included in the pulse, and a related time uncertainty for a single sampled data and the induced Doppler shift bandwidth are given as

$$\Delta t = \frac{\Delta z}{V} \tag{3.12}$$

$$\Delta f_\mathrm{D} = \frac{1}{\Delta t} = \frac{V}{\Delta z}. \tag{3.13}$$

Spectrum width of the Doppler frequency can be estimated from the Doppler equation as

$$\Delta f_\mathrm{D} = \frac{2\Delta V}{c} f_0 \tag{3.14}$$

which deduces the following restraint on measurement uncertainty:

$$\frac{\Delta V}{V} \cdot \Delta z \cong \frac{c}{2f_0} = \frac{\lambda_0}{2}. \tag{3.15}$$

It should be noted that the two Δf_D in the foregoing equations are not identical; therefore, it is not possible to find equality between the equations.

The restraint derived above indicates that the improvement of the velocity uncertainty has to sacrifice the position uncertainty vis-à-vis for a fixed ultrasonic basic frequency.

3.1.5 Detection of Doppler Frequency

Signal processing for detection of Doppler frequency is to extract a modulation frequency from the carrier wave, and it is identical to a demodulation of the echo signal. The echo signal received by the transducer includes a noise component. Hereby we consider only the echo signal from a stationary structure such as a wall or stationary free surface of the liquid. The noise level is usually much higher than that of the Doppler component, and the signal processing has to be carefully designed.

In the demodulation process, a reference signal of the carrier wave (basic frequency) is needed to compare it with the echo signal. There are two ways to establish this reference signal: coherent demodulation and noncoherent demodulation. In coherent demodulation, the transmitted signal is stored locally and used. In the noncoherent demodulation, a component in the echo signal that has the same frequency as the basic frequency is used. Usually the non-Doppler shifted component is much stronger because they are reflected from a solid surface. By this method, only the echo signal provides all the necessary reference of the phase and frequency. As a basis for a detection of the Doppler frequency, we describe briefly only the coherent demodulation.

For simplicity of explanation, we omit here a pulse structure in the following mathematical formulation. A transmitted waveform is described by

$$T(t) = \cos\omega_0 t, \tag{3.16}$$

where $\omega_0 = 2\pi f_0$ is an ultrasonic angular frequency. We also omit the amplitude of the transmitted wave and also hereafter an attenuation/absorption effect in the medium by its propagation.

The received echo signal from the seeding particle can then be expressed as

$$R(t) = R_{\mathrm{S}}(t) + R_{\mathrm{D}}(t) = A\cos(\omega_0 t + \varphi_{\mathrm{S}}) + B\cos(\omega_0 t + \omega_{\mathrm{D}} t + \varphi_{\mathrm{D}}). \tag{3.17}$$

The first term in the above expression is for a component of the echo reflected from the stationary target and the second is for a Doppler shifted component. A and B are their amplitude and φ is their phase relative to the transmitted wave at the time origin. Obviously the Doppler shift frequency is given by the Doppler relationship as

$$\omega_{\mathrm{D}} = \frac{2v}{c}\omega_0. \tag{3.18}$$

Multiplying the echo signal by the transmitted signal (reference signal) gives the following expression for the output signal:

$$\begin{aligned} D(t) &= R(t)\cdot T(t) = [A\cos(\omega_0 t + \varphi_S) + B\cos(\omega_0 t + \omega_D t + \varphi_D)]\cos\omega_0 t \\ &= \frac{A}{2}[\cos\,(\omega_0 t + \varphi_S) + \cos\varphi] + \frac{B}{2}[\cos(\omega_0 t + \omega_D t + \varphi_D) + \cos(\omega_D t + \varphi_D)] \end{aligned} \tag{3.19}$$

Because the Doppler shift frequency ω_D is usually much smaller than the basic frequency ω_0, the carrier component can be easily eliminated using a low pass filter, and then the following signal is given:

$$D_m(t) = \frac{A}{2}\cos\varphi_S + \frac{B}{2}\cos(\omega_D t + \varphi_D). \tag{3.20}$$

By detecting the frequency of the signal processed as above by filtering, the Doppler frequency can be obtained by various algorithms. It is however to be noted that this method cannot give information about the flow direction. Namely, the negative Doppler shift gives the direction of the seeding particle moving away from the transducer and the positive toward the transducer. Detection of the sign has to be treated separately with another method.

3.1.6 Quadrature-Phase Demodulation

The technique to demodulate the echo signal with maintaining its directional information, namely, the sign of Doppler shift, is typical with the quadrature-phase demodulation of the echo signal. This is an alternative coherent demodulation, where in-phase and quadrature coherent signals are used as reference. The quadrature signal is that the phase is shifted by $\pi/2$.

The received echo signal is expressed in the following, again by neglecting the pulse structure:

$$R(t) = A\cos(\omega_0 t + \varphi_S) + B_f\cos(\omega_0 t + \omega_f t + \varphi_f) + B_r\cos(\omega_0 t - \omega_r t + \varphi_r), \tag{3.21}$$

where the subscripts f and r mean the forward and reverse flow components, respectively.

The coherent demodulation of this echo signal can be given using the reference signal of $\cos\omega_0 t$:

$$I(t) = \frac{1}{2}[A\cos\varphi_S + B_f\cos(\omega_f t + \varphi_f) + B_r\cos(\omega_r t - \varphi_r)]. \tag{3.22}$$

The same demodulation can be applied using the quadrature signal of the reference as $\cos(\omega_0 t + \pi/2)$:

$$Q(t) = -\frac{1}{2}[A\sin\varphi_S + B_f\sin(\omega_f t + \varphi_f) - B_r\sin(\omega_r t - \varphi_r)]. \tag{3.23}$$

These two signals are filtered to eliminate the phase term to lead to the following expressions:

$$I(t) = \frac{1}{2}B_{\mathrm{f}}\cos(\omega_{\mathrm{f}}t + \varphi_{\mathrm{f}}) + \frac{1}{2}B_{\mathrm{r}}\cos(\omega_{\mathrm{r}}t - \varphi_{\mathrm{r}}) \tag{3.24}$$

$$Q(t) = -\frac{1}{2}B_{\mathrm{f}}\cos\left(\omega_{\mathrm{f}}t + \varphi_{\mathrm{f}} - \frac{\pi}{2}\right) + \frac{1}{2}B_{\mathrm{r}}\sin\left(\omega_{\mathrm{r}}t - \varphi_{\mathrm{r}} + \frac{\pi}{2}\right). \tag{3.25}$$

These two signals can be considered as real and imaginary parts of a complex time domain waveform:

$$f(t) = I(t) + iQ(t) \tag{3.26}$$

and the instantaneous frequency of this waveform corresponds to the Doppler shift f_{D}.

The most practical signal processing systems based on this complex Doppler signal and various algorithms that have been developed are frequency domain processing, time domain processing, and phase domain processing. Each of these algorithms has its own characteristics and is chosen depending on the requirements and conditions of the system configuration as well as measurement performance.

Here, briefly, we explain a principle of frequency domain processing. For details of the system configuration and actual adaptation to the discrete signal processing system, the reader might refer to the references.

The Fourier transform of the complex Doppler signal $f(t)$ is

$$g(\omega) = \int_{-\infty}^{\infty} f(t)\mathrm{e}^{-i\omega t} \tag{3.27}$$

and the power spectrum is given by

$$S(\omega) = g^{*}(\omega)g(\omega) \tag{3.28}$$

Considering the power spectrum as a probability density function of the signal in the frequency domain, the foregoing power spectrum can be normalized as

$$p(\omega) = \frac{S(\omega)}{\int_{-\infty}^{\infty} S(\omega)\mathrm{d}\omega} \tag{3.29}$$

Then, the mean frequency of the power spectrum is evaluated using the foregoing probability density function as follows:

$$\bar{\omega} = \int_{-\infty}^{\infty} \omega\, p(\omega)\mathrm{d}\omega \tag{3.30}$$

The power spectrum of the signal after quadrature-phase demodulation might have two main components: ultrasonic carrier (ω_0) and Doppler components (ω_f or ω_r). In our application, it is reasonable to assume that only one component of the Doppler components appears in the power spectrum as the measurement volume is sufficiently small and the velocity distribution therein is smooth and flows in the same direction. Thus, the two signals branched after the high pass filter and the low pass filter (both have the same edge frequency at the carrier frequency) will represent the forward flow and reverse flow. The Fourier transform of each signal gives the power spectrum, and the mean frequency can be estimated.

The other algorithms by the time domain processing and the phase domain processing, especially for a discrete data set of the sampled signal, are described by Barber et al. [4]. The autocorrelation algorithm frequently used in the medical field was first described by Kasai et al. [5]. Jensen [6] summarized the system and the algorithms of the Doppler method.

3.2 Practice

Ultrasonic methods are easier to handle in comparison with laser optical methods. However, attention must be paid in practice, especially for quantitative measurement of the flow field. Practically useful notes are first given in this section for general use of flow field measurement. In the latter part of the section, the target configuration is a pipe flow, from which much information could be derived for each new measurement configuration.

3.2.1 What Is Obtained

It is worthwhile to be reminded that a velocity value to be obtained by the ultrasonic Doppler method is a velocity component that is projected onto the measurement line (beam direction) of a randomly oriented true velocity vector, which results from the nature of the Doppler effect of wave propagation. Generally, a flow field is in vector, and it can hardly be approximated to be one dimensional except for a simple pipe flow or in a very small flow region. This point is important when the true velocity vector is to be obtained for flow mapping. Specifically, the velocity distribution to be obtained is expressed as $V_\mathrm{m}(x_\mathrm{m}, t)$, where x_m is a distance from the transducer on the measurement line. The sign of the velocity value is negative when the flow motion is away from the transducer and positive toward the transducer.

In the wall boundary region, a flow is mostly parallel to the wall. Thus, when the transducer is set on the wall, outside or inside, the top surface of the transducer is parallel to the wall and the flow in its neighborhood is perpendicular to the measurement line; this leads to difficulty in measuring the velocity distribution in the wall boundary region.

3.2.2 Selection of Basic Frequency

The basic frequency of the ultrasound is the most basic parameter. It determines system performance and largely affects the success of the measurement. It is then a key issue to determine the basic frequency in designing the measurement system as well as in experimental configuration.

A selection of the optimal basic frequency depends on the requirements and purposes of the measurement. For physics research experiments, high spatial and time resolution would be a key issue and require a smaller wavelength, namely, a higher frequency is preferable. However, selection of a high frequency sometimes limits the maximum measurable velocity to be too low. For rheological studies, many of the fluids have a higher attenuation property of the ultrasonic wave and only the lower frequency could be used, which may induce a larger measurement volume and lead to a lower spatial resolution. There are various points to be considered, and the following various items should be considered.

3.2.2.1 Attenuation of Ultrasonic Beam

Generally but roughly speaking, attenuation of an ultrasonic wave is proportional to the square of the wave frequency, which has to be considered when the measurement requires a higher basic frequency. Lowering the frequency would ease the problem in system configurations. Note that we use an echo signal, which means double the length between the transducer and the target must be counted.

3.2.2.2 Width of the Profile

The largest depth of the profile measurement is determined by the pulse repetition frequency, f_{prf}; this is quite often larger than the profile width that is actually required for data acquisition. For a large profile width, the distance between two data points sometimes becomes so large that the velocity profile to be obtained shows a nonsmooth curve, especially when the flow is turbulent.

3.2.2.3 Maximum Velocity

It is obviously to be determined by the maximum velocity of the flow field. However, it is also important to consider an orientation of the measurement line to the true velocity vector. The direction of the true velocity vector is usually unknown and has to be guessed. The angle between the true vector and the measurement line should not be so small because the uncertainty will also be expanded by the smaller angle, as the correction factor is $1/\cos\theta$.

3.2.2.4 Measurement Volume

This is determined by the pulse width of the emitted ultrasonic pulse. It is usually four to eight cycles of the basic ultrasonic wave. If it is smaller than four, the ultrasonic beam is not as well defined as the pulsed beam. With the larger number of cycles, the measurement volume of two adjacent data points overlaps; this is dependent on the channel distance; a distance between two measurement volumes.

3.2.2.5 Time Resolution and Sampling Speed

The pulse repetition frequency and the number of repetitions for data collection determine the time resolution. For the longer depth measurement, the f_{prf} is low and the time resolution will be low. Also, if the number of repetitions is large, the data collection time becomes large and weakens the time resolution. There is a small time lapse between two successive measurements, namely, two sets of data collection; this results from the time required for signal processing to compute the velocity values of all data points, which forms a velocity profile. Consequently, the sampling speed is usually larger than the time resolution. It is also possible to control this time lapse between two successive profile measurement intentionally. This step is performed for a slowly transient motion where a long measurement time is required with keeping a relatively high time resolution.

3.2.2.6 Condition of Reflectors

As we utilize the echo signal, which is generated by the seeding particle suspended in the fluid, this is an important issue in practical applications of this method. All the design and configuration considerations might be completely different if the reflector exists in itself in the fluid or is intentionally added for this method. When the fluid includes the reflector, such as food materials or blood, and if it is not possible or allowed to control its concentration or size distribution, system parameters might be determined mainly by this factor. In such cases, one has to investigate its

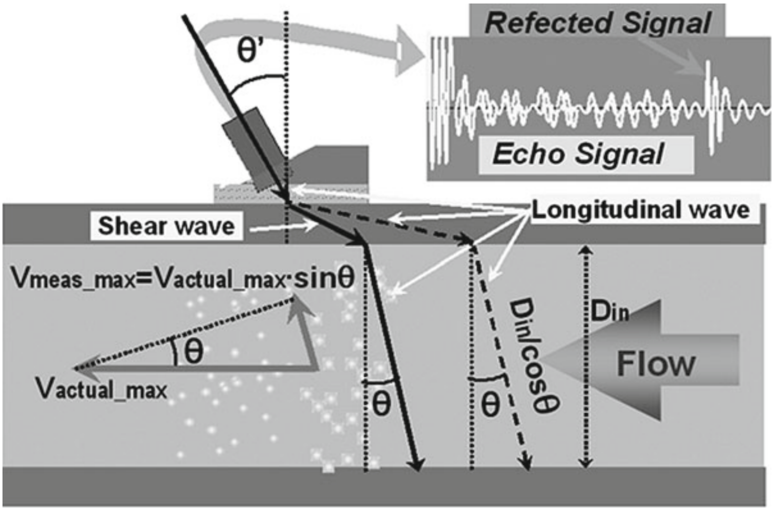

Fig. 3.3 Maximum measurable velocity and depth by UVP in pipe

characteristics carefully before determination of the system parameters. When the fluid is clean and includes few foreign particles, some solid or gas particles have to be added intentionally as a reflector. This is discussed in a later section in more detail.

A more specific case of frequency selection is described below by using a pipe flow configuration (Fig. 3.3).

A lower basic frequency has to be used to make the larger maximum measurable depth and maximum velocity. When the flow is in a single direction, the maximum measurable velocity ($V_{\max}$) is limited as shown in Eq. (3.8).

Hence, when the flow can be assumed to be in a forward single direction, the measurable $V_{\max}$ is doubled, as follows:

$$0 \le V_{\max} \le 2 \cdot c \cdot f_{\text{prf}} / (4 \cdot f_0). \tag{3.31}$$

As the setup limitations of f_{prf} and f_0 are relatively easy in a small-diameter pipe, larger values of f_{prf} and f_0 would be better, because the transducer is set with an appropriate angle to the surface to obtain the velocity profile in a pipe, reflecting a principle of UVP that it can measure the velocity component normal to the measurement line. It is obviously necessary to take into account that the beam is refracted at the wall boundary. As seen in Fig. 3.3, measurable velocity to the pipe axis direction is expressed by $V_{\text{actual\_max}}$, and the incident angle is expressed by θ, the detected velocity by UVP transducer is $V_{\text{actual\_max}} \sin\theta$, and then the measurable maximum velocity, $V_{\text{meas\_max}}$, is

$$V_{\mathrm{meas\_max}} \leq c \cdot f_{\mathrm{prf}} / (4 f_0 \sin\theta). \tag{3.32}$$

The relationship of Eq. (3.32) implies that the larger maximum velocity can be obtained by a small incident angle. It is, however, necessary to pay careful attention to the error, which is strongly affected by the small incident angle.

A measurable maximum depth is also affected by the incident angle. It could be easily understood (Fig. 3.3) that the required measurable depth is larger than the inner diameter of a pipe because of the incident angle. As shown in Fig. 3.3, the required maximum measurable depth with the pipe inner diameter, D_{in}, is expressed as Eq. (3.33):

$$X_{\mathrm{meas\_max}} = D_{\mathrm{in}} / \cos\theta < c / (2 \cdot f_{\mathrm{prf}}). \tag{3.33}$$

Setting the transducer to be perpendicular to the pipe surface, the required measurable depth is the smallest as $X_{\mathrm{meas\_max}} = D_{\mathrm{in}}$, but the measurement is impossible because (as easily understood in Fig. 3.3) a projected velocity component on the measurement line is zero; that is different from laser velocimetry. As shown in Eqs. (3.32) and (3.33), measurable maximum velocity and depth are proportion to and inversely proportional to repeated pulse frequency, f_{prf}, and, therefore, the f_{prf} has to be set to optimize these conditions given by the measuring arrangement and configurations.

3.2.3 Seeding

Ultrasonic Doppler velocimetry uses an echo that is back scattered (180°) at all positions so that a tracer which reflects ultrasound is needed to be mixed into the fluid. In fluid mechanical experiments, solid particles are mixed in with the fluid and used as tracers. The following notes are useful in selecting the appropriate tracer. As to size of the particle, experience suggests that approximately one fourth to one half of the wavelength is adequate. If the particle is smaller than this, the reflection efficiency becomes lower and the energy of echo is too small to maintain a high S/N ratio, leading to a detection error. If the particle is larger, the probability of multiple reflections between particles becomes higher, which would result in a distortion of the profile. The density of the particle is also important. A large difference in densities between fluid and particle might lead to an erroneous result because the particle does not follow the flow faithfully. Further, the concentration of the particles in the fluid is important. Roughly speaking, there should be one particle per measuring volume, but this also depends on the velocity level of the flow field to be measured. The required quantity of reflectors should be expressed not just in terms of concentration but as a flux of particles passing through a measurement volume. Consequently, when the velocity level is high, a good result can be obtained with a lower concentration of particles, whereas for natural convection or flow very near the solid wall, a considerably higher concentration is needed. The quantity of the tracer particle should be as low as possible. In such cases, defects may appear in each instantaneous profile. It is, however, usable when the objective of the measurement is to obtain time-averaged velocity profiles by taking as many profiles as obtainable and then calculating one cumulative average profile. On the other hand, if a transient profile is to be obtained, each profile should have the minimum number of defects, and therefore a high concentration is needed.

A similar problem may be encountered in optical methods such as LDA. One might find good references and practical information from the laser measurement technique.

Some reflector materials are listed in Appendix A.4 for reference purposes.

3.2.4 Selection of Incident Angle

Selection of incident angle is rather easy when the transducer is immersed in fluid, where only the longitudinal wave is involved: it is only a matter of orientation angle between the beam line and the flow velocity vector. The inclination angle can be determined such that the measured component of the velocity vector shall not exceed the detectable maximum velocity of the device.

In contrast, when the transducer is set outside the wall, for instance, the pipe wall, careful consideration must be given to mode change of the wave occurring at the boundary between solid and liquid or generation of a Lamb wave depending on the wall thickness.

The longitudinal wave is emitted from the transducer, and travels through the wedge (if used) and the wall to reach the fluid. Mode change occurs at each interface (Fig. 3.3) from longitudinal wave to shear wave and then again to longitudinal wave. For simplicity, we consider a configuration of a single plate. A longitudinal wave enters the plate, and the longitudinal wave and shear wave exist in the plate because the latter is generated at the outer boundary. As the sound speeds for the two waves are different, refraction angle is different, and the beam path would also be different in the wall (Fig. 3.3). This difference makes both transmission characteristics different, such as transmission or reflection coefficient and refraction angle, and finally the incident angles to fluid. Thus, measurement error cannot be neglected when two kinds of waves (longitudinal and shear) enter the fluid to generate echo. Such a case is enhanced for the small-diameter pipe with a thick wall giving a larger velocity value than a true value.

In an ultrasonic inspection application, an interesting solution technique is used to avoid such a configuration. A wedge made of engineering ceramics or plastic is located between the transducer and the metallic wall. Then, total transmission rate from the transducer to water strongly depends on the incident angle and also longitudinal and shear wave (Fig. 3.4) [7]. The incident angle is a wedge angle of incidence to the metallic pipe surface. Clearly, the incident angle to have a similar order of magnitude in transmission rate for longitudinal wave and shear wave is very

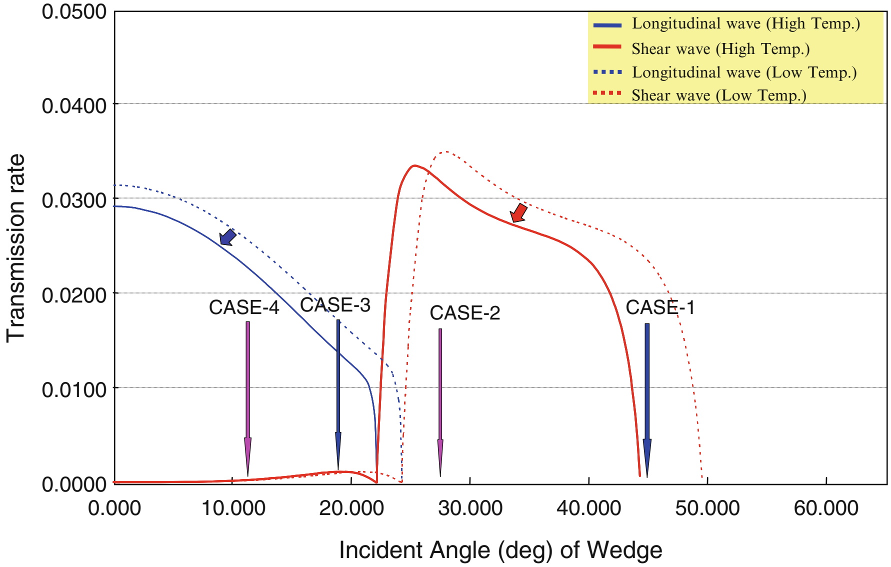

Fig. 3.4 Transmission rate of ultrasonic waves for a combination of engineering plastic and metal: wedge, engineering plastic; pipe, metal; fluid, water

different. A longitudinal wave can transmit with a smaller incident angle whereas the shear wave has a large transmission rate for a large incident angle. There is a clear separation in the incident angles. Then, it is feasible to discriminate the transmitted wave through the metallic wall by choosing the incident angle of the wedge. These curves show a slight difference for different temperature because the sound speed depends on the temperature.

The case 1 angle indicated in the figure corresponds to a critical angle beyond which no wave can be transmitted. At case 2, only the shear wave can transmit, and in case 4 only the longitudinal wave, and in case 3 both longitudinal and shear waves are superimposed.

3.2.5 Selection and Attachment of Wedges

A wedge is placed between the transducer front surface and the wall to fill the gap when the transducer is set inclined to the normal to the wall. This step is sometimes very important to guarantee a good reproducibility of the measurement. For instance, a definition of the beam angle is critical to a quantitative evaluation of velocity value as well as to fix a measurement position on the line. As this method is a line measurement, an error of the angle is amplified at the far location. A small misalignment of the beam induces a large mislocation of the measurement point. At the same time, a gap is often filled with jelly or some soft material, so-called couplants (see Appendix A.3); this induces a mismatching of the acoustic impedance from the

Table 3.1 Candidate materials for the wedge [8]

Material	Acoustic impedance (10^6 kg/m^2 s)	Sound velocity		Heat distortion temperature (°C)
		Longitudinal (m/s)	Shear (m/s)	
Acrylic plastic[a]	3.27	2,730	1,400	70–90
Polyetherimid[b]	3.11	2,450	1,050	~150
Polystyrene[c]	2.41	2,330	1,150	70–90
Polyimide[d]	3.47	2,450	1,060	~360
Polyimide[e]	3.80	2,710	1,390	~470

[a] PMMA
[b] PEI
[c] PS
[d] PI-1
[e] PI-200 (KGK catalog, Japan)

transducer surface to the wall, which weakens the signal intensity of impinging and returning echo in fluid.

This problem has been experienced in the development of a flow meter for which reproducibility of measurement is highly sensitive as a product. The following information might help us to consider the use of wedges.

In the clamp-on type of UVP flow meter, accuracy of the incident angle has to be kept consistent for a wide range of measurement conditions such as high temperatures and thermal cycles. In selecting the wedge material, acrylic and other engineering plastics, or carbon-based metallic cases, are tested (Table 3.1) [8]. Acrylic is easy to work but cannot be used in a high-temperature environment. Engineering plastics are available for high-temperature conditions, but machining is slightly less easy, especially for materials with high temperature capability. Carbon-based materials can be used at elevated temperature and have the advantage that the change of sound speed with temperature is small. On the other hand, brittleness in machining is a disadvantage; this might be overcome by using a composite material. A metal wedge shows good ultrasound propagation but has in general a large acoustic impedance, so that a discontinuity at the interface with other materials would generate a strong reflection of the ultrasonic wave. Especially, a firm contact is not easy between metallic surfaces and special care must be taken. For instance, the pipe surface where the wedge is placed should be treated to be clean by eliminating surface asperity, and then a couplant is used to remove the air layer or bubbles. Figure 3.5 shows an example of application for metal piping using an engineering plastic to measure flow velocity and profile by UVP [9, 10]. The transducer and wedge, in addition to tight contact, need to be integrally fixed on the curved pipe surface with the clamp-on wedge.

3.2.6 Conditioning of Reflector

Because ultrasonic echo is generated by particles suspended in fluid, it is absolutely necessary to have particles as a reflector in fluid in which the velocity profile is to be measured. Originally, when the method was invented in medical applications as

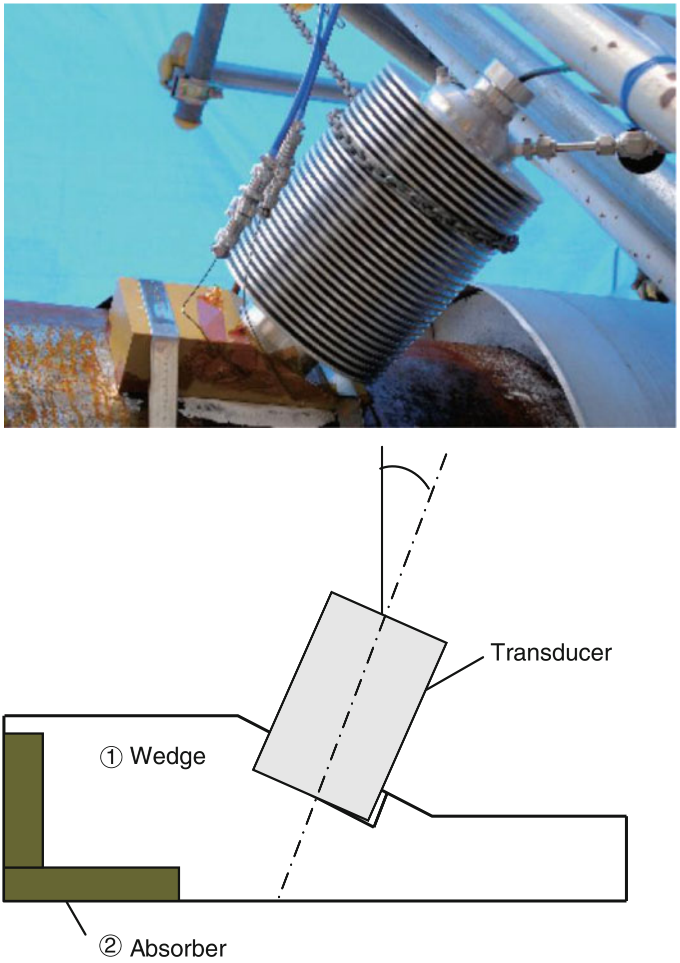

Fig. 3.5 Example of application for metal piping using engineering plastics to measure flow velocity and profile by UVP for metal pipe and water

a cardiovascular flow monitoring device, the reflector was a red blood corpuscle, and there is no possibility of adjusting the condition. However, in our application we can adjust the condition of particles, for instance, material (as reflection coefficient), density (to follow flow), size (as reflection cross section), concentration (for high success rate), etc. Thus, it is called seeding. In general, a particle is selected depending on the measurement configuration as liquids, velocity level, and measurement distance. For a small-scale closed configuration in the laboratory, a solid particle can be used. For a large-scale open configuration, an inexpensive powder is selected for a one-way use. For these cases, selection is rather easy.

In some configurations where the system must be kept clean or no additional material is allowed to mix, such as in a food processing plant, a gas bubble is used.

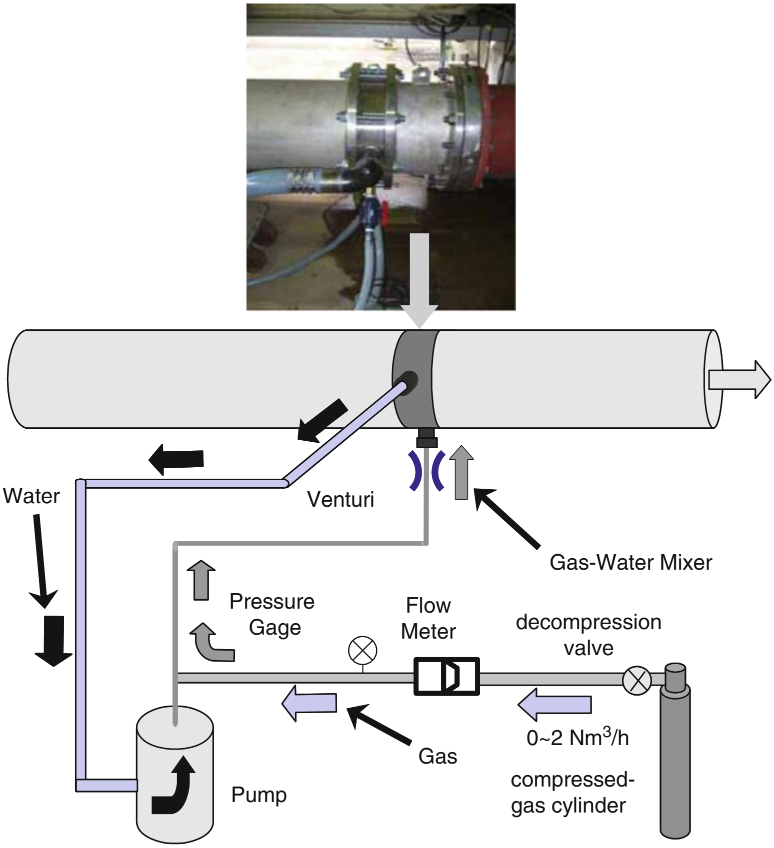

Fig. 3.6 Bubble injection system to miniaturize gas bubbles in fluid through the venturi nozzle tube [11]

The bubble is ideal as a seeding particle because it does not contaminate the fluid or damage fluid properties. The disadvantage is that it is rather large; the density is usually much less than that of fluid so that it is easily separated, and it is not easy to maintain a uniform mixing condition. It is also not possible to control the size of the bubbles for our purpose. When the fluid is clean and gas bubbles are not held within it, it is necessary to inject gas to generate tiny gas bubbles. This difficulty was experienced when the flow meter was developed, and the following information is used for designing a gas injection system.

In water at room temperature, cavitation bubbles disappear at around 0.3–0.5 MPa, and gas injection is used to introduce bubbles into the fluid. However a simple gas injection from a hole is not sufficient because the bubbles coalesce unless flow velocity is fast enough to miniaturize the bubbles by shear. A venturi nozzle tube was used in an air injection bubble generator (Fig. 3.6) [11]. Setting up branch pipes from the main pipe, venturi nozzle tubes are installed on the way back through the pump. Air is injected from just upstream of the venturi nozzle throat and

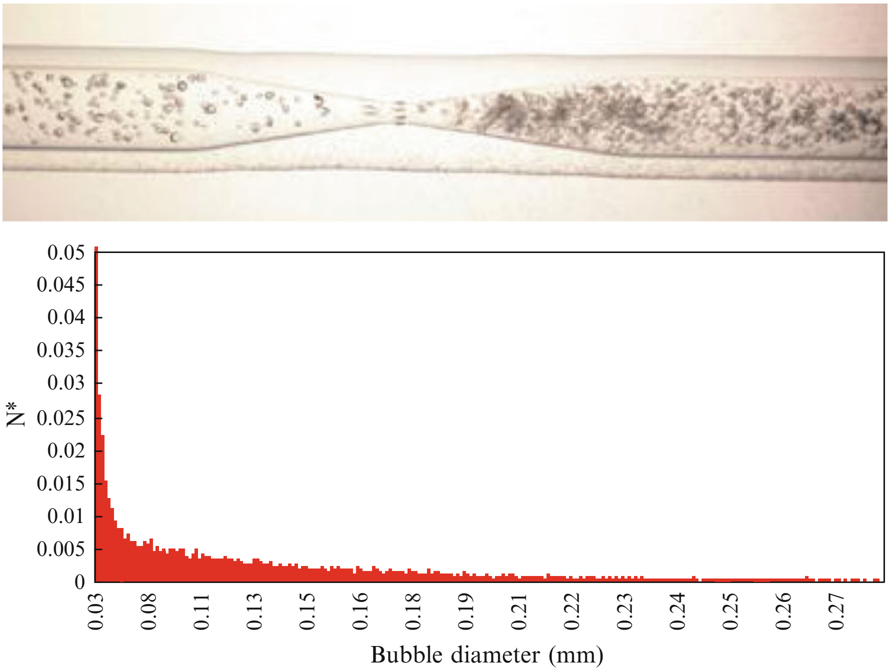

Fig. 3.7 Bubbles miniaturized using venturi nozzle tube (*top*) and bubble size distribution of miniaturized bubbles (*bottom*) [12]

miniaturized at the expansion nozzle. Miniaturized bubbles are supplied as seeding particles. The pump head pressure should be sufficient to inject water from the branched pipe to the main pipe.

Figure 3.7 (top) shows a venturi nozzle used in a bubble generator where water flows from left to right. Bubbles are miniaturized finer just downstream of the throat of the venturi nozzle. From visualized images, bubble size distribution was obtained as shown in the bottom of Fig. 3.7 [12]; this shows that most of the bubbles are less than 0.1 mm in diameter. The finer bubbles are better distributed in uniformity and buoyancy has little influence on their motion. It should be noted that with bubble generation by gas injection it is hard to adjust the size and concentration of particles so that too large a concentration sometimes occurs. If a concentration is too high with a bubble size too large, the influence of multiple scattering of the ultrasonic pulse will become significant, which leads to a larger error in velocity value as well as deterioration of the velocity profile.

The effect of the volumetric flow rate of bubbles gas on measuring flow rates was experimentally investigated. Air was injected upstream of the measuring point up to ~400 ppm (0.04% as a volumetric fraction) in the CENAM calibration test [9], in which it was confirmed that there was a negligible effect of air injection on the flow rates measured by the weighing systems of CENAM, comparing the flow rate measured without air injection with one using air as the primary standard at line conditions. It could be said on an empirical basis that UVP measurement would be successful for a bubble injecting rate of ~10 ppm (=0.001%) to ~1,000 ppm (=0.1%) of volume fraction, but an abrupt worsening is seen beyond this concentration. It is promising that UVP can successfully measure velocity profiles with an extremely small amount of miniaturized bubbles.

3.2.7 Monitoring Echo

Following is the last but important note for successful application of UVP for flow field measurement.

Because an ultrasonic wave is itself invisible, it is very important to monitor the echo signal on the oscilloscope screen, especially for assuring the measurement location of the line where you are measuring in the flow. It should be emphasized that the UVP measurement is a line measurement used to obtain information about a wide area. Therefore, knowing the measurement location is essential.

In a small-scale configuration in the laboratory, the ultrasonic pulse can be reflected by a surrounding structure such as a container wall or top free surface. If this reflected pulse hits the transducer, it can totally destroy the velocity profile. Again it is possible to determine if such a reflection affects the measurement by monitoring the echo signal. It also helps to arrange a measurement line with respect to the annoying structure to avoid such reflected pulse dropping on the transducer.

When one is experienced, it is also possible to know the condition of the reflector particles, if sufficient or too few, by monitoring the echo signal on the screen. As a reflection from a solid surface is fixed at one location and stays at the same position after the emitter pulse, you can find it rather easily. When there is a reflection from a free surface that is moving, you can also find it easily, as the reflection is very strong and stays almost at the same location with a little time fluctuation. In contrast, a reflection from a tracer particle is weak, continuous, and spreads, but it changes from frame to frame of repetition because the particles are moving with the flow.

As such, a monitoring echo on the oscilloscope is important and useful for successful measurement of the flow field by this method.

3.3 Attention Required

When we use UVP to measure velocity profiles in a real situation, there are points to which attention must be paid. These points are related to the fundamental principle of ultrasonics and the measurement method. Here we describe the velocity and

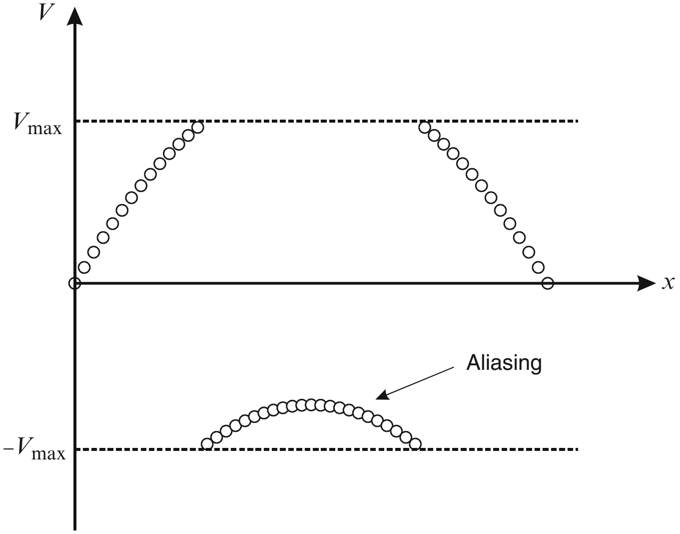

Fig. 3.8 Velocity aliasing

time aliasing, effect of solid boundary, measurement volume, and how to correct the measurement position near the wall.

3.3.1 Velocity Aliasing

Maximum Doppler frequency, $f_{\mathrm{D\,max}}$, is based on the Nyquist sampling theorem, as shown in Eq. (3.8). The maximum velocity, $V_{\max}$, can be calculated from the $f_{\mathrm{D\,max}}$. The UVP can detect the velocity direction, going away from or approaching the sensor. Hence, the velocity range becomes $\pm V_{\max}$. If a velocity exceeds the $V_{\max}$, the data are recorded as velocity aliasing at $V_{\max}$, which follows the sampling theorem. However, the velocity direction changes in the recorded velocity. As a result, negative velocities are recorded (Fig. 3.8). Based on the characteristic, a measured velocity V exceeding $V_{\max}$ can be converted to $V+2V_{\max}$ as the correct velocity. Hence, if the flow direction can be guaranteed, that is, only positive or negative, the maximum velocity range can be expanded to $2V_{\max}$ (or $-2V_{\max}$).

To avoid velocity aliasing, $V_{\max}$ must be set larger, which corresponds to increasing the pulse repetition frequency f_{prf}, or using a lower basic frequency f_0, or both. Change of a transducer setting angle is also used to avoid the aliasing. When reducing the setting angle θ, the projected velocity components decrease. Increasing the f_{prf} has a limitation because the maximum measurable depth $P_{\max}$ decreases. Therefore, decreasing f_0 or changing the setting angle is commonly chosen. However, sensor diameter generally increases with decreasing of the f_0, which increases the measurement volume. Hence, the appropriate ultrasonic basic frequency must be chosen depending on the flow condition.

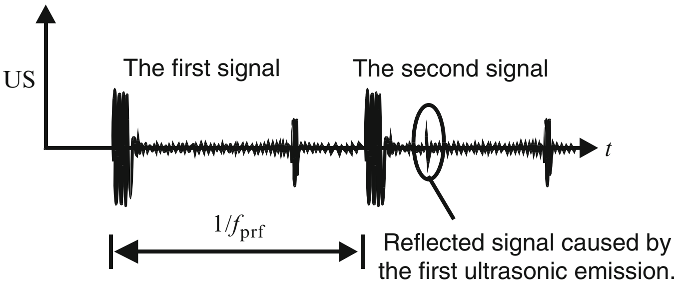

Fig. 3.9 Time-frame aliasing

3.3.2 Time-Frame Aliasing

It was mentioned in Sect. 3.1.3 that increasing f_{prf} decreased P_{max}. If an ultrasonic pulse is reflected on particles or a wall existing outside P_{max}, the reflected signal may appear in the next period of the received signals. This phenomena is called as time-frame aliasing (Fig. 3.9). The time-frame aliasing is considerable if the signals reflected on the surroundings, except the measurement target, are strong. When time-frame aliasing occurs, velocity far from the measurement area appears as if the velocity is in the measurement area.

It is difficult to remove time-frame aliasing from the measured data, and it is almost impossible to modify the velocity to be the same as the velocity aliasing. Therefore, the time-frame aliasing must be taken care of during the measurement. To prevent time-frame aliasing, we recommend that reducing the emission voltage and receiving gain to reduce the reflection other than the measurement targets, or reducing the f_{prf} as low as velocity can be measured. Furthermore, it is also effective to set the scatterer outside the measurement line to obstruct the reflection on the other reflectors.

3.3.3 Temperature

One of the important parameters for the measurement is temperature. If temperature has a distribution in the flow field, sound velocity also changes. Measurement position and the velocity are calculated from the sound velocity. If the sound velocity changes in each position, it directly affects the measurement accuracy. Furthermore, the temperature gradient yields a curved measurement line. As incident and reflected waves go through the same pass, velocity may be calculated regardless of the measurement line. However, the measurement positions are uncertain as the measurement line changes with the temperature.

In another practical problem, efficiency of the ultrasonic emission and sensitivity become worthless under high temperature, and detection of the ultrasonic

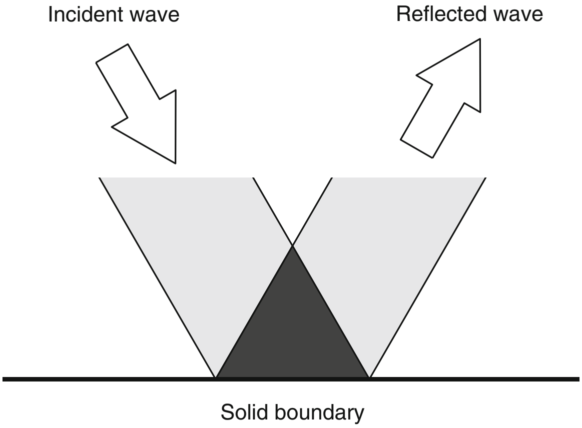

Fig. 3.10 Interference volume between incident and reflected waves near a solid boundary

echo signals is affected. Furthermore, the transducer may break down under higher temperature (see Sect. 2.7). Therefore, temperature of the setting position must be carefully chosen.

3.3.4 Solid Boundary

3.3.4.1 Effect of Reflected Signal on Solid Boundary

Reflection on a solid boundary may affect the velocity measurement. When an ultrasonic transducer is set with an inclined angle to a solid boundary, an interaction volume between the incident and reflected wave exists near the boundary (Fig. 3.10). In this volume, a stationary wave caused by interference between the incident and reflected waves exists, and multiple reflections between the solid boundary and tracer particles may occur. In these cases, it is difficult to measure the correct velocity in the volume. If the solid boundary moves, the wall velocity will be obtained depending on the incident angle.

In these cases, velocity around the solid boundary must be carefully handled because an uncertain velocity profile easily appears. The volume depends on the beam diameter and the number of cycles. With decreasing the diameter and the cycles, the volume decreases. In general, the effect can be negligible if the measurement position is far from several times of the spatial resolutions along the measurement line from the solid boundary. If acoustic impedance of the solid boundary material is close to that of the fluid, for example, acrylic and water, ultrasonic transmission occurs in addition to the reflection. In the case, transmitted wave may reflect on the other side of the wall or other surroundings, and it may affect measurement accuracy. To reduce the effects, setting a scatterer and an ultrasonic absorber, for

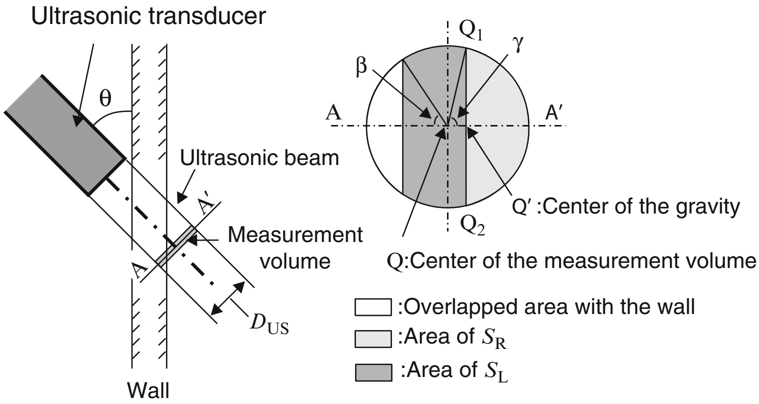

Fig. 3.11 Correction of the measuring position near the channel wall

example, a sponge with water in the case of water and acrylic, on the outer surface of the solid boundary is useful.

3.3.4.2 Correction of Measurement Position Near Wall

In the test section, for a region close to the wall surface, some parts of the ultrasonic measurement volume are located within the wall. This overlapped volume increases with the ultrasonic beam diameter (D_{US}). When the ultrasonic measurement technique is applied to a narrow channel, the overlapped volume cannot be ignored. Aritomi et al. [13] reported a correction method for the measurement volume near the wall.

The ultrasonic beam path near the wall is illustrated in Fig. 3.11. If the ultrasonic beam does not overlap with the solid wall, the cross section of the beam is circular. Q represents the center of the gravity of the area. In a region near the wall, the cross section of the ultrasonic beam is selected as shown in as A–A′. Therefore, the center of gravity changes from Q to Q'. The distance between Q and Q′ causes an error in the data depending on the region of the measurement. Cross-sectional areas of S and S_R can be calculated from the following equations [14]:

$$S = S_R + S_L = \pi r^2 - (\beta r^2 - r^2 \sin\beta \cos\beta), \tag{3.34}$$

$$S_R = \gamma r^2 - r^2 \sin\gamma \cos\gamma, \tag{3.35}$$

$$S_R = S_L. \tag{3.36}$$

According to the foregoing equations, the values of β and γ are calculated at each measuring position, and the correction of the position is determined.

3.3.5 Measurement Volume

The UVP requires a relatively large measurement volume compared to laser Doppler anemometry (LDA). The measurement volume has a disk shape determined by the D_{US} and the channel width, which is determined by number of the wave cycles of the ultrasonic pulse and wavelength. The D_{US} is decided by the ultrasonic pressure field, which is affected by the effective diameter of the piezoelectric element and the basic frequency. Therefore, it is sometimes difficult to reduce the D_{US} depending on the measurement flow fields. Kikura et al. [15] investigated the effect of the measurement volume on velocity data. They compared the experimental data with the direct numerical simulation (DNS) results in mean velocity, variance, and Reynolds stress, and showed that the effect of measurement volume appeared in the buffer region and viscous sublayer. Therefore, measurement accuracy near the wall must consider the solid boundary effects mentioned in Sect. 3.3.4.

References

1. Takeda Y (1986) Velocity profile measurement by ultrasound Doppler shift method. Int J Heat Fluid Flow 7:313–318
2. Takeda Y (1991) Development of an ultrasound velocity profile monitor. Nucl Eng Design 126:277–284
3. Atkinson P, Woodcock JP (1982) Doppler ultrasound and its use in clinical measurement. Academic, New York
4. Barber WD, Eberhard JW, Karr SG (1985) A new time domain technique for velocity measurements using Doppler ultrasound. IEEE Trans Biomed Eng 32:213–229
5. Kasai C, Namekawa K, Koyano A, Omoto R (1985) Real-time two-dimensional blood flow imaging using an autocorrelation technique. IEEE Trans Sonics Ultrasonics SU-32: 458–646
6. Jensen JA (1996) Estimation of blood velocities using ultrasound. Cambridge University Press, New York
7. Tezuka K, Wada S, Mori M, Kikura H, Aritomi M (2008) Analysis of ultrasound propagation in a steel pipe using ultrasonic pulse Doppler method. Thermal Sci Eng 16:95–104
8. KGK catalog ver. 2.0 (Japan). www.PROBE-KGK.com
9. Mori M (2008) Series of calibration tests at national standard loops and industrial applications of new type flow-metering system with ultrasonic pulse-Doppler profile-velocimetry for power plants. In: Proceedings of the 6th international symposium on ultrasonic Doppler methods for fluid mechanics and fluid engineering, pp 13–20
10. Tezuka K, Mori M, Suzuki T, Aritomi M, Kikura H, Takeda Y (2008) Assessment of effects of pipe surface roughness and pipe elbows on the accuracy of meter factors using the ultrasonic pulse Doppler method. J Nucl Sci Technol 45:304–312
11. Mori M, Tezuka K, Takeda Y (2006) Effects of inner surface roughness and asymmetric flow on accuracy of profile factor for ultrasonic flow meter. In: Proceedings of the 14th international conference on nuclear engineering: ICONE14-89729
12. Okubo T, Nanba T, Takeda Y, Furuichi N, Mori M, Tezuka K, Tezuka H (2003) Development of flow rate and profile measurement using ultrasonic Doppler method (15). Micro-bubble generator for reflectors. In: Proceedings of the AESJ Annu Meet 2:29

13. Aritomi M, Zhou S, Nakajima M, Takeda Y, Mori M (1997) Measurement system of bubbly flow using ultrasonic velocity profile monitor and video data processing unit (II). Flow characteristics of bubbly countercurrent flow. J Nucl Sci Technol 34:783–791
14. Taishi T, Kikura H, Aritomi M (2002) Effect of the measurement volume in turbulent pipe flow measurement by the ultrasonic velocity profile method. Exp Fluids 32:188–196
15. Kikura H, Yamanaka G, Aritomi M (2004) Effect of measurement volume size on turbulent flow measurement using ultrasonic Doppler method. Exp Fluids 36:187–196

Chapter 4
Measurement of Fluid Flow

Yuichi Murai, Noriyuki Furuichi, Yasushi Takeda, and Yuji Tasaka

Abstract On the basic of the ultrasonic principle made clear in Chaps. 1–3, flow velocity profiling can be realized if the Doppler method is applicable to the flow system. There are standard velocity fields, which are the most appropriate systems for examining the performance of ultrasonic velocity profiling (UVP) and training users in making UVP measurements. The standard velocity fields have a one-dimensional one-component velocity distribution, irrespective of whether they are steady or unsteady, such as in the case of flow in a rotating circular cylinder and laminar flow in a pipe. Measuring flow in such systems helps clarify the functions of UVP subject to diverse practical problems. Once velocity information is acquired, it is suitably adjusted in post-processing. Post-processing has two purposes: one is to improve the data quality in response to the inclusion of noise in velocity data, and the other is to derive statistical and other quantities.

Keywords Measurement uncertainty • Noise reduction • Post-processing • Standard velocity field • Vector computation

---

Y. Murai (✉) • Y. Tasaka
Faculty of Engineering, Hokkaido University, N13 W8, Sapporo 060-8628, Japan
e-mail: murai@eng.hokudai.ac.jp

N. Furuichi
National Metrology Institute of Japan, National Institute of Advanced Industrial Science
and Technology (AIST), Tsukuba, Japan

Y. Takeda
Hokkaido University, Sapporo, Japan

Tokyo Intstitute of Technology, Tokyo, Japan

Y. Takeda (ed.), *Ultrasonic Doppler Velocity Profiler for Fluid Flow*,
Fluid Mechanics and Its Applications 101, DOI 10.1007/978-4-431-54026-7_4,

4.1 Standard Velocity Field and System Performance [1]

As with other measurement techniques using tracer particles, such as laser Doppler velocimetry (LDV) and particle imaging velocimetry (PIV), selection of the size and concentration of particles sometimes induces a lack of data that causes large deviations in statistical values in UVP measurement. Here a flow in a rotating cylinder is introduced as a stable, standard flow field for evaluation of accuracy and for demonstration. Then, the characteristics of UVP on the data obtained in this system are explained, and how to evaluate the accuracy and precision of the obtained data is discussed. Finally, an example of insufficient seeding conditions that induce lack of data is given.

4.1.1 Rotating Cylinder

We consider a flow in a rotating cylinder as shown in Fig. 4.1. When a rotation of the cylinder with angular velocity of ω is applied in the stationary state, angular momentum is gradually transferred from the cylinder wall to the cylinder center by the viscous diffusion. This process is called spin-up [2, 3]. Here we assume that the flow is axisymmetric and no radial and axial flow components exist as an ideal condition. After the momentum transfer reaches the center of the cylinder within a period of time, the flow takes stationary rigid body rotation that has a constant velocity of the rotation at each radial position. We measure a velocity profile of the flow in this condition along a line parallel to the centerline of the cylinder with Δy displacement from the centerline. Here the azimuthal velocity at a radial position r takes $u_\theta = r\omega$. The velocity component in the x direction, which is the measurement

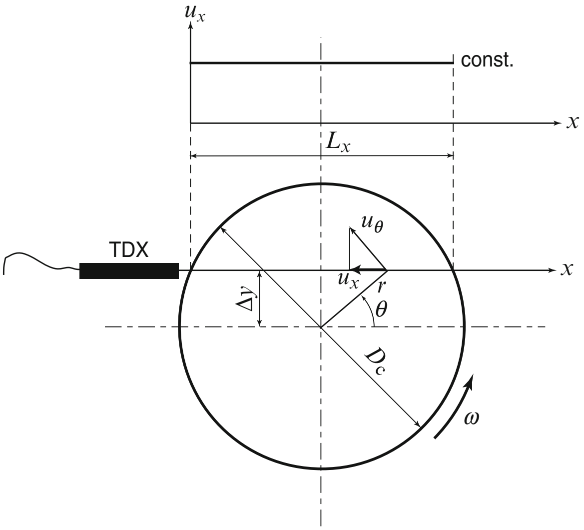

Fig. 4.1 Schematic diagram of measurement system and velocity profile of rotating flow in a cylinder

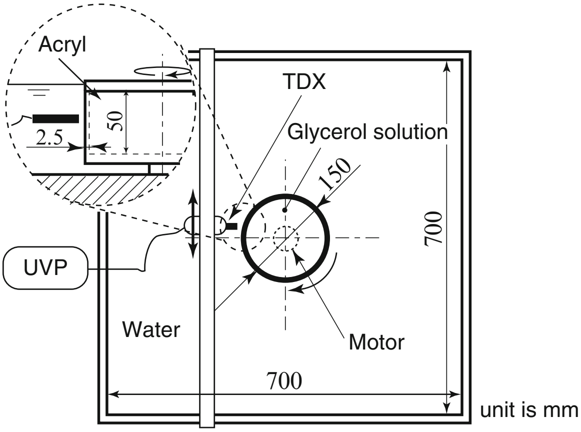

Fig. 4.2 Schema of experimental setup for rotating flow measurement

line direction of UVP at the point, becomes $u_x = u_\theta \sin\theta$. Because the radial position along the measurement line (x direction) is $r = \Delta y / \sin\theta$, the velocity component becomes $u_x(x) = \omega \Delta y$ in the x direction. The spatiotemporal velocity field $u_x(x, t)$ obtained by UVP in the spin-up process represents that the momentum is gradually transferred inside the cylinder, and finally the flow reaches rigid body rotation, that is, $u_x(x, t) = \text{const}$. The time variation of the velocity profile can be derived from the Navier–Stokes equation with the assumption of flow axisymmetry. In the actual measurement, however, Görtler vortices [4] and meridional circulation exist because of centrifugal force [2, 3], and thus the flow does not agree with the theoretical solution of the ideal situation.

Figure 4.2 shows a schema of the experimental setup for measurements of rotating flow. The diameter of the cylinder, thickness of the cylinder wall, and the height of the cylinder are 150, 2.5, and 50 mm, respectively. Nylon powder 50 μm in mean diameter and 1.06 in specific weight is used as tracer particles. The cylinder is fixed at the center of a rectangular vessel 700 mm on the side, and thus filling water inside the vessel allows transmission of ultrasonic waves from outside of the cylinder to the rotating fluid without contact of an ultrasonic transducer at the side wall of the cylinder. A small plate of ultrasonic absorber (see Appendix A.5) is set at the side wall of the vessel and reduces influence of multiple reflections of ultrasonic waves; 23 wt % glycerol solution is used for density matching with the tracer particles. Speed of sound estimated from the time-of-flight technique is $c = 1{,}601$ m/s. We emit four cycles of ultrasonic waves with 4 MHz frequency from a transducer 5 mm in effective diameter.

4.1.2 Example of Measured Data

Here we introduce an example of the measurement. The fluid in the cylinder reaches rigid body rotation with $\omega = 4.20$ rad/s in angular velocity. The ultrasonic transducer is located parallel to the horizontal center line of the cylinder with $\Delta y = 20$ mm in

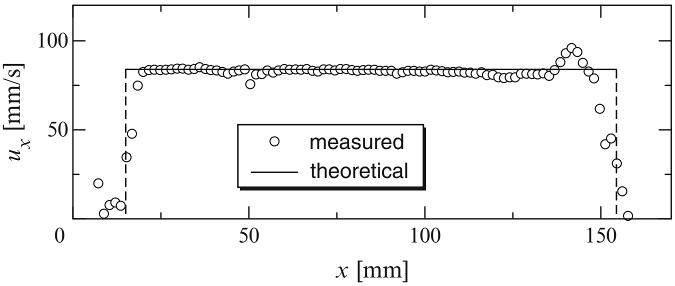

Fig. 4.3 Mean velocity of flow in a rotating cylinder

displacement from the line. Figure 4.3 shows the measurement result; the profile represents averaged velocity of 512 instantaneous profiles. The solid line in the figure is a theoretical value obtained from $u_x(x) = \omega\,\Delta y$, and broken lines indicating the width of the cylinder are calculated from the diameter of the cylinder and Δy. As shown, the obtained profile agrees with the theoretically estimated velocity in a large area. Near the walls, however, the velocity is measured as a smaller value than the theoretical value because of the multiple reflection of ultrasonic waves in the wall. As mentioned in Sect. 2.4, divergence of the ultrasonic wave enlarges the measurement volume. The enlargement increases measurement uncertainties when a large velocity gradient exists in a direction perpendicular to the measurement line. Larger velocities near the wall ($x = \sim 150$ mm) may be caused by the enlargement, that is, the velocity component in the measurement line of the cylinder rotation is detected.

Figure 4.4 shows a spatiotemporal velocity field representing the spin-up process. Experimental conditions are 1,000 cSt silicone oil as the test fluid, 2 MHz as the basic frequency of the ultrasonic wave, $\Delta y = 13.5$ mm, and $\omega = 12.57$ rad/s. Here the speed of sound in the oil is 1,000 m/s. In the figure the azimuthal velocity component $u_\theta(r, t)$ is derived from $u_x(x, t)$ with assumption of axisymmetry.

4.1.3 *Profile Reproduction (Moment)*

UVP provides instantaneous *velocity profiles*; thus, we have to evaluate not only the value of the velocity, but also the shape of the profile. Reproducibility of the value and shape is affected by the characteristics of the ultrasonic waves and the test fluid. For instance, the measurement volume is not constant on the measurement line because of divergence of the ultrasonic beam (cf. Sect. 2.4.3). The velocity measured by UVP is given as a spatial average of velocities in the measurement volume, and thus the value depends on the size of measurement volume. A large influence of the measurement volume on the velocity may induce deformation of the velocity profile. Also, nonuniformity on the distribution of tracer particles may cause the

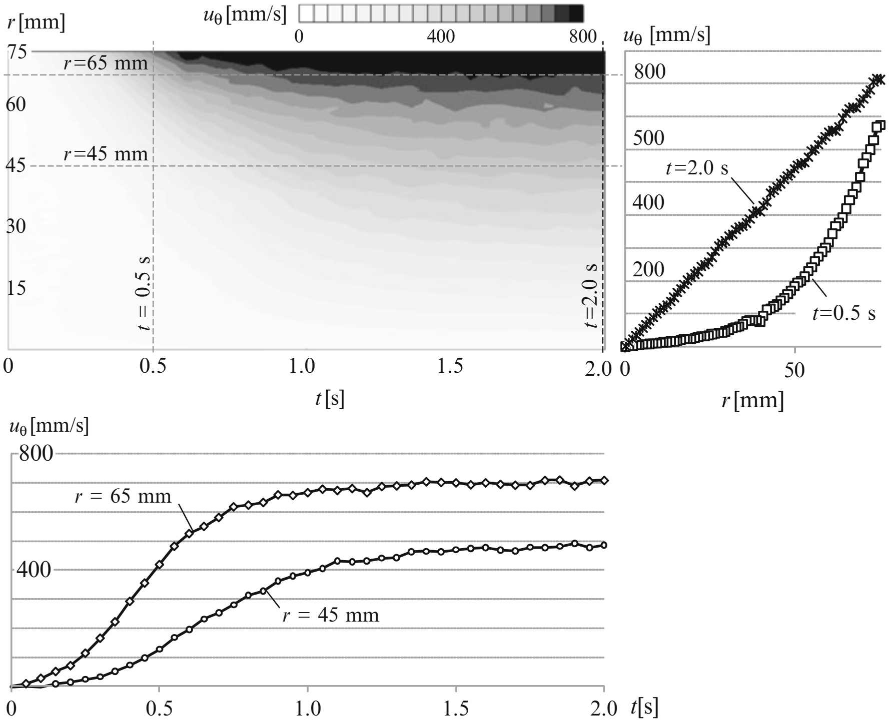

Fig. 4.4 Spatiotemporal velocity field of a spin-up process in a rotating cylinder

deformation of the profile. Here we evaluate the reproducibility of velocity profile on measurement of flow in a rotating cylinder.

The theoretically estimated velocity profile in a normal form is given as

$$\begin{aligned} v(x) &= 1 \quad -\frac{1}{2} \le x \le \frac{1}{2}, \\ &= 0 \quad \text{otherwise.} \end{aligned} \tag{4.1}$$

High-order moments of the profile

$$M_n = \int_{-\infty}^{\infty} x^n v(x) \mathrm{d}x \tag{4.2}$$

give us quantitative evaluation of the reproducibility of the shape. Specifications of the moments are summarized in Table 4.1. For example, the third-order moment (skewness) indicates the symmetry of the profile, and the fourth-order moment (kurtosis) indicates flatness of the profile. These moments can be also used for evaluation of probability density functions of velocity (cf. Sect. 4.2.7).

Table 4.1 Example of high-order moments for evaluation of profile shape

Order	Moment: theoretical		Evaluation factor for the shape			
0	M_0	V	Mean value		1	Mean height
1	M_1	0	Center	X_c	0	Position
2	M_2	$V/12$	Variance		0.28	Variance
3	M_3	0	Skewness	$S=M_3/(M_0\sigma^3)$	0	Symmetry
4	M_4	$V/80$	Kurtosis	$K=M_4/(M_0\sigma^4)$	1.8	Flatness

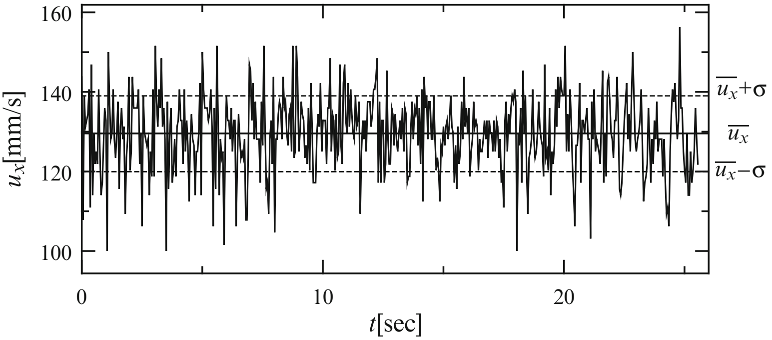

Fig. 4.5 Velocity fluctuation at a point on the measurement line for a flow with rigid body rotation

4.1.4 Accuracy and Precision

Accuracy and *precision* exist as indications of measurement errors. Here we explain their meaning using measurement results of flow in the rotating cylinder. The flow in a rigid body rotation should be stationary, and thus the point-wise velocity should have constant value in the time series. Nevertheless, the time series have a distribution around a mean value because of insufficiency of tracer particles or other reasons. The width of the distribution represents the measurement accuracy, and distance from the correct value to the mean value represents the measurement precision. Namely, a narrower distribution and a small distance indicate high accuracy and high precision, respectively. In this sense, there exist measurements with high accuracy and low precision.

Figure 4.5 shows velocity fluctuation obtained at a point on the measurement line for flows with rigid body rotation. The theoretically estimated correct value is $u_x(x)=\omega\Delta y=129.57$ mm/s. On the other hand, the mean value of the time series of measured velocity is $\overline{u}_x=129.49$ mm/s. In counting the accuracy on the off-axis value Δy, precision of the measurement is high enough. On the other hand, the accuracy can be evaluated by standard deviation of the distribution of velocity. The deviation is $\sigma=9.52$ mm/s and is 7% of the mean value. In the case of lack of data because of insufficient tracer particles, erroneous data would have extremely smaller values than the mean value. Such erroneous data can be eliminated by setting a threshold, e.g., $\overline{u}_x-3\sigma$.

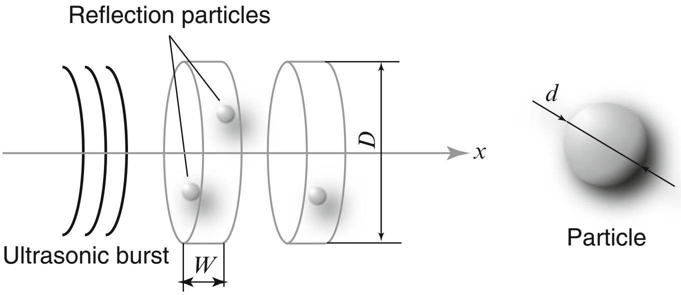

Fig. 4.6 Schematic diagram of measurement volume in UVP

4.1.5 Success Rate

In velocity profile measurement by UVP, the shape of measurement volume resembles a disk, which are discretely arranged in a flow (Fig. 4.6). The volume is determined by a pulse length (wavelength of ultrasonic wave, cycles in a pulse) and an effective diameter of ultrasonic burst. Theoretically, if one or more reflection particle exists in the volume during the measurement, UVP can measure velocity at the volume. Assuming that one particle is in the measurement volume V_m, concentration of particles in liquid γ_p becomes

$$\gamma_p \simeq \frac{V_p}{V_m} = \frac{2d^3}{3WD^2}, \tag{4.3}$$

where V_p is a volume of the particle, $V_\mathrm{p} = \pi d^3/6$, and d, D, W are particle diameter, an effective diameter of ultrasonic burst emitted from an ultrasonic transducer, and width of the measurement volume, respectively. In the actual measurement system, γ_p is very small, approximately 0.001%; this corresponds to 10 mg particles for 1 l water if the particle has the same density as water. When fluid velocity is sufficiently high, the required concentration of particles approaches this value. If flow is slower, however, the required concentration strongly depends on velocity; namely, a sufficient amount of particle flux moving through the measurement volume is required. Particle flux, f_p, which is the number of particles passing through the measurement volume per unit time, is given as

$$f_p = \frac{\pi}{4} D^2 \gamma_p U / V_p, \tag{4.4}$$

where U is velocity of fluid flow. The measurement requires that the particle flux f_p in a measurement time Δt is larger than

$$f_\mathrm{p} \Delta t \geq 1. \tag{4.5}$$

Table 4.2 Measurement conditions

	Symbol	Unit	Value
Speed of sound in 23 wt % glycerol solution	c	m/s	1,601
Ultrasonic waves			
Frequency	f	MHz	4
Cycles	N		4
Effective diameter	D	mm	5
Width of measurement volume	W	mm	0.801
Diameter of tracer particles	d	µm	50

and then

$$\gamma_{\mathrm{p}} U \geq \frac{2d^3}{3D^2 \Delta t} = \text{const.} \tag{4.6}$$

As expressed in this inequality, velocity can be measured by UVP when $\gamma_{\mathrm{p}}U$ is larger than a constant value, which depends on measuring volume, particle size, and measuring time interval. We investigate a necessary and sufficient value of $\gamma_{\mathrm{p}}U$ by estimating error of measurement at several conditions of U and γ_{p} on measurement of flows in a rotating cylinder. Measurement conditions required for calculation of the particle concentration are specified in Table 4.2.

Figure 4.7a shows an instantaneous velocity profile measured in a high particle concentration ($\gamma_{\mathrm{p}} = 0.02\%$). Deviation of the profile is small, and measured velocity is nearly constant inside the cylinder, as predicted by the theory. In comparison with this, the profile measured in insufficient particle concentration (Fig. 4.7b) has a large deviation. Error caused by insufficient particles is defined as follows. UVP repeats emission and reception of ultrasound several times to take an instantaneous velocity profile (repetition number is 32 in this measurement). Insufficient particles cause error of the measured value, and the error appears in the profile as deviation. Furthermore, if there is no particle in the measurement volume during measurement, measured velocity becomes zero. In this estimation, velocity, which is smaller than ten times velocity resolution of the measurement, is attributed as an error caused by insufficiency of particles. The number of spatial sampling points for the estimation is 20 in the range of $x = 40$–70 mm, by taking into account both divergence of ultrasonic beam with respect to distance from the ultrasonic transducer and deviation near the lateral wall. The number of profiles is 512, so that a total sampling number is about 10,000.

The error is estimated for many cases of $\gamma_{\mathrm{p}} = 0.002$–$0.05\%$ and $\omega = 1.0$–7.2 rad/s. Figure 4.8 shows the result of the estimation of the error rate. The horizontal axis and the vertical axis in the figure represent particle flux through the measurement volume $\gamma_{\mathrm{p}}U_{\mathrm{m}}$ and error rate, respectively, where U_{m} is temporal and spatial average of measured velocity, u_x. γ_{p} can be converted into averaged number of particles in the measurement volume n_{p}, shown with γ_{p} in the legend, and then $\gamma_{\mathrm{p}}U_{\mathrm{m}}$ can be also converted into particle number flux, $n_{\mathrm{p}}U_{\mathrm{m}}$. There is a fairly large deviation in the results independent of the amount of γ_{p}. It may be caused

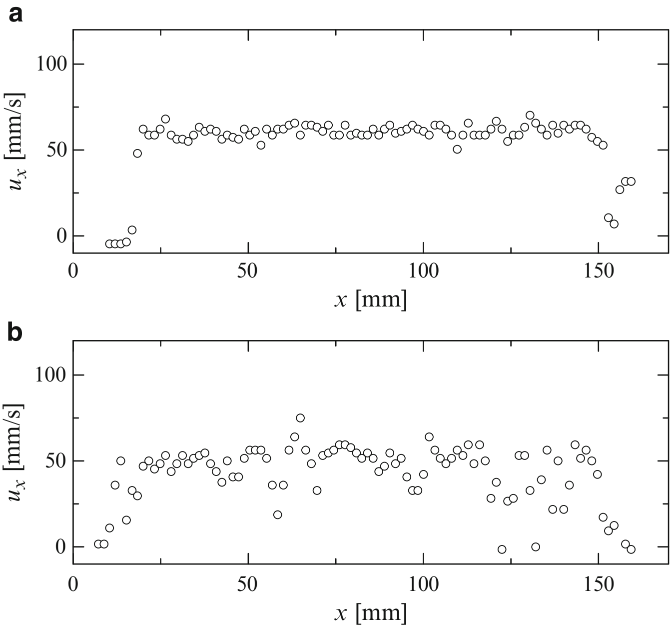

Fig. 4.7 Instant velocity profiles of a flow in a rotating cylinder measured by UVP. (**a**) A case of sufficient tracer particle concentration. (**b**) A case of insufficient tracer particle concentration

Fig. 4.8 Error rate caused by lack of particles versus particle flux through the measurement volume $\gamma_p U_m$ or particle for each particle concentration γ_p, where $n_p U_m$ represents particle number flux converted from $\gamma_p U_m$. The *solid line* represents approximate line of data calculated by least-squares approximation

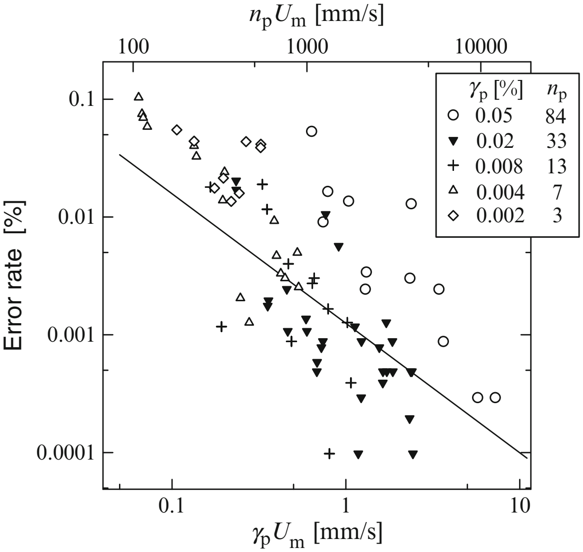

by inhomogeneous seeding; thus, such effects often appear when seeding is poor, as in these measurements. However, the results have a similar trend, that is, the error rate decreases monotonically with respect to $\gamma_p U_m$. The slope of the fitted line on the log–log plot is −1.1, and then measurement error decreases roughly inversely proportional to $\gamma_p U_m$. The necessary seeding concentration can be determined from this relationship. For instance, to keep a measurement deviation below 0.1%, $\gamma_p U_m$ must be set larger than 1 mm/s. In another expression, particle number flux must be set at more than 1,700 mm/s. This result is obtained for flows in a rotating cylinder and thus is not applicable directly to all other measurement systems; that is, the index −1.1 may change in other measurement systems. Furthermore, even in cases of sufficient particle flux, the quality of results is not always ensured. For instance, if the velocity component across the measurement line is dominant, UVP cannot detect a ultrasonic echo from the same particle. Then, aliasing occurs and thus the measurement error increases.

4.2 Post-processing

This section explains several post-processing methods for velocity profile data obtained by UVP. There are two objectives of post-processing: one is the correction of measurement data, and the other is data analysis to estimate quantities such as statistics. The former relates to the measurement principle of UVP; and the latter includes analyses of the one-dimensional one-component velocity data recorded by UVP.

4.2.1 Correction of Angle

UVP measures the flow velocity component in the direction of the measurement line as previously mentioned. The relationship is illustrated in Fig. 4.9.

In both of Fig. 4.9a and 4.9b, **u** is the flow velocity vector and *u* is the velocity component measured by UVP. The *broken line* is the measurement line of UVP, and **n** is a unit vector indicating the direction of the measurement line. Here only the

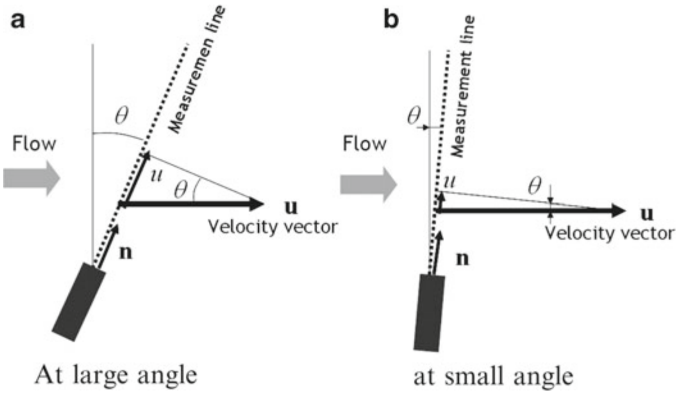

Fig. 4.9 Relationship between flow velocity vector and velocity measured by UVP. (**a**) Large angle. (**b**) Small angle

effective center line of the ultrasonic beam is considered, ignoring the influence of the beam width (see Sect. 2.4). The mathematical relationship among **u**, **n**, and u is

$$u(s,t) = \mathbf{u}(s,t)\cdot\mathbf{n} = u_x n_x + u_y n_y + u_z n_z, \tag{4.7}$$

where s and t are the spatial coordinates along the measurement line and time, respectively. The relationship simply shows that the velocity component u is given by the dot product of the flow velocity vector, $\mathbf{u}=(u_x, u_y, u_z)$, and the unit vector, $\mathbf{n}=(n_x, n_y, n_z)$.

One-dimensional flow, such as laminar pipe flow, has a constant angle θ, in both time and space, regardless of the spatial coordinate on the measurement line. In such a case, the unit vector **n** is constant, and applying $\mathbf{u}=(u_x, u_y, u_z)=(u_x, 0, 0)$ for Eq. (4.7) gives

$$u(s,t) = \mathbf{u}(s,t)\cdot\mathbf{n} = u_x n_x = u_x \sin\theta \rightarrow u_x(s,t) = \frac{u(s,t)}{\sin\theta}, \tag{4.8}$$

where u_x is the velocity component in the mainstream direction. When the angle θ is given, the velocity profile of the mainstream component $u_x(s, t)$ is obtained from the measured velocity profile, $u(s, t)$. For turbulent flow, however, instantaneous velocity vectors deviate in orientation, and Eq. (4.8) does not give the mainstream component immediately. When the time-averaged velocity vector field has only a single component, the time-averaged mainstream velocity profile is estimated by taking the time average of Eq. (4.8) in the measurement time duration, T, as

$$\bar{u}_x(s) = \frac{\bar{u}(s)}{\sin\theta},\ \bar{u}(s) = \frac{1}{T}\int_0^T u(s,t)\mathrm{d}t,\ \bar{u}_x(s) = \frac{1}{T}\int_0^T u_x(s,t)\mathrm{d}t. \tag{4.9}$$

Although the time-averaged flow field is one dimensional, we need to pay attention to error amplification when the angle θ is set small. Setting the angle θ small allows the measurement to consider high-speed flow in the mainstream direction, but a very small setting error in the angle $\Delta\theta$ amplifies the velocity measurement error, which is deduced with Eq. (4.8):

$$u_x = \frac{u}{\sin\theta} \rightarrow du_x = \frac{1}{\sin\theta}\mathrm{d}u - \frac{\cos\theta}{\sin^2\theta}u\mathrm{d}\theta. \tag{4.10}$$

The relative error of the mainstream velocity is given as

$$\Delta u_x = \frac{1}{\sin\theta}\Delta u - \frac{\cos\theta}{\sin^2\theta}u\Delta\theta \rightarrow \frac{\Delta u_x}{u_x} = \frac{\Delta u}{u} - \frac{\Delta\theta}{\tan\theta}. \tag{4.11}$$

Added to the first term, $\Delta u/u$, the uncertainty in the angle setting of the measurement line, which appears as the second term with $\Delta\theta$, affects the final result.

4.2.2 Method of Averaging

UVP can measure the velocity profile in space–time dimensions, and a variety of definitions for averaging the velocity are applied:

$$\text{Time average} \quad U(s) = \frac{1}{T}\int_{t}^{t+T} u(s,t)\mathrm{d}t, \tag{4.12}$$

$$\text{Space average} \quad U(t) = \frac{1}{L}\int_{y}^{y+L} u(s,t)\mathrm{d}s, \tag{4.13}$$

$$\text{Space-time average} \quad U = \frac{1}{LT}\int_{t}^{t+T}\int_{y}^{y+L} u(s,t)\mathrm{d}s\,\mathrm{d}t, \tag{4.14}$$

where T and L are the time-averaging period and space-averaging width, respectively. In pipe flow or any flow within a closed boundary, the cross-sectional average velocity is defined as follows:

- Cross-sectional average:

$$U(t) = \frac{Q}{A}, \quad Q = \int_{A} v_z(s,t)\mathrm{d}A = \int_{A} \frac{u(s,t)}{\sin\theta}\mathrm{d}A, \tag{4.15}$$

where v_z is the velocity component normal to the cross section, A.

Setting the measurement line that crosses the central axis of a circular pipe, the cross-sectional average velocity, which is proportional to the volume flow rate in the pipe [5], is obtained.

- Cross-sectional average velocity in a circular pipe:

$$U(t) = \frac{\int_{0}^{R} v_z(r,t)\,2\pi r\mathrm{d}r}{\pi R^2} = \frac{2\int_{0}^{R} u(r,t)\,r\mathrm{d}r}{R^2\sin\theta}. \tag{4.16}$$

The foregoing definitions of averaging are based on the premise that all the velocity data are correctly recorded by UVP. In practice, spots and bands of near-zero velocity are sometimes included in UVP data for various reasons detailed in Sect. 3.3. For such quality of data, statistics that exclude near-zero data are often used, exemplified as follows:

- Time average excluding near-zero velocity:

$$U(s) = \frac{\int u(s,t)\cdot\phi(s,t)\mathrm{d}t}{\int \phi(s,t)\mathrm{d}t}, \quad \phi = \begin{cases} 1 & \text{for} |u| \geq u_{\min} \\ 0 & \text{for} |u| < u_{\min} \end{cases}, \tag{4.17}$$

where ϕ is a binary function in the space–time two dimensions, taking a value of 1 for significant measured velocity and 0 for near-zero velocity less than $u_{\min}$.

An adequate threshold velocity, $u_{\min}$, needs to be given by the user considering the velocity resolution, Δu, of the UVP measurement to be its lowest value.

4.2.3 *Computation of Vector*

From the one-dimensional one-component velocity distribution measured by UVP, the multi-component or multidimensional flow field can be estimated when the measurement setup is extended. There are two kinds of extensions: one is to provide multiple measurement lines so that a velocity vector is obtained at their crossing point, and the other is to couple the data with additional restriction equations that we know the target flow field satisfies.

4.2.3.1 Velocity Vector Measurement Using Two Measurement Lines

Figure 4.10 shows three combinations of two measurement lines used to obtain a velocity vector. u_1 and u_2 are velocity components that are measured directly by an individual UVP. The practical measurement setup for such a system can be referred to in the chapters of applications (Sects. 6.3 and 7.4). Case (a) in the figure has the following relationships for the flow velocity vector $\mathbf{u} = (u, v)$ at the crossing point.

$$u_1 = \mathbf{u} \cdot \mathbf{n}_1 = \begin{pmatrix} u \\ v \end{pmatrix} \cdot \begin{pmatrix} 0 \\ 1 \end{pmatrix} = v, \tag{4.18}$$

$$\begin{aligned} u_2 = \mathbf{u} \cdot \mathbf{n}_2 &= \begin{pmatrix} u \\ v \end{pmatrix} \cdot \begin{pmatrix} \cos \mathbf{n}_2\, \alpha & \sin \alpha \\ -\sin \alpha & \cos \alpha \end{pmatrix} \begin{pmatrix} 0 \\ 1 \end{pmatrix} \\ &= \begin{pmatrix} u \\ v \end{pmatrix} \cdot \begin{pmatrix} \sin \alpha \\ \cos \alpha \end{pmatrix} = u \sin \alpha + v \cos \alpha . \end{aligned} \tag{4.19}$$

Therefore, the velocity vector is given by

$$\mathbf{u} = \begin{pmatrix} u \\ v \end{pmatrix} = \begin{pmatrix} (u_2 - u_1 \cos \alpha) / \sin \alpha \\ u_1 \end{pmatrix} \tag{4.20}$$

This formula indicates that the smaller the angle of the second measurement line α is set, the faster the measurable flow velocity u can be covered.

Case (b) in Fig. 4.10 is a symmetric arrangement of two measurement lines [6, 7]. The relationships between the flow velocity vector $\mathbf{u}$ and the two velocity components along the measurement lines are described by

$$u_1 = \mathbf{u} \cdot \mathbf{n}_1 = \begin{pmatrix} u \\ v \end{pmatrix} \cdot \begin{pmatrix} \sin \alpha \\ \cos \alpha \end{pmatrix} = u \sin \alpha + v \cos \alpha , \tag{4.21}$$

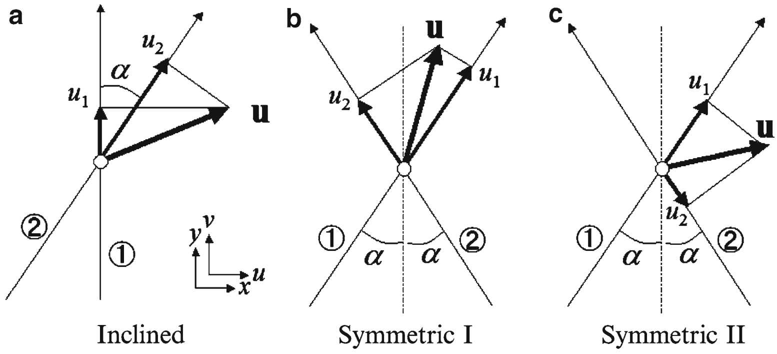

Fig. 4.10 Stereoscopic arrangement of measurement lines for vector computation

$$u_2 = \mathbf{u} \cdot \mathbf{n}_2 = \begin{pmatrix} u \\ v \end{pmatrix} \cdot \begin{pmatrix} -\sin\alpha \\ \cos\alpha \end{pmatrix} = -u\sin\alpha + v\cos\alpha. \tag{4.22}$$

Therefore, the velocity vector is obtained as

$$\mathbf{u} = \begin{pmatrix} u \\ v \end{pmatrix} = \begin{pmatrix} (u_1 - u_2)/2\sin\alpha \\ (u_1 + u_2)/2\cos\alpha \end{pmatrix}. \tag{4.23}$$

4.2.3.2 Velocity Vector Measurement Using Three Measurement Lines

Figure 4.11 shows a typical example of three measurement lines used to obtain all three velocity components. The example case is that the azimuthal angular interval is 120°, the inclination angle to the z-axis is set by α, and the projection of the first measurement line coincides with the x-axis. The relationship between the velocity vector at the triple-crossing point and its components projected into the measurement lines is described as

$$\begin{pmatrix} u_1 \\ u_2 \\ u_3 \end{pmatrix} = \begin{pmatrix} w\cos\alpha + u\sin\alpha \\ w\cos\alpha - (u - v)\sin\alpha/2 \\ w\cos\alpha - (u + v)\sin\alpha/2 \end{pmatrix}. \tag{4.24}$$

Therefore, the velocity vector **u** is obtained as

$$\mathbf{u} = \begin{pmatrix} u \\ v \\ w \end{pmatrix} = \begin{pmatrix} [2u_1 - (u_2 + u_3)]/3\sin\alpha \\ (u_2 - u_3)/\sin\alpha \\ (u_1 + u_2 + u_3)/3\cos\alpha \end{pmatrix}. \tag{4.25}$$

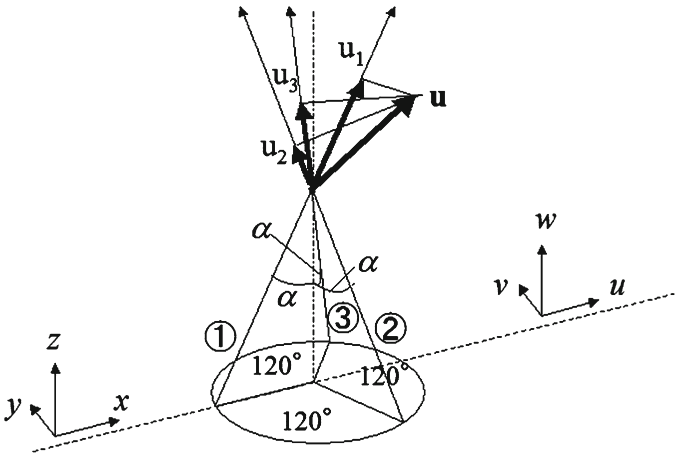

Fig. 4.11 Three-component measurement of velocity vector using three lines

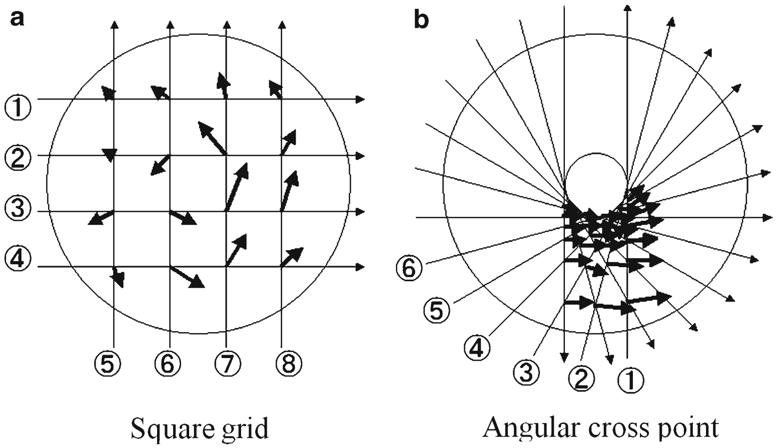

Fig. 4.12 Vector field measurement using grid-arranged measurement lines

4.2.3.3 Velocity Vector Field Monitoring by Arrayed Measurement Lines

The velocity vector field can be measured when a number of ultrasonic measurement lines are arranged within the target domain. Figure 4.12 illustrates two arrangements of the measurement lines. Case (a) shows the generation of square-arranged crossing points by arraying multiple parallel measurement lines in two orthogonal directions. When the array has an interval angle of 60°, triangular distribution of the crossing points is generated to observe the flow field. Case (b) shows the generation of the crossing-point distribution concentrated in the central region by arraying the measurement lines in the angular direction. This array is suitable for monitoring the internal flow of a circular domain [6, 8]. In contrast with inward inspection, a wide

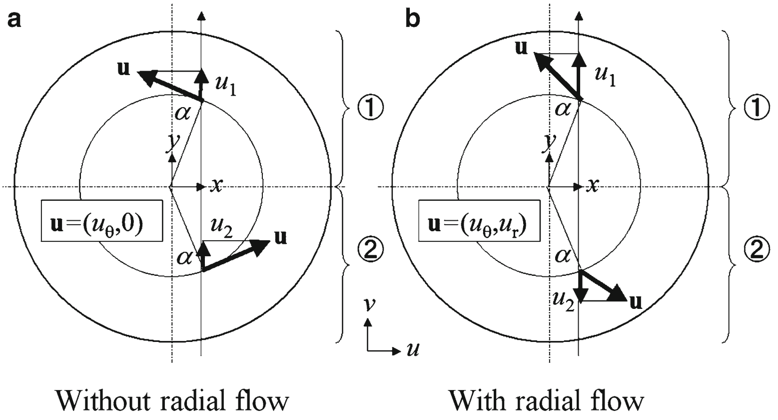

Fig. 4.13 Vector profiling of axisymmetric flow using a single measurement line

flow field can be monitored when the ultrasound measurement lines are set outward. Outward inspection realizes monitoring of environmental flow and large-scale flow.

4.2.3.4 Velocity Vector Measurement for Axisymmetric Flow

When the target flow field is axisymmetric, a two-dimensional flow field can be reconstructed from only the data for a single measurement line. This is an example of the introduction of a physical restriction equation(s) to the vector information analysis. The concept is applied in a similar way when the initial condition, boundary condition, or flow mode is given *a priori*.

Figure 4.13 shows examples of visualization for an axisymmetric flow field using a single measurement line. The measurement line is set to avoid penetration of the axis. The flow velocity components are now described by u_θ in the angular direction and u_r in the radial direction. As shown in case (a) in the figure, when the flow has no radial advection, the velocity projection on the measurement lines is given by

$$\begin{pmatrix} u_1 \\ u_2 \end{pmatrix} = \begin{pmatrix} u_\theta \sin\alpha \\ u_\theta \sin\alpha \end{pmatrix} = \begin{pmatrix} u_\theta x / r \\ u_\theta x / r \end{pmatrix}, \tag{4.26}$$

where the projection velocities u_1 and u_2 are those deeper and shallower than the central axis, respectively, α is the angle of the point along the measurement line, and $\sin\alpha$ is given by the distance from the axis, r, and the coordinate, x. Equation (4.26) tells us that the same velocity profile is obtained from both regions because of symmetry:

$$u_\theta(r) = \frac{u_1(r)}{\sin\alpha} = \frac{r}{x}u_1(r), \quad u_\theta(r) = \frac{u_2(r)}{\sin\alpha} = \frac{r}{x}u_2(r). \tag{4.27}$$

Rewriting the velocity components in Cartesian coordinates, u and v, in x and y directions, the velocity vector is

$$\mathbf{u} = \begin{pmatrix} u \\ v \end{pmatrix} = \begin{pmatrix} -u_\theta \cos\alpha \\ +u_\theta \sin\alpha \end{pmatrix} = \begin{pmatrix} u_1(r)y/x \\ u_1(r) \end{pmatrix}. \tag{4.28}$$

Next, case (b) for radial flow in Fig. 4.13 is explained. When the radial flow velocity component is u_r, the projection velocity components into the two regions are

$$\begin{pmatrix} u_1 \\ u_2 \end{pmatrix} = \begin{pmatrix} u_\theta \sin\alpha + u_r \cos\alpha \\ u_\theta \sin\alpha - u_r \cos\alpha \end{pmatrix} = \begin{pmatrix} u_\theta x/r + u_r y/r \\ u_\theta x/r - u_r y/r \end{pmatrix}. \tag{4.29}$$

The equation shows that u_1 and u_2 have different values. Solving the equation [9], the azimuthal and radial velocity components are given by

$$\begin{pmatrix} u_\theta(r) \\ u_r(r) \end{pmatrix} = \begin{pmatrix} (u_1 + u_2)/2\sin\alpha \\ (u_1 - u_2)/2\cos\alpha \end{pmatrix} = \begin{pmatrix} (u_1 + u_2)r/2x \\ (u_1 - u_2)r/2y \end{pmatrix}. \tag{4.30}$$

Rewriting the velocity components in Cartesian coordinates, the reconstruction of the axisymmetric flow accompanying radial convection is completed as

$$u = \begin{pmatrix} u \\ v \end{pmatrix} = \begin{pmatrix} -u_\theta \cos\alpha + u_r \sin\alpha \\ +u_\theta \cos\alpha + u_r \sin\alpha \end{pmatrix} = \begin{pmatrix} (u_1 + u_2)y/2x + (u_1 - u_2)x/2y \\ u_1 \end{pmatrix}. \tag{4.31}$$

4.2.3.5 Use of Frozen Hypothesis

Let us consider the flow field for which the spatial structure is kept stable. In such a situation, the velocity vector field can be assumed frozen and to move without changing form. The concept is referred to as the *frozen hypothesis* and allows temporal information to be converted to spatial information. Here an example of such a measurement is given.

Figure 4.14a shows the setup of UVP along three different lines for the measurement of a single vortex ring that passes the crossing point. Transducer A measures the translational velocity of the vortex ring that is emitted from the top nozzle, transducer B measures the velocity fluctuation during the passage of the vortex ring, and transducer C measures that in the oblique direction. The vortex ring stably passes the measurement section (i.e., it simply migrates without structural change), and the structure is estimated by converting the temporal information to spatial information according to

$$x = x_0 - U \cdot t \Rightarrow \begin{cases} u_{\mathrm{B}}(r,t) \to u_{\mathrm{B}}(r,z) \\ u_{\mathrm{C}}(s,t) \to u_{\mathrm{C}}(r,z) \end{cases}, \tag{4.32}$$

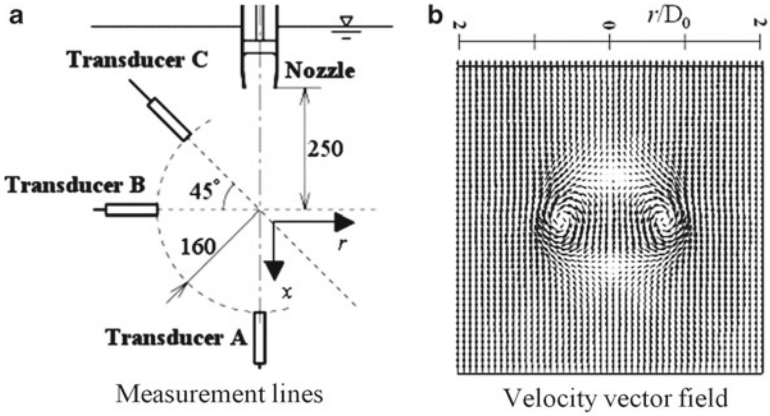

Fig. 4.14 Vortex ring measured with frozen hypothesis for translational advection. (**a**) Set-up of measurement lines. (**b**) Velocity vector field measured

where x_0 is the base coordinate at time $t=0$ and U is the translational velocity of the vortex ring. The conversion provides a space–space two-dimensional velocity distribution of the vortex ring from the data of transducers B and C. The coordinate r is converted from the coordinate s considering the crossing angle of 45°. Consequently, two-dimensional velocity vector information of a single vortex ring, $\mathbf{u}=(u_x, u_r)$, is determined according to

$$\begin{pmatrix} u_\mathrm{B} \\ u_\mathrm{C} \end{pmatrix} = \begin{pmatrix} u_r \\ u_x \sin(\pi/4) + u_r \cos(\pi/4) \end{pmatrix} = \begin{pmatrix} u_r \\ \sqrt{2}/2(u_x + u_r) \end{pmatrix}. \tag{4.33}$$

This relationship can be used to expand the velocity vector field as

$$\mathbf{u} = \begin{pmatrix} u_x \\ u_r \end{pmatrix} = \begin{pmatrix} \sqrt{2}u_\mathrm{C} - u_\mathrm{B} \\ u_\mathrm{B} \end{pmatrix}. \tag{4.34}$$

Figure 4.14b shows the velocity vector distribution of the vortex ring obtained using the foregoing relationships [7]. It is noted that the velocity vector concentration in the direction of migration changes with the translational velocity because of the principle of time-to-space conversion.

4.2.4 One-Dimensional Fourier Transform

Fourier expansion of the velocity profile measured by UVP assesses the frequency of velocity fluctuation and wave number of the spatial distribution. There are multiple purposes of the expansions, such as measurement of the vortex shedding frequency, evaluation of the energy spectrum, judgment of the flow mode, and detection of measurement noise. Furthermore, the Fourier transform of velocity data is effective for finding a stationary object in a flow and the position of solid walls so long as the spectrum changes in their presence.

4.2.4.1 Fourier Transform

The Fourier transform is defined as

$$P(\omega)=\frac{1}{2\pi}\int_{-\infty}^{+\infty}u(t)\mathrm{e}^{-i\omega t}\mathrm{d}t=\frac{1}{2\pi}\int_{-\infty}^{+\infty}u(t)(\cos\omega t-i\sin\omega t)\mathrm{d}t \tag{4.35}$$

and the Fourier inverse transform as

$$u(t)=\int_{-\infty}^{+\infty}P(\omega)\mathrm{e}^{i\omega t}\mathrm{d}\omega=\int_{-\infty}^{+\infty}P(\omega)(\cos\omega t+i\sin\omega t)\mathrm{d}\omega, \tag{4.36}$$

where i and $u(t)$ are the imaginary number unit and original function, respectively. Because UVP obtains the velocity distribution as functions of time and space, we have two kinds of Fourier transform, which gives the frequency spectrum and wave number spectrum as

$$P_\omega(s,\omega)=\frac{1}{2\pi}\int_{-\infty}^{+\infty}u(s,t)\mathrm{e}^{-i\omega t}\mathrm{d}t, \tag{4.37}$$

$$P_k(t,k)=\frac{1}{2\pi}\int_{-\infty}^{+\infty}u(s,t)\mathrm{e}^{-iks}\mathrm{d}s. \tag{4.38}$$

For pipe flow, for example, Eq. (4.37) gives the frequency spectra both in the central region and near the pipe wall simultaneously. Equation (4.38) is used to discuss transient phenomena such as wavy vortex flow and oscillating shear flow. Division by 2π in each formula is required to keep the reversibility of the Fourier transform, but can be omitted when only one is applied. Because actual data are discrete following the spatiotemporal resolution of the velocity measurement, numerical spectrum computation such as the fast Fourier transform (FFT) is more suitable to save computational time. For the number of sampling data, N, while the direct Fourier transform has computational complexity of N^2, FFT has computational complexity of $N \log_2 N$, which is less than N^2 for high N. The number N should be a power of 2 to obtain an accurate result for the FFT, such as 128, 1,024, or 16,384. When the sampling number is narrowly limited, other types of spectrum analysis, such as the minimum entropy method, may work better.

It is worth noting that the power spectrum is a time-averaged squared quantity of the frequency spectrum obtained from Eq. (4.37). In contrast, the energy spectrum is a squared quantity of the wave number spectrum obtained from Eq. (4.38). The former is called so because the quantity evaluates the energy per unit time after the time averaging. The power spectrum cannot be defined for a transient wave like a shock wave, instead, the energy spectrum is invalidly assessed for irregular waves.

4.2.4.2 Autocorrelation

When a flow field has periodicity in space or time, the velocity distribution has correlation between shifted periods. Such a characteristic of the flow field is evaluated by autocorrelation. Normalized autocorrelation, which takes the range from −1 to +1, is defined by the following formulae in time and space:

$$
\begin{aligned}
A_t(s,\Delta t) &= \frac{\int_0^T u(s,t)\cdot u(s,t+\Delta t)\,\mathrm{d}t}{\sqrt{\int_0^T \left[u(s,t)\right]^2 \mathrm{d}t\cdot\int_0^T \left[u(s,t+\Delta t)\right]^2 \mathrm{d}t}} \\
\rightarrow A_t(i,k) &= \frac{\sum_{J=1}^{J}[u_{i,j}][u_{i,j+k}]}{\sqrt{\sum_{j=1}^{J}[u_{i,j}]^2\cdot\sum_{j=1}^{J}[u_{i,j+k}]^2}},
\end{aligned}
\tag{4.39}
$$

$$
\begin{aligned}
A_t(t,\Delta s) &= \frac{\int_0^L u(s,t)\cdot u(s+\Delta s,t)\,\mathrm{d}s}{\sqrt{\int_0^L \left[u(s,t)\right]^2 \mathrm{d}s\cdot\int_0^L \left[u(s+\Delta s,t\right]^2 \mathrm{d}s}} \\
\rightarrow A_t(j,m) &= \frac{\sum_{i=1}^{I}\left[u_{i,j}\right]\left[u_{i+m,j}\right]}{\sqrt{\sum_{i=1}^{I}\left[u_{i,j}\right]^2\sum_{i=1}^{I}\left[u_{i+m,j}\right]^2\cdot}}.
\end{aligned}
\tag{4.40}
$$

Here, autocorrelation and the power spectrum are related via the Fourier transform. Discrete forms are given for both definitions, where time and space are expressed by the coordinates of *i* and *j*, respectively.

4.2.4.3 Cross Correlation

The similarity of the temporal velocity fluctuation between two points is easily investigated using a single set of UVP data. For example, when turbulent eddies migrate upon convection, the velocity fluctuation in the upstream region reappears downstream with a time lag. Computation of the cross correlation allows the reappearance to be quantified. The following formula is that of the normalized cross-correlation coefficient between two velocity fluctuations at location s_1 and s_2, which takes the value from −1 to +1, as a function of the time lag, Δt.

$$
\begin{aligned}
C_t(s_1,s_2,\Delta t) &= \frac{\int_0^T u(s_1,t)\cdot u(s_2,t+\Delta t)\mathrm{d}t}{\sqrt{\int_0^T \left[u(s_1,t)\right]^2 \mathrm{d}t \cdot \int_0^T \left[u(s_2,t+\Delta t)\right]^2 \mathrm{d}t}} \\
\rightarrow C_t(i_1,i_2,k) &= \frac{\sum_{j-1}^{J}[u_1\,|\,i,j][u_2\,|\,i,j+k]}{\sqrt{\sum_{j-1}^{J}[u_1\,|\,i,j]^2 \cdot \sum_{j-1}^{J}[u_2\,|\,i,j+k]^2}}.
\end{aligned}
\tag{4.41}
$$

Taking the maximum value of the cross correlation within the variation of Δt, it gives a two-dimensional distribution of the maximum cross correlation, $C_t(i_1, i_2)$, which is called a "recurrent map" in the field of information processing. Figure 4.15 shows a measurement example of the recurrent map for two vertical lines before and after a baffle in an open channel. The map indicates that the structure of turbulence above the baffle is maintained between the two locations while the lower parts are separated without significant correlation [6].

Swapping time and space in the above formula leads to the following cross-correlation coefficient that is used to evaluate the similarity of a spatial distribution at two time instants:

$$
\begin{aligned}
C_s(t_1,t_2,\Delta s) &= \frac{\int_0^L u(s,t_1)\cdot u(s+\Delta s,t_2)\mathrm{d}s}{\sqrt{\int_0^L \left[u(s,t_1)\right]^2 \mathrm{d}s \cdot \int_0^L \left[u(s+\Delta s,t_2)\right]^2 \mathrm{d}s}} \\
\rightarrow C_t(j_1,j_2,m) &= \frac{\sum_{i-1}^{I}[u_1\,|\,i,j][u_2\,|\,i,m+j]}{\sqrt{\sum_{i-1}^{I}[u_1\,|\,i,j]^2 \cdot \sum_{i-1}^{I}[u_2\,|\,i,m+j]^2}}.
\end{aligned}
\tag{4.42}
$$

This formula is known as two-point cross correlation and can quantitatively evaluate the periodicity and persistency of turbulence or unsteady flow characteristics.

4.2.5 Two-Dimensional Fourier Fransform

Dealing with the wave number and frequency simultaneously, the two-dimensional Fourier expansion is effectively utilized for the UVP dataset. The original definition, which is applied for a two-dimensional scalar distribution such as in image analysis, is

$$
P(k,m) = \frac{1}{4\pi^2}\int_0^{L_x}\int_0^{L_y} f(x,y)\mathrm{e}^{-i(kx+my)}\mathrm{d}x\mathrm{d}y, \tag{4.43}
$$

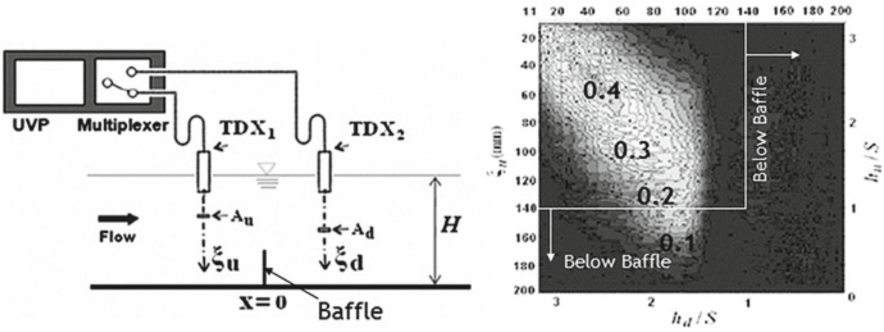

Fig. 4.15 Recurrent map of turbulence crossing over a baffle

where k and m are the wave numbers in x and y directions, respectively. According to this formula, the two-dimensional Fourier transform for the spatiotemporal velocity distribution of UVP can be defined as

$$P(k,\omega) = \frac{1}{4\pi^2}\int_0^L \int_0^T u(s,t)\mathrm{e}^{-i(\omega t+ks)}\mathrm{d}t \cdot \mathrm{d}s, \tag{4.44}$$

where k and ω are the wave number and angular frequency, respectively. It is noted that the two-dimensional spectrum has different dimensions for the two directions, and care should be taken when the spectrum density and peak intensity are evaluated according to the product of the two dimensions.

Figure 4.16 shows an example of the UVP measurement of Taylor–Couette flow in a layer between two concentric two annuli (see Sect. 5.1.1) [10]. Figure 4.16a is the spatiotemporal two-dimensional velocity distribution, showing periodical fluctuations both in space and time. Figure 4.16b depicts the two-dimensional power spectrum of the wavy velocity fluctuation as a function of frequency, f, and wave number, k.

4.2.6 *Proper Orthogonal Decomposition*

When periodicity in not only time but also space is poor in a UVP measurement, it is normally difficult to find a coherent structure by analysis on frequency domain such as Fourier transform. In this case, a proper orthogonal decomposition (POD) might be suitable to extract the features of the spatiotemporal field. POD is widely used to recognize patterns in image analysis, and this analysis method is sometimes used to analyze a flow field, especially one obtained by the PIV method. In UVP measurement, because the measurement component is a one-dimensional space and time domain, the POD method is also applicable. Some examples applied to Taylor vortex flow and sudden expiation flow have been presented [11, 12].

The details and characteristics of POD are not described in this book. Reference books are listed at the end of this section [13]. Here, the overview of POD for the UVP measurement results of a velocity field between the one-dimensional velocity

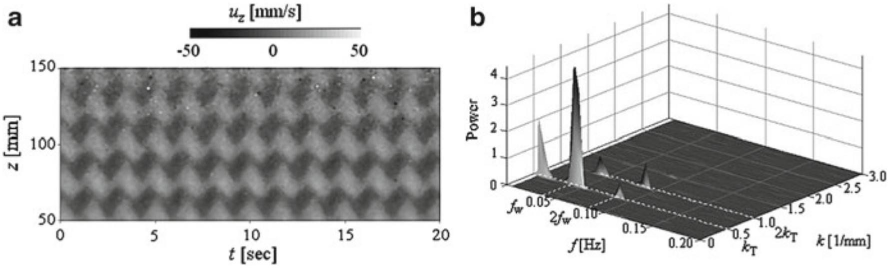

Fig. 4.16 Measurement of wavy Taylor vortex flow. (**a**) Spatiotemporal velocity distribution. (**b**) Two-dimensional spectrum

component and space $u(x, t)$ is explained. The velocity field $u(x, t)$, whose measuring region $\{0 \sim X, 0 \sim T\}$ can be decomposed by the random coefficient $a^{(n)}(t)$ for eigenvector $\varphi^{(n)}(x)$ and eigenvalue $\lambda^{(n)}$, is as follows:

$$u(x,t) = \sum_n a^{(n)}(t)\phi^{(n)}(x). \tag{4.45}$$

In the Fourier transform, eigenvector in this formula corresponds to the basic function cos*nx*, sin*nx*, and the random coefficient corresponds to the Fourier series. Therefore, the velocity field $u(x, t)$ is decomposed to the random function concerned with spatial structure by POD.

Eigenvector $\phi^{(n)}(x)$ and eigenvalue $\lambda^{(n)}$ can be obtained by solving the eigenvalue problem of the following variance–covariance matrix:

$$\begin{pmatrix} R_{11} & R_{12} & \cdots & R_{1J} \\ R_{21} & \ddots & & \vdots \\ \vdots & & \ddots & \vdots \\ R_{I1} & \cdots & \cdots & R_{IJ} \end{pmatrix}. \tag{4.46}$$

Here, the correlation coefficient R_{ij} is obtained by the following formula:

$$R_{ij} = \frac{1}{T}\sum_t u(t,i)u(t,j). \tag{4.47}$$

As an important feature, kinetic energy E over the measurement region is obtained by a summation of eigenvalues:

$$E = \int_0^X u^2(x)\mathrm{d}x = \sum_n \lambda^{(n)}. \tag{4.48}$$

This means that each eigenvector obtained by this analysis contributes individuality to kinetic energy. It can be considered that eigenvectors show the coherent structure in the measuring flow field.

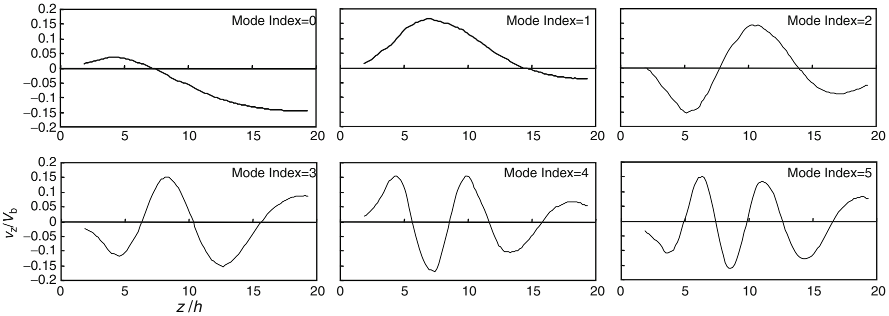

Fig. 4.17 Eigenvectors in sudden expiation flow at $Re_d = 2{,}200$

An example of an eigenvector obtained by the POD for the measurement result by UVP at sudden expiation flow (Sect. 5.1.5) is shown in Fig. 4.17. From the point of view of observation of spatial structure, the eigenvector is aligned in decreasing order of large contribution to the kinetic energy of its large eigenvector. Eigenvectors shown in this figure occupy 85% of total kinetic energy. It seems that this example simply shows that the lower-frequency component is larger than the contribution to kinetic energy. However, the eigenvector obtained by POD is random function in contrast to the Fourier transform whose basic function is a normal sin or cos wave. The meaning of structure indicated by eigenvectors should be treated very carefully considering the background of the measurement flow field.

A spatiotemporal velocity field can be reconstructed using selected eigenvectors. Random coefficient $a^{(n)}(t)$ for eigenvalue $\lambda^{(n)}$ is calculated by the following formula:

$$a^{(n)}(t) = \int_0^X u(x,t)\phi^{(n)}(x)\mathrm{d}x, \tag{4.49}$$

By the selected eigenvector and the random coefficient applied to Eq. (4.45), the velocity field is reconstructed. This method is valid to find a fluctuation of space and temporality of coherent structure.

Singular value decomposition (SVD) is also known for the similar purpose of post-processing. SVD is one of the steps in dynamic model decomposition (DMD) that simplifies a distribution with a limited number of inverse matrices approximated [14]. It is called *snapshot POD*, which is also effective to express the velocity distribution with a few eigenvalues.

4.2.7 Turbulent Statistics

In this section, a series of turbulent statistics for UVP data are introduced. Turbulent statistics are quantities that express characteristics of temporal velocity fluctuations and are separate from mean velocity characteristics.

4.2.7.1 Velocity Deviation

$$\sigma^2(s) = \frac{1}{T}\int_0^T [u(s,t) - \overline{u}(s)]^2 \, \mathrm{d}t, \quad \overline{u}(s) = \frac{1}{T}\int_0^T u(s,t)\mathrm{d}t, \tag{4.50}$$

where T is the sampling width of the measurement. The square root of the value is called the standard deviation of velocity. The deviation increases not only with original velocity fluctuation in the flow but also with the random error factor of the measurement system. The measurement quality is thus carefully checked before evaluation of the turbulent statistics.

4.2.7.2 Turbulent Intensity

$$E(s) = \frac{1}{T}\int_0^T \frac{1}{2}\rho\,[u(s,t) - \overline{u}(s)]^2 \, \mathrm{d}t, \quad e(s) = E(s)\left[\frac{1}{T}\int_0^T \frac{1}{2}\rho u^2(s,t)\mathrm{d}t\right]^{-1}, \tag{4.51}$$

where $E(s)$ is also called the turbulent energy and ρ is the density of fluid. $e(s)$ is the dimensionless turbulent intensity normalized by the kinetic energy of mean flow. The square root of $e(s)$ is called the turbulence ratio. Because turbulent flow has three-dimensional velocity fluctuation, the foregoing quantities only assess a componential characteristic. In the case of anisotropic turbulence seen in a wall boundary layer or in pipe flow, we have to pay attention to the biased sensing of the turbulence when a measurement line that is nonorthogonal to the mainstream is set [15].

4.2.7.3 Reynolds Stress

Reynolds stress is derived from the Navier–Stokes equation by Reynolds decomposition; that is, replacing all the velocity components, u, v, and w, with the sum of the mean and fluctuating components. The decomposition has the following elements.

$$\tau = \rho \begin{bmatrix} \overline{u'u'} & \overline{u'v'} & \overline{u'w'} \\ \overline{v'u'} & \overline{v'v'} & \overline{v'w'} \\ \overline{w'u'} & \overline{w'v'} & \overline{w'w'} \end{bmatrix}, \quad \begin{cases} u' = u - \overline{u} \\ v' = v - \overline{v} \\ w' = w - \overline{w} \end{cases}, \tag{4.52}$$

The matrix is symmetric, and the diagonal components are given by the velocity deviations explained previously. The other three terms, which exist symmetrically in the matrix, are called Reynolds shear stress terms. The stress terms express momentum transport caused by turbulence, which is described by

$$\overline{u'v'} = \overline{(u-\bar{u})(v-\bar{v})} = \overline{uv - \bar{u}v - u\bar{v} + \bar{u}\,\bar{v}} = \overline{uv} - \bar{u}\,\bar{v}, \tag{4.53}$$

$$\overline{u'w'} = \overline{(u-\bar{u})(w-\bar{w})} = \overline{uw - \bar{u}w - u\bar{w} + \bar{u}\bar{w}} = \overline{uw} - \bar{u}\,\bar{w}, \tag{4.54}$$

$$\overline{v'w'} = \overline{(v-\bar{v})(w-\bar{w})} = \overline{vw - \bar{v}w - v\bar{w} + \bar{v}\bar{w}} = \overline{vw} - \bar{v}\,\bar{w}. \tag{4.55}$$

We now focus on the Reynolds shear stress component of Eq. (4.53). The description on the left-hand side of the equation is the time-average of the product of two velocity fluctuations. In contrast, the right-hand side of the equation is obtained by the time-averaging of the velocity itself. The difference to the experimentalist is that the intermediate estimation of the Reynolds shear stress is given only in the latter case when a long time measurement is being processed. The equation tells us that u and v must be measured as a function of time, simultaneously, and we need to employ multiple measurement lines, as mentioned in Sect. 4.2.3. For set (b) in Fig. 4.10, the Reynolds shear stress is computed as

$$\overline{u'v'} = \overline{(u-\bar{u})(v-\bar{v})} = \overline{\left(\frac{(u_1-u_2)-(\overline{u_1}-\overline{u_2})}{2\sin\alpha}\right)\left(\frac{(u_1+u_2)-(\overline{u_1}+\overline{u_2})}{2\sin\alpha}\right)}. \tag{4.56}$$

Decomposing the equation gives

$$\overline{u'v'} = \frac{\overline{(u_1-\overline{u_1})(u_1-\overline{u_1})+(u_1-\overline{u_1})(u_2-\overline{u_2})-(u_2-\overline{u_2})(u_1-\overline{u_1})-(u_2-\overline{u_2})(u_2-\overline{u_2})}}{4\sin\alpha\cos\alpha}. \tag{4.57}$$

Further decomposition leads to 16 terms; however, time-averaging of the terms that have a combination of instantaneous velocity and mean velocity becomes zero, and we thus obtain the Reynolds shear stress profile as

$$\overline{u'v'} = \frac{\overline{(u_1^{\,2}-\overline{u_1}^{\,2})-(u_2^{\,2}-\overline{u_2}^{\,2})}}{4\sin\alpha\cos\alpha} = \frac{\overline{u_1'^2}-\overline{u_2'^2}}{2\sin 2\alpha}. \tag{4.58}$$

The foregoing equation means that the stress is measured simply by the difference in velocity fluctuations between two measurement lines [16].

Figure 4.18 illustrates the case of a circular pipe flow or a rectangular channel flow measurement. Different profiles in the velocity deviation are obtained along two measurement lines, and their difference is the Reynolds shear stress. This idea is valid not only at the crossing point but also along the entire measurement line when turbulent characteristics are kept the same within a short distance in the main flow direction. Thus, changing the distance between two measurement lines does not affect the final result. Moreover, if the turbulent characteristics are symmetric with respect to the central line, a single-line measurement is enough

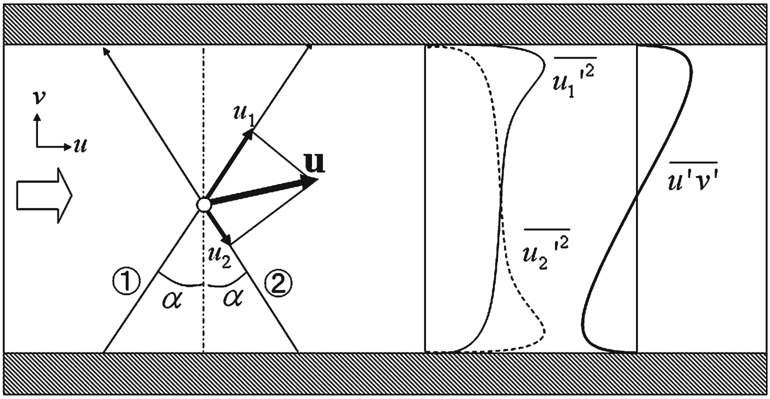

Fig. 4.18 Reynolds shear stress profiling from velocity variances in two directions

to estimate the turbulent characteristics because a mirror image in the profiling can be assumed.

4.2.7.4 Turbulence Scale Relative to Sampling Scale

Careful attention must be paid to the sampling resolution relative to various scales of turbulence. When the spatial sampling interval is larger than the smallest scale of turbulence, the turbulence at a high wave number is underestimated. The same underestimation occurs when the temporal sampling interval is longer than the fastest scale of turbulence. Thus, turbulence in most cases will be underread as it increases superficially with random noise included in the measurement. This note of caution is not specific to UVP, but is general to all kinds of velocity measurements such as PIV, particle tracking velocimetry, hot-wire technique, and laser Doppler anemometry.

4.2.8 Noise Reduction

This section explains several typical techniques for noise reduction that are suitable for application to spatiotemporal two-dimensional velocity distribution. Here we focus on digital signal noise in the form of a velocity distribution, which arises separately from analog noise originating from the ultrasound transducer. To reduce noise, the detection of noise and hence the generation mechanism for noise in UVP must be understood. Here only the scattered random error is set as a common problem while the handling of systematic and organized error is omitted because they must be basically eliminated through optimization of the measurement conditions.

4.2.8.1 Spatiotemporal Median Filter

As the velocity distribution is continuous in space and time, the velocity at a point has a value similar to values of the surrounding points. Noise, in contrast, will have a value isolated from the surroundings. A median filter can replace such an isolated velocity with an appropriate value. This process already includes noise reduction. The filter's function is to employ the fifth-largest value among the nine values in a 3 × 3 two-dimensional elementary distribution that is centered on the target point. A high spurious value is naturally eliminated with this filter and does not leave any trace in the filtered distribution.

Figure 4.19 shows a simulation example of noise reduction using a median filter. The top and bottom of the figure are the cases of a 10% noise ratio to the entire data and a 40% ratio, respectively. The position and magnitude of the noise are given randomly. The middle figure depicts the data after a single filtering operation, in which most apparent noise is removed. Further iterative operation does not change the data once the noise is removed (right figure). This is one of the advantages of the median filter over other filters that smooth the data as the filtering is operated. The disadvantage of the median filter is that noise having a wavelength longer than two sampling intervals cannot be erased. Although expansion of the matrix size to 5 × 5 or larger will solve this problem, the merit of integer value operation is lost and results in a stronger smoothing effect.

4.2.8.2 Moving-Average Filter

The moving-average filter is a filter that replaces the velocity data at a target point, $u(i, j)$, with the averaged value around it. The filter is defined by

$$u^*(i,j) = \frac{\sum_{m=-1}^{+1}\sum_{n=-1}^{+1} w(m,n)\cdot u(i+m, j+n)}{\sum_{m=-1}^{+1}\sum_{n=-1}^{+1} w(m,n)}, \tag{4.59}$$

where $w(m, n)$ is a weight coefficient in two dimensions, and it can be given by the tables shown in Figs. 4.20 and 4.21. The moving-average filter is categorized as an averaging filter because noise is reduced by the averaging effect. The moving-average is such that averaging is operated successively along the arrangement of data to update the correction, which means the value of u in the nominator of Eq. (4.59) includes a mix of new and old values, dependent on the computing route of the filtering operation.

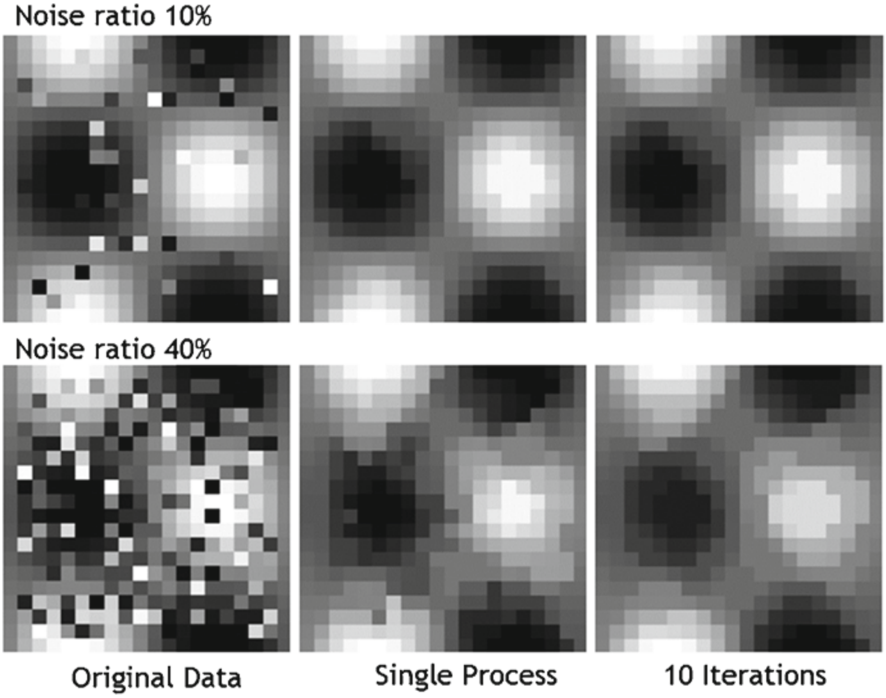

Fig. 4.19 Noise reduction using median filtering

Figure 4.20b is the case that averaging is implemented only in space, and Fig. 4.20c is the case in which the averaging is implemented only in time. These two cases employ a rectangular weight coefficient of 1-1-1. Cases (d) and (e) employ a 1-2-1 form, which is suitable for the reduction of oscillatory noise. Case (f) is the two-dimensional version, which works for the noise pattern of a checkered flag.

Figure 4.21b is the weight coefficient for averaging inside a square domain, and Fig. 4.21c is that for reducing a single isolated instance of noise. Case (d) has a coefficient in proportion to the inverse square distance from the center; cases (e) and (f) have priority in space and time, respectively. A heterogeneous weight works well a few iterative operations but becomes ineffective when high-density data are processed.

Figure 4.22 shows simulation examples of noise reduction using an averaging filter. Here the case is for a square averaging filter. Dot-type noise disappears with a single operation, but the error remains in a diffused pattern. Ten operations completely smooth the dot noise; however, the global pattern collapses owing to the strong smoothing effect. Thus, the averaging filter does not remove noise but just shifts the noise component from a high wave number region to a low wave number region. The Gaussian filter, which removes fluctuations with wavelength shorter than a given Gaussian radius, λ [17], is also classified as an averaging filter. The effect of the Gaussian filter is equivalent to the iterative operation of the filter in case (d) in Fig. 4.21.

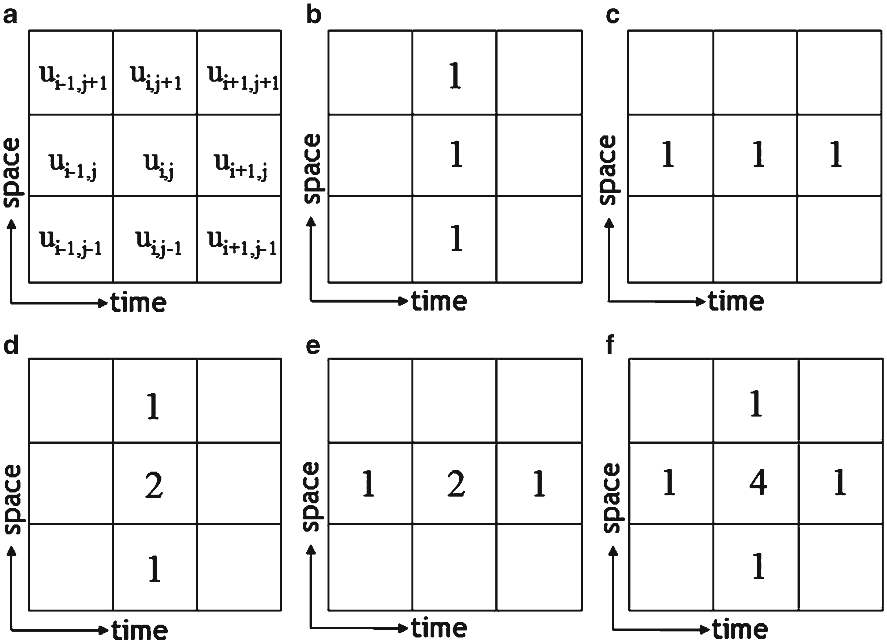

Fig. 4.20 Weight coefficient for moving-averaging filter: simple cases. (**a**) Definition. (**b**) Space rectangular. (**c**) Time rectangular. (**d**) Space triangular. (**e**) Time triangular. (**f**) Space-time pyramid

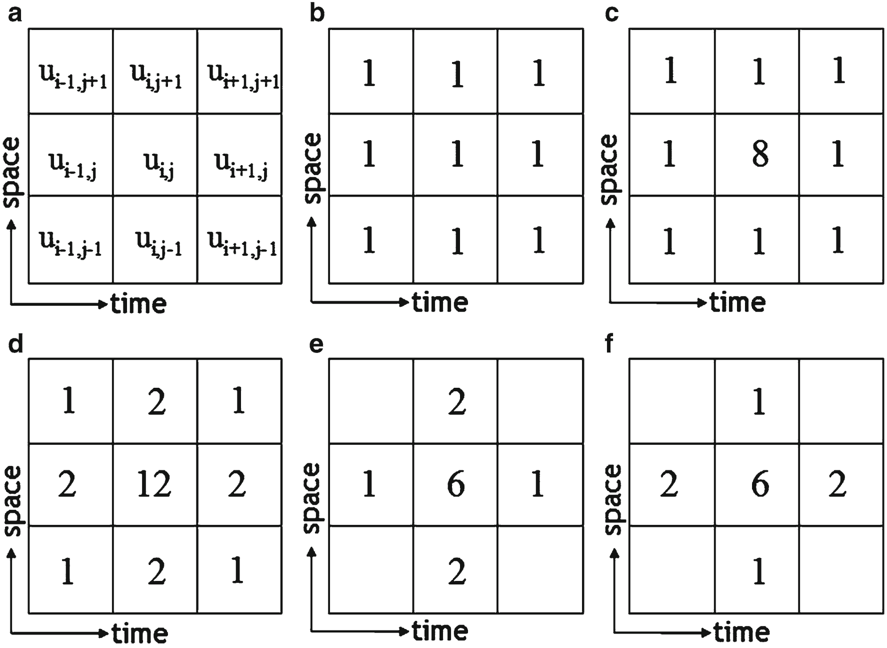

Fig. 4.21 Weight coefficient for moving-averaging filter: advanced cases. (**a**) Definition. (**b**) Uniform square. (**c**) Isotropic weight. (**d**) Inverse distance weight. (**e**) Space-oriented weight. (**f**) Time-oriented weight

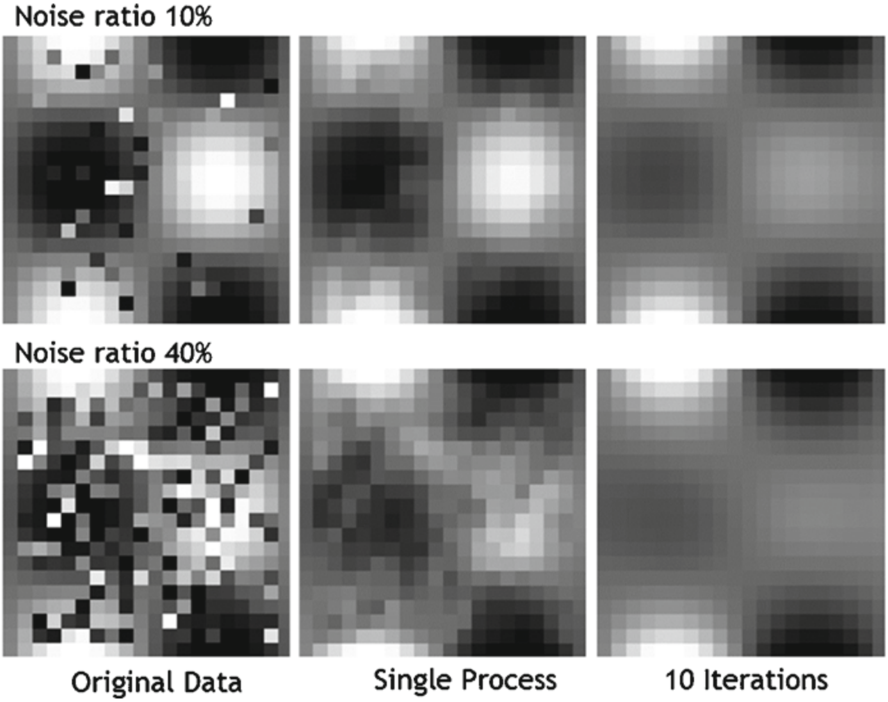

Fig. 4.22 Noise reduction using averaging filter

4.2.8.3 Frequency Filter

In general classification, the median filter is applied to utilize the nature of integer value operation (i.e., grid-type discrete data in two dimensions), and the new value is chosen from several candidate values. In comparison, the moving-average filter is based on the relaxation of an unordinary value using the averaging effect. The frequency filter differs from those two filters, detecting noise in the frequency domain for subsequent erasing. In noise identification, the Fourier transform, which is explained in Sects. 4.2.4 and 4.2.5, is used. The frequency filter for one-dimensional data is applied with the following procedure.

First, we carry out the Fourier transform on velocity data $u(t)$ to obtain the frequency spectrum P as

$$P(\omega) = \frac{1}{2\pi}\int_{-\infty}^{+\infty} u(t)\mathrm{e}^{-i\omega t}\,\mathrm{d}t. \tag{4.60}$$

The transmission spectrum X is multiplied with the frequency spectrum:

$$P'(\omega) = P(\omega)\cdot X(\omega) \tag{4.61}$$

and the inverse Fourier transform is then taken to give the corrected velocity data u' as

$$u(t) = \int_{-\infty}^{+\infty} P'(\omega) \mathrm{e}^{i\omega t} \mathrm{d}\omega = \int_{-\infty}^{+\infty} P(\omega) X(\omega) \mathrm{e}^{i\omega t} \mathrm{d}\omega. \tag{4.62}$$

When high-frequency noise reduction is desired, the transmission spectrum X is better given as unity in the low-frequency region and zero in the high-frequency region; this is so-called low-pass filtering (LPF). When there is noise in the intermediate frequency band, a notch filter, which has a low value of X in the correspondent frequency, can be applied.

When a two-dimensional Fourier transform is applied, more functioned filtering can be formulated with the combination of two frequency bands and the wave number. POD is another way to reduce noise that exists in a specific mode involved in the flow.

4.2.8.4 Other Feasible Filters

There are other types of noise reduction, most of which utilize the statistical nature of measurement data. They were originally used for the diagnosis of irregular data, employing a threshold that is set at several times as the standard deviation. A typical example is that the datum is judged erroneous when it is outside the region within $U \pm 3\sigma$ when the body of the data has a mean value of U and standard deviation σ. A number of good textbooks are available for learning the fundamentals.

References

1. Takeda Y, Haefeil M (1991) Velocity profile measurement by ultrasonic Doppler shift method: evaluation of shape reproducibility. In: Keffer JF, Shah RK, Ganic EN (eds) Experimental heat transfer, fluid mechanics and thermodynamics. Elsevier, New York
2. Greenspan HP (1990) The theory of rotating fluids. Breukelen Press, Brookline
3. Benton ER, Clark A Jr (1974) Spin-up. Annu Rev Fluid Mech 6:257–280
4. Drazin P, Reid W (1981) Hydrodynamic stability. Cambridge University Press, New York
5. Mori M, Takeda Y, Taishi T, Furuichi N, Aritomi M, Kikura H (2002) Development of a novel flow metering system using ultrasonic velocity profile measurement. Exp Fluid 32:153–160
6. Jamshidnia H, Takeda Y (2010) An experimental study of the effect of a baffle on the flow structure in a rectangular open channel using UVP. J Fluid Sci Technol 5:542–557
7. Kitaura H, Murai Y, Takeda Y, Thomas PJ (2010) Velocity vector field measurement of vortex ring using UVP. Trans JSME Ser B 76:2143–2151
8. Takeda Y (1987) Measurement of velocity profile of mercury flow by ultrasound Doppler shift method. Nucl Technol 79:120–127
9. Furuya N, Tasaka Y, Murai Y, Takeda Y (2009) Development of rheometry based on UVP for visco-elastic liquid. Proceedings, 6th International Symposium on Ultrasonic Doppler Methods, pp 57–60
10. Takeda Y, Fischer WE, Sakakibara J (1994) Decomposition of the modulated waves in a rotating Couette system. Science 28:502–505

11. Takeda Y (1999) Quasi-periodic state and transition to turbulence in a rotating Couette system. J Fluid Mech 389:81–99
12. Furuichi N, Takeda Y, Kumada M (2003) Spatial structure of the flow through an axisymmetric sudden expansion. Exp Fluid 34:643–650
13. Holmes P, Lumly JL, Berkooz G (1996) Turbulence, coherent structures, dynamical systems and symmetry. Cambridge University Press, New York
14. Schmid PJ (2010) Dynamic mode decomposition of numerical and experimental data. J Fluid Mech 656:5–28
15. Taishi T, Kikura H, Aritomi M (2002) Effect of the measurement volume in turbulent pipe flow measurement by the ultrasonic velocity profile method. Exp Fluid 32:188–196
16. Murakawa H, Kikura H, Aritomi M (2002) Measurement of Reynolds stress in bubbly flow using ultrasonic Doppler method. Proceedings, 3rd International Symposium on Ultrasonic Doppler Methods in Fluid Mechanics and Fluid Engineering, Lausanne, Switzerland, pp 97–102
17. Ido T, Murai Y, Yamamoto F (2002) Post-processing algorithm for particle tracking velocimetry based on ellipsoidal equations. Exp Fluid 32:326–336

Part II
Applications

Chapter 5
Practical Applications

Yuji Tasaka, Beat Birkhofer, Noriyuki Furuichi, Hiroshige Kikura, Hisato Minagawa, Yuichi Murai, Hideki Murakawa, Masaaki Motozawa, Samsun Nahar, Hironari Obayashi, Tatsuo Sawada, A.K. Jeelani Shaik, Yasushi Takeda, Kenichi Tezuka, Yoshiyuki Tsuji, Takatoshi Yanagisawa, Sanehiro Wada, Johan Wiklund, and Erich J. Windhab

Abstract Because of the advantages of the ultrasonic velocity Doppler profiler (UVP), namely in spatiotemporal velocity field measurements and in its applicability for opaque liquids, UVP has a wide field of application in science and industry. The following chapter introduces carefully selected examples of applications covering relatively basic areas of application. The focus of the contents in this chapter is categorized into (1) studies of flow instability and transition (Sect. 5.1), (2) measurements and investigations of liquid metal flows (Sect. 5.2), (3) developments of new rheometry (Sect. 5.3), (4) determinations of rheological properties (Sect. 5.4), (5) studies of magnetic fluids (Sect. 5.5) and (6) gas–liquid two-phase flow (Sect. 5.6), (7) measurements of flowrate in turbidity flows (Sect. 5.7), and

---

Y. Murai • Y. Tasaka (✉)
Faculty of Engineering, Hokkaido University, N13 W8, Sapporo 060-8628, Japane-mail: tasaka@eng.hokudai.ac.jp

B. Birkhofer
Sika Services AG, Zürich, Switzerland

N. Furuichi
National Metrology Institute of Japan, National Institute of Advanced Industrial Science and Technology (AIST), Tsukuba, Japan

H. Kikura
Tokyo Institute of Technology, Tokyo, Japan

H. Minagawa
The University of Shiga Prefecture, Shiga, Japan

H. Murakawa
Graduate School of Engineering, Kobe University, Kobe, Japan

M. Motozawa
Tokyo University of Science, Chiba, Japan

S. Nahar • A.K.J. Shaik • E.J. Windhab
Swiss Federal Institute of Technology Zürich (ETH-Zürich), Zürich, Switzerland

Y. Takeda (ed.), *Ultrasonic Doppler Velocity Profiler for Fluid Flow*,
Fluid Mechanics and Its Applications 101, DOI 10.1007/978-4-431-54026-7_5,

(8) determinations of flows in a deforming tube for biomedical applications (Sect. 5.8). The measurement and post-processing techniques used in this chapter are described in detail in Chaps. 4 and 7, and detailed explanations of these aspects are omitted in this chapter.

Keywords Flow instability • Flowmeter • Liquid metal • Magnetic fluid • Peristaltic flow • Rheology • Two-phase flow

5.1 Flow Instability and Transition

The study of flow transitions from laminar to turbulent flows is an important topic in fluid dynamics. Based on the idea of linear stability of flows, infinitesimal perturbations in flows grow exponentially with time (or space in the case of convective instability) at the beginning of the flow transition. Then, viscous effects of the fluids suppress the growth and provide a new stable state of flow. The perturbations are described as normal modes, for instance, the velocity perturbation $\boldsymbol{u}'(\boldsymbol{x}, t)$ [here the velocity vector $\boldsymbol{u}'=(u', v', w')$, positional vector $\boldsymbol{x}=(x, y, z)$ and time t] is described as

$$\boldsymbol{u}'(x,t) = \mathrm{e}^{st}\hat{\boldsymbol{u}}(\boldsymbol{x}), \quad s = \sigma + i\omega \tag{5.1}$$

where $\hat{\boldsymbol{u}}(\boldsymbol{x})$, σ, and ω indicate the spatial pattern, growth rate, and frequency of the perturbation. The σ value for each *mode* of perturbation changes with increases in the nondimensional parameters that dominate the flow states (e.g., Reynolds number, Rayleigh number). A flow becomes unstable when σ becomes larger than zero

---

H. Obayashi
Japan Atomic Energy Agency (JAEA), Ibaraki, Japan

T. Sawada
Keio University, Yokohama, Japan

Y. Takeda
Hokkaido University, Sapporo, Japan

Tokyo Institute of Technology, Tokyo, Japan

K. Tezuka • S. Wada
Tokyo Electric Power Company, Yokohama, Japan

Y. Tsuji
Nagoya University, Nagoya, Japan

T. Yanagisawa
Japan Agency for Marine-Earth Science and Technology (JAMSTEC), Yokosuka, Japan

J. Wiklund
The Swedish Institute for Food and Biotechnology (SIK), Göteborg, Sweden

for a mode of the perturbations. Flows may show spatial periodicity, leading to $\hat{u}(x)$ in Eq. (5.1) being described, for example, as

$$\hat{\boldsymbol{u}}(\boldsymbol{x}) = \mathrm{e}^{ikx}\tilde{\boldsymbol{u}}(y,z) \tag{5.2}$$

where k stands for the wave number in the x direction. As a result of flow instability, the most unstable mode of perturbations that has temporal and/or spatial periodicity appears as the new stable state. In the process of flow transitions other modes also become unstable and nonlinear interactions between these show as chaotic flows. As mentioned in the previous chapters, UVP provides spatiotemporal velocity information, $u(x, t)$, and thus UVP is able to represent the flow behaviors in flow instability. The following introduces some work about the flow instability and transition by means of UVP. The textbook (for flow instabilities) [1] gives further details of flow instability.

5.1.1 Taylor–Couette Flow [2–5]

Taylor–Couette flow indicates flows in rotating, coaxial double cylinders and shows a variety of flow patterns depending on the speed and direction of the rotation of the cylinders [6]. Figure 5.1 shows a coordinate system of the flow, where R_i and R_o represent the diameters of the inner and outer cylinders, respectively. The Reynolds number that dominates the flow state is defined by the frequency of rotation of the inner cylinder Ω, the gap between the cylinders, $d = R_\mathrm{o} - R_\mathrm{i}$, and the kinematic viscosity of the fluids, ν, as $Re = \Omega R_\mathrm{i} d/\nu$. For extremely small Re values the flow has only an azimuthal component (Couette flow). In the case of a rotating inner cylinder and a fixed outer cylinder, an array of toroidal vortex rings (Taylor vortices) appears as the primary instability of the flow (Taylor vortex flow; Fig. 5.2a). Then, azimuthal waves occur on the vortices as the secondary instability with increasing of Re (wavy vortex flow, WVF; Fig. 5.2b). For the WVF regime, UVP with an ultrasonic transducer mounted upon the fluid layer parallel to the rotating shaft (z direction) translates the flow as a spatiotemporal velocity distribution, $u_z(z, t)$ (as suggested in Fig. 5.3). There are periodic patterns in space and time, and these represent Taylor vortices and azimuthal waves. Therefore, a Fourier analysis of the distribution provides the wave number of vortices and the frequency of waves (a 2D Fourier analysis provides both; see Sect. 4.2.5). Figure 5.4a shows an example of the power spectrum, where the spectrum is spatially averaged to reduce the noise from measurement errors. There are clear peaks on the spectrum, and these correspond to the main frequency of the waves, f_1, and its harmonics, $2f_1$, $3f_1$. At further higher Re, another peak, f_m, that is not a harmonics of f_1, appears as the modulation of the waves (modulated wavy vortex flow, MWV) (Fig. 5.4b). Every peak on the spectrum can be represented by a combination between f_1 and f_m, e.g., $f_5 = f_1 - 2f_\mathrm{m}$.

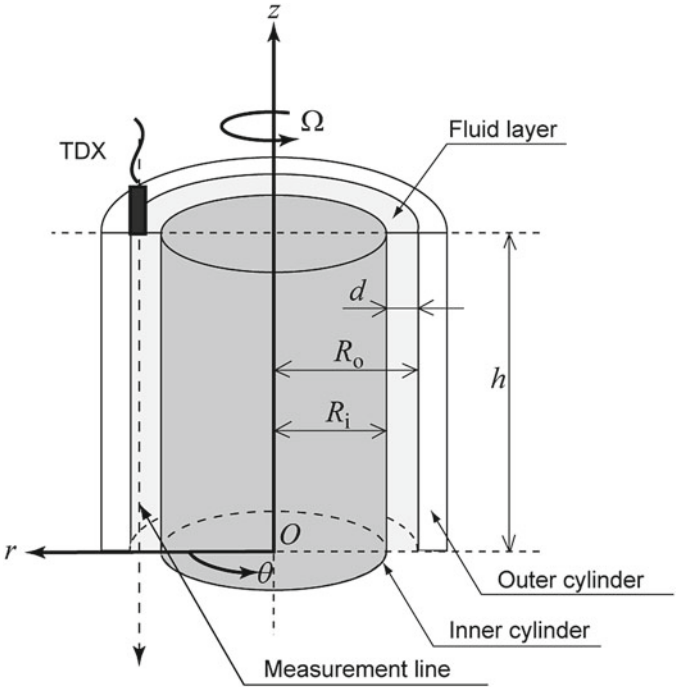

Fig. 5.1 Coordinate system of Taylor–Couette flow

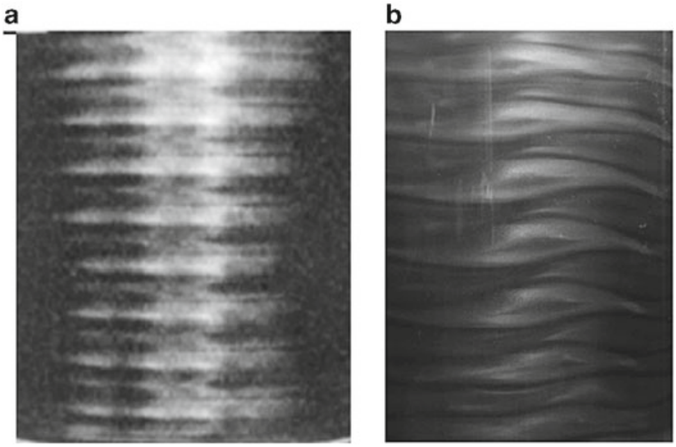

Fig. 5.2 Visualized images of Taylor–Couette flow. (**a**) Taylor vortex flow. (**b**) Wavy vortex flow

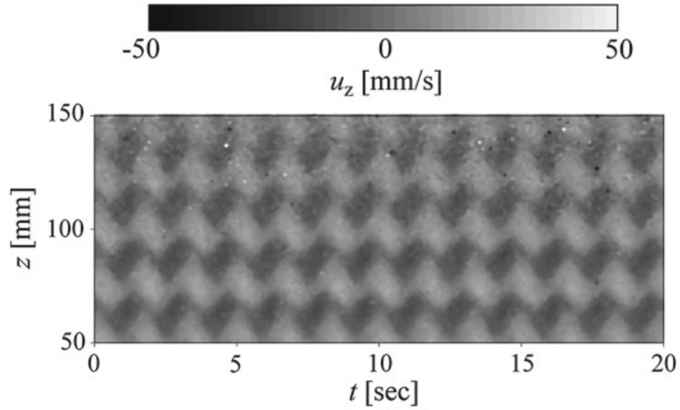

Fig. 5.3 Spatiotemporal velocity distribution measured by UVP in wavy vortex flow (WVF) regime

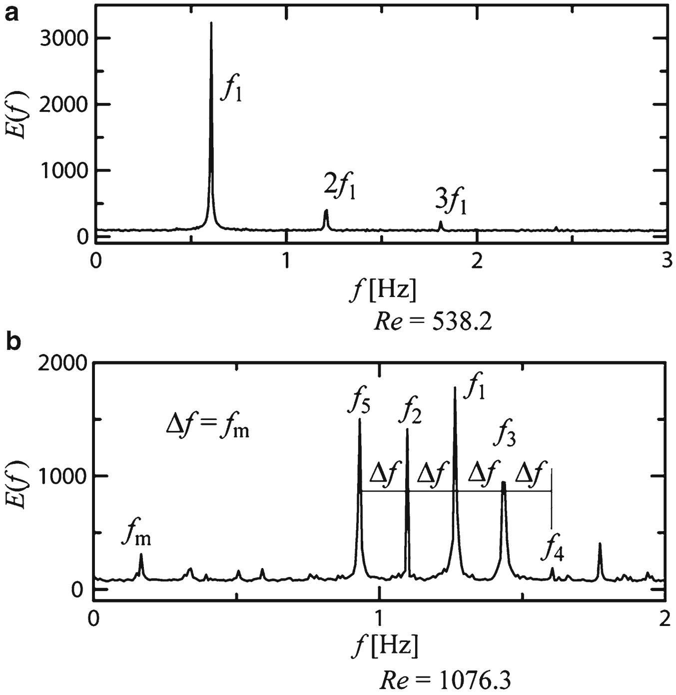

Fig. 5.4 Spatially averaged power spectra of axial velocity fluctuation. (**a**) $Re = 538.2$. (**b**) $Re = 1{,}076.3$

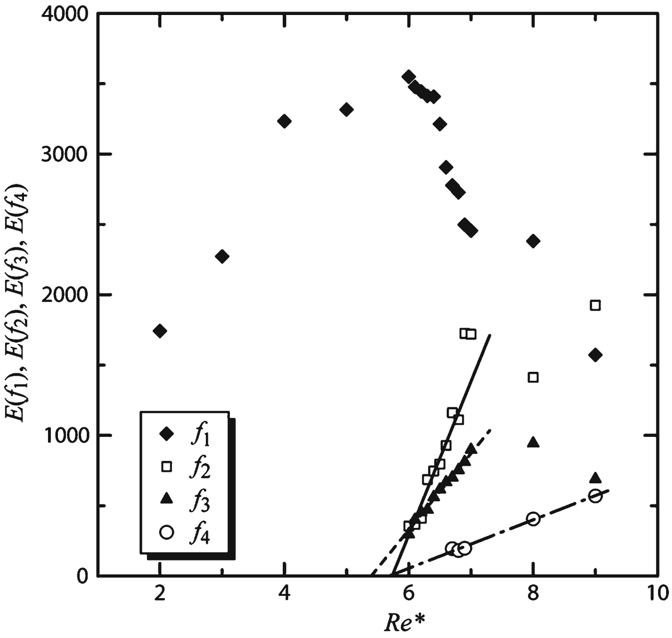

Fig. 5.5 Excitation function of waves

Variations of peak values in each frequency component represent a transition between flow regimes. Figure 5.5 shows an excitation function that represents the growth of frequency components with respect to the Reynolds number, *Re*, where *Re* is reduced by the critical Reynolds number at the onset of the primary instability, Re_c, as $Re^* = Re/Re_c$. Here, the peak value of the frequency component f_1 that originates in the azimuthal wave increases with increases in *Re*; it then decreases with the appearance of other frequency components. Thus, the flow regime changes from WVF to MWV. The increase in the frequency components is caused by growth of the modulation component f_m, and thus the zero cross point of the variation indicates the critical Reynolds number for the onset of MWV, determined as $Re_m = 753.5$ ($Re_m/Re_c = 5.59$).

5.1.2 Wake of Two Cylinders in Tandem [7]

The von Kárman vortex street appearing in the wake of two-dimensional bluff bodies is a well-known example of flow instability phenomena. Here the nondimensional vortex shedding frequency, $St = fd/U$ (Strouhal number), takes a value of 0.21 for cylinder wakes in a wide range of Reynolds numbers, $Re = Ud/\nu$, where *f*, *d*, *U*, and ν are the vortex shedding frequency, cylinder diameter, upstream streamwise velocity, and kinematic viscosity of the fluids, respectively. For the wake of two cylinders in tandem (Fig. 5.6), the flow takes two modes depending on *Re* and also depending

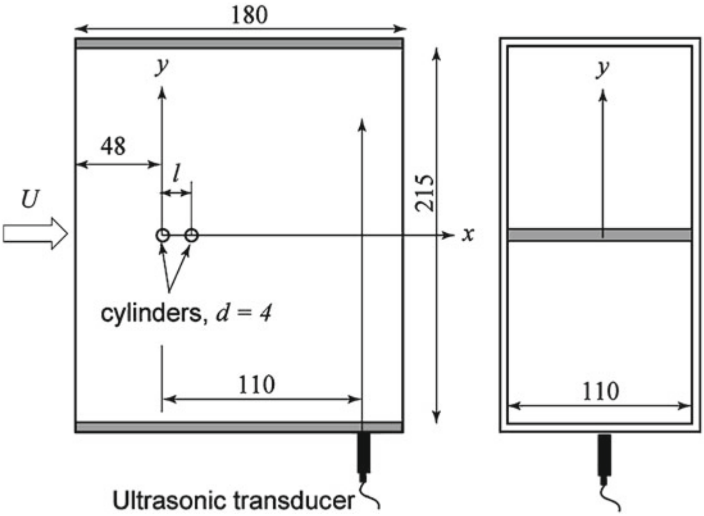

Fig. 5.6 Coordinates of a wake of two cylinders in tandem and measurement arrangement (reprinted with permission from [7]. Copyright (2006), American Institute of Physics.)

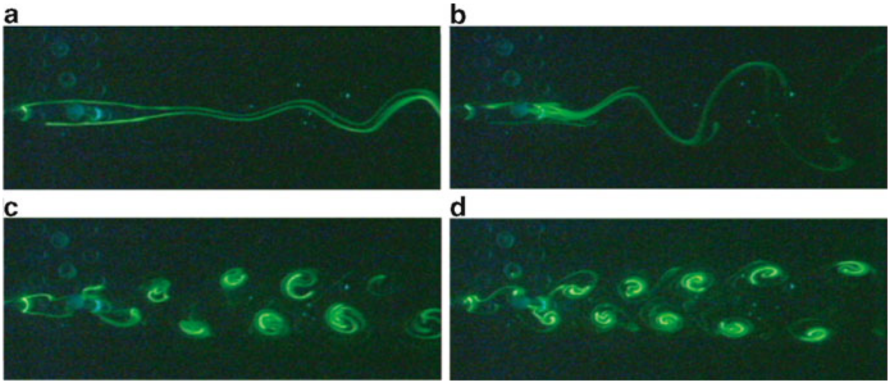

Fig. 5.7 Dye visualization of streamlines around the cylinders for $\Gamma = 5$. (**a**) $Re = 130$. (**b**) 150 (slow mode). (**c**) 150 (fast mode). (**d**) 130 (reprinted with permission from [7]. Copyright (2006), American Institute of Physics.)

on a gap ratio, $\Gamma = l/d$ (l is the distance between the center of the cylinders). Figure 5.7 shows a dye visualization of streamlines around the cylinders at each Re for $\Gamma = 5$. In the case of a s*low mode* (e.g., Fig. 5.7a, b), the streamline is closed between the cylinders, and thus the cylinders appear as one elliptical cylinder. The wake performs a slow oscillation but does not create vortices in this area of the visualization. On the other hand, in the case of a *fast mode* (e.g., Fig. 5.7c, d), the flow is unsteady just behind the upstream cylinder. The frequency of the fluctuation is larger than that in the slow mode, and the wake of the cylinder displays vortex shedding.

As expected from the numerical study [8], the transition between the two modes displays hysteresis: the flow regime changes from the slow mode to the fast mode at a

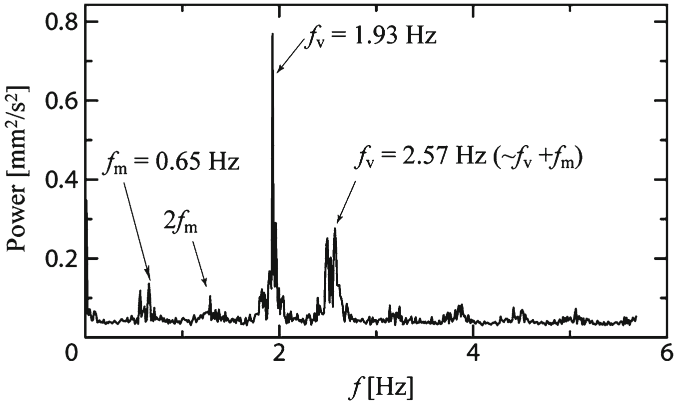

Fig. 5.8 Spatially averaged power spectrum of velocity fluctuation in the fast mode (reprinted with permission from [7]. Copyright (2006), American Institute of Physics.)

certain Reynolds number, Re_{t1}, with increasing Re at a fixed gap ratio, Γ (Fig. 5.7b, c), but the flow maintains the regime until $Re = Re_{t2}$ even if Re becomes smaller than Re_{t1} (Fig. 5.7c, d); this means that the flow is in a bi-stable condition, and the flow shows as two stable conditions, a slow and a fast mode, at the same Re. The UVP measurements can provide a quantitative representation of changes on the bi-stable condition with respect to Γ. Figure 5.6 also shows measurement configurations in the test section. All the cylinders and a 4 MHz ultrasonic transducer are mounted in a rectangular measurement unit with a 215 mm × 110 mm cross section and set in a water tunnel. The UVP measures the vertical velocity profiles of the wake, $v(y, t)$, and the Fourier transform gives the primary frequency of the velocity fluctuation. Figure 5.8 is an example of a spatially averaged power spectrum of $v(y, t)$, where the spectra obtained at each y position are averaged in a range of y values to reduce the noise caused by the measurement error. The spectrum is from a flow in the fast mode, and has a secondary frequency component f_m in addition to the vortex shedding frequency f_v. In comparison with the flow visualization, the f_m represents a modulation frequency of the vortex shedding and is not observed in the slow mode. Figure 5.9 shows variations in the Strouhal number, St, with respect to Re at each Γ. Here the jump in St from small values to large values indicates the flow transition from the slow mode to the fast mode. As seen here the variation shows different behaviors with increasing and decreasing Re. For further details of this study, please refer to Tasaka et al. [7].

5.1.3 Experimental Simulation of Flows in a Czochralski Crystal Puller [9]

Flow instability may affect the quality of deposition of materials. Here, an experimental simulation of flows in the Czochralski crystal puller (Cz-CP) is introduced as an example of this. The actual crystal puller consists of molten silicon contained in a heated crucible and a seed crystal mounted on the bottom face of a cylinder with

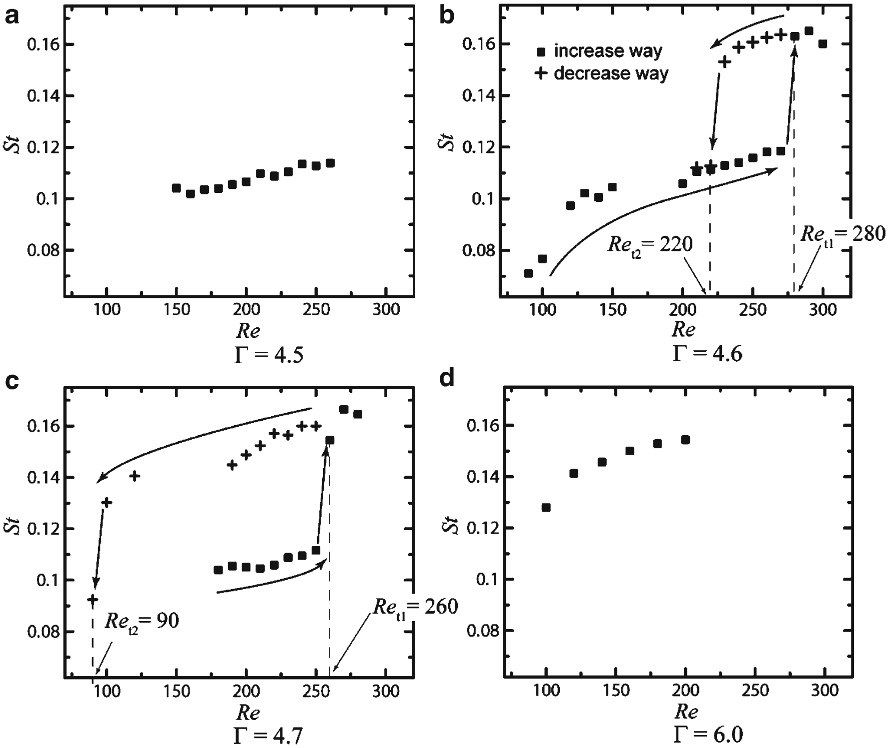

Fig. 5.9 Variations of Strouhal number, *St*, with respect to Reynolds number. (**a**) *Re*, at gap ratio Γ=4.5. (**b**) 4.6. (**c**) 4.7. (**d**) 6.0 (reprinted with permission from [7]. Copyright (2006), American Institute of Physics.)

the vertical axis concentric with that of the crucible. The seed crystal just touches the free surface of the molten silicon. Both the crucible and the cylinder are rotated, and the entire device is operated at temperatures in excess of 1,000°C to keep the silicon in the liquid phase. By slowly pulling the seed crystal away from the melt, a new crystal is extracted.

Because it is physically difficult to investigate flow phenomena at the operating conditions of an actual Cz-CP, a simplified simulated device is used (Fig. 5.10). The experimental apparatus consisted of a simulated 100-mm-diameter and 140-mm-high crucible, with a simulated 30-mm-diameter and 40-mm-long crystal mounted on a small stainless steel flange. The simulated crystal is a cylinder with a flat bottom and sharp bottom edge. Both the crucible and crystal were made of Perspex. The test fluid is a 30 wt % glycerol solution with seeding particles of polymer (density, 1.02 kg/m^3) mixed in the fluid. A 7.8-MHz ultrasonic transducer is mounted horizontally 2 mm below the surface of the fluid.

A color-coded image of the radial velocity component (V_r) is given in Fig. 5.11. The magnitude of the velocity is divided into a color-coded log scale as indicated in the upper right-hand corner. In the regions where the flow velocities are below ~0.7 mm/s, the coloring scheme represents this in black. Figure 5.11a shows the

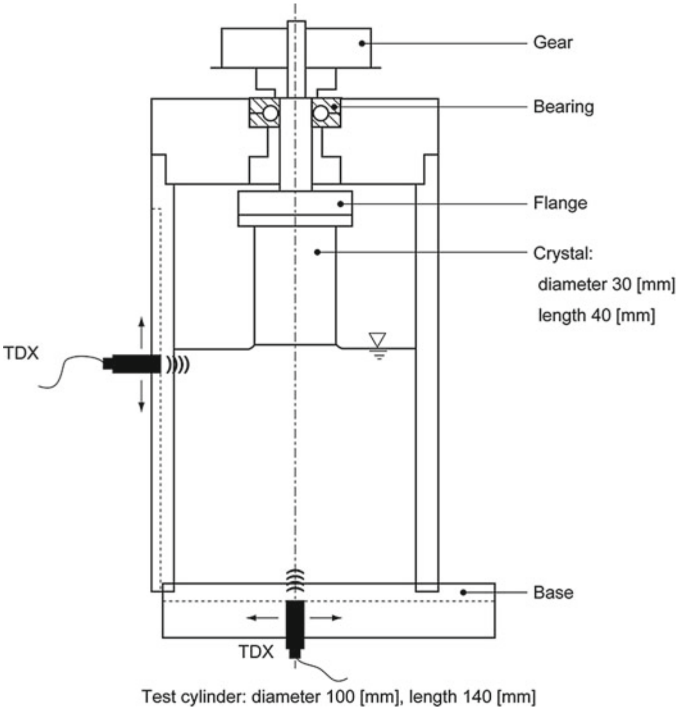

Fig. 5.10 Schematic representation of the simulated Czochralski crystal puller (reprinted from [9] with permission from Elsevier)

initial transient, from zero rotation to a preselected rotation rate (200 rpm). Figure 5.11b additionally shows the continuation of this run until a steady state is achieved. The interpretation of the color plot in Fig. 5.11 can be aided by imagining the Cz-CP (Fig. 5.10) placed horizontally so that the top and bottom boundaries in the figure span the diameter of the crucible and the central region represents the region beneath the rotating crystal. The interpretation of this particular figure is explained in Fig. 5.12. The rotation-induced fluid motion is scanned along a line of measurement starting from the wall of the crucible on which the transducer is attached.

5.1.4 Temporally Irregular Flow Transition Under Rotating Free Surfaces [10]

Rotating flows accompanied by a free surface show temporally irregular motion [11]. This motion is termed *surface switching*, as in the configuration shown in Fig. 5.13, where a fluid layer of tap water in an open-ended cylindrical container is rotated by a bottom disk. The fluid layer has a depression in the free surface, with

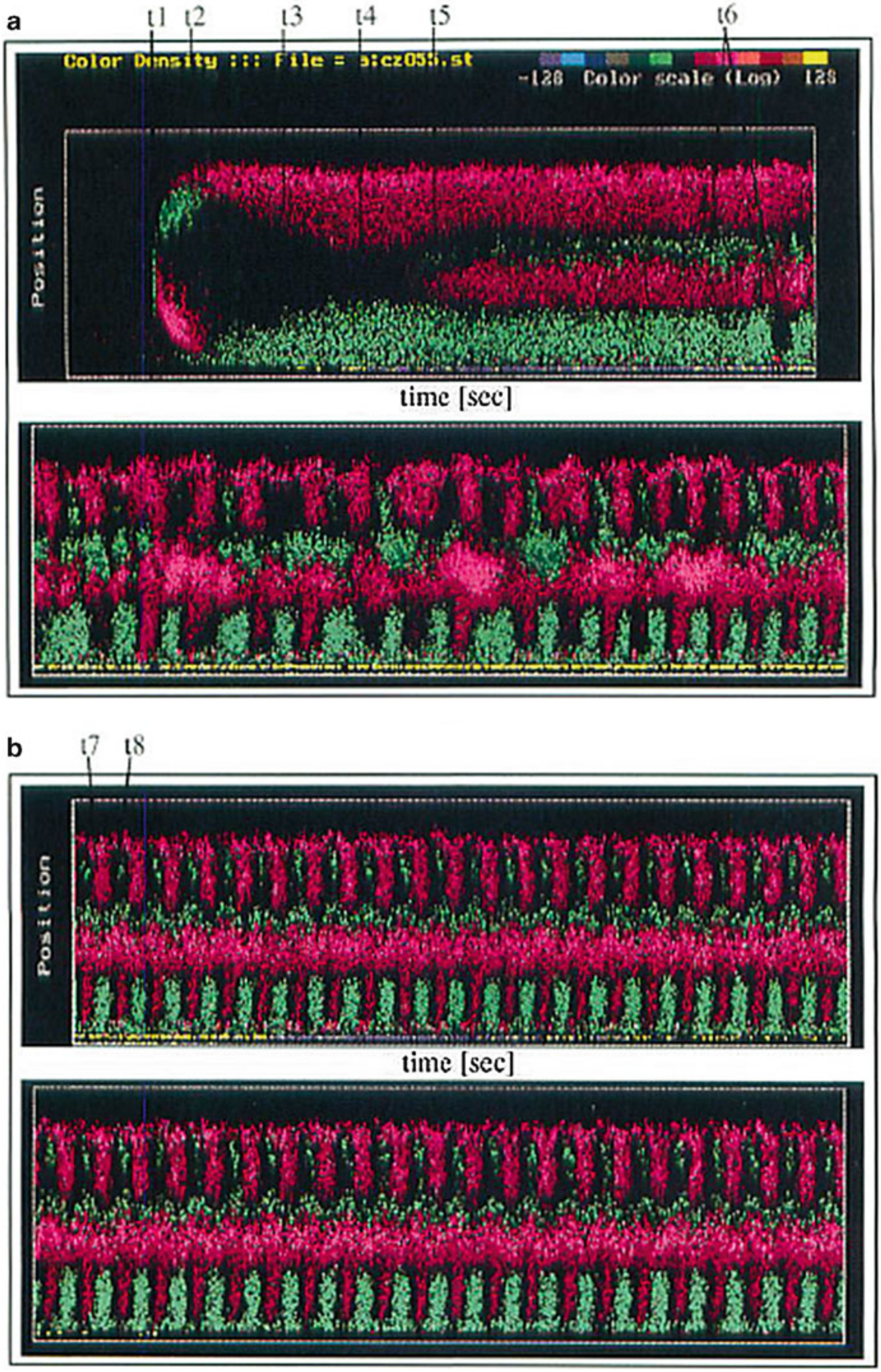

Fig. 5.11 Color-coded velocity profile as a function of position and time. (**a**) Transient signal of the radial velocity component. (**b**) Continuation of the run to steady state (reprinted from [9] with permission from Elsevier)

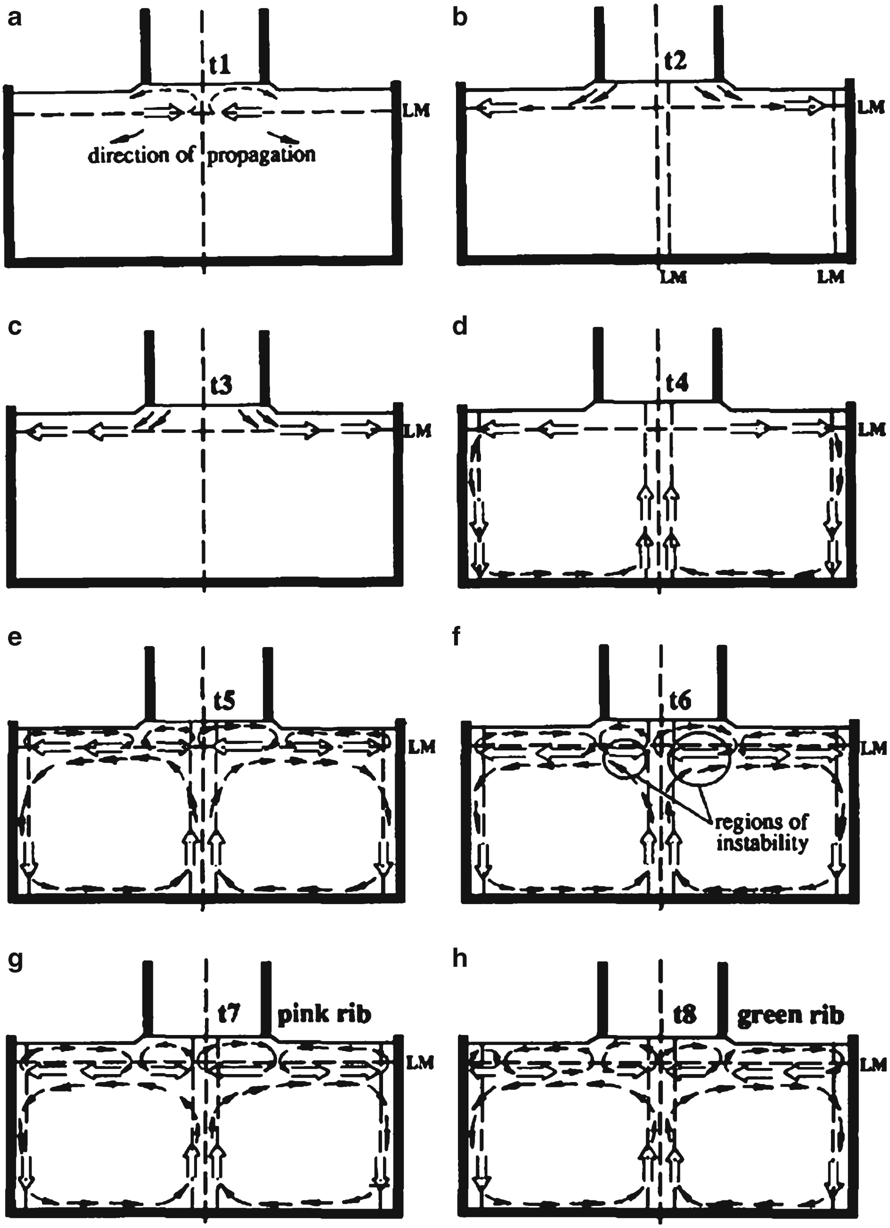

Fig. 5.12 Qualitative sketch of the two-dimensional flow pattern in the Cz-CP during the initial transient to steady state; corresponding time for (**a**) to (**h**) are indicated in Fig. 5.11 as t1 to t8 (reprinted from [9] with permission from Elsevier)

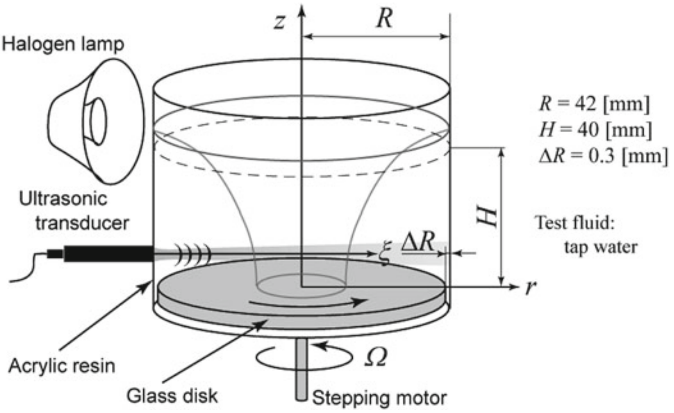

Fig. 5.13 Experimental setup

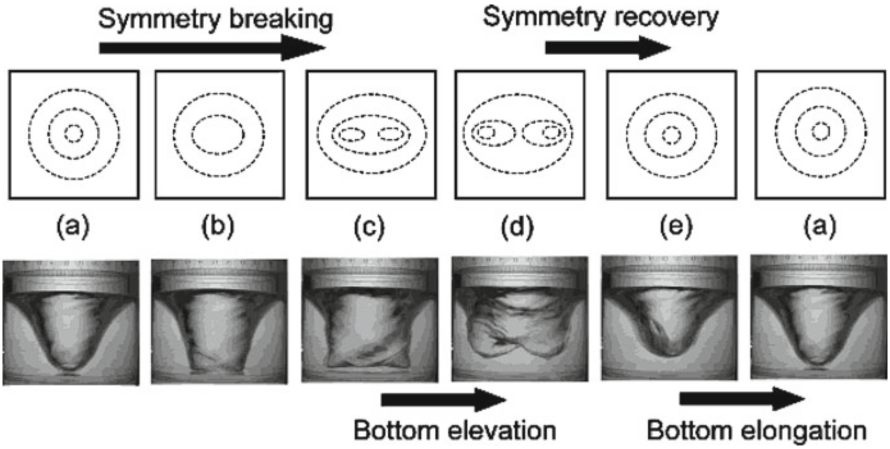

Fig. 5.14 Process of the surface switching: front view of the free surface (*bottom*) and schematic representation of top view of the free surface (*top*). Note that the *left* and *right* panels are the same [10] (reproduced with permission.)

the depth depending on the speed of rotation on the disk. The tilt angle of the free surface is dominated by the centrifugal and gravity forces working on the fluid. At higher speeds of rotation the free surface attaches to the bottom, and the attaching free surface forms a circular hollow in the fluid layer (Fig. 5.14a). For a case that satisfies the conditions on the speed of rotation, height of the fluid layer, and other parameters, the attaching free surface changes the shape of the horizontal cross section from circular to ellipsoidal (Fig. 5.14b, c), and detaches from the bottom (Fig. 5.14d). The detached free surface displays a vertical oscillation and may suddenly recover axi-symmetry in its cross-sectional shape (Fig. 5.14e); this is followed by the free surface reattaching to the bottom (Fig. 5.14a). The process just summarized appears irregularly, with the frequency depending on the size of the gap

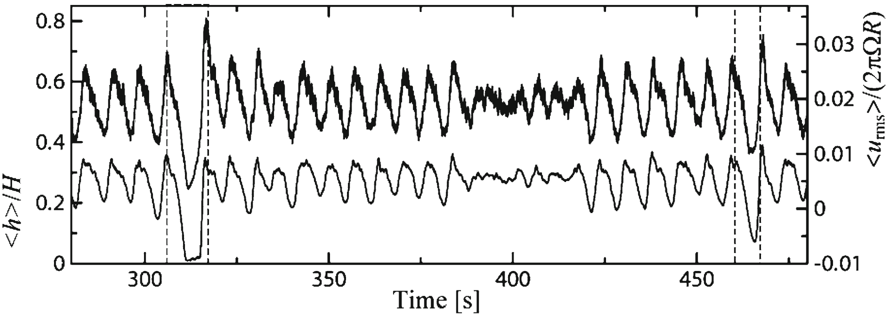

Fig. 5.15 Variations in the surface height and corresponding velocity fluctuations in the switching process [10] (reproduced with permission.)

between the disk and cylinder, and the edge shape of the disk. Here further details of the study are omitted, and the following explains the representation of transient flows under temporally irregular surface switching.

The radius of the cylinder is $R = 42$ mm and the gap size is 0.3 mm. The height of the fluid layer is $H = 40$ mm. A 4-MHz ultrasonic transducer is mounted at the side wall of the cylinder 8 mm above the disk, and thus the UVP measures the spatiotemporal velocity distribution of the radial velocity component, $u_r(r, t)$, along the horizontal centerline of the cylinder. The speed of rotation on the disk is $\Omega = 13.2$ Hz, and the corresponding Reynolds number for the flow of rotation on the disk is $Re = 2\pi\Omega R^2/\nu = 1.46 \times 10^5$, where ν is the kinematic viscosity of the fluid. To represent the flow condition the time variation of the spatial root mean square of velocity fluctuation, $u_r'(r, t)$, is adopted:

$$u_{\mathrm{rms}}(t) = \left[\frac{1}{(\eta_2 - \eta_1)R}\int_{\eta_1 R}^{\eta_2 R} u_r'(r,t)\,\mathrm{d}r\right]^{1/2} \tag{5.3}$$

Here, η_1 and η_2 are 0.49 and 0.67, respectively. This value indicates the degree of turbulence in the flow and takes small values for laminar flows. Figure 5.15 shows variations of u_{rms} and the height of the free surface at the center of the cylinder, h, where the brackets < > mean the moving average on the variations for averaging periods of 0.53 s for h and 0.52 s for u_{rms}, respectively. There is a correlation between the variations; namely, u_{rms} takes relatively larger values for the free surface taking relatively higher positions, and vice versa. The free surface approaches to the bottom disk around 310 and 470 s, and this motion corresponds to the symmetry recovery process in the surface switching (shape transition from Fig. 5.14d–a). The corresponding u_{rms} has extremely small values and quickly increases with elevation of the free surface. These variations of u_{rms} indicate that the surface switching accompanies the laminar–turbulent flow transition, and turbulent mixing of the flow sustains the free surface, being at relatively higher positions, by the changing pressure balance in the fluid layer. The laminar–turbulent flow transition in the switching process has also been observed by a flow visualization using suspended flakes [12].

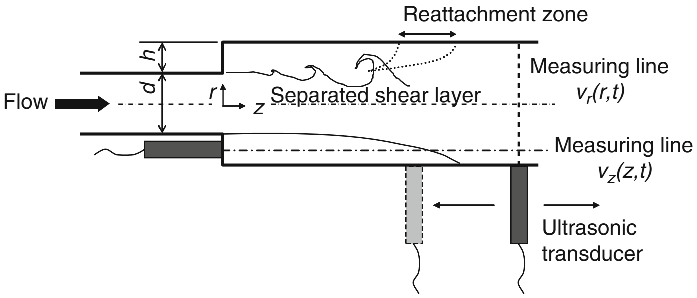

Fig. 5.16 Experimental apparatus for velocity measurement of flow in sudden expansion of pipe [13] (with kind permission from Springer Science+Business Media)

5.1.5 *Flow Transition in Sudden Expansion of a Pipe*

Separation and reattachment of flow can be seen in many engineering fields, and has been experimentally investigated from many points of interest such as focusing on the high heat transfer mechanism around the reattachment region. Behavior of the separated shear layer, which determines the reattachment point, is strongly influenced by recirculation of flow. In spite of its simple geometry, the three-dimensional characteristics (the spanwise structure) of the separated shear layer are not negligible, making the flow structure rather complex. To discuss flow structure in such flow fields, measurement of the spatiotemporal velocity field is essential. In this section, as a typical example of separated shear flow, the axisymmetric flow field in sudden expansion of a pipe is introduced with the measurement results of its spatiotemporal velocity by UVP. The transition mechanism to turbulence is also discussed [13].

The experimental apparatus is shown in Fig. 5.16. Pipe diameter, d, is 25 mm at upstream and 45 mm at downstream. The step height is 10 mm and expansion ratio is 1.8. As the sudden expansion part is located 84d downstream from the inlet nozzle, the velocity profile is considered fully developed before reaching the step (sudden expansion part). The streamwise and azimuthal components of the velocity are $v_z(z,t)$ and $v_r(r,t)$, respectively. The measuring region for v_z spans $z/h = 2$–20.

Typical spatiotemporal velocity fields measured by UVP are shown in Fig. 5.17. V_b indicates bulk velocity in the upstream of the step. Horizontal axis shows dimensionless time and vertical axis denotes streamwise position. Figure 5.17a–c shows the measurement results in the case of (a) laminar, (b) transition, and (c) turbulent regions in the upstream of the step based on Reynolds number. In each figure, a reverse flow (shown as a right-down stripe) and vortex shedding from the separated shear layer (shown as a right-up stripe) are clearly observed. The inclination angle of the right-up stripe corresponds to the traveling velocity of vortex shedding from the separated shear layer. In the case of turbulent flow shown in Fig. 5.17c, the traveling velocity of the vortices is slower in dimensionless time compared to other figures.

Variation of the length of a separation bubble can also be observed easily by this measurement. From laminar to transition region, the length of separation bubble increases with Reynolds number but decreases drastically in the case of turbulent

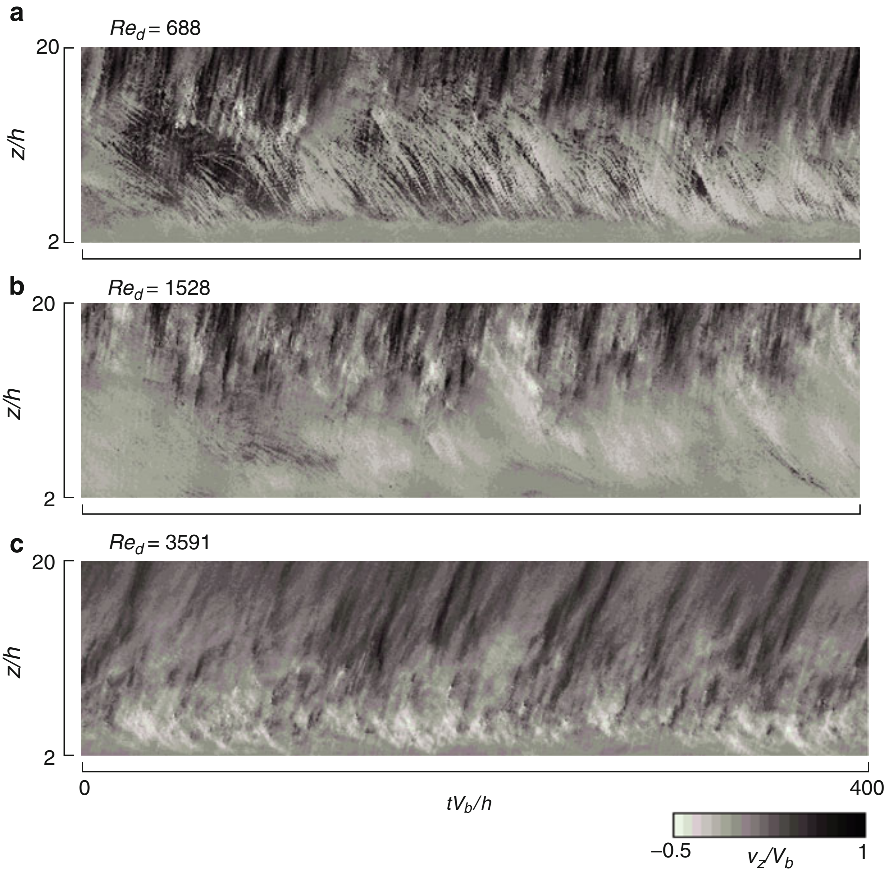

Fig. 5.17 Spatiotemporal velocity field downstream of sudden expansion at (**a**) $Re_d = 688$. (**b**) 1,528. (**c**) 3,591 [13] (with kind permission from Springer Science+Business Media)

region. The characteristic of the reattachment phenomena is determined by the balance between entrainment at the separated shear layer and recirculation flow. UVP measurement is very suitable for the measurement of these flow fields because recirculation flow and wake flow including vortex shedding can be measured simultaneously.

For example, the transition of the reattachment point can be effectively investigated by using this measurement method. From the instantaneous velocity profiles, it can be seen that the point at which velocity changes from minus to plus varies spatially as a result of the fluctuation of separated shear layer and the shedding of separation bubble. This zero cross point should be related to the instantaneous reattachment point. The time-averaged location of zero cross point is shown in Fig. 5.18 together with reattachment points obtained by other studies. It is well known that the reattachment length shows such a trend with Reynolds number that it increases with Reynolds number for laminar upstream flow, decreases gradually for transition, and is almost stable for turbulent.

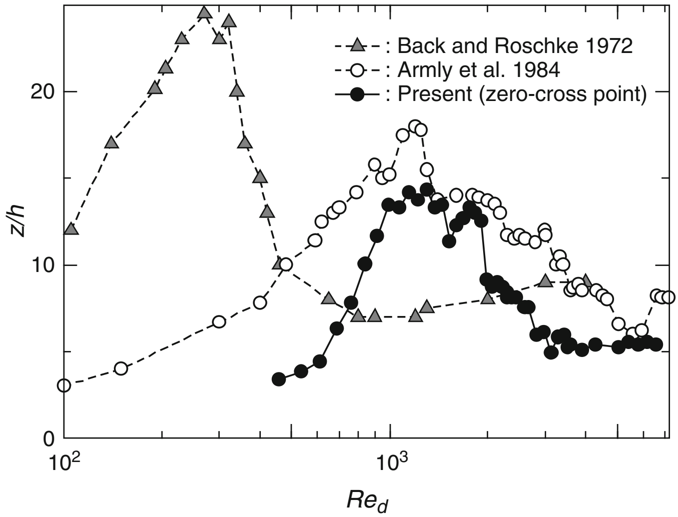

Fig. 5.18 Variation of reattachment point and zero velocity point [13] (with kind permission from Springer Science+Business Media)

Variation of the zero cross point obtained by UVP measurement is almost in agreement qualitatively with Armly's result [14], especially pertaining to the rapid decrease at around $Re_d = 1{,}500$ followed by gradual decrease of reattachment length at a larger Reynolds number.

To obtain a spatial characteristic of this flow field, an analysis by proper orthogonal decomposition (referred to in Sect. 4.2.6) is suitable. Figure 5.19 shows the transition scheme of the first ten eigenvalues with Reynolds number. Each eigenvalue increases with Reynolds number. On the other hand, in the transition region of $1{,}000 < Re_\mathrm{d} < 2{,}000$, the jump of eigenvalue can be observed at two Reynolds numbers, which is the same as the zero cross point as shown in Fig. 5.18.

Variation of global entropy with Reynolds number is shown in Fig. 5.20. Global entropy H is obtained by the following equations:

$$H = -\frac{1}{1\mathrm{n}N} \Sigma p^{(n)} 1\mathrm{n} p^{(n)} \tag{5.4}$$

$$E = \sum_n \lambda^{(n)} \tag{5.5}$$

where $p^{(n)} = \lambda^{(n)}/E$, and N is the number of data points. Figures 5.20 and 5.21 show the variation of global entropy for streamwise velocity component $v_z(z,t)$ and radial velocity component $v_r(r,t)$, respectively.

In both figures, the jump of the global entropy toward decreasing direction at $Re_d = 1{,}500$, 2,000 can also be observed clearly. As a similar result is also observed in other experimental systems [5], this phenomenon can be considered common in the transition to turbulent flow.

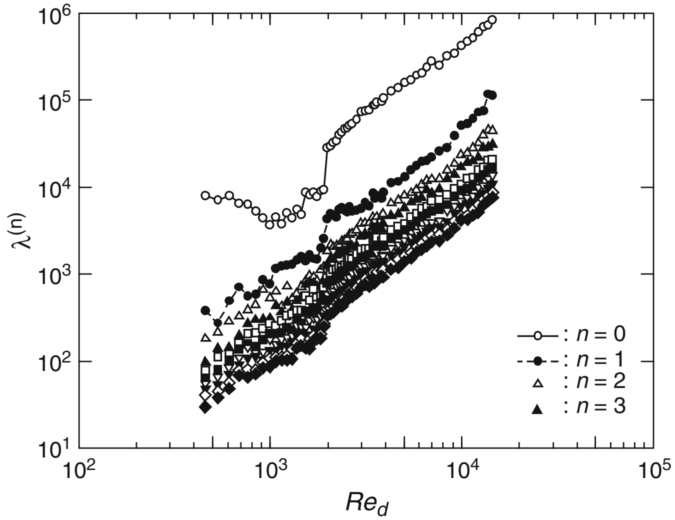

Fig. 5.19 Variation of eigenvalue $\lambda^{(n)}$ for $v_z(z,t)$ [13] (with kind permission from Springer Science+ Business Media)

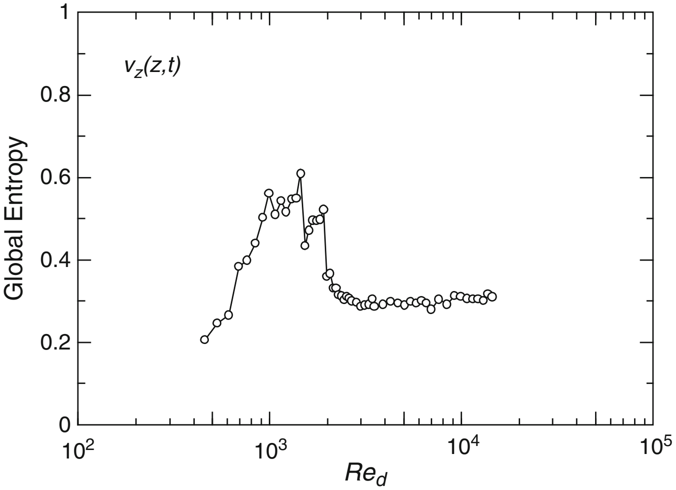

Fig. 5.20 Variation of global entropy for $v_z(z,t)$ [13] (with kind permission from Springer Science+Business Media)

5.1.6 Flow Field on a Heated Rotating Disk

A flow field on a heated rotating disk is a complex phenomenon, considering that it consists of forced convection induced by rotating movement of the disk and natural convection caused by heating of the disk. It has been studied by many researchers as a basic study subject to clarify the heat transfer mechanism of a rotating field.

Fig. 5.21 Variation of global entropy for $v_r(r,t)$

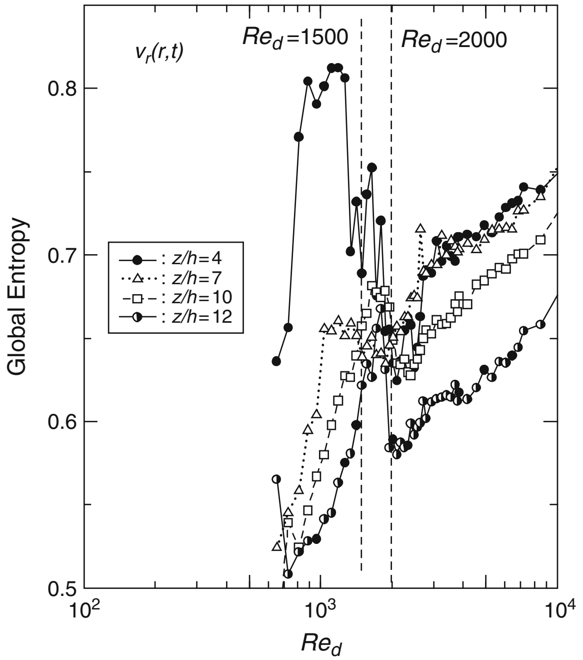

When the rotating speed of the disk is large, the flow structure on the heated rotating disk shows a simple boundary layer because the flow field is dominated by forced convection induced by rotating of the disk. When heating is rapid, the flow field is approximately similar to the flow field on a heated horizontal plate because natural convection is dominant. However, an analysis of the flow field under mixed convection becomes more complex because of instability between the flow induced by buoyancy and rotating of the disk. A flow that is laminar on an unheated rotating disk becomes turbulent when the rotating disk is heated. It is noted that the vortex structure stretching to the rotating direction of the disk occurs under the transitional condition between the dominance of forced and natural convection. This vortex structure may be generated by instability between the buoyancy and centrifugal forces. It is very interesting to study such an unsteady flow structure under mixed convection. In this section, some measurements and analysis results of this flow field obtained by UVP, especially those concerning the transitional behavior between natural and forced convections [15], are introduced.

An experimental apparatus is shown in Fig. 5.22. Radius of the rotating disk submerged in a water tank (620×720×400 mm) is $R=85$ mm. The water is 400 mm deep with a free surface. The rotating disk consists of a copper plate 5 mm thick with an insulator inside. An ultrasonic transducer directed to the center of the disk was set outside of it. Because the measurement lines all pass through the center point of the disk, the velocity component is $v_r(r,t)$. Measurement line of the transducer is set at $z=1.5$ mm above the surface of the disk. Nylon powder (density 1.02, particle diameter 100 μm) is mixed into the water as tracer.

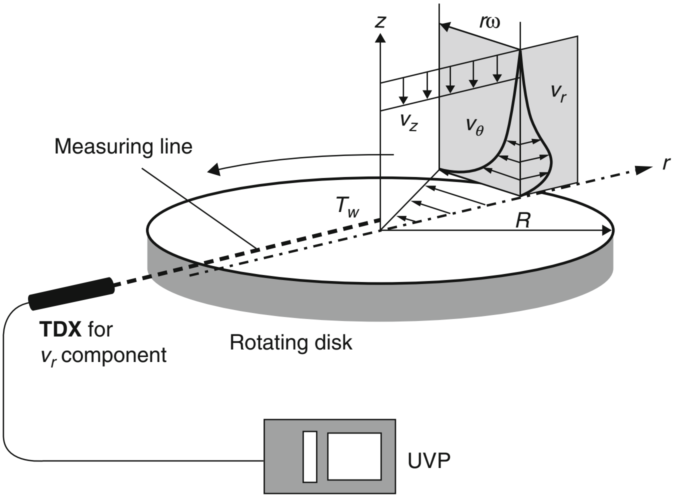

Fig. 5.22 Experimental system of heated rotating disk

The parameters of this experiment are rotating angular speed of the disk (ω) and temperature difference between the water and the surface of the disk (ΔT). Rotating velocity of the disk was varied from 5 to 25 rpm (Reynolds number is $Re_\omega = 0.66 \times 10^4$–$3.29 \times 10^4$): this is laminar condition in the nonheating case. Temperature difference between the surface of the rotating disk and the water was varied at $\Delta T = 2.5$–55°C (Grashof number is $Gr = 0.23 \times 10^8$–5.07×10^8). The temperature of the water is maintained at $T = 40$°C to obtain a constant ultrasonic velocity.

A spatiotemporal velocity field measured by UVP is shown in Fig. 5.23. In Fig. 5.23a, where angular speed is the highest, velocity component v_r increases with radius position because of centrifugal force. Because the effect induced by the heating is small compared to that of rotation, no instability is observed. On the other hand, in Fig. 5.23b and c, clear stripes shown by the white dotted lines can be observed. This right-up stripe shows that the vortex moves from the center of the disk toward the outside. Under certain Re_ω and Gr conditions, vortex stretching in the azimuthal direction is generated by instability induced by natural convection. This vortex moves in the azimuthal direction with slightly slower speed than the disk rotation and travels toward the outside. This vortex is generated at around $r/R = 0.5$ in Fig. 5.22b. In Fig. 5.22c, the generation point is not fixed and a flow moving toward the center of the disk induced by natural convection can be observed. In Fig. 5.22d, the flow field is almost dominated by natural convection, and it is difficult to observe any vortex structure.

As the periodicity of the flow structure in relationship to vortex generation is not significant and velocity components in different directions are measured on the measuring line simultaneously, two-dimensional Fourier transform (explained in Sect. 4.2.5) is considered suitable to discuss such a flow field. Using this method, spectra of flow heading toward the outside of the disk and the one heading toward

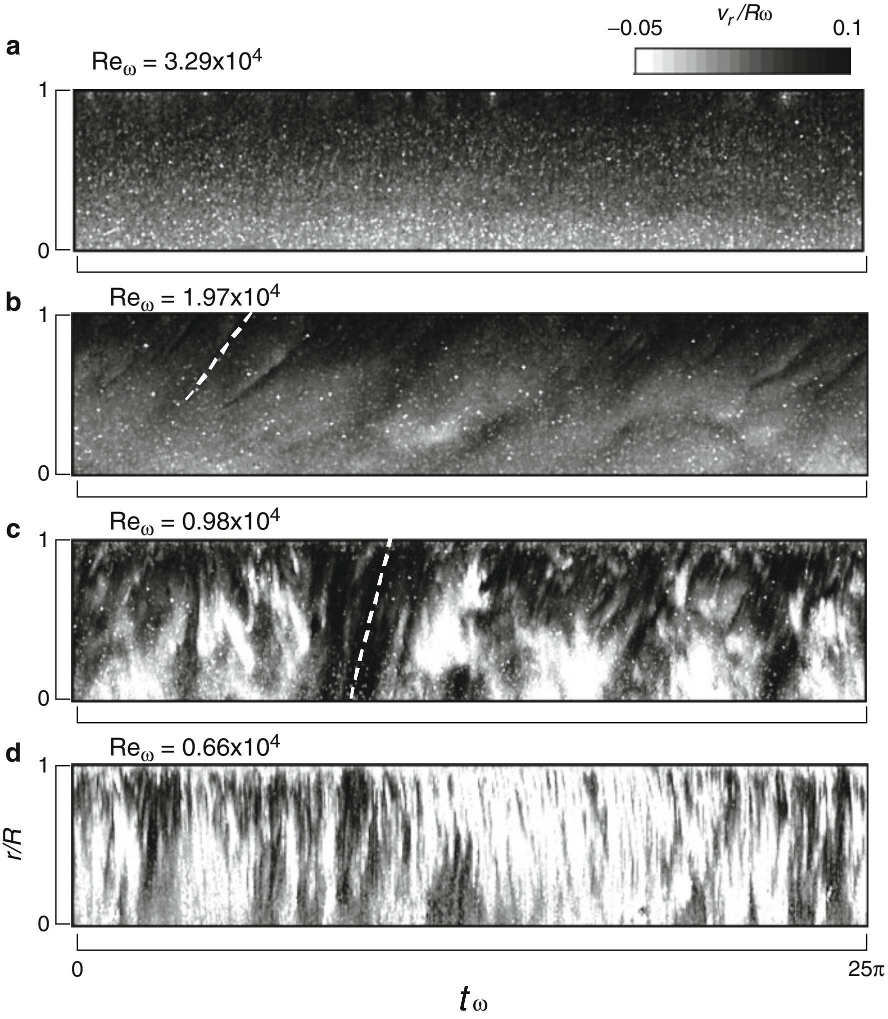

Fig. 5.23 Spatiotemporal velocity field. (**a**) $Re_\omega = 3.92 \times 10^4$. (**b**) 1.97×10^4. (**c**) 0.98×10^4. (**d**) 0.66×10^4

the center of the disk can be separated. By performing reverse Fourier transform, spatiotemporal velocity fields for the two velocity components in opposite directions can be obtained.

The spatiotemporal correlation of the reconstructed velocity field in the direction toward the outside of the disk is shown in Fig. 5.24. Based on these correlation results, discussion can be made on vortex generation, its scale, and traveling velocity, hence enabling the clear classification of forced convection, mixed convection, and natural convection regions, respectively.

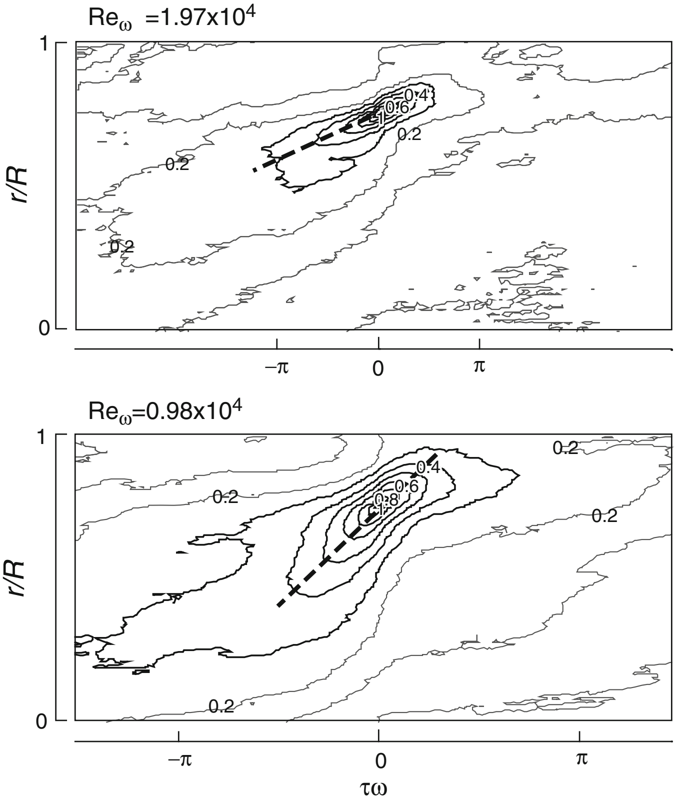

Fig. 5.24 Spatiotemporal correlation

5.2 Liquid Metals

In this section, we summarize the applications of UVP to the measurement of liquid metals. Neither LDV (laser Doppler velocimetry) nor PIV (particle image velocimetry) can be used for the measurement of opaque liquids. It is one of the advantages of UVP application to this kind of liquid. We report first the measurement of thermal convection in a confined cell of mercury, second the thermal convection of gallium controlled by magnetic force, and finally describe the flow of lead-bismuth eutectic alloy in a spallation target.

5.2.1 Thermal Turbulence in a Confined Cell

Thermal convection is a subject of longstanding interest and has many applications in science and engineering. Heat transport problems are also frequently encountered in technological applications. Filling the fluid in a confined cell, and heating uniformly the bottom plate, we know that the heat is transferred by thermal conductivity at first. The temperature difference between upper and lower plate ΔT becomes large; then, thermal convection plays the role of heat transfer. The control parameter of this system is the Rayleigh number, *Ra*, defined as $Ra = \alpha \Delta T g L3/\nu\kappa$, with g being the gravitational acceleration, L the height of the cell, and α, ν, and κ the thermal expansion coefficient, kinematic viscosity, and thermal diffusivity, respectively. For high Rayleigh numbers such as $10 \leq Ra$, we can observe thermal turbulence.

One of the recurrent themes of confined thermal turbulence in the Rayleigh–Bénard apparatus is the relationship between large-scale circulation (LSC), which is often called “wind,” and a plume emitted from the top/bottom walls. The wind survives even when the dynamic parameter, Rayleigh number *Ra*, is very large [16]. The wind’s direction occasionally changes rapidly but is not periodic [17]. The progress in understanding several aspects of turbulence in the Rayleigh–Bénard convection is summarized in a recent review paper [18]. On global wind dynamics, it is found that the large-scale circulation breaks its rotational invariance of the cell for cylindrical samples with aspect ratio $\Gamma = 1$, which generates oscillations of the circular plane. Funfschilling et al. [19] reported that the orientation of the upper half of the LSC undergoes azimuthal oscillations, but they are out of phase with those of the lower half. They call this motion torsional mode. Xi et al. [20] found a sloshing mode in a $\Gamma = 1$ cylindrical cell that occurs in addition to the torsional mode. The sloshing mode consists of a translational or off-center motion that is perpendicular to the vertical circulation plane of the LSC. The off-center motion oscillates time-periodically around the cell’s central vertical axis, with amplitude being nearly independent of the turbulent intensity. In this subsection we summarize our recent results on LSC of a low-Prandtl-number fluid.

5.2.1.1 Experimental Setup

Figure 5.25 shows a schematic drawing of the convection cell, which is a vertical cylinder with its inner diameter and height being $D = 10$ and $L = 5$, 10, or 20 cm, respectively (the aspect ratio $\Gamma \equiv D/L$ is thus 2, 1, or 0.5). The side wall and upper and lower plates are made of stainless steel. The temperature of the upper plate is regulated by passing cold water through a cooling chamber fitted on the top of the plate. The lower plate is heated uniformly at a constant rate with a heat pipe. The temperature difference ΔT between the two plates is measured by a thermocouple embedded inside the plates. One of the dominant control parameters in this experiment is the Rayleigh number *Ra*.

During our experiment, only the bottom temperature is changed, so the average temperature of mercury at the center is not constant. *Ra* is changed from 10^6 to 4×10^8, and its relationship to the Nusselt number, *Nu*, is $Nu = 0.095 Ra^{0.294}$; this is similar to the results of Takeshita et al. [21], Cioni et al. [22], and Glazier et al. [23] We also performed another experiment using a large-scale cell with diameter, height, and aspect ratio of 30.6 cm, 61.2 cm, and $\Gamma = 0.5$, respectively. The Rayleigh number

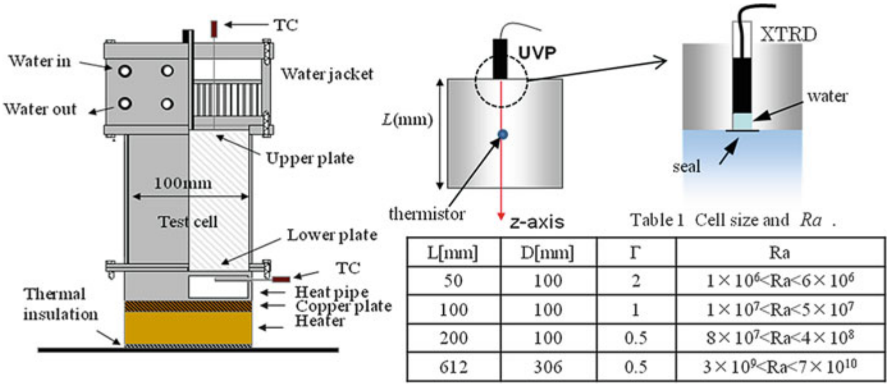

Table 1 Cell size and *Ra* .

L[mm]	D[mm]	Γ	Ra
50	100	2	$1\times10^6<Ra<6\times10^6$
100	100	1	$1\times10^7<Ra<5\times10^7$
200	100	0.5	$8\times10^7<Ra<4\times10^8$
612	306	0.5	$3\times10^9<Ra<7\times10^{10}$

Fig. 5.25 Schematic view of experimental apparatus and coordinate system [28] (Copyright (2006) by The American Physical Society.)

is up to 7×10^{10}. Using ultrasonic velocimetry [24–26], instantaneous velocity is measured at 128 points on the centerline of a cell, and temperature fluctuation is simultaneously measured by a small thermistor at the cell center. LSC in low-Pr-number convection is characterized by frequency spectra and the joint probability density function of temperature and velocity. Dependence on the aspect ratio and *Ra* has been reported [27–29].

A piezoelectric ultrasonic transducer, 5 mm in diameter and 8 cm in length, is mounted on the top of the outer surface (Fig. 5.25). Velocity is measured simultaneously at 128 points 0.74 mm apart from each other on the centerline of the cell. The vertical axis is z and its origin is at the upper plate. The velocity is defined as positive in $+z$ direction and negative for $-z$. It is expressed as $\tilde{w}(t)$.

The data are sampled every 0.132 s. The velocity resolution is about 0.7 mm/s under this condition. The sampling volume, or the space resolution, is the shape of a disk whose diameter is 5 mm and thickness is 0.74 mm. Instantaneous temperature fluctuation is measured by a small thermistor located at the cell center. Its diameter is 0.254 mm and response time is 10 ms. Simultaneous measurement of velocity and temperature is performed in the different aspect ratios ($\Gamma=0.5$, 1, 2) and Rayleigh numbers.

Tracer particles are selected according to the flow velocity, liquid density, and total measuring time. The particle density is to be matched with that of liquid mercury. Small density differences cause the rise and sedimentation of particles. In our experiment, we mixed a powder of gold-palladium alloy into the mercury as a tracer. The composition of the alloy was designed so that its density coincides with that of the mercury, 13.48 g/cm^3 at 45°C, which is the mean temperature of the two plates at the highest *Ra* attainable in our measurement. The tracers enable us to measure the whole profile of the velocity field along the z-axis.

In a preliminary test, a transducer is attached with traversing system controlled by a stepping motor. The transducer is sunk beneath the mercury, and it is moved at a constant speed (a few mm/s). We add the gold-palladium powder until a clear echo signal is observed. At 0.6 g/l the traversing speed is equal to the speed measured by

UVP. This information helps us to decide the mixing ratio as 1.0 g/l. The weight ratio of the particles is less than 10^{-4}, and it is almost negligible if compared with the purity of the mercury (99.5%); the physical properties of mercury are not changed by the tracer particles.

Because of the starting depth, the transducer should be set at 5 mm inside from the surface. The surface of the cell is covered with a thin vinyl film and the cavity is filled with water. It is important to use the thin vinyl film for reducing the reflection from it and to not disturb the flow field. We want to measure close to the wall; therefore, the starting depth is set at 5 mm for $\Gamma = 1.0$ cell. For the smaller aspect ratio cells, however, because the maximum depth is restricted, the transducer is set 40 mm inside from the surface. This setting enables us to measure all the profile across the cell. We can obtain more than 90% echo from the transducer during all experiments.

5.2.1.2 Thermal Turbulence in Mercury

In Fig. 5.26 we show the instantaneous velocity distribution. The vertical axis is the distance from the upper wall, and the horizontal axis indicates time. We only monitor the vertical component of velocity on the centerline of the cell. Positive and negative signs indicate the downward and upward velocity, respectively. The origin of the z-axis is set at the upper plate. Velocity fluctuations are classified into eight levels between the maximum and minimum values, and they are identified each in their own color.

In the case of $\Gamma = 2$, the downward and upward flows oscillate in opposition of phase. The flow from the bottom goes though the cell and reaches the top, and vice versa. Coherent motion is comparable to the cell height L. The average velocity distribution along the z-axis, $U(z)$, is approximately zero. The cell-center velocity changes its sign periodically, causing a sharp peak in the frequency spectrum (see [28]). The flow from the bottom wall does not always reach the opposite plate for $\Gamma = 1$. Around the top plate, the downward flow is dominant, and the upward flow sweeping the bottom reaches it occasionally.

Thus, $U(z)$ is positive at $0 < z/L < 1/2$ and negative at $1/2 < z/L < 1$. At the cell center we can observe periodic change of the velocity direction, but it is not as clear as at $\Gamma = 2$. This observation is consistent with finding that the spectral peak is not so sharp at $\Gamma = 1$ as at $\Gamma = 2$, and the normalized frequencies differ slightly [28], possibly because the flow pattern or the wind differs depending on the aspect ratio.

Periodic oscillation is not observed at $\Gamma = 0.5$, as is clearly shown in the time–frequency spectrum [28]. As indicated in the contour map (Fig. 5.26c), the upward flow is dominant around the top plate and the downward flow is stationary over the bottom plate. The flow sweeping the bottom (top) plate hardly reaches the top (bottom) plate. Then, $U(z)$ is negative at $0 < z/L < 1/2$ and becomes positive at $1/2 < z/L < 1$. Thus, the distribution is opposite that of $\Gamma = 1$. It is also noted that the contour map is slightly tilted. In the lower half region ($1/2 < z/L < 1$), the contour has a negative slope, which means that a lump of fluid goes down on the centerline with almost

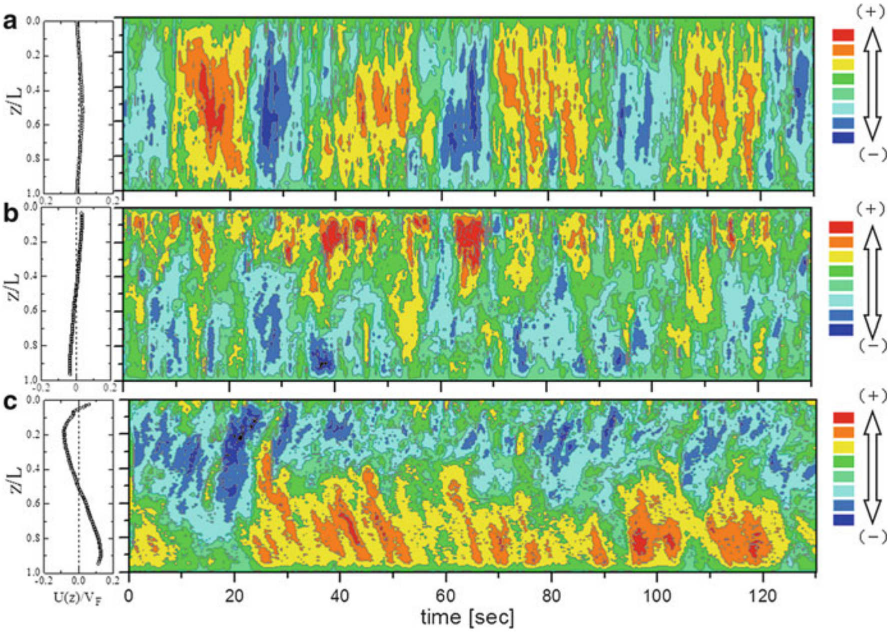

Fig. 5.26 Contour of instantaneous velocity fluctuation on the centerline of the cell. (**a**) $\Gamma = 2$. (**b**) $\Gamma = 1$. (**c**) $\Gamma = 0.5$ [28] (Copyright (2006) by The American Physical Society.)

steady velocity. In the upper half region ($0 < z/L < 1/2$), the opposite motion, going upward on the centerline, is ascertained. To summarize, we conclude that the wind is across the z-axis in the case of $\Gamma = 1$: this provides an elliptical pattern whose axis departs from the z-axis with an angle of θ (Fig. 5.27a). However, θ should fluctuate rather than be constant. If the upper region is populated by plumes, the wind circulation shifts down and the downward velocity is monitored at the cell center.

When the plumes from the lower plate become strong, upward velocity is observed at the cell center. The plumes are repeated alternatively. The time lag between these two states is $\tau \cong \frac{L}{U_c}$, and the frequency peak is given by $f_c \cong \frac{1}{\tau}$. This is the process of velocity oscillation observed in this experiment. The mean velocity at the side wall V_W is constant even if these oscillations occur. When the flow pattern rotates in the azimuthal direction, V_W reverses. However, we still have little information about the origin of azimuthal rotation and the reverse period of V_W.

The flow pattern of $\Gamma = 0.5$ is shown in Fig. 5.27b. Following the discussion of the contour map in Fig. 5.26c, a lump of fluid moves on the centerline. It goes upward in the upper half region, and downward in the lower half, so we imagine that the axisymmetric toroidal rings exist steadily near the upper and lower plates. A similar tilted contour map has been observed up to $Ra = 7 \times 10^{10}$. At the cell center, the upward and downward flows exist alternatively, but they are not periodic. Thus, there is little coupling between top and bottom plumes [27].

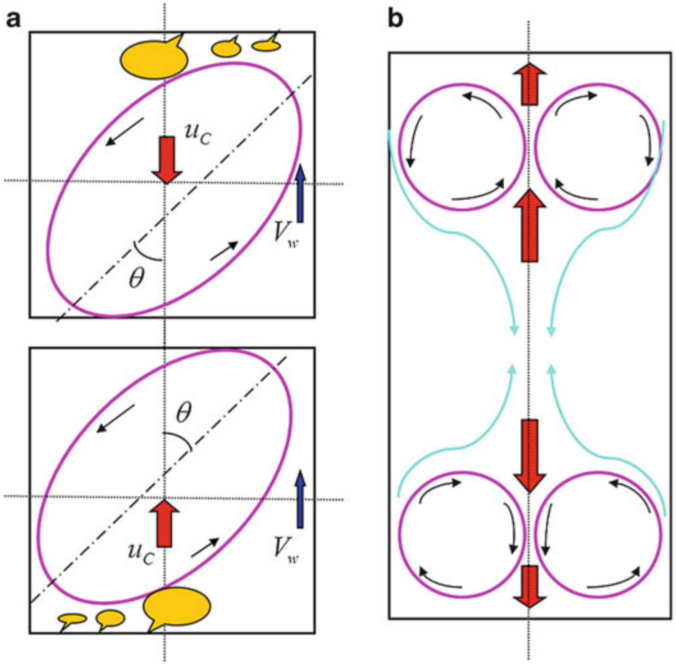

Fig. 5.27 (**a**) Elliptical flow pattern of $\Gamma = 1$. (**b**) Flow pattern of $\Gamma = 0.5$ [28] (Copyright (2006) by The American Physical Society.)

Figure 5.28 shows the joint probability density functions (jpdf) of velocity and temperature, whose axes are normalized by their average and standard deviation. The flow in $\Gamma = 0.5$ has a strong negative correlation with temperature fluctuation. The upward flow carries the warm temperature bolus, and downward flow (Fig. 5.28a) is wrapped in the cold temperature. The correlation coefficient is approximately 0.5 and does not show the strong *Ra* number dependence. Neither velocity nor temperature fluctuation has periodic oscillation; therefore, the flow from the bottom (top) with warm (cold) temperature passes the cell center at random [29].

In the case of $\Gamma = 1$, there are also the upward and downward flows, which correspond to the double peak on the vertical axis in the jpdf (Fig. 5.28b). On the other hand, the temperature fluctuates in a wide range, which looks Gaussian like. Calculating the correlation coefficient, it is almost zero independent of *Ra* [29]. Therefore, it is said that there is no relationship between velocity and temperature fluctuations. Although the flow at the cell center indicates periodic oscillation, we could not determine a clear peak frequency in the temperature fluctuation. Therefore, the warm (or cold) plumes spread around the cell center, or the lumps of warm (or cold) temperature do not survive within the LSC. This condition is different from the observation in a large-Pr-number working fluid, such as water, in which the temperature shows weak periodic oscillation at the cell center. For $\Gamma = 2$ (Fig. 5.28c), the flow becomes more complicated. The jpdf shows a local peak in each quadrant,

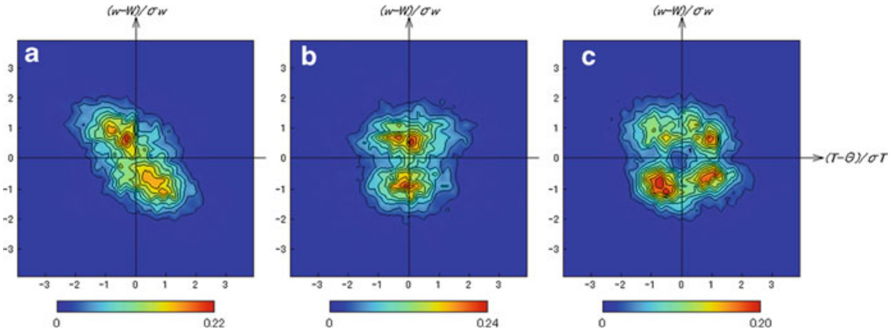

Fig. 5.28 Joint probability density functions of velocity and temperature fluctuations at cell center. (**a**) Aspect ratio $\Gamma = 0.5$, $Ra = 3.26 \times 10^8$. (**b**) Aspect ratio $\Gamma = 1$, $Ra = 3.71 \times 10^7$. (**c**) Aspect ratio $\Gamma = 2$, $Ra = 3.63 \times 10^6$. The vertical axis is velocity in z-direction and the horizontal axis is temperature. They are normalized by their standard deviation (reprinted from [29] with permission from Elsevier)

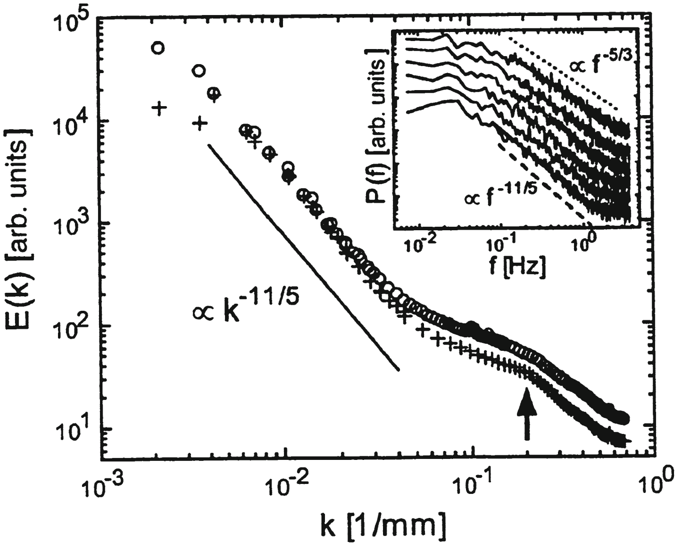

Fig. 5.29 Energy spectral density $E(k)$ calculated by subtracting the mean profile (°) and the first two POD eigenmodes in addition (×). By fitting, $\beta = -2.15 \pm 0.02$ and -2.22 ± 0.02 are obtained for $E(k) \infty k^{\beta}$ for the two cases. *Arrow* indicates the lateral resolution. *Inset:* Frequency power spectra $P(f)$ at $z = 0$, 50, …, 250 mm (from *bottom* to *top*) [27] (Copyright (2004) by The American Physical Society)

which means that the upward flow carries both the warm and cold fluid lumps, and also the downward flow has the same trend. The frequency spectra in both velocity and temperature show a clear peak depending on the Rayleigh number. Therefore, the upward flow and downward flow reverse periodically, and they carry the warm and cold lumps alternatively. There may be several rolls in the cell. It is not easy to estimate the flow patterns at this stage.

We show, in Fig. 5.29, the energy spectral density $E(k)$ directly calculated from the results of the multipoint velocity measurements. Measurements were performed over three different z ranges of $127 \times \Delta z$ with $\Delta z = 3.62$, 2.17, and 0.72 mm. In each measurement, the center of the range is set at $z = L/2$ and 10,240 profiles were sampled. Data from the three Δz overlap each other in Fig. 5.29 (the arrow indicates the transverse resolution) [27].

To avoid a bias from the mean profile $W(z)$, we subtracted it from each measurement and calculated $E(k)$ (circles). To be more careful we subtracted the slow dynamics caused by the first two POD eigenmodes together with the mean profile (crosses). For both plots, there exists a scaling range in which the power law $E(k) \infty k^{\beta}$ holds. By fitting, $\beta = -2.15 \pm 0.02$ and -2.22 ± 0.02 were obtained for the circles and the crosses, respectively. Both are close to −11/5 derived in Bolgiano–Obukhov theory for thermal turbulence (represented by the solid line in Fig. 5.29), which is distinct from −5/3 for the isotropic case. Historically the frequency power spectra $P(f)$ have been calculated from local time series [27]. In the inset of Fig. 5.29 we show $P(f)$ at positions located every 50 mm along the z axis, $= 0, 50, \ldots, 250$ mm, together with power laws with exponents of −11/5 (dashed line) and −5/3 (dotted line) for comparison. Each $P(f)$ was calculated from the velocity time series consisting of 10,240 samples. The slope of $P(f)$ changes with the position. At $z = 0$ mm, the slope is -2.14 ± 0.03, which is close to −11/5. However, at the cell center $P(f)$ has no relationship to $E(k)$ because the mean velocity $W(z)$ is zero. At $z = 250$ mm, the slope is -1.72 ± 0.02. Here the fluctuation-to-mean ratio $W(z)/\sigma$ remains near 1; thus, Taylor's hypothesis is not valid in turn. Then, $P(f)$ is different from $E(k)$ in thermal turbulence [27].

5.2.2 *Suppression of Oscillatory Convection by a Horizontal Magnetic Field*

Liquid metals are characterized by low viscosity with high thermal conductivity, that is, low Prandtl number, and their behavior in thermal convection is very different from the convection of water and gases (Prandlt number ~1). In addition, liquid metals have high electric conductivity. Electric currents are induced in the liquid metal flowing in the magnetic field, which generates Lorentz forces. The Lorentz force in turn deforms the flow behavior, making the flow very different from non-magnetic field situations. The study of liquid metal convection is important not only for fundamental fluid mechanics but for both engineering and geoscience applications. However, the usual optical methods for flow measurements cannot be applied to observe flows in liquid metal. Most experimental studies on liquid metal convection have focused on the measurement of the heat transport of the system (Nusselt number) and the temperature fluctuations at different points in the fluid layer related to turbulence. Here we introduce an experiment on thermal convection of a liquid metal with an applied magnetic field, in that UVP is used to visualize the flow structure and its time variation. We use gallium as a liquid metal, because its melting temperature is 29.8°C and it is easy to handle.

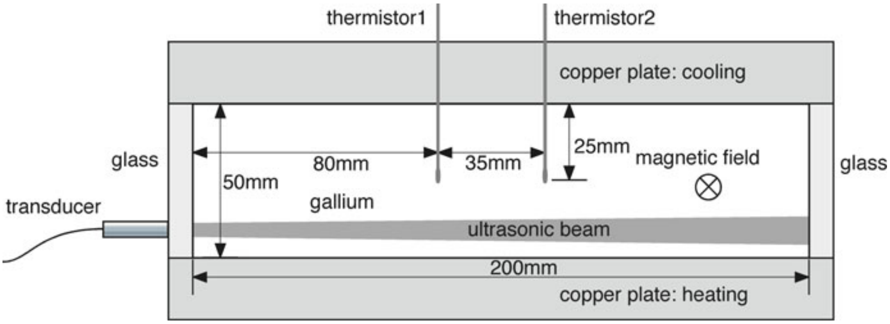

Fig. 5.30 Side view of the vessel

Figure 5.30 shows the vessel for the liquid gallium convection under a vertical temperature difference. A horizontal magnetic field is applied by a Helmholtz coil system. The inside measurements of the vessel are 200 mm long, 50 mm wide, and 50 mm high. The lines of measurement for UVP are set along the long horizontal direction of the vessel, as indicated by "ultrasonic beam," and the projected component of the flow velocity on this line is measured. Further details of the experiment are provided in references [26, 30–32].

We show in Fig. 5.31 the visualization of the flow pattern associated with abrupt increase of an applied magnetic field. In this experiment, Ra is 1.3×10^5. Temporal variations of the flow pattern is shown in the top panel, and temperature fluctuations at the same duration measured by thermistors are shown in the bottom panel. The UVP data indicate that there exist four oscillatory rolls of convection in the duration of no magnetic field (from 0 to 250 s). A typical timescale of this oscillatory motion (~30 s) is comparable to the circulation time of the flow for a roll. As the ultrasonic beam line is set near the bottom of the vessel, the sign of the velocity profile tells us that the structure of the flow pattern has downwelling regions at both side walls and at the center, with upwelling regions around 50 mm and 160 mm; this is consistent with the measurement of temperatures, that is, the temperature at thermistor 2 (near the center) is lower than that of 1. The timing and amplitude of the temperature fluctuations correlate well with the fluctuation in the flow pattern recorded by the UVP and indicate that the oscillatory behavior of the flow induces temperature fluctuations. The UVP data also show that, when a horizontal magnetic field of $Bh = 18$ mT is applied, the pattern keeps a four-roll but the oscillation disappears and the flow assumes an almost two-dimensional steady state. The amplitude of the temperature fluctuations also decreases drastically, indicating that the axis of the roll structure is aligned in the direction of the applied magnetic field and that an almost steady state of flow is realized. The observed suppression of fluctuations and alignment of roll axis under a horizontal magnetic field is consistent with theoretical studies [32]. We can reconstruct a three-dimensional (3-D) flow structure from the UVP measurements at several positions (Fig. 5.32).

As shown here, measurement of flow velocity by UVP can provide much information on the behavior of a flow. In this case of thermal convection in a liquid metal,

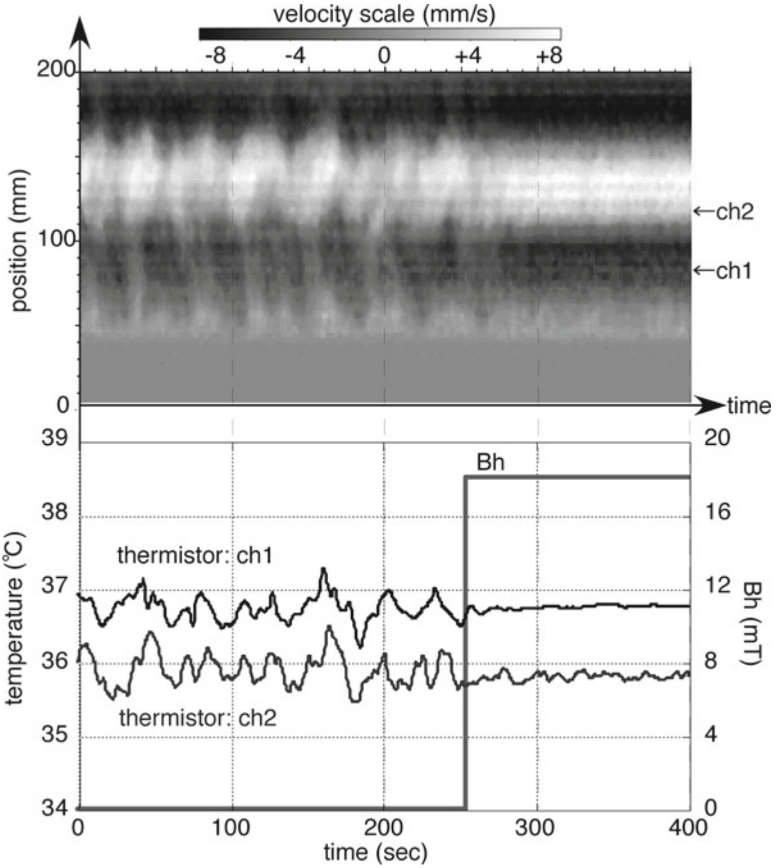

Fig. 5.31 Flow pattern by the UVP (*top*), and temperature fluctuations by thermistors (*bottom*), for the same duration (adapted with permission from [31]. Copyrighted by the American Physical Society.)

simultaneous measurements of temperature at several points and UVP are very cooperative. Thermistors have much more resolution on temperature than that of velocity by UVP; hence, it is appropriate for the statistical character of turbulence. On the other hand, UVP plays a key role for catching global structure with its time variations.

5.2.3 Measurement of Liquid Metal Flow in Nuclear Facilities

5.2.3.1 Background

The study and development of the technology for the purpose of protecting the environment as a modern international trend are enforced. Among these, from the

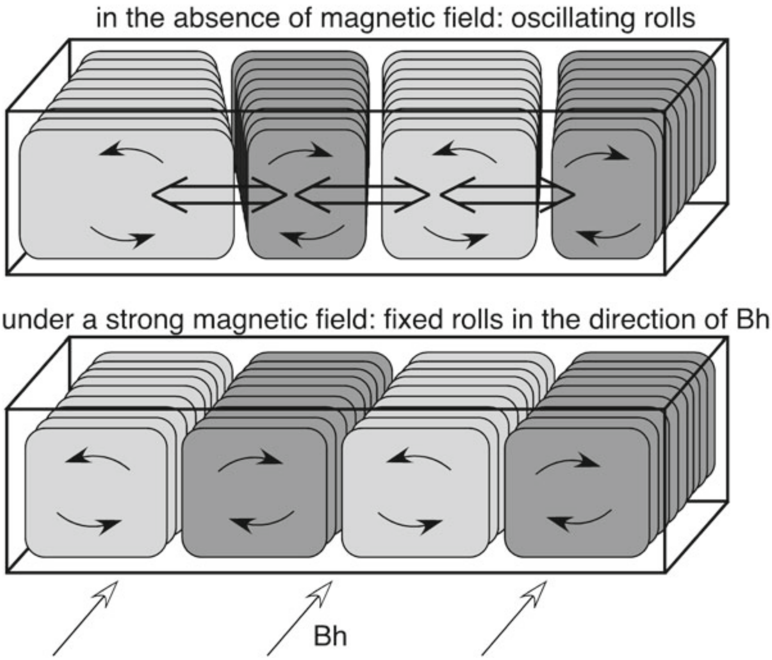

Fig. 5.32 Schematic view of the behavior of the convective flow (adapted with permission from [31]. Copyrighted by the American Physical Society.)

point of view of global warming measures, nuclear power generation comes into the limelight as a source of "clean energy" that does not exhaust carbon dioxide at the time of operation. However, nuclear power generation produces nuclear waste, which is extremely harmful to the environment, with power generation. Establishment of a complex system including processing and disposal of the nuclear waste is required to use atomic energy as a source of clean energy.

Research and development of this processing and disposal has not progressed sufficiently. The reasons include technical problems as well as anxiety about safety and radioactive waste. In the study of disposal of waste from a nuclear system are included research and development of the technique using the fast breeding reactor "Monju" and the accelerator-driven system (ADS). Monju uses sodium cooling, and ADS adopts a cooling system using the lead bismuth eutectic (LBE) alloy as a spallation neutron source. In these systems, optimization of the system for high efficiency and securing the safety of the whole system are required. To solve these problems, evaluation of the properties of heat transfer and the measures of erosion and corrosion of materials is required. Therefore, it is urgent to understand the flow behavior of the coolant [33–35] that is closely related to heat transfer and erosion/corrosion. Erosion/corrosion by the heavy liquid metal begins with the embrittlement of materials, including their chemical characteristics, and the phenomenon in which the embrittled materials are eroded locally is promoted by a flow. The erosion/corrosion of the materials is confirmed at the region having disturbed flows such as downstream from an elbow section or an orifice. However, because the depth of erosion/corrosion is inconsistent with the occurrence region, grasp of the causative flow behavior has been required. In past studies, some predictive analysis of the liquid metal flow by computational fluid dynamics (CFD) including the evaluation of the properties of heat transfer has been performed.

However, different results were reported by each turbulence model used. Therefore, verification of the analysis results by the expansion of velocity data given by the experimental measurement and the precision improvement of the predictive calculation are necessary. In addition, in ADS developed in Europe, a windowless target system where there was no solid–liquid boundary at the position of a beam incidence was confirmed. One of the technical problems includes the freely interfacial control that is a beam window, and grasp of the true flow ground by experimental measurement is regarded as important. In this system, because the control of free surface of the coolant that acts as a beam window is one of the technical problems, it is important to grasp the actual flow behavior by experimental measurement. However, past experimental measurement of liquid metal flow has been limited to a temporary method that predicted velocity information by measured temperature distribution. The general heavy liquid metal was opaque. Furthermore, except mercury or liquid gallium, the liquid metal used as a coolant for the nuclear system has a high melting point and is used under high-temperature conditions. Practically, the velocity measurement technique in liquid metal flow is limited to neutron radiography (NRG) and UVP. In fluid measurement, NRG is a section measurement method as is PIV, and it brings much useful information from the flow field. On the other hand, it has some problems: sectional extraction is difficult, and the tracer particles suspended in the flowing medium are large. Because the device is very complicated to use and huge under the present conditions, it lacks in versatility and convenience. The use of NRG for measurements in idealized systems such as laboratories is appropriate. UVP acquires less information about the flow field than NRG, but its versatility is high and it could expect application to flow measurements in actual system. A measurement example that applied UVP to actual liquid metal flow in high temperature conditions is shown in the following subsection.

5.2.3.2 Spallation Target Model and Measurement Configuration

Figure 5.33 shows a schematic illustration of the mock-up model (JAEA lead bismuth loop-2, JLBL-2) of a spallation target (target test facility, TEF-T). This loop has an annular flow channel constructed by a coaxially arranged double cylinder. The diameter of the inner cylinder was 35.5 mm and that of the outer cylinder was 63 mm. In consideration of erosion/corrosion, SUS316 stainless steel was adopted as the main material. LBE flow in the annular region that has a gap of 3 mm between two cylinders was driven by an electromagnetic pump (EMP), and flow rate was observed by an electromagnetic flow meter (EMF). Because the inner cylinder was made of iron, and it forms a saturated magnetic field, the EMP could drive only LBE in the annular region. The flow joins in the inside of the bend section, then

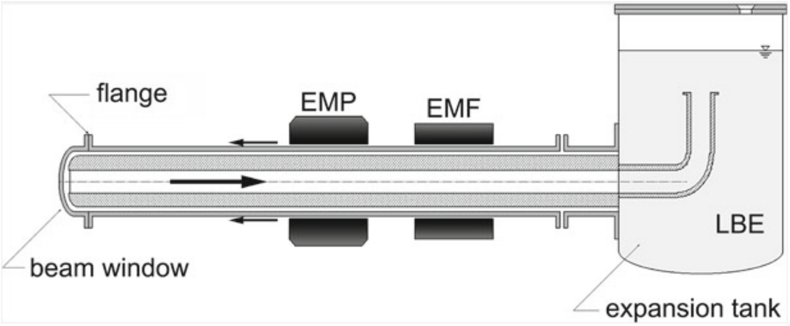

Fig. 5.33 Schematic illustration of JAEA lead bismuth loop-2 (JLBL-2)

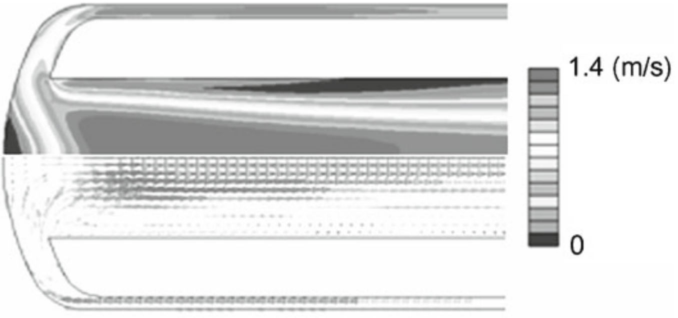

Fig. 5.34 Result of CFD analysis for beam window of spallation target

turns over and returns to an expansion tank through the inside of an inner cylinder. The total length of the loop is 1,504.5 mm. The inventory of LBE was 20 l, and the maximum flow rate was about 40 l/min. Maximum temperature was 250°C. In the design of an actual spallation target, because a proton beam is striking the bend section, which functions as a beam window, the properties of heat flux motion around the beam window are extremely important. As a result of CFD analysis (shown in Fig. 5.34), stagnant flow was formed in the inside of the center of a window where the incident point of the proton beam was, and it was expected that the cooling performance decreased remarkably. Therefore, the actual LBE flow was measured by UVP to verify the result of present CFD analysis by the velocity information given by the experiment. UVP-Duo (Met-Flow S.A.) was used for a measurement system, and the ultrasonic transducer of the heat-resistant model (Japan Probe) was used for the emission/reception of the signals. The basic frequency of the transducer was 4 MHz. The temperature of LBE was set to 150°C constant, because the maximum temperature of the transducer was 150°C. The argon gas bubbles that were supplied from a gas addition device installed in the expansion tank was used for the reflecting/scattering particles of the ultrasonic signals. In the flow measurement of the heavy liquid metal, it is appropriate to use solid metal particles that have specific gravity

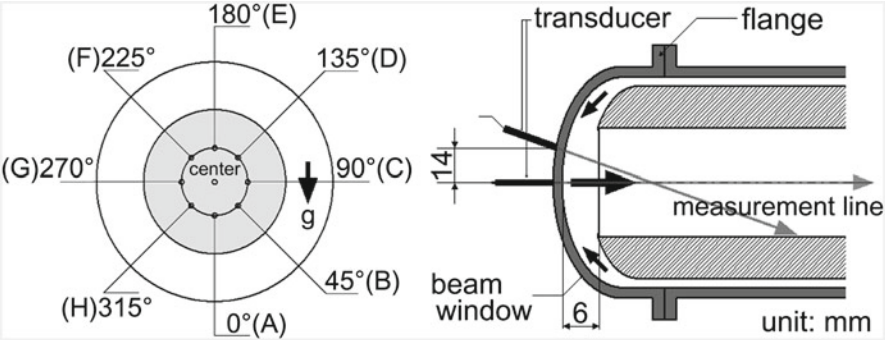

Fig. 5.35 Experimental configuration of the measurement line on the window sphere

in accord with the flowing medium. However, as for the use of the solid particles, there are some problems such as damage of the flow channel and method of removing the used particles. Therefore, in the actual model, it is desirable to use the micro gas bubbles that can be removed easily by the vent system. The beam window has a spherical shape and is 3.5 mm thick. The left side of Fig. 5.35 is a front view of the beam window. The measurement position is located at the center of the window sphere, and eight points (A–H) on an arc have this point as their center. The radius of this arc is 14 mm, and measurement positions are located at every 45°. As well, the ultrasonic transducer is installed perpendicular to the surface of the window sphere as a countermeasure to prevent the refraction phenomenon of the ultrasonic signals that is caused at the wall surface of the window sphere.

5.2.3.3 Measurement Results of Actual LBE Flows

Figure 5.36 shows the measurement results on the centerline by changing the velocity conditions in the annular region. In this figure, the horizontal axis represents the measured position and corresponds to the distance on the centerline, assuming the edge of the loop as the origin. The vertical axis represents averaged velocity data; that is, the number of averaged velocity profiles is 1,024. The averaged velocity conditions in the annular region were set to four phases ($U_1=0.25$, $U_2=0.50$, $U_3=0.75$, $U_4=1.00$ m/s). Under all velocity conditions, in the averaged velocity profiles provided by this experiment, the velocity data show zero data from the position of starting measurement to around the distance of 15 mm. At the inner wall surface around the beam window, the LBE flows coming from annular region collide with each other. Therefore, a local stagnant region is formed near the center of the edge of the loop. It is thought that this result represents a stagnant region of the LBE flow that extends around 15 mm from the inner wall surface at the center of the window. Even if the LBE flow rate in JLBL-2 increases, the formation of this stagnant region could not be avoided. When a proton beam is incident in the JLBL-2, countermeasures apart from increasing the LBE flow rate are necessary; further, it

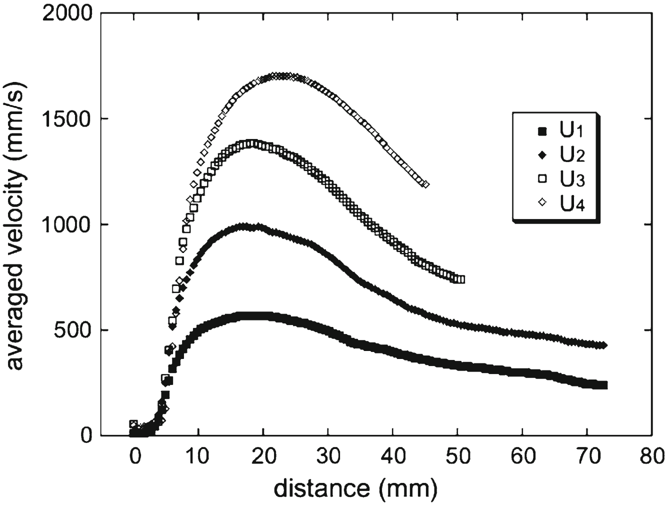

Fig. 5.36 Averaged velocity profile at the centerline of JLBL-2, where velocity conditions are $U_1 = 0.25$, $U_2 = 0.50$, $U_3 = 0.75$, $U_4 = 1.00$ m/s

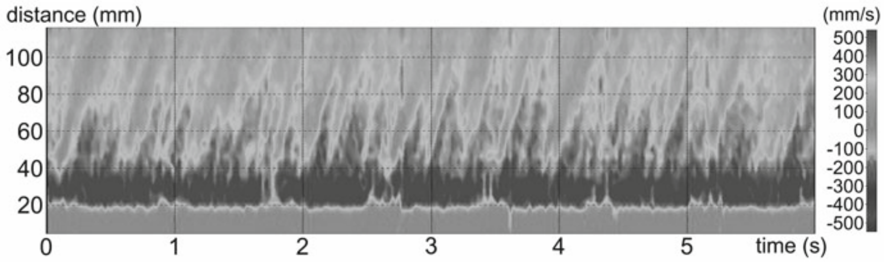

Fig. 5.37 Space–time representation of the time-dependent one-dimensional velocity profile, where velocity condition is $U_1 = 0.25$ m/s

is thought that this dead region interferes with the cooling of the target model loop. Also, velocity rises suddenly and decreases slowly after it reaches the maximum velocity. The location of the maximum velocity was 22–38 mm. By increasing the velocity conditions, the maximum velocity profiles show a proportional relationship. However, in the downstream side after maximum velocity, the tendency of the velocity decrease did not have a proportional relationship. By CFD analysis (cf. Fig. 5.34), it is predicted that the recirculation region was formed on the surface of the inner cylinder from its edge. When a recirculation domain exists stably, the LBE flow will be accelerated because the flowing width is narrowed artificially. The measured result shows the process that velocity gradually decreases after LBE flow passed this recirculation region. Figure 5.37 shows a color density plot of the data set on the space-time domain. The velocity condition was U_1. The horizontal axis shows the time, and the vertical axis shows the distance on the centerline of JLBL-2.

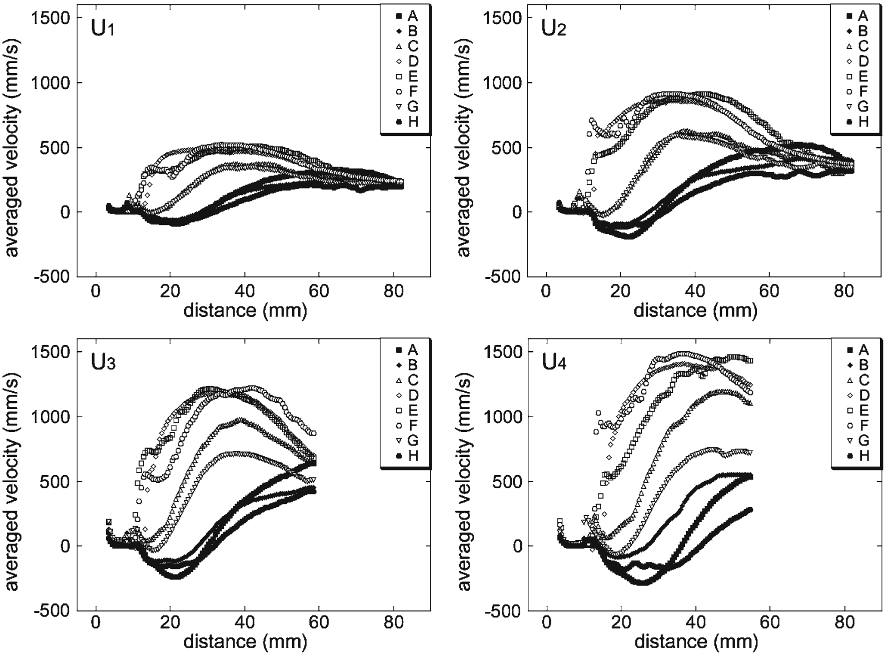

Fig. 5.38 Measurement results from the surrounding points of A–H

The color shows the velocity. In this figure, almost all velocity data are positive. It is observed that there occurs a spatiotemporal oscillation in the measured area after the distance of 40 mm. The velocity data show an oblique line that appears periodically in time. Because the obstacle did not exist on a measurement line, these lines show the motion of a fluid volume moving on the measurement line. A moving velocity of this volume that calculated by the inclination of the velocity stripes is about 2.3 mm/s, and it is equivalent to about half of maximum velocity (0.5 m/s). It is thought that this flow structure is eddies that discharged from the recirculation region that moved along the centerline. By the result of present CFD analysis, it was predicted that the flow in this loop had an axsymmetric flow. Because the mock-up loop was installed horizontally, gravity did not act on axsymmetry for the structure of the flow channel. In addition, it was expected that the flow around the beam had a complicated flow structure because it was very difficult to make a uniform flow in the annular region. To confirm the three-dimensional flow structure, the velocity profiles on eight measurement lines that surrounded the center of the window (cf. Fig. 5.35) were measured by UVP.

Figure 5.38 shows the measured results and a quasi-three-dimensional flow structure in JLBL-2. The horizontal axis shows the distance on an inclined measurement line from the inner surface of a window, and the vertical axis shows the averaged velocity. Almost all these velocity profiles show zero velocity between 5 and 8 mm from the start position, and this range was the stagnant region around the beam window in JLBL-2. In the velocity condition of U_1, the flow structure around a beam window was symmetric in the horizontal direction. However, it was not symmetric in the gravity direction. The averaged velocity profiles of the upper side (D, E, F) were faster than those of the lower side (A, B, H). The velocity profiles of the lower side changed from negative to positive continually. These data show the formation of the roll-shape vortex existing constantly. The symmetric flow structure for the horizontal direction was kept at velocity less than $U_2 = 0.5$ m/s. At first, in the case of velocity conditions greater than $U_3 = 0.75$ m/s, the symmetry of C and G collapsed. In the velocity condition of $U_4 = 1.00$ m/s, the symmetry of the other region collapsed, and it was confirmed that a flow having a complicated three-dimensional structure was formed around the beam window.

5.2.3.4 Influence of Wettability in UVP Measurement

By the predictive calculation, the maximum temperature of a beam window was about 500°C in the actual condition of ADS. In this temperature condition, wettability between LBE and the materials is improved by the effects of corrosion and beam irradiation. In the present experimental measurement, the temperature was set to a low temperature condition around the melting point of LBE because of the maximum temperature of the transducer. In past studies of the erosion/corrosion caused by LBE, most of the influence of the corrosion was not observed at 150°C. Therefore, it was expected that the wettability between LBE and the stainless steel was insufficient at the low temperature condition. When wettability was not sufficiently secured, it would be necessary to change the boundary condition in the solid–liquid boundary for predictive calculations. In addition, this phenomenon has a bad influence on flow measurement by the UVP system. Figure 5.39 shows an example of UVP measurement in a poor wetting condition between LBE and a beam window of JLBL-2. In this figure, the velocity condition was $U_3 = 0.75$ m/s and the temperature was set to 150°C. In comparison with Fig. 5.36, the velocity profile drops extremely at the measurement positions of 30 mm and 40 mm. This dropping velocity profile was often observed at the position where the measurement line contacts with an obstacle. However, as shown in Fig. 5.35, because there is no obstacle on the measurement line, it is thought that this result includes the wrong information. When the wettability between LBE and the inner wall of the vessel is insufficient, a part of the ultrasonic burst signal from a transducer propagates the inside of vessel while repeating a reflection, because the signal cannot pass to LBE in a solid–liquid boundary. Subsequently, the signal is reflected in the edge of the container and produces a strong reflection echo. In the case of the introduced example about JLBL-2, a flange for fixation is equivalent to the edge of the vessel. As a result of having calculated the distance using the sound velocity of SUS316 stainless steel (5,790 m/s) and the detection time of the echo observed by an oscilloscope, it accorded with the distance from a transducer to a flange. Because the reflection echo from a metal vessel is very much stronger than the feeble echo from the fine particles in the flowing medium, the decline of the S/N ratio is not avoided

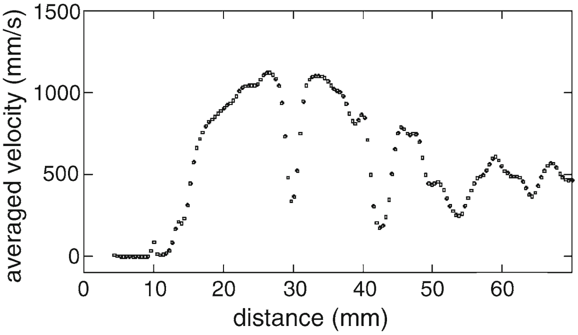

Fig. 5.39 Measurement example at poor wetting condition

at the position. Usually, the solid wall is fixed, and the movement velocity becomes zero. As a result, the result shown in Fig. 5.39 was provided because the velocity information of the solid wall that did not move was accumulated to the speed-measured velocity profile. As well as the case that wettability is insufficient, the measurement person should be careful about the influence of the reflected signals that propagate in a vessel. Therefore, the monitoring of the state of *echo* and *measured velocity profile* is important. In the introduced result shown in Sect. 5.2.3.3, the problem of wettability was improved. The inner surface of a beam window was treated by polishing, flatting, and finally coating with nickel and solder. LBE and nickel have good wettability. As the thickness of the coating layer was consistently less than 20 μm, this layer does not disturb the LBE flow.

5.2.3.5 Summary

Acquisition of data verifying the results of the predictive calculations and flow behavior that was not predicted by CFD analysis was possible by UVP measurement. Therefore, it is thought that UVP is a measurement technique that can be applied to the measurement of heavy liquid metal flow at a high temperature condition. On the other hand, because of the heat-resistant problem of the ultrasonic transducer, there are still few examples in the actual environment. In the development of the heat-resistant transducer, Eckert et al. [36–38] succeeded in measurement at temperatures greater than 500°C by using an acoustic waveguide. In addition, transducer development is being pushed forward by some makers. Recently, in the study and development of nuclear systems, measurement and control of the flowing coolant are regarded as an important issue to ensure safety. Data acquisition by experimental measurements is required to realize verification and improvement of precision of predictive calculations. In addition, metallic materials are usually used for the cooling system ducts, even transparent fluids such as supercritical water are used, to endure high temperature and high pressure conditions. To secure the safety of the system, in addition to a predictive calculation, it is important that the internal flow is confirmed by an experimental measurement beforehand. In such a scenario, UVP is an extremely effective method because it can realize flow measurements regardless of the transparency of the vessel.

5.3 Rheometry

5.3.1 In-line Rheometry

The monitoring of production processes in chemical and food engineering is important to control the quality of products. The process governs the microstructure of the product, which determines the rheological and other properties. The noninvasive in-line rheometry concept, based on the combination of the pulsed ultrasound (Doppler)-based velocity profile (UVP) technique and pressure drop (PD) measurements in a pipe section was developed to characterize the rheology of non-Newtonian models, fat and nucleated fat crystallization, and fiber and other suspensions during flow under different production processes [39–46]. This method enables determination of in-line rheological properties such as shear rate-dependent shear stress and viscosity, which can be compared with those measured with an off-line laboratory rheometer. The UVP + PD technique was also used for pipe flow of opaque particle suspensions [47], droplet dispersions, and aqueous solutions of polymers [39, 48, 49]. The non-Newtonian model suspensions, and food and other suspensions, are considered in Sect. 5.3.1 and 6.2, respectively.

The basic idea of ultrasonic in-line rheometry described here is the use of the influence of the shear rate-dependent viscosity on the shape of the laminar pipe flow velocity profile. A simple example should help to explain this. The left part of Fig. 5.40 shows the rheological behavior of two different power law fluids. The power law (see Sect. 5.3.1.5) can be used to approximate the flow behavior of many non-Newtonian liquids relevant to the food and chemical industries. The special case of a power law index $n = 1$ describes a Newtonian liquid such as pure water or oil. The corresponding velocity profile for a laminar flow, shown in the right part of Fig. 5.40, is then parabolic. If the fluid is shear thinning ($n < 1$), a typical property of many suspensions and polymers, viscosity decreases with shear rate. Then, the

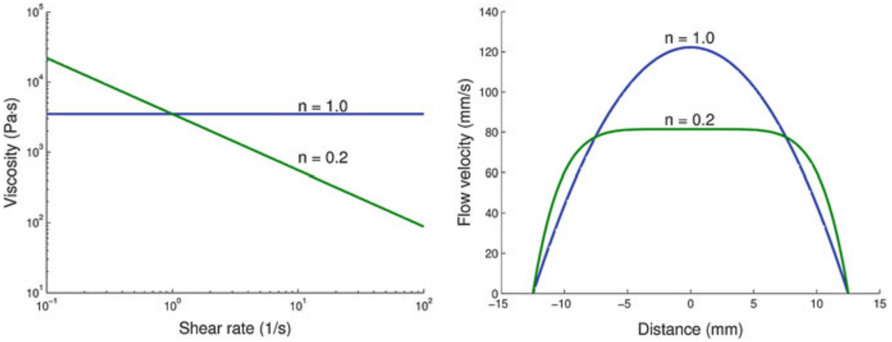

Fig. 5.40 Relationship of shear rate-dependent viscosity (*left*) and the corresponding fully developed velocity profile in a laminar, stationary pipe flow for two power law fluids ($\eta = K\dot{\gamma}^{n-1}$). The volume flow rate of the two profiles is equal

corresponding velocity profile has a blunted shape, as also shown in the right part of Fig. 5.40. The concept of UVP-based in-line rheometry is the use of the shape of the measured flow velocity profile in combination with pressure drop measurements to derive rheological information about the fluid.

5.3.1.1 Measurement Setup

A minimal UVP+PD setup consists of a straight pipe section with an ultrasound transducer and two pressure sensors (either absolute or differential). The pipe section should be long enough to allow the flow to be fully developed, with no influence from the closest bends. It can be helpful to integrate temperature sensors, a flow meter, or other auxiliary measurements depending on the process. The entry lengths for a fully developed flow profile have to be considered. It is also important to avoid pipe diameter changes or other irregularities of the pipe geometry, which could influence the velocity profile, for example, by introducing small eddies at the pipe wall.

5.3.1.2 Flow Adapter

The most critical part of the measurement section is the fixation of the ultrasound transducer in a so-called flow adapter. At the time of writing there exist no commercial solutions for the transducer mounting. The solutions presented in the literature range from transducers mounted outside the pipe and using a water bath for the coupling [39] to specially designed transducers with a corresponding delay line matched to the pipe curvature. The individual solutions depend on many parameters such as temperature, pressure, pipe diameter, importance of a valid measurement in the wall region, and application type (laboratory setup or industrial process monitoring), to name just a few. Also the pressure field (especially the near-field length) of the transducer and the acoustic properties (impedance, attenuation) of the wall material have to be considered [50].

5.3.1.3 Electronics and Profile Estimation

Most installations use the commercial velocity profilers from Met-Flow or Signal Processing (both in Switzerland). It is also possible to use home-made pulser-receiver electronics [51] or devices originally developed for medical applications [39, 52].

There are different signal processing approaches available to obtain the velocity profile from the ultrasound signal. Most often used are time- and frequency-domain algorithms working with the demodulated I/Q data. Time-domain (cross-correlation) algorithms are used in the aforementioned commercial devices; fast Fourier transformation (FFT) is often used in custom devices. FFT itself has the advantage to make the complete Doppler frequency distribution available, which simplifies the detection of artifacts in the velocity profile. The RheoFlow system presented by Wiklund et al. [49] and Wassell et al. [46] allows simultaneous velocity estimation using time domain, FFT, and spectral estimators.

5.3.1.4 Software

For meaningful data processing it is often necessary to write custom software with versatile functionality: (1) synchronized data acquisition from the ultrasound electronics, pressure sensors, and possibly other sensors such as thermocouples; (2) if necessary, velocity profile estimation based on the radiofrequency (RF) or I/Q data from the ultrasound electronics (for real-time processing, often the data transfer is the bottleneck); (3) rheological calculations using the velocity profile and pressure drop; and (4) visualizations. Such software [53] is most useful if it can be used for a real-time visualization of a running process as well as post-processing based on stored measurement data [49]. Flowcharts describing the whole process from data acquisition to rheological model parameter estimation are presented by Ouriev [41], Birkhofer [43], Wiklund [44], and Wiklund et al. [49].

5.3.1.5 Non-Newtonian Fluid Models

Power Law Model

Consider the flow of a non-Newtonian fluid in a cylindrical pipe of radius R and length L. Equating the force $2\pi rL\tau$ caused by the shear stress τ at radius r of a cylindrical fluid element of length L to the force $\pi r^2\Delta P$ from pressure drop ΔP gives [54] the linear increase in shear stress τ with radius r as

$$\tau = \frac{\Delta P}{2L} r \tag{5.6}$$

The relationship between the shear stress τ and shear rate $\dot{\gamma}$ for a non-Newtonian fluid can be assumed to be given by power law:

$$\tau = K\dot{\gamma}^n \tag{5.7}$$

where n is the power law exponent and K is the consistency index or viscous coefficient.

The shear rate is related to radial gradient of velocity v of fluid at radius r in the pipe as $\dot{\gamma} = -\mathrm{d}v/\mathrm{d}r$. Thus, combining the foregoing two equations for the shear stress and integrating with the condition that $v = 0$ at $r = R$ gives the radial velocity profile for power law fluids:

$$\nu = \frac{R}{1+1/n}\left(\frac{R\Delta P}{2LK}\right)^{1/n}\left(1-\left(\frac{r}{R}\right)^{1+1/n}\right) \tag{5.8}$$

Fitting the experimental data of the velocity profile along the pipe radius with the corresponding pressure drop to this equation enables the determination of the power law constants *n* and *K*, which can be used to predict the shear rate-dependent viscosity η given by

$$\eta = \frac{\tau}{\dot{\gamma}} = K\dot{\gamma}^{n-1} \tag{5.9}$$

The variation in shear rate and viscosity along the radius of the pipe can then be obtained as

$$\dot{\gamma} = \left(\frac{r\Delta P}{2LK}\right)^{1/n} \tag{5.10}$$

and

$$\eta = K\left(\frac{r\Delta P}{2LK}\right)^{1-1/n} \tag{5.11}$$

Other Fluid Models

The same analysis can be made for other non-Newtonian fluids exhibiting Bingham and Herschel–Bulkley type of flow behavior, for example [55]. As a result, several rheological models have been used in UVP+PD systems to determine the shear rate-dependent viscosity and for rheological model parameter estimation.

5.3.1.6 Gradient Method

As alternative to the aforementioned model fitting it is also possible to derive rheological information directly from the velocity profile and pressure drop using the gradient method. It uses directly the gradient $\dot{\gamma} = -dv/dr$ of the velocity profiles at different radial positions. The corresponding shear stress τ is obtained using the pressure drop ΔP so that $\tau = (\Delta P)/(2L)$. The latter approach has the advantage that it requires no a priori knowledge of the flow behavior of the systems, but it also has the disadvantage of requiring high spatial resolution and high data quality (see Müller et al. [40] and Wiklund and Stading [56]).

5.3.1.7 Limitations and Main Sources of Error

Results from many scientific investigations have shown that the most important limitation and source of error with the UVP + PD method is that it is not possible to accurately measure from the transducer front because of the ultrasonic transducer near-field. Historically, the transducers have been installed inside small cavities and pulled back from the liquid–wall interface in most of the recent publications on the UVP + PD method. This method results in, for example, non-zero velocities at the walls, accumulation of solids in the cavities, nonuniform particle distribution, and nonconstant sound velocity along the beam axis in front of the transducer. In addition, the determination of wall position becomes difficult. As a consequence, a range of power law-fitted parameters, for example, can be obtained just by varying the wall position in small increments, thus leading to inaccurate results [43, 44, 56]. This problem may be eliminated by the introduction of a next-generation transducer, which is currently under development [44, 46, 56, 57].

Another problem is the difficulty in determining the velocity of sound along the beam axis and the physical limitation with the finite diameter and length of the ultrasonic pressure field. The sample length and intensity are functions of the transducer characteristics, such as the diameter of the piezo, but also the pulse duration and energy dissipation after pulse emission is important. The resulting sample volume has a drop shape at the tail caused by transducer ringing or the gradual decay of the stored energy. The measured velocity profile is always a convolution of the ultrasound pulse with the sample volume [58–62], which results in a distortion of the velocity profile shape, especially toward the pipe wall. The deconvolution methods suggested in literature are often not directly applicable because the (depth-dependent) pulse shape inside the fluid is not exactly known. Because of the influence of the pressure field on the details of the shape of the measured velocity profile, the derived rheological properties can be sensitive to ultrasonic parameters such as the transducer type, pulse length, amplifications, and pulse frequency. Therefore, it is often easier to monitor dynamic changes of a system than to measure absolute values.

It is normal not to see an exactly zero velocity at the wall in most velocimetry techniques because of the finite sampling volume mentioned before, although velocity data near the wall are expected to be very close to zero. The measured velocity profile data near the pipe wall thus often appear to violate the no-slip condition and exhibit apparent wall slip. From a phenomenological standpoint the apparent velocity in the sampling volume element that includes the wall can be considered as the apparent slip velocity. In a few studies people have tried to use UVP + PD to determine slip velocity. For example, Dogan et al. [42] investigated diced tomato concentrates and Ouriev [63] investigated highly concentrated disperse suspensions. However, because of the finite size of the sample volume, it is difficult to calculate the exact thickness of this layer and to determine wall slip using UVP + PD.

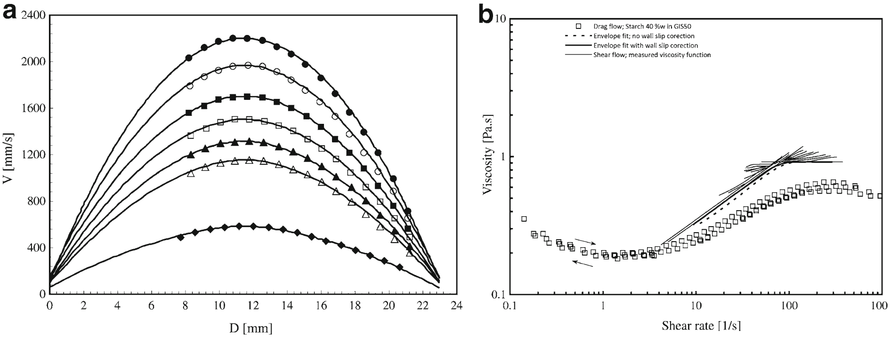

Fig. 5.41 (**a**) Velocity profiles of pressure-driven shear flow experiments (*symbols*) at different volume flow rates of shear-thickening suspension of 40% wt starch in water-diluted 50% wt glucose syrup. *Solid lines*, fitted. (**b**) Shear rate-dependent viscosity determined from pressure-driven shear flow experiments (in-line UVP and shear stress measurements) compared with that measured using drag shear flow off-line rotational rheometer for the aforementioned shear-thickening suspension. (Replotted from the results of Ouriev [41] and Ouriev and Windhab [65])

5.3.1.8 Application Examples

The noninvasive UVP+PD method allows measurements not possible with common rheometers, such as instantaneous radial velocity profiles and yield stress directly in line. Furthermore, it has advantages over commercially available process rheometers and off-line instruments in being noninvasive, applicable to opaque and concentrated suspensions, and having small sensor dimensions and relatively low cost. An overview of the investigations on UVP+PD measurements carried out by several research groups and the potential of the methodology for industrial applications is given below.

The UVP+PD methodology has been successfully applied to a range of model and industrial fluids and suspensions for rheological characterization in line. Some early investigations by Müller et al. [40] and Wunderlich and Brunn [64] focused on simple Newtonian model systems such as glycerine/water solutions and non-Newtonian aqueous polyacrylamide solution, hydroxypropyl guar gum solution [40]. The main objective of the aforementioned studies was to show proof of concept and that the UVP+PD method is a promising new methodology for process monitoring and control.

Shear-Thickening Suspensions

Ouriev [41] and Ouriev and Windhab [65] used the UVP+PD method and investigated shear-thickening model suspensions of 40% wt cornstarch particles in water-diluted 50% wt glucose syrup during steady flow in a 23-mm-diameter pipe. Their measured velocity profiles at different volume flow rates are shown (symbols) in Fig. 5.41a. They fitted the experimental velocity profiles to the non-Newtonian power law model with

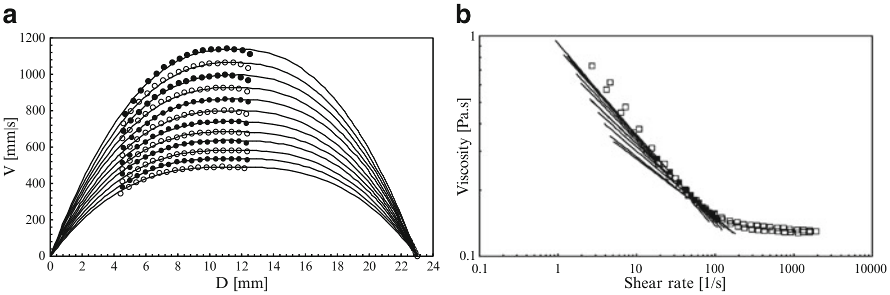

Fig. 5.42 (**a**) Velocity profiles of pressure-driven shear flow experiments at different volume flow rates of shear-thinning suspension of 30% wt of starch in silicon oil AK50. Comparison of average measured (*symbols*) flow velocity profiles V with those fitted by the power law (*solid line*). (**b**) Shear rate-dependent viscosity determined (envelope fit, *closed squares*) from pressure-driven shear flow experiments (in-line UVP and shear stress measurements) compared with that measured using drag shear flow (*open squares*) experiments (off-line laboratory rotational rheometer) for the aforementioned shear-thinning suspension. The *solid line* corresponds to the power law-fitted viscosity function. (Replotted from the results of Ouriev [41] and Ouriev and Windhab [65])

flow index n combined with the slip velocity at the pipe wall (solid lines). In general, $n > 1$ for shear-thickening suspensions. They showed that, as the maximum flow velocity of the velocity profile increased, the flow index n decreased while the wall slip velocity increased. However, the wall slip velocity was found to decrease after the Newtonian flow index $n = 1$ was attained. The variation in viscosity with shear rate computed with the power law model using the velocity profiles and pressure drops (with and without wall slip corrections) is compared (Fig. 5.41b) with that measured using off-line rotational rheometer (drag shear flow). The viscosity decreases as the shear rate increases from about 0.1 to 2 1/s, and then viscosity increases as the shear rate increases until about 300 1/s. Thus, the suspension can be seen to be shear thinning and shear thickening, respectively, in these two shear rate ranges. The radial velocity gradients of velocity profiles increase with increase in volume flow rate and pressure drop, which decreases the power law exponent n. The viscosity predicted by power law model using the in-line UVP+PD method was close enough to that measured using an off-line rheometer over about 3 to 10 1/s shear rate range, while a difference at higher shear rates was observed. The authors proposed that these differences were the result of viscoelastic properties of shear-thickening suspensions.

Shear-Thinning Suspensions

Most industrial fluids exhibit shear-thinning behavior, that is, the viscosity decreases with increasing shear rate. The UVP+PD method has therefore been used in a number of studies for measuring instantaneous velocity profiles and rheological behavior of shear-thinning model and industrial suspensions.

Figure 5.42a shows the experimental velocity profiles for a model of concentrated shear-thinning suspension of 30% cornstarch particles (20 μm average diameter) in silicon oil (AK50) during steady flow at different volume flow rates in a 23-mm-diameter pipe investigated by Ouriev [41] and Ouriev and Windhab [65].

The investigated suspension was Newtonian at low solid fraction, with a power law index *n* equal to 1. The power law index decreased as the solids concentration increased. The velocity profile of shear-thinning suspension was more flattened at the center of the pipe and steeper at the sides at low volume flow rates. The comparison between the shear rate-dependent viscosity results [41, 65] of pressure-driven shear and drag (off-line rheometer) shear flow experiments are shown in Fig. 5.42b. It can be seen that the viscosity decreases as the shear rate increases from about 1 to 100 1/s, thus representing the suspension to be shear thinning. Here the viscosity predicted by the power law model using an in-line UVP velocity profile at higher volume flow rate with the corresponding pressure drop agrees reasonably well with that measured using an off-line rheometer over the same shear rate range.

Other shear-thinning fluids such as viscoelastic surfactant solutions (shampoo and body lotion) have also successfully been characterized in-line during steady laminar flow in a pipe using the UVP + PD method [55, 66].

The shear rate-dependent viscosity predicted by the power law model using the values of the exponent *n* and constant *K* obtained by fitting the velocity profiles agreed well with that measured using an off-line Anton Paar rheometer [55]. A few groups have also studied various shear-thinning slurry suspensions, for example, Powell and Pfund [67] and Kotzé et al. [68].

5.3.2 Transient Rheometry

There are a number of time scales in terms of rheological properties. Some of them take place explicitly in a flow system subject to transient process. In particular, viscoelastic fluid shows a clear oscillatory response to given transient shearing action, departing from non-Newtonian fluid that has only a variation of viscosity. A similar property exists even in the mixture of Newtonian fluids as a result of the action of interface among the phases. Because UVP can measure the velocity profile in space–time two dimensions, it is a feasible tool for the quantitative evaluation of such rheological properties [45, 46, 56, 69]. Here we explain two kinds of transient flow configurations by which UVP works suitably as rheometry.

5.3.2.1 Spinning Flow Rheometry

Measurement of flow inside a rotating container was explained in Sect. 4.1. In the case of an impulsive start of the rotation from the stationary state, the unsteady process of inward momentum transfer from the container wall can be measured by UVP [70]. Analyzing the unsteady response, we can extract the rate of momentum diffusion, that is, the shear stress. Once shear stress is measured, viscosity is given

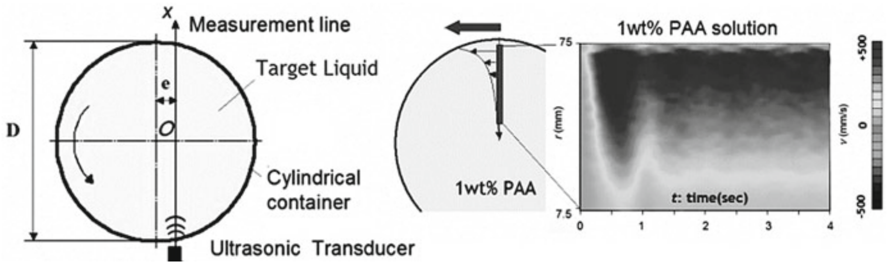

Fig. 5.43 Spinning flow measurement and its sample data. *PAA*, polyacrylamide

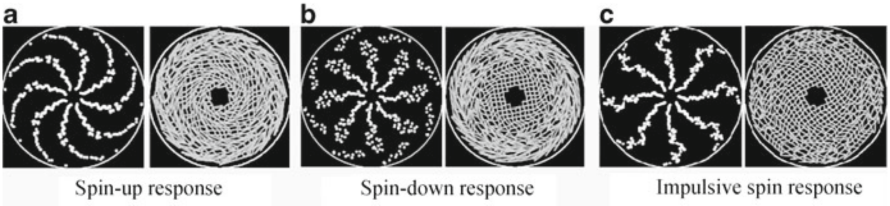

Spin-up response Spin-down response Impulsive spin response

Fig. 5.44 Visualization of fluid distortion by time integration of velocity profiles. (**a**) Spin-up response. (**b**) Spin-down response. (**c**) Impulsive response

in the case of Newtonian fluid. For a non-Newtonian fluid, unknown constants in the shear stress model can be estimated.

Figure 5.43 shows the UVP measurement line for a rotating circular container. With this configuration, there is no pressure gradient in the azimuthal direction, and therefore angular momentum conservation is evaluated only from the velocity without information of pressure. The measurement example shown is the flow of a viscoelastic liquid that is a 1% aqueous solution of polyacrylamide (PAA). The flow driven by the cylindrical wall propagates to the central part and then returns in several cycles of oscillatory behavior. The final state has rigid rotation that matches the rotation of the rotating container. Rheological properties of the PAA solution are quantified from the initial momentum transfer until the rigid rotation.

Figure 5.44 depicts the distribution of the fluid distortion, which is visualized by time integration of the azimuthal velocity. Here the velocity vector field is computed by the method mentioned in Sect.4.2.3. Figure 5.44a shows the spin-up response, which is unsteady distortion caused by a sudden start of rotation from a stationary state. Figure 5.44b is the spin-down response, which is flow caused by the rapid stopping of the rotating container from a rigidly rotating state. Figure 5.44c is the impulse response, which is given by a 45° displacement of the cylinder in a very short time starting from the stationary state. In all cases, the fluid inside the core of the cylinder is hardly distorted owing to elastic recovery of the shear displacement. UVP is a good tool to visualize fluid distortion as in the sample shown here.

PAA solution, which is targeted here, is a viscoelastic fluid, and its shear stress is modeled as

$$\tau = E\gamma = E\int \frac{\partial \gamma}{\partial t}dt = E\int \left(\frac{\partial v}{\partial r} - \frac{v}{r}\right)dt \quad (\tau < \tau_{\mathrm{y}}), \tag{5.12}$$

$$\tau = K\left(\frac{\partial v}{\partial r} - \frac{v}{r}\right)^{n} + \tau_{\mathrm{y}} \quad (\tau \geq \tau_{\mathrm{y}}), \tag{5.13}$$

where τ_{y} is the yield stress, E is the elastic modulus, γ is the shear strain, v is the azimuthal velocity, r is the radial distance from the rotating axis, t is time, K is the viscous strength (different from the viscosity itself), and n is the viscous index. This kind of stress model for viscoelastic fluid is called the Hershel–Bulkley model. Below the yield stress, fluid deforms elastically, and beyond the yield stress, the stress distribution becomes a function of the shear rate. Through UVP, several parameters in the model can be determined as explained below.

In spinning flow, the momentum conservation equation in the azimuthal direction is described using the shear stress, τ, as

$$\rho\left(\frac{\partial v}{\partial t} + u\frac{\partial v}{\partial r} + \frac{uv}{r} + v\frac{\partial v}{r\partial \theta}\right) = \frac{1}{r^2}\frac{\partial}{\partial r}(r^2\tau) \rightarrow \rho\frac{\partial v}{\partial t} - \frac{1}{r^2}\frac{\partial}{\partial r}(r^2\tau) = 0, \tag{5.14}$$

where u is the flow velocity in the radial direction and is sufficiently small to neglect in the simplified equation shown on the right side. UVP obtains the velocity profile information of $v(r,t)$, and the only unknown variable in Eq. (5.15) is τ. Thus, the shear stress distribution $\tau(r,t)$ can be calculated from the differential equation using the integral formula:

$$\tau = \frac{\rho}{r^2}\int_0^r \frac{\partial v}{\partial t}r^2 dr = \rho\left[\int_0^r \frac{\partial v}{\partial t}dr - \frac{2}{r^2}\int_0^r \frac{\partial v}{\partial t}rdr\right]. \tag{5.15}$$

In this equation, the density variation in the radial direction is assumed negligible. By substituting the distribution of τ into the left-hand side of Eqs. (5.12) and (5.13), the values of E, K, n, and τ_{y} are estimated. Originally, these values are obtained independently for all the coordinates of the spatiotemporal two-dimensional domain, and the best estimates of the four properties must be determined among them. The least-squares approach is one of the available options to obtain the best estimates. The approach considers the best estimates to have the least value of a cost function regarding the error of the momentum conservation equation, i.e., Eq. (5.14). The cost function has the following form parameterized by four properties, time, t, and space, s:

$$g(K,E,n,\tau_{\mathrm{y}};t,s) = \left[\rho\frac{\partial v}{\partial t} - \frac{1}{r^2}\frac{\partial}{\partial r}(r^2\tau)\right]^2. \tag{5.16}$$

Applying this formula for all data in the spatiotemporal domain, the integral value, G, is defined as

Fig. 5.45 Shear-thinning characteristics of PAA solution measured by UVP

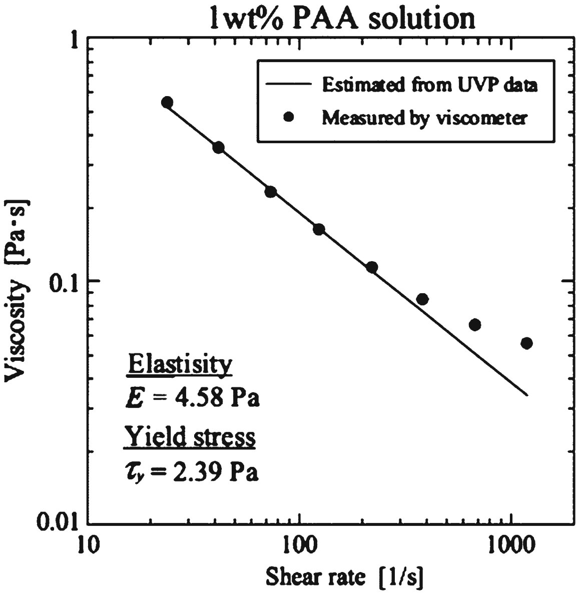

$$G(K,E,n,\tau_y) = \iint g(K,E,n,\tau_y;t,s)dtds \rightarrow \min. \tag{5.17}$$

The best estimates of the four parameters are found when the function *G* takes a minimum value. Computing all the distribution of *G* in four-parameter space may be too costly to implement, and hence suitable acceleration algorithms are recommended to find the best estimates more quickly; for example, the Newton–Raphson iterative scheme, random-searching scheme, genetic algorithm, and other recursive schemes.

Figure 5.45 presents measurement data of the viscosity of the PAA solution, which are obtained employing the aforementioned method [71]. The solid circles are the viscosity separately measured with a rotary rheometer, and a single line in the figure is the viscosity measured by UVP. The line expresses the values of *K* and *n*, simultaneously, and with the data the known feature of the PAA solution, which is a shear-thinning characteristic, was confirmed quantitatively. The yield stress and elastic modulus are also obtained. The point is that only a single run of the spinning measurement allows the four parameters to be measured because the single dataset of the spatiotemporal velocity distribution includes both high and low regions of shear rate. Moreover, the suitability of the rheological model can be assessed with the value of *G*, which is expected to be small when the suitability is high. Discrepancy of the data at a shear rate higher than 200 s^{-1} in the figure is the result of the mismatch of the rheological model that is introduced in the analysis.

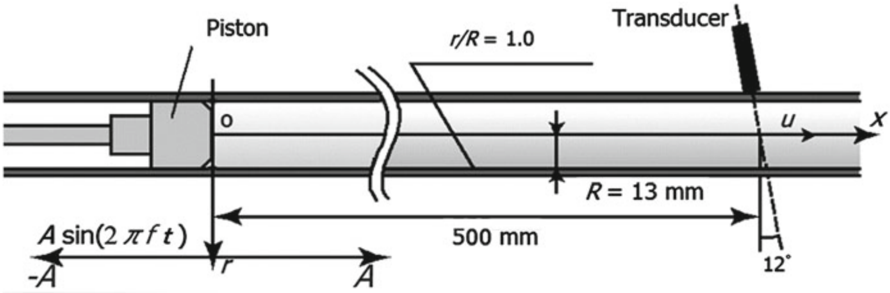

Fig. 5.46 Velocity profiling of an oscillatory pipe flow driven by a piston

5.3.2.2 Oscillating Pipe Flow Rheometry

The flow pattern in a pipe can be described with a single dimensionless parameter, that is, Reynolds number. Laminar pipe flow has a parabolic velocity profile inside, and turbulent pipe flow is approximated by exponential laws. When the volume flow rate of the pipe flow is subject to oscillation, the internal flow has complex structure including a phase lag in the velocity fluctuation between two radial coordinates. It is known that there is an annular leading effect for such oscillatory pipe flow, which has a phase advance near the pipe wall, and phase delay in the core region. UVP technique can be applied to study this one-velocity-component time-dependent flow phenomenon, that is, a spatiotemporal two-dimensional flow. Non-Newtonian fluids exhibit many different responses in the velocity distribution, and UVP can thus be used to study the rheological properties of non-Newtonian fluids in oscillatory pipe flow. In addition, a change in the oscillation frequency expands the range of rheometrical investigations in particular for fluids that have multiple elements in the relaxation time. Driving of the flow using a piston, which gives a fixed displacement to the internal fluid, helps with two-parameter control so that complex rheological fluids can be investigated effectively.

Figure 5.46 is a schematic diagram of the oscillatory pipe flow device. The measurement line of UVP is set sufficiently far from the piston head so that the secondary flow effect does not remain along the measurement line.

Figure 5.47 presents three examples of a spatiotemporal two-dimensional velocity distribution in a single cycle of the oscillation. The ordinate is the spatial coordinate of the pipe diameter. In the case of water (Fig. 5.47a), the velocity profile at any instant is parabolic. Figure. 5.47b shows the response of dilute PAA solution, which has a delay in the core region of the pipe. Figure 5.47c is the response of a deeply concentrated solution, which has a double layer of oscillatory flow [72].

Figure 5.48 is the radial distribution of the phase shift determined from the velocity data. The ordinates of (a) and (b) in the figure are the phase shift from the piston motion, and positive and negative values indicate advances and delays of the response. In the case of water (a), a large phase shift is found near the pipe wall,

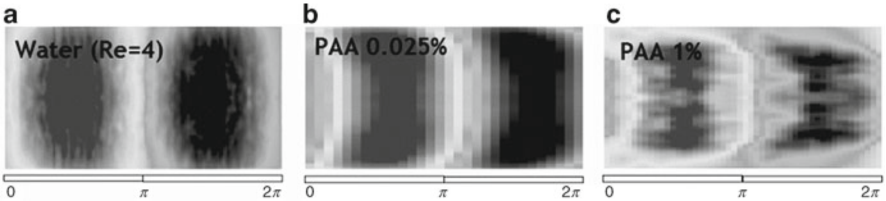

Fig. 5.47 Comparison of velocity profiles in a single cycle of oscillation. (**a**) water (Re = 4). (**b**) 0.025 wt% PAA solution. (**c**) 1 wt% PAA solution

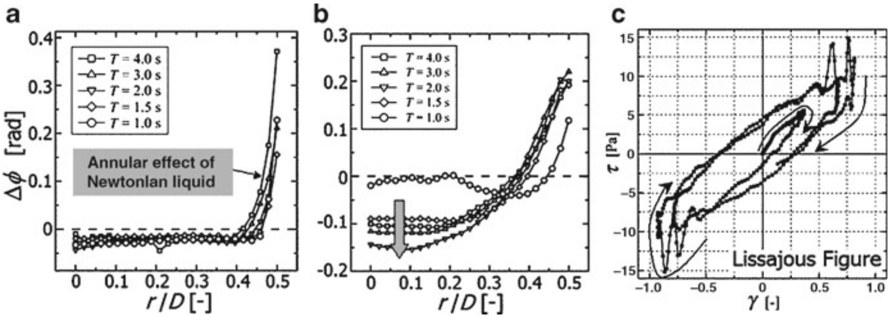

Fig. 5.48 Phase shift of the velocity response in oscillatory pipe flow for (**a**) Water. (**b**) PAA solution. (**c**) Shear rate - stress curves for PAA solution

which is explained by the annular leading effect of Newtonian fluid as mentioned previously. In the case of PAA solution (b), the annular effect expands widely but weakens. The dynamic characteristics of the shear rate–stress relationship are shown in (c) for a single location. Although there is perfect linearity between the shear rate and stress for Newtonian fluid, the PAA solution becomes nonlinear and has hysteresis shown by a closed curve.

To summarize, the UVP technique can be used to study the rheological properties of the two kinds of flow configurations described here: spinning flow and oscillation pipe. However, there are, of course, other types of configuration for which the suggested UVP technique can be used for in-line rheometry. For instance, a vibrating sphere in a target fluid can be used to estimate stress tensor components, and regularly arranged vortices such as Karman and Taylor vortices are suitable flow fields to be assessed by UVP. A common feature in these examples is that the momentum transfer is effectively evaluated as a temporal change in the spatial velocity distribution, which makes the rheological investigation more logical than the use of conventional rheometers that only sense integrated physical quantities, such as torque, drag, and the pressure difference. Additionally, very often the target fluids that have unknown properties are opaque; therefore, the advance of UVP is clearly promising when practical applications are considered.

5.4 Rheological Characterization

5.4.1 Concentrated Polydisperse Suspensions

The UVP + PD methodology has also been successfully applied to a range of industrial fluids and suspensions, including fluids containing large particles and fibers, for example, mineral slurries and several kinds of foods [42–44, 47, 51, 55, 56, 68, 73, 74]. Investigated industrial suspensions differed in continuous phase, solids concentration, and particle shapes and sizes. Soft and hard particles with size distributions from submicrometer to micrometer to large solid pieces up to 3–4 cm in length were used. Examples are aggregating clay particles, spherical glass beads, rod-like pulp and fruit fibers, kidney-shaped seeds, and odd-shaped herb, fish, and vegetable pieces. In addition, the investigated industrial suspensions differed significantly in flow behavior from strictly Newtonian to highly shear thinning. A summary of some of the fluid systems investigated using the UVP + PD method is presented in Table 5.1.

5.4.2 Fiber Suspensions and Yield Stress Measurements

The UVP technique and the UVP + PD rheometric method are of special interest for the paper pulp industry. Pulp suspensions are opaque, non-Newtonian fluids containing regions of relatively high fiber concentration that tend to form a continuous rigid fiber network structure throughout the suspension above a certain critical consistency. This rigid fiber network extends across the pipe diameter at very low flow velocities and can be considered as a plug that moves at a constant velocity. As the flow rate increases, the fiber network plug begins to break up from its outer surface to form a mixed flow regime with a water and fiber annulus surrounding the rigid fiber plug in the center of the pipe. The stress required for breakup is frequently called disruptive shear stress or yield stress. Both UVP and the UVP + PD method have been used for noninvasive velocity profiles measurements, as well as rheological in-line characterization, in pulp suspensions at high concentrations up to 7.8% (w/w) [55, 73]. An example of velocity profiles measured in pulp suspensions is shown in Fig. 5.49. Simultaneous UVP and laser Doppler anemometry (LDA) measurements in an experimental pipe flow loop showed that LDA works with limited penetration depth to a few millimeters, whereas the UVP technique had a sustained penetration depth throughout the pipe diameter and that combined with simultaneous pressure drop measurements, the UVP + PD method can be used to determine rheological properties of pulp suspensions [73]. It was further shown the yield stress can be measured in line by determining the plug radii. Recently, the UVP + PD method was shown to be a new powerful tool for noninvasive visualization, especially in the near-wall gradient layer of fiber suspensions [45] and for studying an axial cellulose fiber jet. The UVP + PD method has also been used to determine

Table 5.1 Summary of some fluid systems investigated using the UVP + PD method

Investigated systems	Particle shape	Particle distribution	$C_{\max}$ % (w/w)	Particle sizes
Dairy products	~Spherical	–	~8	1–6 µm
Glycerol + glass beads	Spherical	Monodisperse	~5	4–15 µm
Polymeric solutions	–	–	–	–
(Xanthan, PEG etc.)	–	–	–	100 nm–80 µm
Mineral slurries	Agglomerates	Polydisperse	~20	11–90 µm
Rapeseed oil + PA12 particles	Spherical	Monodisperse	–	–
Bimodal	~25	30–300 µm	–	–
Syrup + starch particles	~Spherical	Polydisperse	~30	~1 mm
Tomato sauce	Fibers	~Monodisperse	~30	1–1.2 mm
Strawberry yogurt	Seeds, kidney shaped	Monodisperse	~8	0.2–2 mm
Marmalade, fruit soup	Fibers	Polydisperse	35	0.2–5 mm
Fruit jams	Fibers, mixture	Polydisperse	35	~1–4 mm
Pasta sauce	Fibers, mixture	Polydisperse	–	2–2.4 mm
Cellulose pulp	Fibers	~Monodisperse	~8	0.5–1 cm
Cheese sauce + carrot cubes	Cubic	~Monodisperse	<1	Up to 2–3 cm

Source: Reprinted from Wiklund and Stading [56]

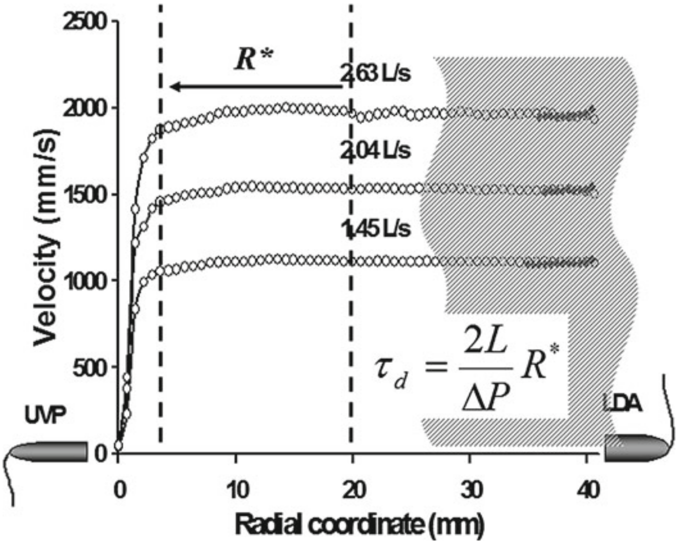

Fig. 5.49 Velocity profiles measured using UVP (*open circles*) and LDA (*diamonds*). The disruptive shear stress (yield stress) can be determined directly in line from the plug radius using the pressure drop measured over the distance *L*. (Replotted from the results of Wiklund and Stading [73])

yield stress in other suspensions, such as tomato concentrates and starch gels [42, 75] and concentrated cornstarch model suspensions by Ouriev [41] and Ouriev and Windhab [65].

5.5 Magnetic Fluids

5.5.1 Introduction

Magnetic fluid [76] is a stable colloidal dispersion of small surfactant-coated ferromagnetic particles in a liquid carrier, such as water or kerosene. These magnetic particles are about 10 nm in size. The preparation of a stable magnetic fluid involves a delicate balance between the attractive and repulsive forces on each particle. Therefore, the magnetic particles are in Brownian motion and magnetic fluid can be treated as a Newtonian fluid under no magnetic field. However, once a magnetic field is applied to a magnetic fluid, several interesting flow phenomena, which are not seen in a Newtonian fluid, can be observed [77] because of the combination of strong magnetism and liquidity. For instance, when the magnetic field is applied to magnetic fluid, apparent viscosity of the magnetic fluid increases in the region where the magnetic field exists. As a result of the change of the apparent viscosity, the velocity field typically changes [78]. Applying these unique characteristics of magnetic fluids, many applications of magnetic fluid have been developed in the mechanical engineering and biomedical engineering fields. Moreover, the thermophysical properties of magnetic fluid have also attracted attention [79, 80] and have been applied to many technologies in the thermal engineering field, because magnetic fluid has also interesting thermophysical properties such as temperature-dependent magnetization and good heat conductivity.

In mechanical engineering, magnetic fluid is applied as a working medium in dampers [81], audio speakers [82], and so on. One of the most successful applications of magnetic fluid is in audio speakers, in which magnetic fluid is filled around the voice coil. As the magnetic fluid provides the centering and sealing effects, productivity of the audio speakers increases, and air modulation noise in the gap can be eliminated. In addition, because thermal conductivity of a magnetic fluid is much greater than that of air, the magnetic fluid provides a lower heat resistance between the coil and pole plate. As a result, the operating temperature of the voice coil can be reduced.

Magnetic fluid is also used in many biomedical applications such as contrast enhancement for magnetic resonance imaging [83], drug delivery [84], and magnetic fluid hyperthermia [85, 86]. Particularly, magnetic fluid hyperthermia has attracted great attention. When an alternating current magnetic field is applied to magnetic nanoparticles, these particles generate heat. This thermophysical property of magnetic fluid allows heating up a specific point of a human body, such as a tumor that has been dosed with magnetic fluid, without affecting the surrounding parts of the body.

To better understand these characteristic flow behaviors of the magnetic fluid, it is necessary to measure the internal velocity fields. However, because magnetic fluid is opaque, optical methods such as laser Doppler velocimetry (LDV) and particle image velocimetry (PIV) cannot be applied to measuring the velocity fields. Against these optical methods, the UVP method is suitable for measuring the velocity profile of magnetic fluid, and many difficult measurements of the unique magnetic fluid flow have been carried out in the past two decades [87–89]. In this section, practical measurements of the oscillating flow and the Taylor vortex flow of a magnetic fluid [87] are introduced.

5.5.2 *Influence of Magnetic Field on Sound Velocity in Magnetic Fluid*

Sound velocity in the measuring liquid is an important parameter for UVP measurement. However, the magnetic field influences the sound velocity in a magnetic fluid [90]. When the magnetic field is applied to a magnetic fluid, the inner particles in the magnetic fluid coagulate and form a chainlike cluster [91]. These coagulation and chainlike structures in the magnetic fluid influence sound velocity in the magnetic fluid. Therefore, before UVP measurement of magnetic

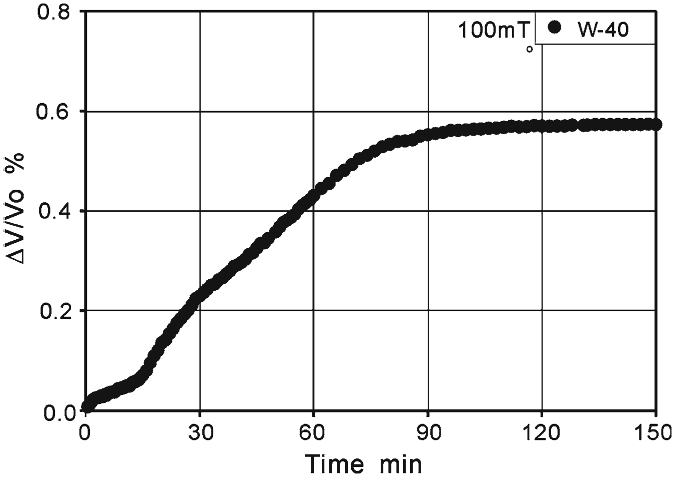

Fig. 5.50 Influence of magnetic field on sound velocity in a magnetic fluid

fluid flow, it is necessary to investigate the influence of the magnetic field on sound velocity in the magnetic fluid.

Figure 5.50 shows the time-series change of sound velocity in the water-based magnetic fluid W-40 (produced by Taiho Industrial Co.) applying a magnetic field. The change of sound velocity in the magnetic fluid was evaluated by $\Delta V/V_0$. Here, ΔV is defined by $\Delta V = V - V_0$, where V and V_0 are sound velocities with and without an external magnetic field, respectively. In this experiment, the magnetic field intensity was kept at 100 mT. When the magnetic field is applied to the test magnetic fluid, sound velocity increases with elapsed time of magnetic field application. This change seems to be caused by growth of the chainlike clusters. However, because the change of sound velocity is rather small, this change does not influence the UVP measurements. In contrast, the temperature of a magnetic fluid also has a strong influence on sound velocity in the fluid compared to the influence of the magnetic field. Therefore, it is important to control the temperature of the magnetic fluid at a constant during UVP measurement.

5.5.3 Velocity Profile Measurement of Oscillating Flow of a Magnetic Fluid

Figure 5.51 shows a schematic diagram of the experimental apparatus for oscillating flow. The test section is made of a transparent acrylic pipe having inner diameter (R) 30 mm, outer diameter 40 mm, and length 3,000 mm. One end of the pipe is connected to the tank (300 mm × 300 mm × 300 mm), which is located at 540 mm height from the center of the pipe. The other end of the pipe is connected to the

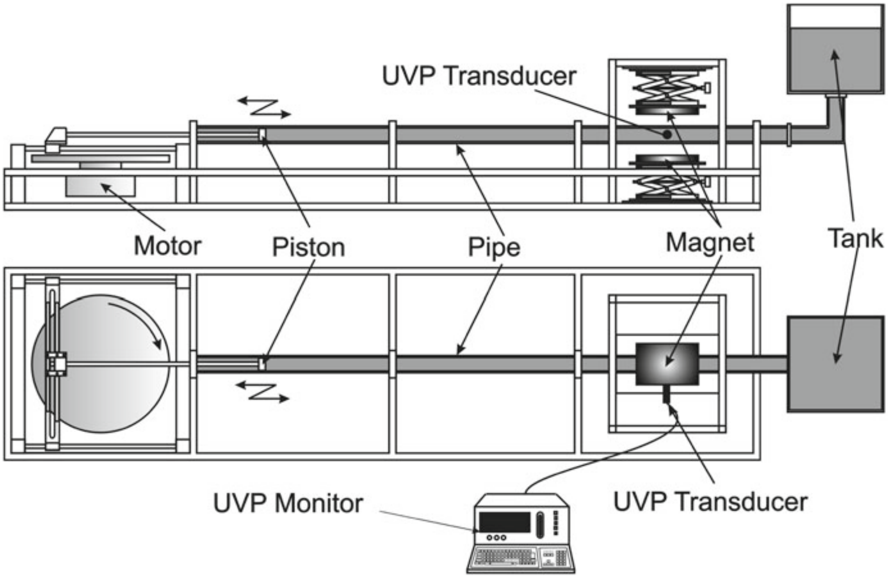

Fig. 5.51 Experimental apparatus of oscillating flow measurement

Fig. 5.52 Position of UVP transducer

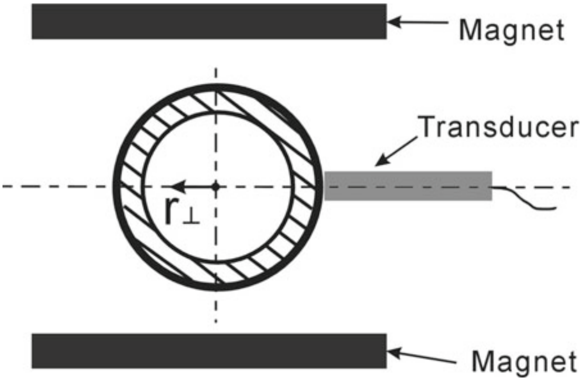

piston. Oscillating flow is generated by the oscillating piston, which is driven by a crank system. Piston frequency can be controlled by the inverter. Two permanent magnets (150 mm × 100 mm × 25 mm) are placed on both sides of the pipe (Fig. 5.52), and the magnetic field intensity can be controlled over a range from 20 mT to 110 mT by changing the interval of the two magnets.

The UVP transducer is fixed on the outer wall of the pipe with an angle of 14° at the measurement position where the magnetic field exists. The measurement line is parallel to the two magnets, and radial direction along the ultrasonic beam is defined as $r_\perp$ (Fig. 5.52). In this experimental system, there are some problems for UVP measurement. Because the test section is made of a transparent acrylic pipe and the transducer is placed on the outside, this experimental setup leads to distorted velocity profiles. In addition, it is possibility that non-zero velocity would be obtained at the wall because of convolution of the ultrasound pulse with distance when propagation is through a solid wall material. This problem can be corrected by using a complex deconvolution procedure.

The UVP monitor used in this measurement is a model XW-PSi (produced by Met-Flow). The ultrasonic frequency of the transducer is 4 MHz. The flow is seeded by porous SiO_2 particles 0.9 μm in mean diameter (product name, MSF-10 M; Liquidgas Co.). A water-based magnetic fluid W-40 (Taiho Industrial) is used as a test fluid. The kinematic viscosity is $\nu = 4.35$ mm^2/s, and the sound velocity in the magnetic fluid is $c = 1{,}420$ m/s at 20°C.

In this experiment, the piston frequency is kept at 0.053 Hz and Wormersley number is $W = 4.2$, which is defined by

$$W = R\sqrt{\frac{\omega}{\nu}}, \tag{5.18}$$

where R is radius of the pipe and ω is angular velocity of the piston. The Wormersley (W) number is an important dimensionless parameter for an oscillating flow and indicates the ratio of unsteady inertia and viscosity forces.

Oscillating flow is one of the typical unsteady flows. In addition, in the case of magnetic fluid flow, the velocity profile of the magnetic fluid flow changes with pre-application time of the magnetic field before generation of the oscillating flow and with elapsed time of applying magnetic field. Therefore, UVP measurement is performed considering this elapsed time change. Figure 5.53 shows the timing chart of the oscillation of the piston. Measurement starts when the piston first achieves the center position between top and bottom, dead center of the crank. This position is defined as the base phase $\varphi = 0$. UVP measurements of the velocity profile under magnetic field are begun after pre-application of magnetic field. Because the magnetic field is applied parallel to the pipe for T_a minutes before measurements, the chainlike cluster is formed in the direction of the magnetic field line. After T_a minutes, oscillating flow is generated by the piston, and measurement starts from the first cycle with synchronizing with the piston cycle.

Figure 5.54 shows the velocity profile of the oscillating flow of the magnetic fluid under no magnetic field. Ensemble averaged velocity profiles were calculated by 30 cycles of measuring data at the same phase. In this figure, normalized velocity v^* and normalized radius r^* are defined by the following equations:

$$v^* = \frac{v}{R_k\omega}, \quad r^* = \frac{r_\perp}{R} \tag{5.19}$$

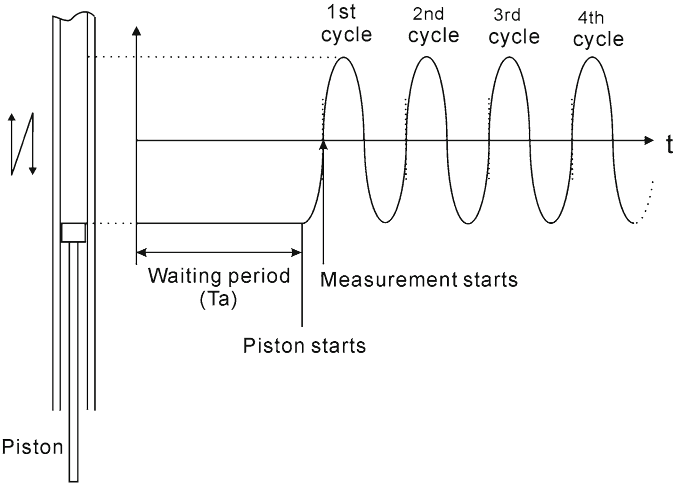

Fig. 5.53 Timing characteristics of velocity profile measurement

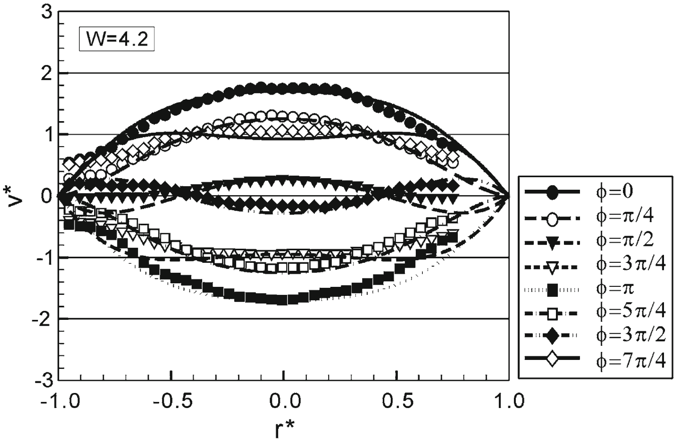

Fig. 5.54 Velocity profiles of oscillating flow of magnetic fluid under no magnetic field ($W = 4.2$)

where R_k is radius of a crank and $R_k = 100$ mm, ϕ corresponds to the phase difference from the middle point of top and bottom dead points, and $r^* = -1$ and 1 indicate the side wall where the transducer is fixed and the opposite side wall, respectively. A solid line is the theoretical velocity profile of a Newtonian fluid in a laminar oscillating pipe flow. Because magnetic fluid can be treated as a Newtonian fluid under no magnetic field, the measured velocity profiles of the magnetic fluid flow have good agreement with the theoretical velocity profiles of a Newtonian fluid flow. The annular effect [92], which is the characteristic reversed-flow phenomenon in the center region of the pipe in the oscillating flow of the Newtonian fluid, can be obtained in magnetic fluid flow. In addition, this annular effect becomes more typical under the oscillating flow of larger Wormersley number.

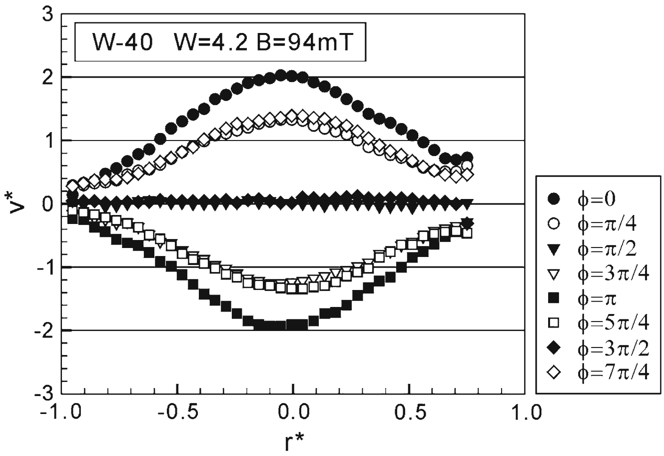

Fig. 5.55 Velocity profiles of oscillating flow of magnetic fluid under magnetic field ($W=4.2$, 94 mT, $T_a=0$)

Figure 5.55 shows the velocity profile of the oscillating flow of the magnetic fluid under a magnetic field. The magnetic field intensity is 94 mT. In this experiment, a magnetic field is applied to the magnetic fluid flow with $T_a=0$. This figure indicates that the annular effect disappears when applying the magnetic field. When the magnetic field is applied to a magnetic fluid, it is well known that the apparent viscosity increases with increasing magnetic field. As a result of the increase of apparent viscosity, the annular effect disappears.

Finally, Fig. 5.56 shows the velocity profiles at the same conditions as Fig. 5.55, but a magnetic field is pre-applied to the fluid for 90 min ($T_a=90$) before the measurement. In this measurement, the velocity profile changes with elapsed time from the start of the oscillating flow. Therefore, the velocity profile obtained from the measuring data of the only second cycle is presented in this figure. We confirmed that this velocity profile became the ordinary velocity profile shown in Fig. 5.55 after several cycles. In this measurement, remarkable changes of the velocity profiles related with the chainlike cluster formation are observed, which cannot be explained by the increase of the apparent viscosity owing to the magnetic field. The chainlike clusters are grown toward the center area of the pipe by the pre-application of the magnetic field, and these clustering structures prevent flowing. However, these clusters collapse gradually after the beginning of an oscillating flow.

5.5.4 *Velocity Profile Measurement of Taylor Vortex Flow of a Magnetic Fluid*

Figure 5.57 shows the experimental apparatus with a sketch of the flow pattern that is called Taylor vortex flow (see Sect. 5.1.1). The test section consists of concentric cylinders made of Plexiglas to permit more than 90% transmissivity of ultrasound

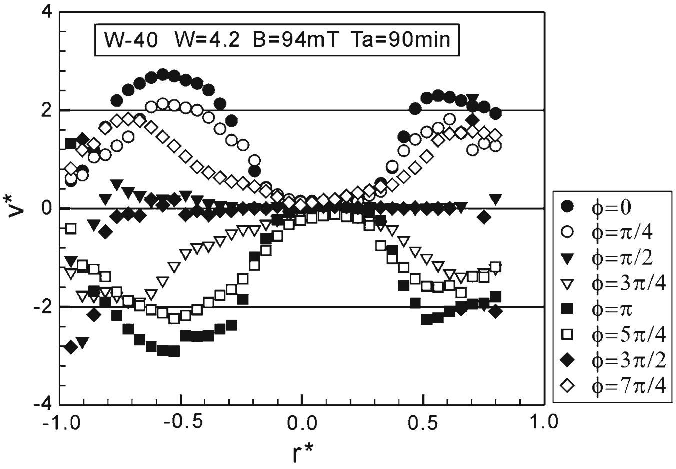

Fig. 5.56 Velocity profiles of the oscillating flow of the magnetic fluid under magnetic field (W=4.2, 94 mT, T_a=90 min)

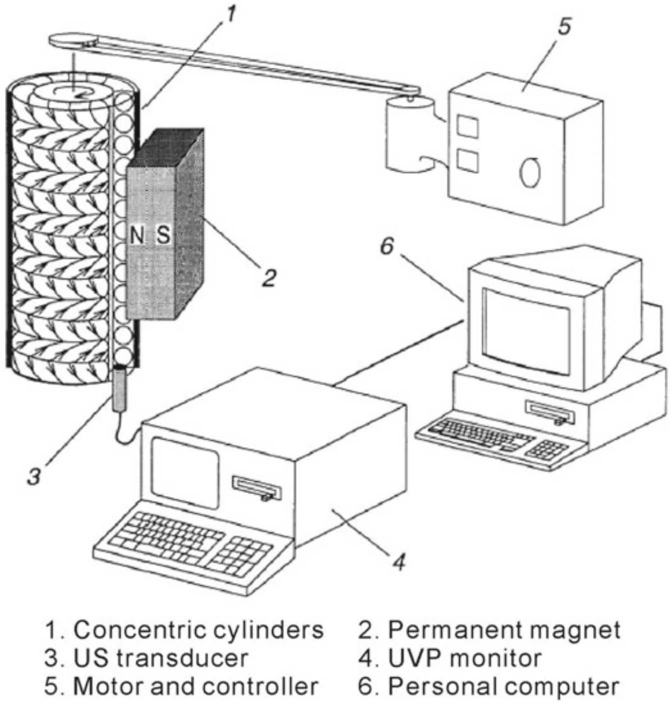

Fig. 5.57 Experimental apparatus of Taylor vortex flow of a magnetic fluid [86] (with kind permission from Springer Science+Business Media)

between the magnetic fluid and wall material. The inner cylinder was rotated by a belt connected to a variable speed electric motor. The motor permits the angular velocity Ω to be varied continuously for a rotating frequency f ranging from 0.5 to 10 Hz. The outer cylinder was stationary, which enabled us to make measurements at various angular positions. The length of the cylinder was $L=160$ mm. The radius of the inner cylinder was $R_{\mathrm{i}}=15$ mm and that of the outer cylinder $R_{\mathrm{o}}=23$ mm, giving a gap of $d=R_{\mathrm{o}}-R_{\mathrm{i}}=8$ mm, an aspect ratio of $L/d=20$, and a radius ratio $\eta=R_{\mathrm{i}}/R_{\mathrm{o}}=0.65$. The working fluid was magnetic fluid W-40 (Taiho Industries), a water-based magnetic fluid, which has a 40% weight concentration of magnetite (Fe_3O_4) particles, a kinematic viscosity 15.4 mm^2/s, and a density $\rho=1.35\times10^3$ $\mathrm{kg/m}^3$ at 25°C. The Reynolds number is given by $Re=\Omega R_i d/\nu$ and a reduced Reynolds number $Re^*=Re/Re_{\mathrm{c}}$. The critical Reynolds number Re_{c} at which Taylor vortices first appear in an infinitely long cylinder depends only on the radius ratio [93], and for $\eta=0.65$ this is $Re_{\mathrm{c}}=75$.

The measuring system used for velocity measurements was UVP (MetFlow; Model X1-PS) with a personal computer for data analysis. In the present investigation, the ultrasound transducer was located at the outer wall of one of the end plates, and axial velocity components were measured along the inner rotating wall of the gap. An ultrasound beam about 5 mm in diameter was emitted, and a measuring volume resulted with a cross section of the major axis of 5 mm × 0.705 mm, resembling a thin disk shape. The ultrasound transducer was operated with a basic frequency of 4 MHz, pulse repetition frequency 3,906 Hz, velocity resolution $\Delta v=2.69$ mm/s, and time resolution $\Delta T=37$ ms. The sound velocity in the magnetic fluid is $c=1{,}420$ m/s.

A nonuniform magnetic field was applied perpendicularly to the cylinder axis using a 70 mm × 70 mm × 45 mm permanent magnet positioned outside the cylinders. The location of the magnet was 20 mm from the end plate of the cylinder (Fig. 5.57), which was determined by considering the end effect on the Taylor vortex flow and the measurable length. The typical magnetic field distribution ($B_0=79$ mT) around the cylinder is shown in Fig. 5.58a; the location of the transducer for measurements is shown in Fig. 5.58b. Three different intensities of magnetic fields were applied using a permanent magnet by changing the distance l between the cylinders and the magnet. Figure 5.59 shows the distributions of the magnetic field induction at the mid-height of the column ($z=0$ line in Fig. 5.58a). The horizontal axis is the radial coordinate in the gap normalized by the diameter of the outer cylinder and starting from the outer wall. The characteristic magnetic induction is defined at the $(y, z)=(0, 0)$ point and was $B_0=36$, 57, and 79 mT. The magnetic intensity decreases with distance.

In the absence of a magnetic field, the flow is axisymmetric, and therefore it was only necessary to measure at one angular position. With the magnetic field using the present magnet, however, it was found that there was an angular dependence of the velocity. Therefore, velocity profiles were measured at eight angular positions around the system (Fig. 5.58b) with 45° interval. The angular position is measured from point A (in Fig. 5.58b) that is closest to the permanent magnet and increases in the direction of rotation.

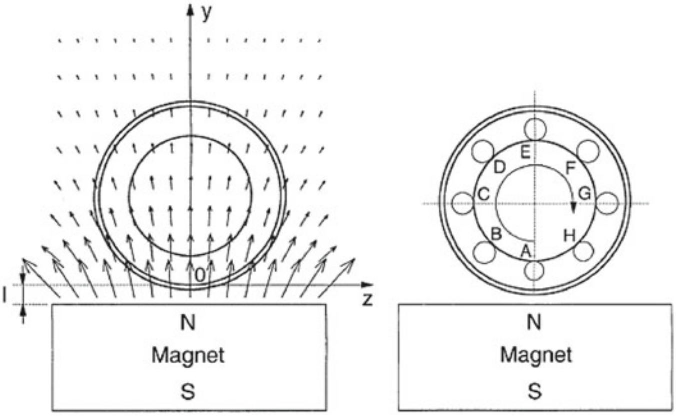

Fig. 5.58 (**a**) Measured magnetic field. (**b**) Measuring position for axial velocity distribution [86] (with kind permission from Springer Science+Business Media)

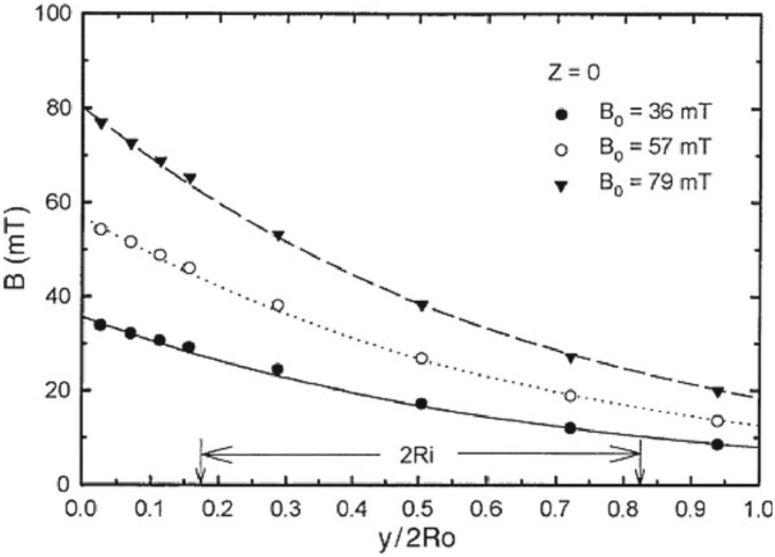

Fig. 5.59 Magnetic field distribution across the diameter of the cylinders [86] (with kind permission from Springer Science+Business Media)

The velocity profile was obtained by placing the ultrasound transducer on the outer wall of the end plate at the inner wall position (Fig. 5.60). For the range of Reynolds number ($Re = 100–160$) studied here, there was no temporal change in the axial velocity component. We therefore first calculated a time average of 1,024 profiles. Typical time-averaged velocity profiles covering the interior four pairs of Taylor cells for various strengths of magnetic field at $R^* = 1.72$ are shown in Fig. 5.60 together with an illustration of streamline patterns within Taylor cells. The distance between two centers of adjacent Taylor cells is not constant, but they form a pair;

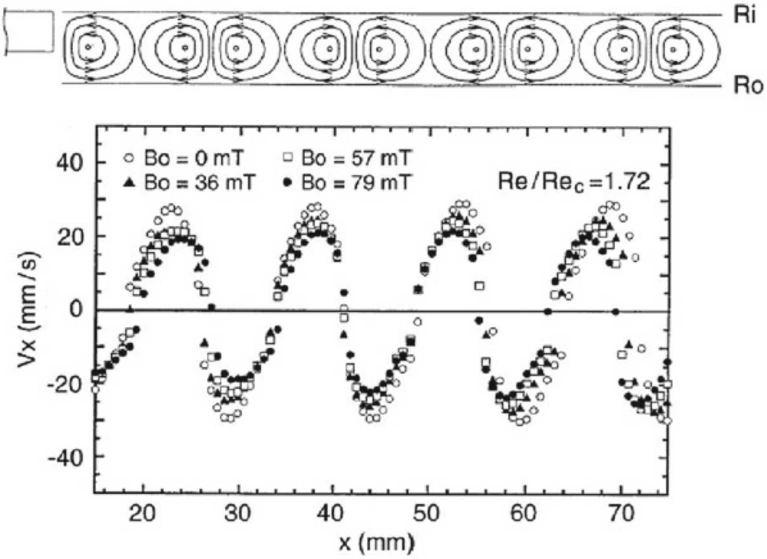

Fig. 5.60 Time-averaged velocity profile [86] (with kind permission from Springer Science+Business Media)

these pairs are periodically structured. Escudier et al. [93] investigated the axial and tangential velocity by applying a laser Doppler anemometer to the Taylor vortex flow and constructed streamline plots of the radial–axial flow field. They showed the same pattern in the axial velocity distribution and flow field. In addition, this figure shows that the velocity level decreases with increasing magnetic field intensity.

To investigate the deformation of Taylor cells and the effect of the magnetic field on the flow structure quantitatively, we calculated the averaged velocity profile, estimating the amplitude from the velocity values of the peak and valley defined as $A = V_{\text{peak}} - V_{\text{valley}}$. The square of the intensity $|A|^2$ is plotted against Reynolds number in Fig. 5.61. It shows a linear increase for $Re < 150$, and the intercept of the line on the abscissa is the estimated critical value Re_c. For the zero field case in Fig. 5.61, Re_c was estimated to be 75, which is in good agreement with the analytical value for the present radius ratio of 0.65. It seems reasonable to consider that the magnetic fluid is Newtonian unless a magnetic field is applied.

The same analysis was made for various intensities of magnetic field (Fig. 5.62). In all cases, the change in $|A|^2$ is linear for $Re < 150$. However, the line shifts to the higher Re side when the magnetic field increases. According to this shift, Re_c becomes larger. In Fig. 5.63, the critical Reynolds number is plotted versus intensity of the magnetic field. This change might be caused by delay of onset of the instability or by a change of apparent viscosity from the applied magnetic field. Considering that the slope of the variation of $|A|^2$ in Fig. 5.62 is more or less the same in all cases, it is very unlikely that the magnetic field directly affects the onset of instability. It is thought to be more reasonable that the apparent viscosity changes by the magnetic field.

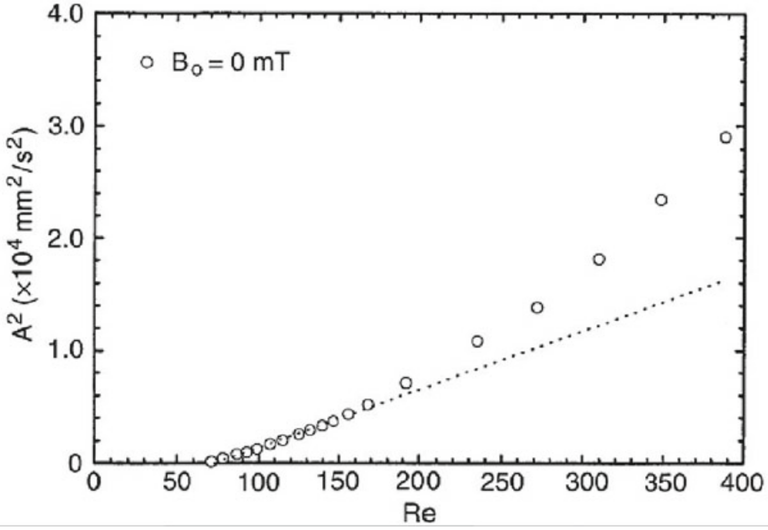

Fig. 5.61 Reynolds number dependence on the square of maximum axial velocity [86] (with kind permission from Springer Science+Business Media)

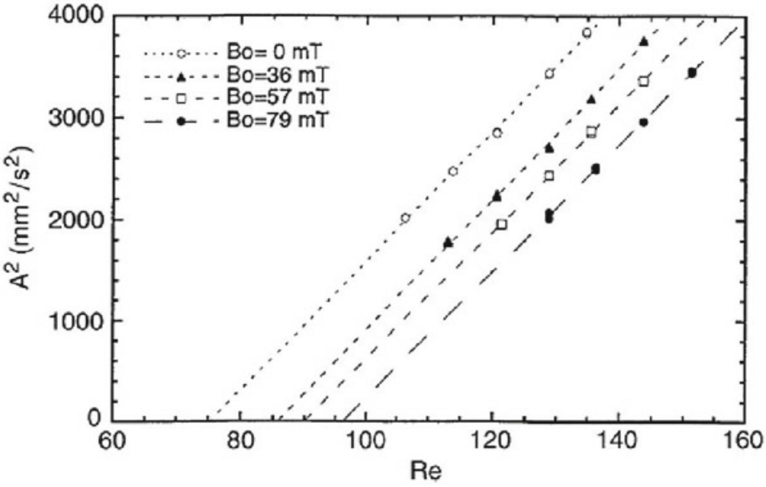

Fig. 5.62 Influence of the magnetic field on the square of maximum axial velocity at each Reynolds number [86] (with kind permission from Springer Science+Business Media)

Moreover, to investigate the angular dependence of the flow, velocity profiles were measured at angular positions in 45° steps (as defined in Fig. 5.58b). Note that inner cylinder rotates clockwise. Because the applied magnetic field in the present experiments was nonuniform, it was expected that the motion of fluid flow might not be the same at each angular positions. Figure 5.64 shows the time-averaged velocity distributions at these angles under a magnetic intensity $B_0 = 79$ mT and with the case without a magnetic field. When the magnetic field is applied, the

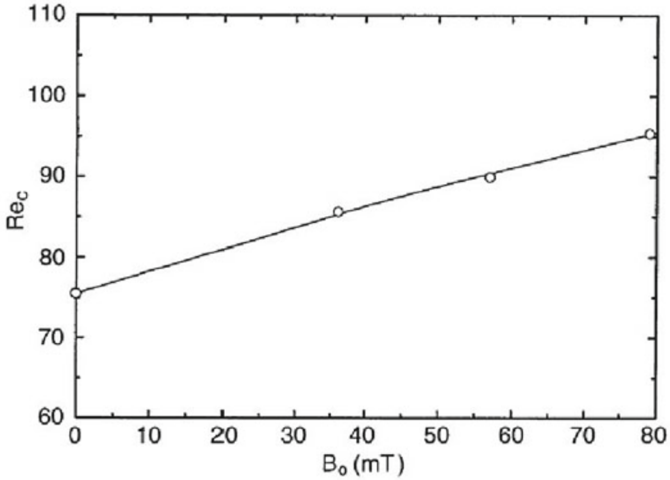

Fig. 5.63 Magnetic field dependence on the critical Reynolds number [86] (with kind permission from Springer Science+Business Media)

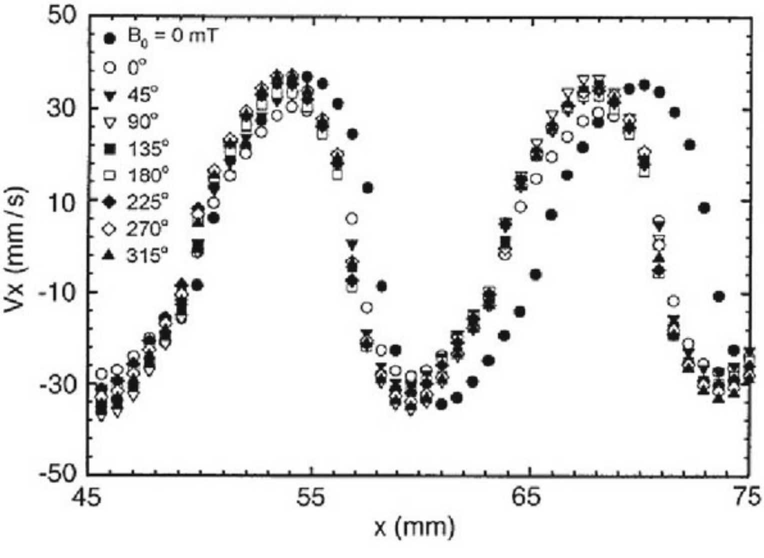

Fig. 5.64 Time-averaged velocity distributions at each angular position under a magnetic field [86] (with kind permission from Springer Science+Business Media)

wavelength becomes smaller at all positions by roughly the same amount for all cases. However, the maximum velocity shows an interesting tendency.

Figure 5.65 shows the angular distribution of the time-averaged maximum velocity at $x = 54$ mm and the intensity of radial components B_r of the magnetic field (gap space-averaged) normalized by $B_0 = 79$ mT. At point A, the intensity of the magnetic field is largest and the maximum velocity $V_{x\,\max}$ has its smallest value. On the other hand, at C, $V_{x\,\max}$ has its largest value and the magnetic field is small.

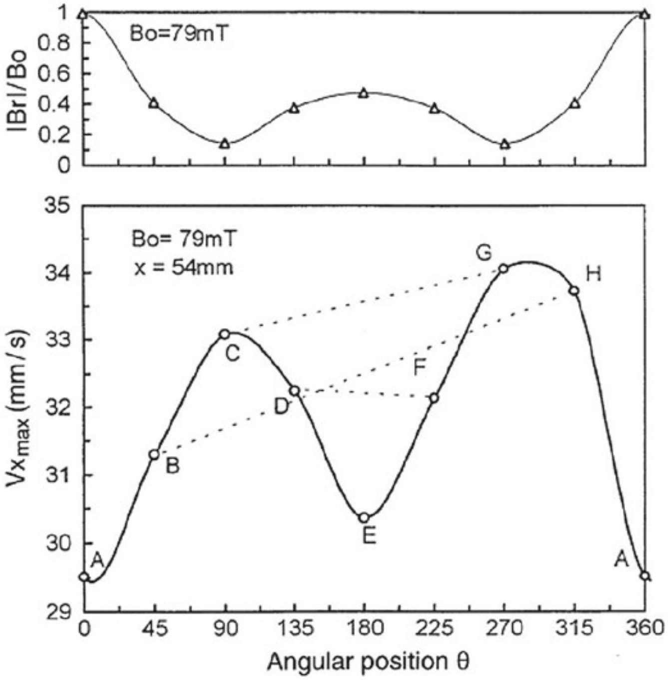

Fig. 5.65 Angular distribution of the radial magnetic field intensity (*top*) and maximum velocities at various angles (*bottom*) [86] (with kind permission from Springer Science+Business Media)

The same relationship can be seen at E and G. These results indicate a strong influence of the magnetic field on the magnitude of the velocity. The velocity magnitude decreases with increasing magnetic field intensity. The magnetic field (B_r) distribution is mirror symmetric with respect to the 180° point (E), whereas the $V_{x\,\max}$ distribution deviates from symmetry. The $V_{x\,\max}$ at G is larger than at C and $V_{x\,\max}$ at H is larger than at B. This difference is considered to be caused by the influence of the upstream velocity. As it flows azimuthally from A to H, a point upstream of B (i.e., at A) has smaller velocity whereas one upstream of H (i.e., at G) has a larger velocity; this is valid for comparison between C and G and between D and F. The magnitude of this difference is larger for B–H than C–G and furthermore it is very small for D–F: it depends on the magnitude of the velocity difference.

5.6 Gas–Liquid Two-Phase Flow

Gas–liquid two-phase flow, which is the flow of a mixture of gas and liquid, is used in chemical plants, metal refinement processes, nuclear cooling systems, and water treatment facilities, and is also observed in marine devices and the natural environment. The flow has a variety of patterns dependent on the void fraction, and there

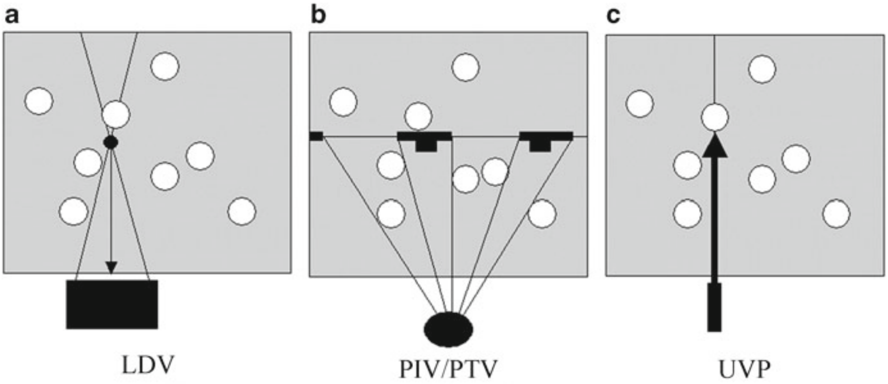

Fig. 5.66 Measurement effectiveness for gas–liquid two-phase flow. (**a**) LDV. (**b**) PIV/PTV. (**c**) UVP

has been a long history of research in an effort to understand and control the flow. The most fundamental target of measurement is the void fraction that fluctuates in space and time. In pipe flow, for example, there are a number of very different flow patterns, such as bubbly flow, plug flow, slug flow, churn flow, froth flow, annular flow, and mist flow. Because the void fraction has high correlation with fluctuation in pressure, the dynamic transport characteristics of two-phase flow are often assessed with pressure measurement. In contrast, there has been a short history of measuring the velocity field to investigate the behavior of gas–liquid two-phase flow. Most convectional velocity measurement techniques cannot be immediately applied to two-phase flow because the gas–liquid interface disturbs the working principle of the measurement [94]. UVP is one such technique, and hence various problems arise when it is applied to gas–liquid two-phase flow. An obvious and paramount problem is that the ultrasound pulse does not transmit through the gas–liquid interface, which prevents measurement beyond the interface. For this reason, the use of other signals such as X-ray, neutron ray, and gamma ray signals, has been alternatively developed for two-phase flow measurement. However, measurement restrictions for two-phase flow are not severe when using the UVP technique compared with those when using optical methods such as laser Doppler velocimetry, as is described in the following section.

Figure 5.66 compares measurement principles for bubbly flow. Laser Doppler velocimetry (LDV) provides two laser beams to measure the velocity at the crossing point (Fig. 5.66a). The system requires three paths of light in total, which includes the path from the crossing point to the aperture. When a bubble blocks one of the paths, measurement does not work at all. Figure 5.66b shows particle imaging velocimetry (PIV), which includes particle tracking velocimetry here. PIV has multiple factors that disturb the measurement in two-phase flow. First, bubbles break the sheet of light. Second, bubbles that exist between the sheet and a camera produce an ineffective area for measurement. Third, the ineffective area for PIV is further expanded by the displacement of bubbles between two consecutive image frames as shown by the difference in bands on the sheet in the figure. The use of

UVP, however, requires only a single path of ultrasound in two-phase flow, and the probability of a bubble's disturbance of the measurement is the lowest among these three principles of measurement. In addition, as opposed to LDV and PIV, UVP obtains all velocity data along the measurement line until the first bubble. Although the size of the measurement volume varies greatly among the techniques, UVP is the most effective in obtaining the velocity information for multiphase media.

Several demonstrations of two-phase flow measurement are presented hereafter. Relevant information is the interface detection by ultrasound as mentioned in Sect. 7.2 and void profiling with ultrasound as described in Sect. 7.3. The speed of sound in multiphase flow varies with local density and acoustic impedance. This problem is classified by the length scale of the ultrasound pulse relative to that in multiphase media. Here we are concerned only with the situation in which the ultrasound beam is not disturbed by the interfaces.

5.6.1 Slug Flow in a Horizontal Pipe

Gas–liquid two-phase flow in a horizontal circular pipe has a nonaxisymmetric structure because of gravity, and strong unsteadiness from momentum interaction also occurs between the two phases. In this context, measurement of the internal velocity profile as well as the phase distribution becomes more important than in the case of single-phase flow. The method to measure the flowrate of two-phase flow employing UVP is now elaborated. There are two types of techniques for realizing multiphase flow metering. One is conversion to homogeneous flow using a strong mixer installed before the section of the flow metering device, by which the total flowrate is measured using fluid properties such as the corrected mean density and effective viscosity. The other method is the complete separation of the two phases before the flow metering section using a separator, by which the flowrate of each phase is measured with an ordinary flow meter for single-phase flow. In comparison with these two methods, UVP does not require either a mixer or separator [95]. Originally, the flowrate of the phase i is defined as

$$Q_i = \int f_i \cdot u dA, \tag{5.20}$$

where f_i the volume fraction of phase i and u is the velocity profile perpendicular to the cross section A. As u is obtained by UVP, f_i also measured by ultrasound that is reflected from the interface. Thus, the accuracy of flow metering depends on the accuracy of the measurement of f_i.

Figure 5.67 shows a high-speed image of a single-bubble interface for slug flow (a) and ultrasound signal profiles relevant to the interface (b) in the same synchronized instant. The measurement setup is the same as in the application in Sect.7.2. For slug flow, the echo intensity is stably obtained because of the turbulent interface.

Figure 5.68 shows an example of a single gas bubble interface for slug flow, which was measured by backlight computed tomography using an array of mirrors

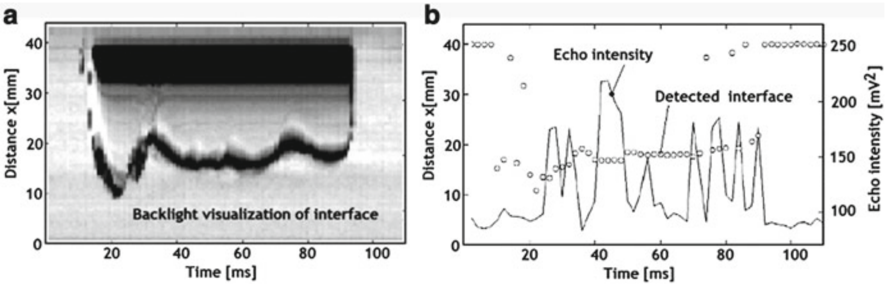

Fig. 5.67 Interface detection for passage of a large gas bubble in slug flow. (**a**) Backlight image. (**b**) Detected interface

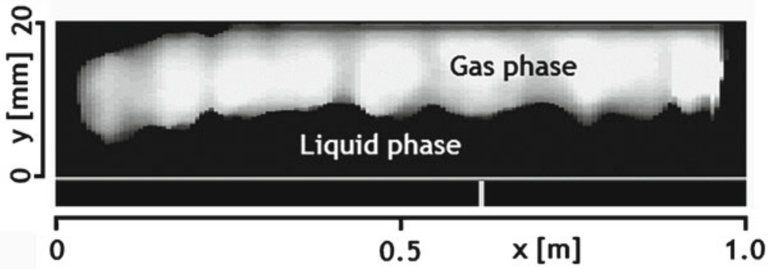

Fig. 5.68 Computed tomography (CT) measurement result of gas-phase structure for examination

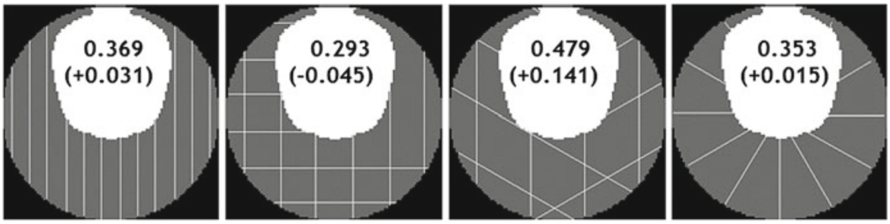

Fig. 5.69 Arrangement patterns of UVP measurement lines for circular pipe

[96, 97]. Using these computed tomography data, the accuracy of ultrasound interface detection for different arrangement patterns of the measurement lines is examined numerically.

Figure 5.69 presents the arrangement patterns: a parallel arrangement, orthogonal grid arrangement, triangular grid arrangement, and azimuthal arrangement. All these cases have 12 lines of ultrasound measurement for comparison. The values given in the figure are the cross-sectional void fractions computed from the measured positions of interfaces; the values in parentheses are the differences from the true values. There are two methods of arranging measurement lines in each pattern: the one-way and two-way arrangements of ultrasound transducers. In the one-way method, the ultrasound line is from one side of a pipe wall to the other. In the two-way method, there are ultrasound lines from both sides of the pipe wall so that the

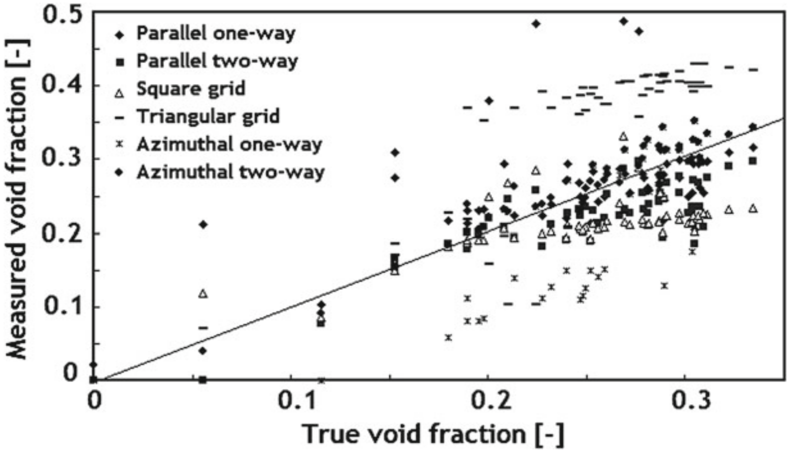

Fig. 5.70 Measurement uncertainty of void fraction

gas phase in the pipe is estimated more clearly although the number of transducers is doubled.

Figure 5.70 shows the relationship between the true void fraction and the void fraction measured by ultrasound. The true void fraction is computed from the computed tomography data. For the same number of measurement lines, the simulation reveals that the two-way arrangement of measurement lines in the azimuthal direction (shown by solid circles), provides the best accuracy among six combinations of the conditions. Investigating such performance for a range of 1 to 36 measurement lines, the necessary number of measurement lines is determined such that error in the void fraction of less than 5% is guaranteed.

Figure 5.71 depicts the accuracy of the ultrasound liquid flowrate measurement in comparison with the liquid flowrate measured employing the volume method. The accuracy is relative error of 5% in the range shown.

5.6.2 Taylor Bubble in a Vertical Tube

A Taylor bubble is recognized as a simpler case of gas–liquid two-phase slug flow, for which there is interesting physics around the bubble. UVP is applied to investigate the ensemble-averaged velocity vector field of the liquid phase for repetitive passage of the bubbles [98, 99], while the individual flow field, varies especially in the wake region owing to the nature of turbulence. The combination of tap water and room air is used under the condition of constant liquid temperature. The ultrasonic reflectors were low-density polyethylene particles with mean diameter of 160 μm and mean weight concentration of 0.0375 wt %. The test section had an internal diameter of 54 mm and was located along a 3-m-long transparent tube (Fig. 5.72). Two ultrasonic transducers with basic frequency of 4 MHz and effective beam diameter of 5 mm were

Fig. 5.71 Comparison of liquid flowrate to volume-type flow meter

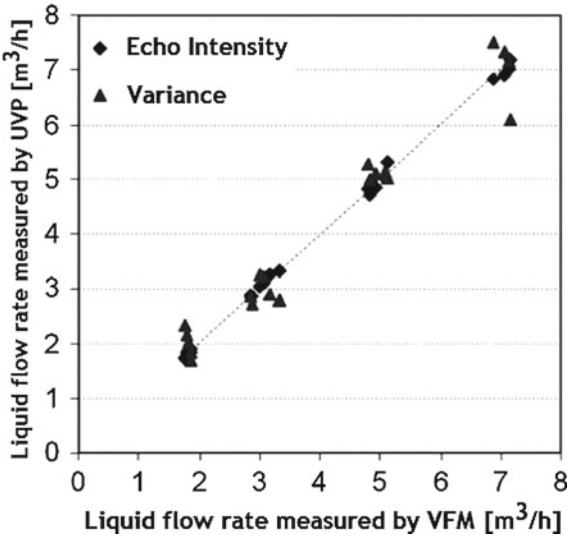

Fig. 5.72 UVP measurement setup for vertical gas–liquid two-phase flow [98]

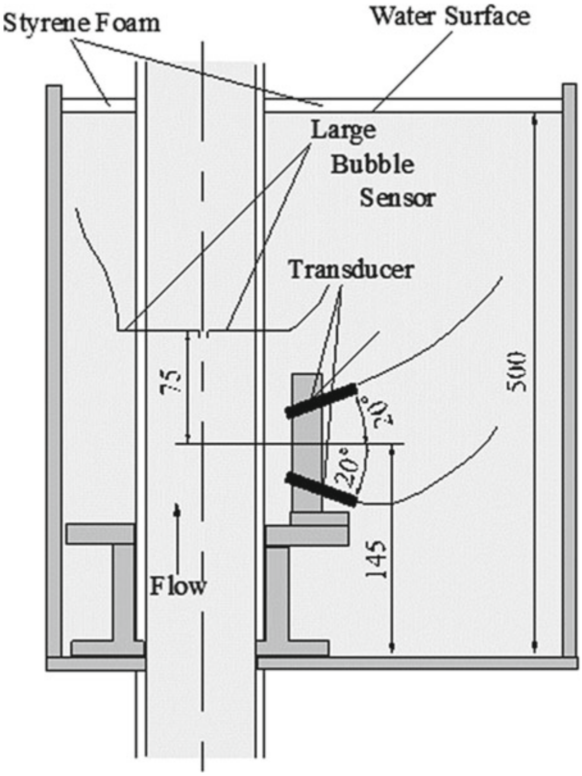

Fig. 5.73 Entire flow field [98]

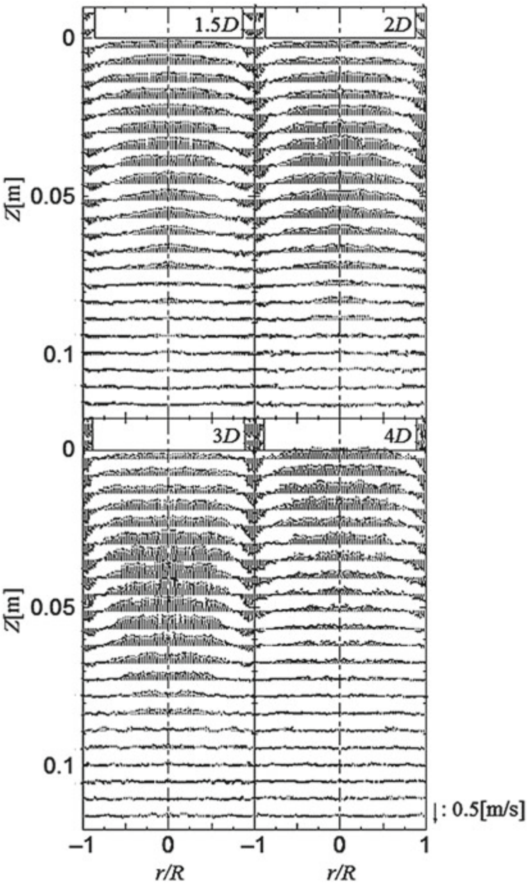

fixed on the outside of the tube, at angles of plus and minus 20° from the horizontal plane. The equipment was submerged in a water tank to reduce ultrasonic attenuation. Thin styrene foam was floated upon the water surface in the tank so that the signal-to-noise ratio was maintained against acoustic noise because of the wavy surface. An electric sensor was used to detect the bubble passage in the tube, and UVP data were processed to obtain statistics of the velocity distributions.

Figure 5.73 shows an example of the velocity vector distribution inside the liquid phase around a Taylor bubble. Flow is quiescent above the bubble but strongly driven in the wake region and in the liquid film that clings to the internal wall of the tube. It should be noted that the setup for UVP in this situation often leads to distorted velocity profiles and non-zero velocities at the wall owing to convolution of the ultrasound pulse with distance when it propagates through the solid wall material; this can be corrected, for example, using a complex deconvolution procedure.

Figure 5.74 is an enlargement of the distribution of the velocity vector around the top of the bubble. Four cases in the figure are for different vertical lengths of the bubble, which is understood to unimportant. In contrast, the wake structure is affected by the length of the bubble, as shown in Fig. 5.75, because the liquid

Fig. 5.74 Flow around the top of the bubble [98]

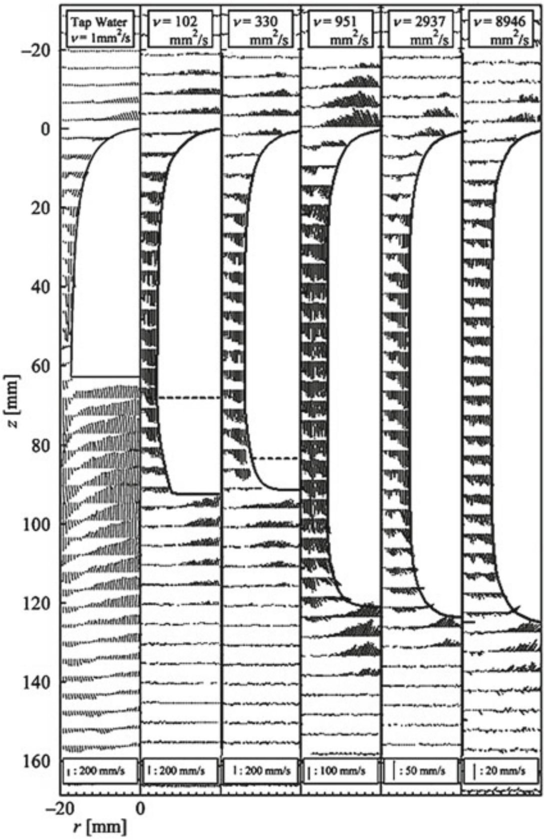

flowrate inside the falling film beside the bubble changes with the length, and it sways the circulation of flow in the wake region.

Figure 5.76 shows the measurement results for the change in viscosity [100]. The leftmost result is for water as the liquid phase, and the other results are for silicone oil with viscosity increasing toward the right side of the figure. It is noted that the size of the vector is drawn relative to the velocity of the rising bubble, which is low in highly viscous liquid. In the case of water (i.e., the case of lowest viscosity), the falling film provides falling flow near the wall beneath the bubble, and it raises the central flow to form a large-scale circulation. In highly viscous cases, by contrast, the falling flow hardly remains in the wake, and the bubble interface becomes a smooth curve at the bottom edge. As a result, the wake region has stationary flow.

5.6.3 Vertical Bubbly Flow

Two-phase bubbly flow in a vertical pipe has been one of the most fundamental flow fields in many industrial applications. The UVP has been also applied for the vertical two-phase flow. When the UVP is applied to a two-phase bubbly flow, ultrasonic

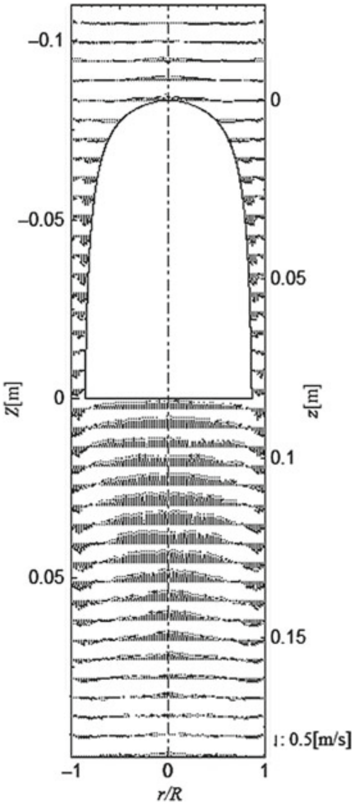

Fig. 5.75 Wake structure behind bubble [98]

pulses are reflected on both the seeding microparticles in the liquid phase and the gas–liquid interfaces. Hence, the velocity data measured by the UVP include the velocity information of both phases. Zhou et al. [101] and Suzuki et al. [102] developed a phase-separation technique, which is also a problem in laser Doppler anemometry (LDA). By applying statistical methods to measured velocity profiles, detection of bubble position is made possible when the bubbles crossing the measuring line. Here, examples of measuring liquid velocity distributions and Reynolds stress in the bubbly flow are described [103]. The other technique for measuring multiphase flow using a multi-wave transducer is shown in Sect. 7.1.

The relationship between a bubble and the measurement line is illustrated in Fig. 5.77. If a bubble crosses the measuring line, a typical velocity profile appears because of the relative velocity between liquid and bubble. In measurement of the countercurrent flow, the rising velocity of the bubble is recorded as positive and the liquid main flow velocity is recorded as negative. In co-current upward flow, both velocities are positive. Therefore, a measurement position where the maximum velocity appears in the profile can be considered as the gas–liquid interface in the typical velocity profile. Based on this concept, liquid velocity distributions in bubbly flow are obtained using statistical methods [102, 103].

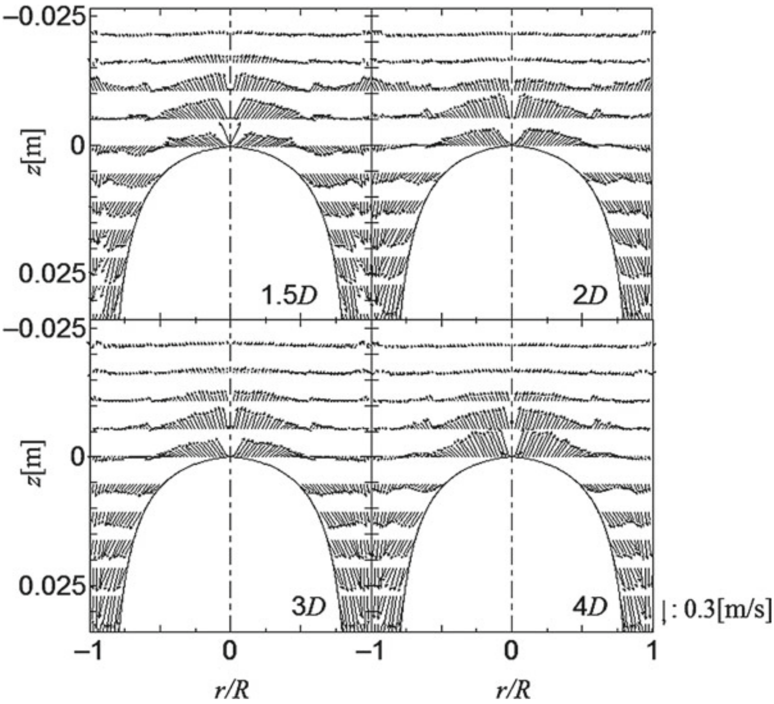

Fig. 5.76 Influence of difference in viscosity [100]

Figure 5.78 shows an example of ensemble-averaged liquid velocity profile around a bubble in a vertical rectangular channel with width of 20 mm. The J_L and J_G are superficial liquid and gas velocities, respectively. The working fluids were air and tap water. The flow was co-current bubbly flow, and the temperature was kept at 20° ± 0.5°C. Nylon tracer particles with an average diameter of 80 μm were seeded in the water. The origin of the horizontal axis was set to the bubble's surface (Fig. 5.77). The horizontal axis indicates the normal distance from the bubble's surface having an inclination of 45° from the gravitational direction. The vertical axis indicates the normalized ensemble-averaged relative velocity between local liquid velocity and time-averaged liquid main flow velocity at the same position in the channel. The value was normalized by the relative velocity at the bubble's surface.

In the vicinity of a bubble, the liquid has a large velocity gradient in any flowrate conditions. The steep gradient of the liquid velocity is observed in the area less than 2 mm away from the bubble's surface as moving away from the bubble's surface, the decrease in velocity becomes small and the local velocity gradually merges into the main flow. It is also observed that this characteristic velocity profile is independent from flowrate conditions.

In understanding the liquid turbulent structure induced by bubbles motion, Reynolds stress is an important parameter. The Reynolds stress profiles can be

Fig. 5.77 Coordinate system around a bubble

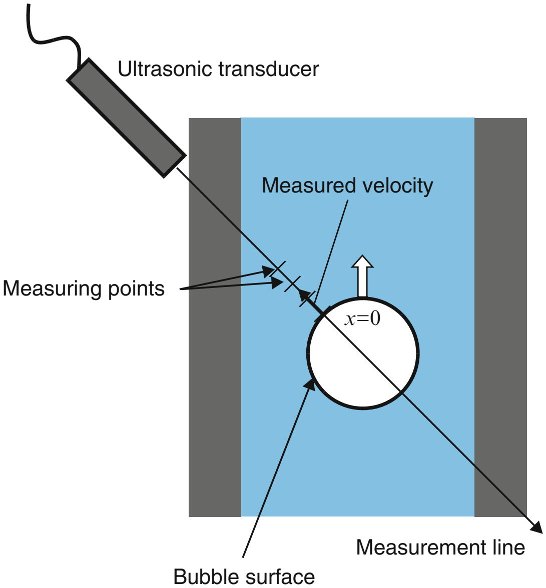

Fig. 5.78 Ensemble-averaged velocity profile around a bubble

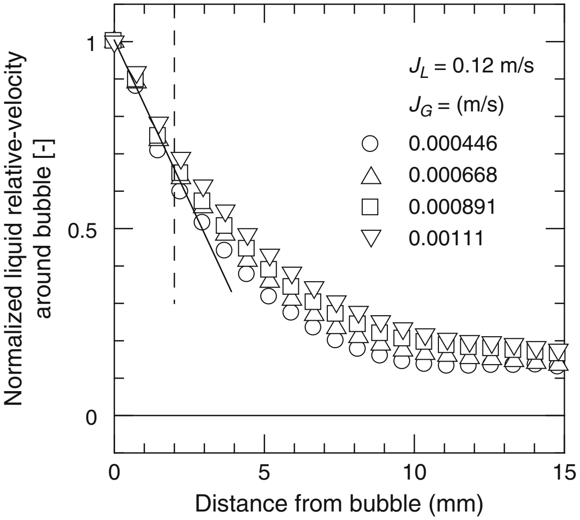

calculated from two-directional velocity components. The transducers (TDXs) were set at different angles (θ_1 and θ_2) from the axial flow direction. The mean Reynolds stress profiles can be calculated as follows [104, 105]:

$$\tilde{Q} = \tilde{U}\cos\theta + \tilde{V}\sin\theta, \tag{5.21}$$

$$\tilde{U} = \overline{U} + u, \quad \tilde{V} = \overline{V} + v, \tag{5.22}$$

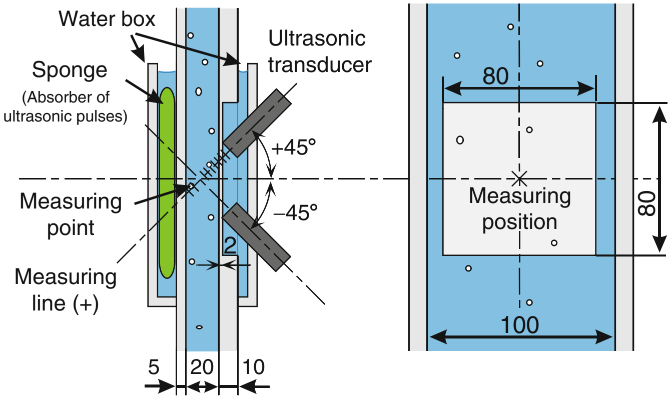

Fig. 5.79 Schematic diagram of the test section

$$q_1 = v\cos\theta_1 + u\sin\theta_1, \quad q_2 = v\cos\theta_2 + u\sin\theta_2, \tag{5.23}$$

where $\tilde{U}$ and $\tilde{V}$ are the instantaneous horizontal and vertical velocities, and $\tilde{Q}$ is the instantaneous velocity along the measuring line. $\bar{U}$ and u denote the time-averaged velocity and velocity fluctuation, respectively. Fluctuating velocity components (q_1 and q_2) on the two measuring lines are calculated by Eq. (5.21). If θ_1 equals θ_2, based on Eqs. (5.21)–(5.23), the Reynolds stress yields the following:

$$-\rho\overline{uv} = \rho\frac{\overline{q_1^2} - \overline{q_2^2}}{2\sin 2\theta} = \rho\frac{q_1'^2 - q_2'^2}{2\sin 2\theta}, \tag{5.24}$$

where q' denotes the standard deviation of the velocity fluctuation along the measurement line direction.

Figure 5.79 illustrates the test section located between the upper tank and air–water mixer. The size of the vertical rectangular channel is $100 \times 20 \times 1{,}700$ mm^3. Two TDXs were installed on the outer surface of the test section with a contact angle of 45° off the vertical, one facing upward and the other facing downward. The outer surface of the test channel and the TDXs were submerged to equalize the acoustic impedance.

Reynolds stress profiles measured in single-phase and two-phase bubbly flows are shown in Fig. 5.80. The Reynolds stress increases with Reynolds number (*Re*). It is found that the Reynolds stress profiles are affected by the bubble injection such that the values of the Reynolds stress increased with the bubble injection. The differences between the values of the Reynolds stress in a single-phase flow and that in a bubbly flow decrease as the liquid flowrate increases. Furthermore, the Reynolds stress is significantly affected near the wall ($y/D < 0.4$). These results show that

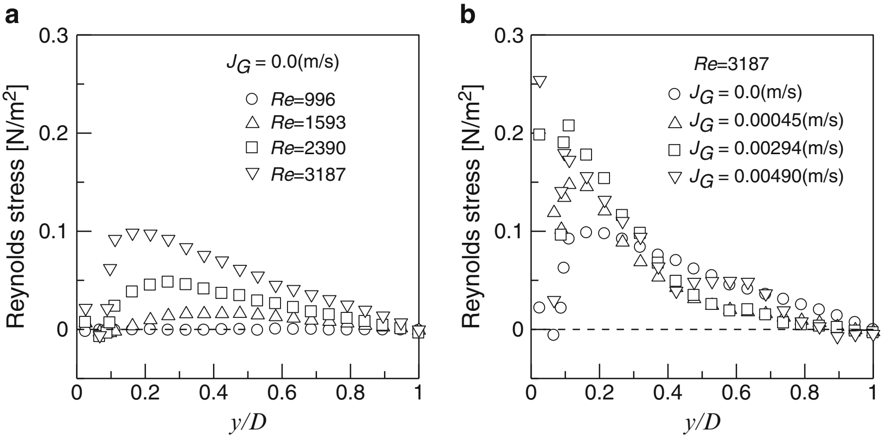

Fig. 5.80 Reynolds stress profiles. (**a**) Single-phase flow. (**b**) Two-phase bubbly flow [103] (reprinted by permission of the publisher (Taylor & Francis Ltd, http://www.tandf.co.uk/journals).)

bubble injection plays a major role in turbulence, particularly around the near-wall region; this effect decreases with a decreasing liquid flowrate.

Speed of sound in bubbly flow changes with void fraction, but it also depends on temperature of water when bubbly flow in boiling condition is targeted (see Sect. A.1). In such a case it becomes very important to continuously measure the speed of sound along the pulsed beam axis.

5.7 Turbidity Flow

Turbidity flow is defined as flow of seawater and river water in this chapter. Large amounts of water are utilized in the generation of electricity in electric power plants, including nuclear, thermal, and hydropower stations. Accurate flowrate measurements of the major process systems in such power plants are important to evaluate plant performance accurately. Electric power output can be uprated by increasing the flowrate in process systems, which requires accurate flow measurement. In addition, accurate evaluations of equipment performance enable utility companies to reduce maintenance costs by optimizing equipment maintenance intervals. The environmental impacts of discharges from power plants have also attracted attention recently.

Recently, ultrasonic Doppler method has been gaining popularity as the basis for state-of-the-art flow meters because it captures the instantaneous velocity profile along the ultrasonic beam path in the pipe [106–108]. In addition, it can be applied by a clamp-on device that is noninvasive and considered to be suitable for measuring the flowrate in actual power plants.

5.7.1 *Background of Flowrate Measurements at Hydropower Plants*

Pitot tubes have been widely used for several years to measure the fluid velocity in power plant water supply. The flow rates in steel penstocks have been used to calculate the efficiency of hydraulic turbines in power plants [109]. However, installation of Pitot tubes requires the shutdown of the plant and system drain-down to insert the Pitot tube into the steel penstock. The require downtime results in a significant loss of power generation. Also, many experts are required to install and take measurements from the Pitot tubes. In addition, sensor holes on the Pitot tubes are likely to become clogged with dust or sand from river water. At present, the use of transit-time ultrasonic flow meters is predominant, replacing Pitot tubes. The underlying principle of transit-time ultrasonic flow meters requires a meter factor, that is, a correction factor, to derive the flowrate from the ultrasound transit time between two ultrasonic transducers. This meter factor is heavily influenced by the velocity profile across the pipe. As a result, large measurement errors may result if the flow pattern is different from the reference case used at the factory, or if the inner surface the pipe is very rough compared to reference patterns. In contrast, the ultrasonic Doppler method can measure the velocity profile of the fluid using a transducer installed on the outer surface of a pipe and does not require this kind of correction factor to calculate the flowrate. This method allows highly accurate measurements and does not affect process systems. In addition, the installation costs are significantly more tolerable because no plant shutdown is required, and this is, therefore, an attractive and practical measuring method.

5.7.2 *Flowrate Measurements in Steel Penstock at Hydropower Plants*

At present, the use of transit-time ultrasonic flow meters is predominant, replacing Pitot tubes for flowrate measurement in steel penstock. Tezuka et al. [110, 111] and Suzuki et al. [112] are doing research on the application of ultrasonic Doppler method for an actual power plant.

5.7.2.1 Installation of Ultrasonic Transducer on Pipe

Ultrasonic parameters should be carefully selected depending on the pipe size, wall thickness, and flow velocity to obtain sufficiently strong ultrasonic echoes. A major difficulty in measurements in large piping is that the Nyquist constraint balancing between maximum measurable depth and maximum measurable velocity becomes very challenging. Ultrasonic transducers are installed on the surface of the steel penstock using a Plexiglas wedge with an angle of inclination θ, and the velocity

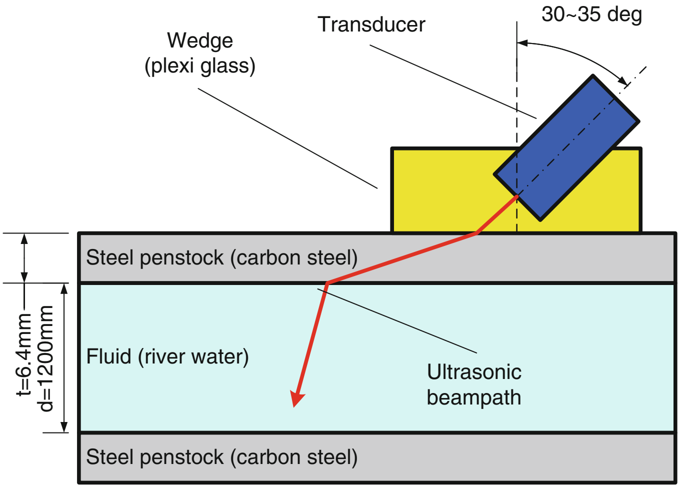

Fig. 5.81 Schematic diagram of ultrasonic transducer installed on pipe surface [110]

profiles inside the steel penstock are measured along the ultrasonic beam path. Figure 5.81 shows the layout of the ultrasonic transducers and the ultrasound beam path used in the field tests.

The incidence angle of ultrasonic transducers is defined as the angle between the transducer and a line perpendicular to the pipe surface. This angle is set between 30° and 35°, which is greater than the critical angle of a longitudinal wave in the pipe wall. The ultrasonic transducer is braced by an ultrasonic wedge made of Plexiglas in which the speed of sound is approximately 2,700 m/s at 20°C. The wedge is firmly held on the pipe surface by steel bands. The material that couples the wedge and the pipe surface is very important for good ultrasonic transmission because the surface of steel penstocks is very rough from extended exposure to severe natural conditions. In some cases, a couplant for shear wave transducer or a metal foil is used to achieve firm contact between the wedge and the pipe wall. Any pipe coating should be removed before mounting ultrasonic transducers to maximize ultrasonic transmission through the pipe wall. The center frequency of ultrasonic transducer is designed to be around 0.5 MHz, the number of cycles per pulse is around 6, and the sensor diameter is around 50 mm. This is a relatively large transducer compared to that used in laboratory experiments because a large transducer is preferable in terms of sensor sensitivity and the divergence angle of the main lobe of ultrasound. The divergence angle should be as small as possible for a large pipe to produce a strong echo from the far side of the pipe.

5.7.2.2 Injection of Tracer Particles into Fluid

River water has only a small number of particles to function as ultrasonic reflectors, which are required for ultrasonic Doppler method. Therefore, sufficient quantities of miniature air bubbles should be injected into the steel penstock. Miniature bubbles

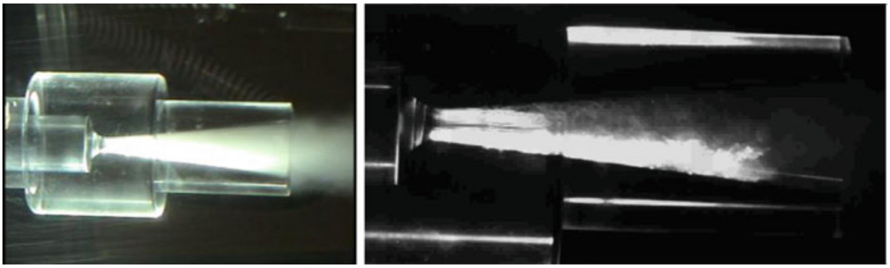

Fig. 5.82 Photograph of microbubbles generated at the throat of a Venturi nozzle [106]

are generated in the pipe inlet. A mixture of water and air goes into a Venturi nozzle, producing microbubbles at the outlet of the nozzle. The water injection rate is 0.03 m^3/min, and the amount of air is controlled so that the volumetric void fraction in the main flow is high enough to produce Doppler signals. When a mixture of water and air passes through the nozzle throat, air bubbles are compressed by the sudden increase of static pressure at the nozzle throat and fragmented into multiple bubbles by the turbulence downstream of the Venturi neck. Cavitation bubbles are also expected to form at the interface between the water jet and the static water. The design of the injection nozzle is not completely optimized; however, it did function well enough to create bubbles small enough to work as ultrasonic reflectors. Those tiny bubbles are suitable for enabling measurement by ultrasonic Doppler method.

Figure 5.82 shows the experimental results of observing bubble generation through the Venturi nozzle with the flowrate of 50 l/min and 0.5 MPa. Bubbles are generated at the nozzle throat, flowing and diffusing into the mainstream. Bubble diameters are estimated as about 10–30 μm.

5.7.2.3 Flow Profile Measurements at Hydropower Plants

Velocity profile measurements are conducted across a horizontal diameter at approximately 9D (D, diameter of the pipe) from the inlet of the steel penstock with the pipe diameter of 1.2 m at actual power plants. Microbubbles are injected at the inlet of the steel penstock. In addition to the measurements at position 9D, flow rates were also measured at 15D. Figure 5.83 shows the actual attachment of ultrasonic transducers on the pipe surface at a hydropower plant.

A comparison of the velocity profiles at the same generating power at the horizontal diameter positions 9D and 15D is shown in Fig. 5.84. Compared with 9D, the flow velocity profile at 15D is approaching full development, faster in the central region and slower adjacent to the pipe wall; this indicates that the ultrasonic Doppler method can detect the profile difference resulting from the distance from the inlet of the steel penstock.

A comparison of the velocity profiles measured by Pitot tube and by ultrasonic Doppler method is shown in Fig. 5.85. Pitot tube flow rate measurements were conducted radially at five different points. Although the Pitot tube measurement was carried out about 30 years ago, these velocity profiles are in good agreement.

Fig. 5.83 Ultrasonic transducer and wedge installed on the surface of a steel penstock (reprinted from [111] with permission from Elsevier)

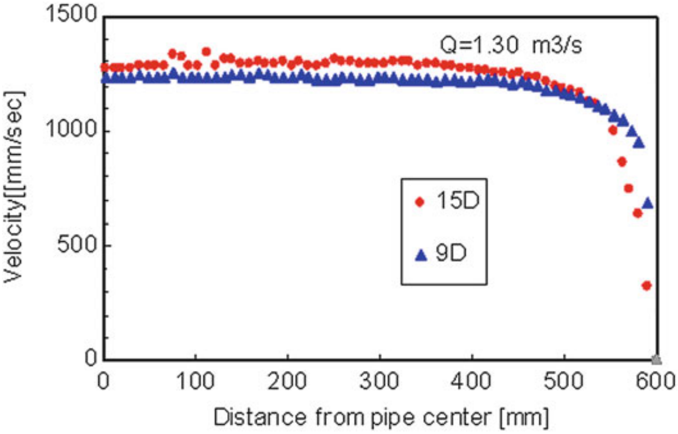

Fig. 5.84 Velocity profiles at the horizontal diameter positions of 9D and 15D [110]

5.7.3 Flowrate Measurements of Open Channels

Wada et al. [107], Ito et al. [108], and Yokoyama et al. [113] are conducting research on flowrate measurement of open channel flow such as in a river. Figure 5.86 shows a photograph of a river located upstream of a hydropower station and transducers that were applied for flowrate measurements. The correctional dimensions of the river are 5 m × 4 m and the mean velocity of the river flow is around 2 m/s. The result of flowrate measurements using the ultrasonic Doppler method and a propeller meter is illustrated in Fig. 5.87. As a reference meter, a propeller meter was traversed over the river cross section to obtain a velocity profile of 25 measuring points. A calibration test on site and improvement of the bubble injection system are expected in the future.

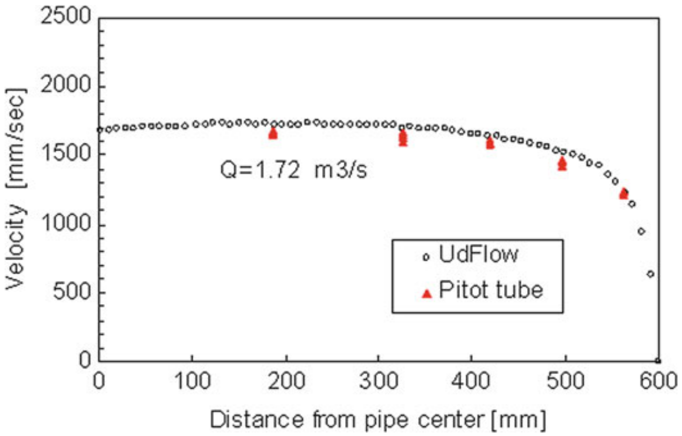

Fig. 5.85 Comparison of velocity profile for 400 kW between Pitot tube and ultrasonic Doppler method [110]

Fig. 5.86 The river located upstream of a hydropower station and transducers [107]

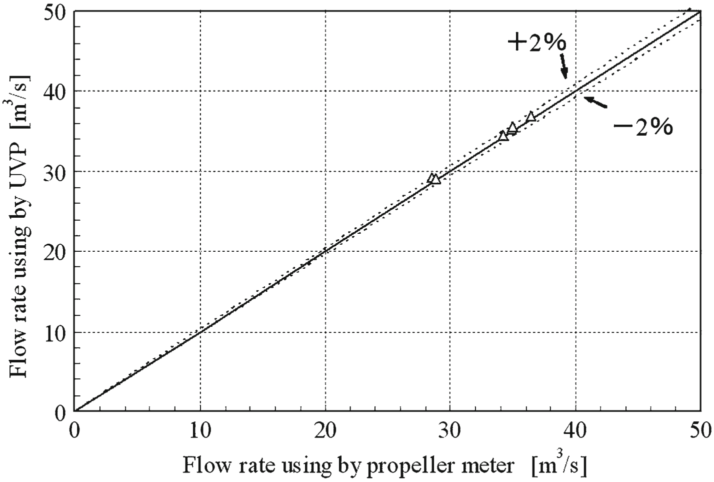

Fig. 5.87 Comparison of flowrate between using a propeller meter and the ultrasonic Doppler method [107]

5.8 Biomedical Fluid Flow

5.8.1 Steady Flow of Non-Newtonian Fluid in an Elastic Tube

Non-Newtonian fluid flow characteristic investigations in inflatable and collapsible elastic tubes are relevant to bio-fluid mechanics encountered in the human body such as blood flow in arteries and veins, food flow in pharynx, esophagus, and small intestine, and other applications. The flow behavior in elastic tubes depends on many aspects such as fluid microstructural properties, elastic tube solid mechanics, deformed tube interaction with fluid [114], and applied stresses inducing fluid flow [115]. Flow field measurement in collapsible tubes has been little performed because of the lack of applicable methods. UVP (pulsed ultrasound Doppler-based velocity profile) is a noninvasive method for measuring the instantaneous velocity profile in liquid flow along the ultrasonic beam axis [24]. This method has been extensively used by several authors to measure the velocity profiles of the steady flow of non-Newtonian fluids and particulate suspensions in noncollapsible tubes or pipes [56, 74].

We encountered the challenge and successfully applied the UVP technique for monitoring steady and unsteady flow fields through a collapsible elastic tube as demonstrated by Nahar et al. [116]. The study included the velocity profile measurement of a shear-thinning carboxymethyl cellulose (CMC) aqueous solution for steady laminar flow through a collapsed elastic tube (20 mm ID, 1 mm thick, 320 mm long) using a Starling Resistor setup. As the external pressure P_e increased higher than the critical value, the tube buckled from the circular shape (Fig. 5.88a) into a line or area contacted two-lobed shape (Fig. 5.88b). The transmural pressure P_{tm} (outlet pressure in tube $P_0 - P_e$) at the downstream was more negative than that at the upstream (inlet pressure in tube $P_i - P_e$) because P_0 decreased due to strong tube collapse with reduced cross-sectional area A. The compressive transmural pressure of about −30 mbar at the downstream results in a decrease in A about an order of magnitude from that of the undeformed tube, and the corresponding maximum flow velocity at the tube center increased by about a factor of two.

The measured velocity profiles in the undeformed tube were found to be parabolic (Fig. 5.88c). In contrast, a two-lobed tube shape was formed at an applied external pressure P_e of about 105 mbar, and a bimodal velocity profile (Fig. 5.88d) was obtained for the corresponding tube shape in the plane above the horizontal axis of tube center. The observed two-lobed shape was nearly symmetric, and the maximum velocity in both lobes increased about a factor of two over that in the undeformed circular-shaped elastic tube.

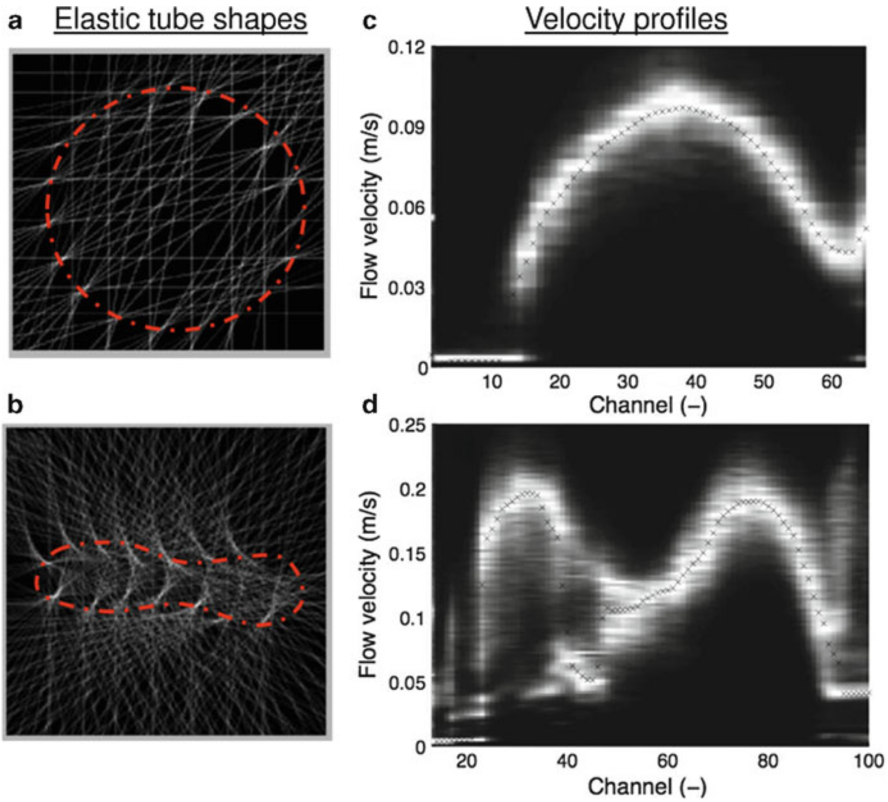

Fig. 5.88 (**a**, **c**) Elastic tube shapes obtained by tube shape image analysis (computed tomography) during CMC solution steady flow ($Q = 17$ ml/s) and the corresponding velocity profiles as a function of channel numbers (channel width and distance are 0.38 mm) along the tube diameter for undeformed elastic tube at $P_e = 18$ mbar (**b**, **d**) and deformed elastic tube at $P_e = 105$ mbar (reprinted from [116] with permission from Elsevier)

5.8.2 Peristaltic Flow of Non-Newtonian Fluid in an Elastic Tube

The in vitro investigation of a modeled small intestine is under progress based on the flow behavior of a non-Newtonian fluid during peristaltic propulsion through an elastic tube, which enables understanding of the interaction between wall motion and fluid flow. Peristaltic flow is the essential physiological transport mechanism encountered in the most tubular organs of the human body, such as swallowing food through the esophagus, the transport of urine from the kidney to the bladder through the ureter, and the carrying and mixing motion of the chyme in the small intestine [117]. Some experimental and theoretical features of peristaltic flow were studied extensively by several authors using Newtonian fluids [117–119]. For more realistic non-Newtonian fluid systems, systematic work is still lacking. However, most of the physiological fluids and foods are known to be

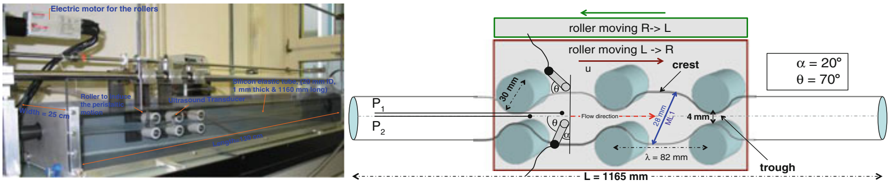

Fig. 5.89 Experimental setup for peristaltic flow measurements with UVP

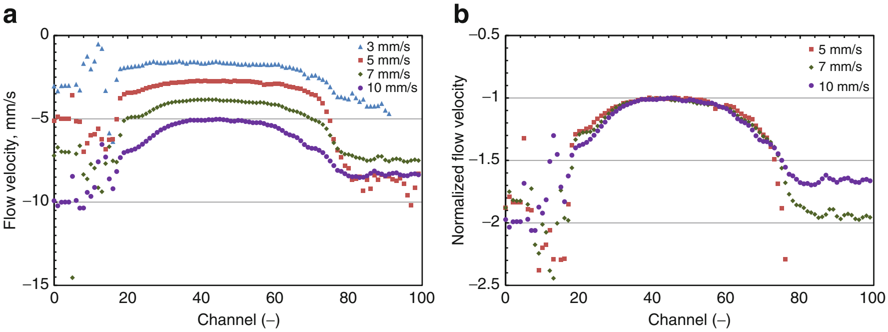

Fig. 5.90 (**a**) Experimentally measured velocity profiles. (**b**) The corresponding normalized velocity profiles in the wave crest with horizontal position of the ultrasound transducer under different speeds of peristalsis as the peristaltic wave moved from right to left

non-Newtonian, and their rheological properties (shear and extensional viscoelasticities) play an important role in the peristaltic flow characteristics. The peristaltic transport of a power law fluid in an axisymmetric porous tube was studied theoretically under lubrication analysis, where the effect of shear-thinning and shear-thickening properties of fluid were investigated on peristaltic pumping, trapping, and reflux phenomena [120].

In vitro small intestinal flow characteristics of the non-Newtonian model fluid have been investigated by transient '3-wave'-squeezing of an elastic tube using a special experimental setup (Fig. 5.89). The peristalsis involves both contraction and expansion type of flow (trough and crest of a wavelength), and the UVP technique has been implemented for investigating appropriate peristaltic propulsion of a shear-thinning fluid in an elastic tube. The experiment was carried out under different speeds of peristalsis while moving the peristaltic wave in both directions (left to right or right to left, depending on study interest). The velocity profiles were monitored both in the crest and trough zone with the ultrasound transducer positioned at different optimized positions in moving and fixed frames. The results indicated that higher wave speed of peristalsis resulted in higher radial velocity, which is of specific interest in improvement of mixing and mass transfer of nutrients. Maximum radial velocity was detected near the tube wall (Fig. 5.90a) because the moving rollers to impose the peristalsis were in direct contact with the tube wall.

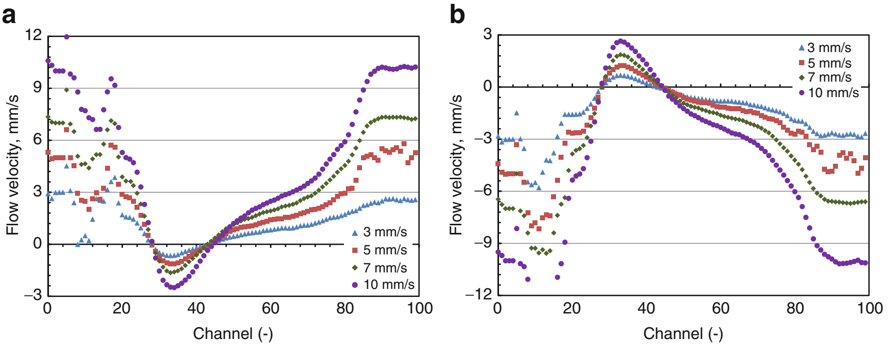

Fig. 5.91 Experimentally measured velocity profiles in the wave trough with horizontal position of the ultrasound transducer under different speeds of peristalsis as the peristaltic wave moved in both directions (**a**) Left to right. (**b**) Right to left

The accuracy of the measurement was high enough, which was confirmed by symmetric and overlapping feature of the normalized velocity profiles at different peristaltic speeds (Fig. 5.90b).

The velocity profiles were also measured at the second wave trough (of the '3-wave'-squeezing; Fig. 5.89) having the same history of wave propulsion as the peristaltic wave moving in both directions (Fig. 5.91a: left to right; Fig. 5.91b: right to left). Here again the higher wave speed of the peristalsis resulted in higher radial velocity with a negative/positive magnitude at the peak value depending on the direction of wave speed, which can be an indication of existence of local back flow. The measured velocity profiles are seen to be mirror image of each other while peristaltic motion is altering the moving direction. In both cases the magnitude at the peak value remains the same (opposite sign indicating the moving direction), which also improves the good focusing and positioning of the ultrasound transducer and the measurement accuracy as well.

Further research will be interesting to couple the detailed knowledge gained about non-Newtonian peristaltic flow with mass transport investigations across an elastic membrane tube wall.

References

1. Drain P, Reid W (1981) Hydrodynamic stability. Cambridge University Press, New York
2. Takeda Y, Fischer WE (1993) Measurement of energy spectral density of a flow in a rotating Couette system. Phys Rev Lett 70(23):3569–3571
3. Takeda Y, Ficher WE, Sakakibara J, Ohmura K (1993) Experimental observation of the quasiperiodic modes in a rotating Couette system. Phys Rev E 47(6):4130–4134
4. Takeda Y, Fischer WE, Sakakibara J (1994) Decomposition of the modulated waves in a rotating Couette system. Science 263:502–505
5. Takeda Y (1999) Quasi-periodic state and transition to turbulence in a rotating Couette system. J Fluid Mech 389:81–99

6. Andereck C, Liu SS, Swinney HL (1986) Flow regimes in a circular Couette system with independently rotating cylinders. J Fluid Mech 164:155–183
7. Tasaka Y, Kon S, Schouveiler L, Le Gal P (2006) Hysteretic mode exchange in the wake of two circular cylinders in tandem. Phys Fluids. doi:10.1063/1.2227045
8. Mizushima J, Suehiro N (2005) Instability and transition of flow past two tandem circular cylinders. Phys Fluids. doi:doi:10.1063/1.2104689
9. Tokuhiro A, Takeda Y (1993) Measurement of flow phenomena using the ultrasonic velocity profile method in a simulated Czochralski crystal puller. J Crystal Growth 130:421–432
10. Tasaka Y, Iima M (2009) Flow transition in the surface switching of rotating fluid. J Fluid Mech 636:475–484
11. Suzuki T, Iima M, Hayase Y (2006) Surface switching of rotating fluid in a cylinder. Phys Fluids. doi:10.1063/1.2359740
12. Tasaka Y, Ito K, Iima M (2008) Visualization of a rotating flow under large-deformed free surface using anisotropic flakes. J Visualization 11(2):163–172
13. Furuichi N, Takeda Y, Kumada M (2003) Spatial structure of the flow through an axisymmetric sudden expansion. Exp Fluids 34:643–650
14. Armly BF, Drust F, Pereira JCF, Shönung B (1983) Experimental and theoretical investigation of backward-facing step flow. J Fluid Mech 127:473–496
15. Furuichi N, Yoshida M, Kumada M (2005) An unsteady flow structure on a heated rotating disk under mixed convection. Heat Trans Asian Res 34(6):407–418
16. Belmonte A, Tilgner T, Libchaber A (1994) Temperature and velocity boundary layers in turbulent convection. Phys Rev E 50:269–279
17. Sreenivasan KR, Bershadskii A, Niemela JJ (2003) Mean wind and its reversal in thermal convection. Phys Rev E 65:056306
18. Ahlers G, Grossmann S, Lohse D (2009) Heat transfer and large scale dynamics in turbulent RB convection. Rev Mod Phys 81:503–537
19. Funfschilling D, Brown E, Ahlers G (2008) Torsional oscillations of the large scale circulation in turbulent RB convection. J Fluid Mech 607:119–139
20. Xi HD, Zhou SQ, Zhou Q, Chan TS, Xia KQ (2009) Origin of the temperature oscillation in turbulent thermal convection. Phys Rev Lett 102:044503
21. Takeshita T, Segawa T, Glazier JA, Sano M (1996) Thermal turbulence in mercury. Phys Rev Lett 76:1465–1468
22. Cioni S, Ciliberto S, Sommeria J (1997) Strongly turbulent Rayleigh–Bénard convection in mercury: comparison with results at moderate Prandtl number. J Fluid Mech 335:111
23. Glazier JA, Segawa T, Naert A, Sano M (1999) Evidence against ultrahard thermal turbulence at very high Rayleigh numbers. Nature (Lond) 398:307–310
24. Takeda Y (1986) Velocity profile measurement by ultrasound Doppler shift method. Int J Heat Fluid Flow 7:313–318
25. Ito T, Tsuji Y, Kukita Y (2001) Application of ultrasonic velocity profile meter to vortex shedding and empirical eigenfunction analysis. Exp Fluids 31:324–335
26. Tasaka Y, Takeda Y, Yanagisawa T (2008) Ultrasonic visualization of thermal convective motion in a liquid gallium layer. Flow Meas Inst 19(3–4):131–137
27. Mashiko T, Tsuji Y, Mizuno T, Sano M (2004) Instantaneous measurement of velocity fields in developed thermal turbulence in mercury. Phys Rev E 69:036306
28. Tsuji Y, Mizuno T, Mashiko T, Sano M (2006) Mean wind in convective turbulence of mercury. Phys Rev Lett 94:034501
29. Hayakawa T, Tsuji Y (2010) Mean wind: its velocity and temperature fluctuation in low-Pr-number thermal convection. Physica D 239:1353–1358
30. Yanagisawa T, Yamagishi Y, Hamano Y, Tasaka Y, Yoshida M, Yano K, Takeda Y (2010) Structure of large-scale flows and their oscillation in the thermal convection of liquid gallium. Phys Rev E 82:016320
31. Yanagisawa T, Yamagishi Y, Hamano Y, Tasaka Y, Yano K, Takahashi J, Takeda Y (2010) Detailed investigation of thermal convection in a liquid metal under a horizontal magnetic field: suppression of oscillatory flow observed by velocity profiles. Phys Rev E 82:056306

32. Yanagisawa T, Yamagishi Y, Hamano Y, Tasaka Y, Takeda Y (2011) Spontaneous flow reversals in Rayleigh–Bénard convection of a liquid metal. Phys Rev E 83:036307
33. Reolfs F, Siccama NB, Willemsen SM (2007) Development of an Euler–Euler two-phase model for application in the windowless XT-ADS spallation target design. Proceedings, ICAPP, paper 7092
34. Batta A, Class A (2007) A numerical investigation on geometrical designs of the windowless XT-ADS spallation target. Proceedings, ICAPP, paper 7479
35. Batta A, Class A (2008) Free surface modeling and simulation of the water experiment for the XT-ADS spallation target. Proceedings, ICAPP, paper 8049
36. Eckert S, Gerbeth G (2002) Velocity measurements in liquid sodium by means of ultrasound Doppler velocimetry. Exp Fluids 32:542–546
37. Eckert S, Gerbeth G, Melnikov VI (2003) Velocity measurements at high temperatures by ultrasound Doppler velocimetry using an acoustic wave guide. Exp Fluids 35:381–388
38. Eckert S, Willers B, Gerbeth G (2005) Measurements of the bulk velocity during solidification of metallic alloys. Metallurg Mater Trans A 36:267–270
39. Kowalewski TA (1980) Velocity profiles of suspension flowing through a tube. Arch Mech 32(6):857–865
40. Müller M, Brunn P, Harder C (1997) New rheometric technique: the gradient-ultrasound pulse Doppler method. Appl Rheol 7(5):204–210
41. Ouriev B (2000) Ultrasound Doppler based in-line rheometry of highly concentrated suspensions. PhD thesis, ETH, Zürich
42. Dogan N, McCarthy M, Powell R (2002) In-line measurement of rheological parameters and modeling of apparent wall slip in diced tomato suspensions using ultrasonics. Food Eng Phys Properties 67(6):2235–2240
43. Birkhofer BH (2007) Ultrasonic in-line characterization of suspensions. PhD thesis, ETH, Zurich. http://e-collection.ethbib.ethz.ch/view/eth:29828
44. Wiklund J (2007) Ultrasound Doppler based in-line rheometry: development, validation and application. PhD thesis, Lund University
45. Fock H, Wiklund J, Rasmuson A (2009) Ultrasound velocity profile (UVP) measurements of pulp suspension flow near the wall. J Pulp Pap Sci 35:26–33
46. Wassell P, Wiklund J, Stading M, Bonwick G, Smith C, Almiron-Roig E, Young NWG (2010) Ultrasound Doppler based in-line viscosity and solid fat profile measurement of fat blends. Int J Food Sci Technol 45(5):877–883
47. Dogan N, McCarthy MJ, Powell RL (2005) Application of an in-line rheological characterization method to chemically modified and native corn starch. J Texture Stud 36:237–254
48. Köseli V, Zeybek Ş, Uludağ Y (2006) Online viscosity measurement of complex solutions using ultrasound Doppler velocimetry. Turk J Chem 30(6):297–305
49. Wiklund J, Shahram I, Stading M (2007) Methodology for in-line rheology by ultrasound Doppler velocity profiling and pressure difference techniques. Chem Eng Sci 62:4277–4293
50. Thompson RS, Tortoli P, Aldis GK (2000) Selective transmission of a focused Doppler ultrasound beam through a plastic layer. Ultrasound Med Biol 26(8):1333–1346
51. Dogan N, McCarthy MJ, Powell RL (2005) Measurement of polymer melt rheology using ultrasonics-based in-line rheometry. Measurement Sci Technol 16:1684–1690
52. Petit P, Birkhofer B, Lootens D (2010) Wall shear measurement based on ultrasonic velocimetry for process in-line rheometry. In: Wiklund J, Bragd EL, Manneville S (eds) Proceedings, 7th international symposium on ultrasonic Doppler methods for fluid mechanics and fluid engineering, pp 17–20
53. Choi YJ, McCarthy KL, McCarthy MJ (2005) A MATLAB graphical user interface program for tomographic viscometer data processing. Comput Electron Agric 47(1):59–67
54. Wilkinson WL (1960) Non-Newtonian fluids: fluid mechanics, mixing and heat transfer, vol 1. Pergamon, London
55. Wiklund J, Johansson M, Shaik J, Fischer P, Windhab E, Stading M, Hermansson A-M (2002) In-line ultrasound based rheometry of industrial and model suspensions flowing through pipes. In: Papers of the third international symposium on ultrasonic Doppler methods for fluid mechanics and fluid engineering. EPFL Lausanne, Paul Scherrer Institut, pp 69–76

56. Wiklund J, Stading M (2008) Application of in-line ultrasound Doppler-based UVP-PD rheometry method to concentrated model and industrial suspensions. Flow Meas Instrum 19(3–4):171–179
57. Kotze R, Wiklund J, Haldenwang R, Fester VG (2010) Measurement and analysis of flow behaviour in complex geometries using ultrasonic velocity profiling (uvp) technique. Flow Meas Sci J 22(2):110–119
58. Jorgensen JE, Campau DN, Baker DW (1973) Physical characteristics and mathematical modeling of pulsed ultrasonic flowmeter. Med Biol Eng 11(4):404–421
59. Jorgensen JE, Garbini JL (1974) An analytical procedure of calibration for the pulsed ultrasonic Doppler flow meter. Trans ASME/J Fluids Eng 96:158–167
60. Hughes PE, How TV (1993) Quantitative measurement of wall shear rate by pulsed Doppler ultrasound. J Med Eng Technol 17(2):58–64
61. Hughes PE, How TV (1994) Pulsatile velocity distribution and wall shear rate measurement using pulsed Doppler ultrasound. J Biomech 27(1):103–110
62. Tortoli P, Guidi G, Newhouse VL (1995) Improved blood velocity estimation using the maximum Doppler frequency. Ultrasound Med Biol 21(4):527–532
63. Ouriev B (2002) Investigation of the wall slip effect in highly concentrated disperse systems by means of non-invasive UVP-PD method in the pressure driven shear flow. Colloid J 64(6):740–745
64. Wunderlich T, Brunn PO (1999) Ultrasound pulse Doppler method as a viscometer for process monitoring. Flow Meas Instrum 10(4):201–205
65. Ouriev B, Windhab EJ (2002) Rheological study of concentrated suspensions in pressure-driven shear flow using a novel in-line ultrasound Doppler method. Exp Fluids 32:204–211
66. Brunn PO, Wunderlich T, Müller M (2004) Ultrasonic rheological studies of a body lotion. Flow Meas Instrum 15(3):139–144
67. Powell R, Pfund D (2005) Non-invasive diagnostics for measuring physical properties and processes in high level wastes. Technical report, University of California Davis (US). http://www.osti.gov/bridge/product.biblio.jsp?osti_id=841672
68. Kotzé R, Haldenwang R, Slatter P (2008) Rheological characterisation of highly concentrated mineral suspensions using an ultrasonic velocity profiler. In: Chara Z, Bareš V (eds) Proceedings, 6th international symposium on ultrasonic Doppler methods for fluid mechanics and fluid engineering, pp 99–102
69. Norton I, Spyropoulos F, Cox P, Birkhofer B (2010) Doppler ultrasound-based rheology. In: Norton I, Spyropoulos F, Cox P (eds) Practical food rheology: an interpretive approach. Wiley Online Library
70. Murai Y, Tasaka Y, Sakurai K, Oyama K, Takeda Y (2010) Ultrasound Doppler rheometry from spin response of viscoelastic and bubbly Liquids. In: Proceedings, 7th international symposium on ultrasonic Doppler methods for fluid mechanics and fluid engineering, pp 9–12
71. Murai Y, Sakurai K, Oyama K, Tasaka Y, Takeda Y (2010) Ultrasound Doppler rheometry for viscoelastic liquids. In: Proceedings, 5th Pacific rim conference on rheology (USB Book of Abstracts) A-2-4:1–2
72. Oyama K, Tasaka Y, Murai Y, Takeda Y (2009) Ultrasonic investigation of oscillating pipe flow of visco-elastic fluid. In: Proceedings, international Symposium on food rheology and structure, Zurich, pp 480–481
73. Wiklund J, Stading M, Pettersson AJ, Rasmuson A (2006) A comparative study of UVP and LDA techniques for pulp suspensions in pipe flow. AIChE J 52(2):484–495
74. Birkhofer BH, Jeelani SAK, Windhab EJ, Ouriev B, Lisner KJ, Braun P, Zeng Y (2008) Monitoring of fat crystallization process using UVP-PD technique. Flow Meas Instrum 19(3–4):163–169
75. Dogan N, McCarthy MJ, Powell RL (2003) In-line flow and rheology measurements of complex, opaque fluids with velocimeter based rheometry using ultrasonics. In: Fischer P, Marti I, Windhab EJ (eds) Proceedings, 3rd international symposium on food rheology and structure (ISFRS 2003), pp 453–454
76. Rosensweig RE (1985) Ferrohydrodynamics. Dover, New York, Chapter 2

77. Ido Y (2005) Basic equations and constitutive equations of micropolar magnetic fluids with E-B analogy and the Abraham expression of electromagnetic momentum. JSME Int J Ser B 48:488–493
78. Kamiyama S, Koike K, Oyama T (1983) Pipe flow resistance of magnetic fluids in a nonuniform transverse magnetic field. J Magn Magn Mater 39:23–26
79. Motozawa M, Chang J, Sawada T, Kawaguchi Y (2010) Effect of magnetic field on heat transfer in rectangular duct flow of a magnetic fluid. Phys Procedia 9:190–193
80. Iwamoto Y, Yamaguchi H, Niu XD (2011) Magnetically-driven heat transport device using a binary temperature-sensitive magnetic fluid. J Magn Magn Mater 323:1378–1383
81. Ohno K, Suzuki H, Sawada T (2011) Analysis of liquid sloshing of a tuned magnetic fluid damper for single and co-axial cylindrical containers. J Magn Magn Mater 323:1389–1393
82. Ferrotec Corporation home page: http://www.ferrotec.com/
83. Bulte JWM (2005) Magnetic nanoparticles as markers for cellular MR imaging. J Magn Magn Mater 289:423–427
84. Pankhurst QA, Connolly J, Jones SK, Dobson J (2003) Applications of magnetic nanoparticles in biomedicine. J Phys D: Appl Phys 36:R167–R181
85. Jordan J et al (1999) Magnetic fluid hyperthermia (MFH): cancer treatment with AC magnetic field induced excitation of biocompatible superparamagnetic nanoparticles. J Magn Magn Mater 201:413–419
86. Kikura H, Takeda Y, Durst F (1999) Velocity profile measurement of the Taylor vortex flow of a magnetic fluid using the ultrasonic Doppler method. Exp Fluids 26:208–214
87. Sawada T, Kikura H, Tanahashi T (1999) Kinematic characteristics of magnetic fluid sloshing in a rectangular container subject to non-uniform magnetic fields. Exp Fluids 26:215–221
88. Yamanaka G, Kikura H, Takeda Y, Aritomi M (2002) Flow measurement on an oscillating pipeflow near the entrance using the UVP method. Exp Fluids 32:212–220
89. Motozawa M, Iizuka Y, Sawada T (2008) Experimental measurements of ultrasonic propagation velocity and attenuation in a magnetic fluid. J Phys Cond Mater 20:204117
90. Jeyadevan B, Nakatani I (1999) Characterization of field-induced needle-like structures in ionic and water-based magnetic fluids. J Magn Magn Mater 201:62–65
91. Pipkin AC (1964) Annular effect in viscoelastic fluids. Phys Fluids 7:1143–1146
92. Di Prima RC, Swinney HI (1981) Instabilities and transition in flow between concentric rotating cylinders. Hydrodynamic instabilities and the transition to turbulence. Top Appl Phys 45:139–180
93. Escudier MP, Gouldson IW, Jones DM (1994) Circular Couette flow and Taylor vortices in shear-thinning liquids. In: Adrian RJ et al. (eds) Development in Laser Techniques and Applications to Fluid Mechanics, Springer-Verlag, Berlin
94. Murai Y, Fujii H, Tasaka Y, Takeda Y (2006) Turbulent bubbly channel flow investigated by ultrasound velocity profiler. J Fluid Sci Technol 1–1:12–23
95. Gonzalez SR, Murai Y, Takeda Y (2009) Ultrasound based gas–liquid interface detection in gas–liquid two phase flows. Adv Chem Eng 37:1–27
96. Murai Y, Oiwa H, Sasaki T, Kondou K, Yoshikawa S, Yamamoto F (2005) Backlight imaging tomography for gas–liquid two-phase flow in a helically coiled tube. Meas Sci Technol 16:1459–1468
97. Murai Y, Inaba K, Takeda Y, Yamamoto F (2007) Backlight imaging tomography for slug flows in straight and helical tubes. Flow Meas Instrum 18:223–229
98. Minagawa H, Fukazawa T, Nakazawa Y, Yamada S, Shiomi Y (2006) Measurement of averaged liquid velocity field around large bubbles using UVP. Trans JSME Ser B 72:345–352
99. Minagawa H, Yamada S, Yasuda T, Shiomi Y (2008) Effect of pipe diameter on the flow field around single large bubble rising in stagnant water in a vertical pipe. Jpn J Multiphase Flow 22–2:154–160
100. Minagawa H, Yamada S, Yasuda T, Shiomi Y (2008) Effect of liquid viscosity on the average velocity field around single large bubbles in a vertical pipe. Trans JSME Ser B 74(740):811–817
101. Zhou S, Suzuki Y, Aritomi M, Matsuzaki M, Takeda Y, Mori M (1998) Measurement system of bubbly flow using ultrasonic velocity profile monitor and video data processing unit. (III)

Comparison of flow characteristics between bubbly cocurrent and countercurrent flows. J Nucl Sci Technol 35:335–343

102. Suzuki Y, Nakagara M, Aritomi M, Murakawa H, Kikura H, Mori M (2002) Microstructure of the flow field around a bubble in counter-current bubbly flow. Exp Thermal Fluid Sci 26:221–227
103. Murakawa H, Kikura H, Aritomi M (2003) Measurement of liquid turbulent structure in bubbly flow at low void fraction using ultrasonic Doppler method. J Nucl Sci Technol 40:644–654
104. Durst F, Melling A, Whitelaw JH (1981) Principle and practice of laser Doppler anemometry. Academic, London
105. Tropea C (1983) A note concerning the use of a one-component LDA to measure shear stress terms. Exp Fluids 1:209
106. Tezuka K, Wada S, Endo T, Oshimi H (2009) Number densities of micro bubbles suited to the ultrasonic Doppler method. In: Proceedings of JSME Fludis Engng Conf 2009. CD-ROM No. 1805
107. Wada S, Endo T, Tezuka K, Uenishi Y (2009) Evaluation of open-channel flow rate measurement at hydraulic power station using ultrasonic pulse-Doppler velocity-profile method. Proc Inst Elect Eng Jpn 7:130
108. Ito D, Kikura H, Aritomi M, Wada S (2009) Simultaneous measurement of bottom shape and flow rate in open channel using ultrasonic array sensor. In: Proceedings of JSME Fludis Engng Conf 2009. CD-ROM No. 1808
109. Japanese Electrotechnical Committee (1992) Standard of the Japanese Electrotechnical Comittee (Chapt. 7). Denkishoin, Japan
110. Tezuka K, Suzuki T, Mori M, Kanamine T (2005) Application of ultrasonic pulse-Doppler velocity-profile flowmeter for hydraulic power plant. In: Proceedings of JSME Fludis Engng Conf 2005. CD-ROM No. 1109
111. Tezuka K, Mori M, Suzuki T, Kanamine T (2008) Ultrasonic pulse-Doppler flow meter application for hydraulic power plants. Flow Meas Instrum 19(3–4):155–162
112. Suzuki T, Tezuka K, Mori M (2006) industrial application of new type flow-metering system using ultrasonic-Doppler profile-velocimetry. In: 23rd IAHR symposium on hydraulic machinery and system, p 263
113. Yokoyama H, Kojima S, Okubo T, Tasaka Y, Takeda Y, Yoshida S (2006) Environmental flow measurement using ultrasonic velocity profiler. Trans JSME Ser B 72(719):1694–1701
114. Heil M (1997) Stokes flow in collapsible tubes: computation and experiment. J Fluid Mech 353:285–312
115. Grotberg JB, Jensen OE (2004) Biofluid mechanics in flexible tubes. Annu Rev Fluid Mech 36:121–147
116. Nahar S, Jeelani SAK, Windhab EJ (2012) Influence of elastic tube deformation on flow behavior of a shear thinning fluid. Chem Eng Sci 75:445–455
117. Lew HS, Fung YC, Lowenstein CB (1971) Peristaltic carrying and mixing of chyme in the small intestine (an analysis of a mathematical model of peristalsis of the small intestine). J Biomech 4:297–315
118. Yin FCP, Fung YC (1971) Comparison of theory and experiment in peristaltic transport. J Fluid Mech 47(1):93–112
119. Weinberg SL, Eckstein EC, Shapiro AH (1971) An experimental study of peristaltic pumping. J Fluid Mech 49(3):461–479
120. Rao AR, Mishra M (2004) Peristaltic transport of a power-law fluid in a porous tube. J Non-Newtonian Fluid Mech 121:163–174

Chapter 6
Industrial Applications

Noriyuki Furuichi, Beat Birkhofer, Yuichi Murai,
A.K. Jeelani Shaik, Johan Wiklund, and Erich J. Windhab

Abstract Because of many advantages of ultrasonic velocity profile (UVP) measurement, the range of industrial applications is very wide. In this chapter, flowrate measurement, food and suspension flow, and measurement around a ship are introduced as examples of applications for UVP measurement in the industrial field. In the fields of flowrate measurement, studies concerning with the accuracy of this flowrate measurement method and calibration results of an actual flow are described, including application examples such as open channel and multi-line measurement. In the field of food and suspension flow, taking advantage of its applicability to opaque fluid, a velocity measurement is performed for fluid such as tomato soup and chocolate. Using the in-line UVP+PD method, measurements of transient flow such as thermal processing and liquid displacement, which are very important in the food industry, are performed. Measurement around a ship is an application example taking advantage of the compact installation possible for an ultrasonic sensor. Ultrasonic

---

N. Furuichi (✉)
National Metrology Institute of Japan, National Institute of Advanced
Industrial Science and Technology (AIST),
1497-1 Teragu, Tsukuba 300-4201, Japan
e-mail: furuichi.noriyuki@aist.go.jp

B. Birkhofer
Sika Services AG, Zürich, Switzerland

Y. Murai
Faculty of Engineering, Hokkaido University, Sapporo, Japan

A.K.J. Shaik • E.J. Windhab
Institute of Food, Nutrition and Health, Swiss Federal Institute of Technology Zürich
(ETH-Zürich), Zürich, Switzerland
e-mail: jeelani@ethz.ch; erich.windhab@hest.ethz.ch

J. Wiklund
The Swedish Institute for Food and Biotechnology (SIK), Göteborg, Sweden

Y. Takeda (ed.), *Ultrasonic Doppler Velocity Profiler for Fluid Flow*,
Fluid Mechanics and Its Applications 101, DOI 10.1007/978-4-431-54026-7_6,

transducers are installed on the bottom of the actual ship, and measurement examples of velocity profile and Reynolds stress are introduced.

Keywords Flowrate • Food • Ship

6.1 Flowrate Measurements

6.1.1 *Overview and Problems of Current Ultrasonic Flow Meters*

The ultrasonic flow meter is used in many places in industry these days because it has many advantages over other types of flow meter as a result of small pressure loss, wide range of flowrate and pipe size, clamp-on installation, and free maintenance, etc. On the other hand, flowrate given by ultrasonic flow meter is strongly influenced by the velocity profile in the pipe. There is a possible erroneous value measured if the velocity profile in the pipe is not realized as expected because of such factors as distorted flow and swirl flow. This disadvantage might be overcome by adopting multiple line measurement. It is, however, limited by space limitation on installing transducers on a pipe wall, as well as the high cost of instrumentation.

Basically, a volumetric flowrate is estimated from the bulk velocity of flowing fluid multiplied by the cross-sectional area of the pipe. There are several methods to measure bulk velocity. For instance, an electromagnetic flow meter measures an electromotive force that is in proportion to the bulk velocity. A turbine flow meter adopts a measurement of the rotating speed of the turbine installed in the flow that is proportional to the bulk velocity.

An ultrasonic flow meter currently on the market is based on a transit-time method; it measures the bulk velocity using line-averaged velocity information along the ultrasonic path. The principle of the transit-time ultrasonic flow meter is shown in Fig. 6.1.

Flowrate Q is obtained by measuring a time-of-flight (TOF) shown as $t_{A \to B}$, $t_{B \to A}$ between the transducer A and B and estimated as

$$Q = V_{\mathrm{b}} A = \left(\frac{V_{\mathrm{L}}}{k} \right) A \tag{6.1}$$

$$V_{\mathrm{L}} = \frac{L(t_{B \to A} - t_{A \to B})}{2 \sin \alpha \, t_{B \to A} t_{A \to B}} \tag{6.2}$$

Here, V_{b} is a bulk velocity, V_{L} is a line-averaged velocity along the ultrasonic path, A is an area of the pipe, and k is a correction factor to assumption of the velocity profile. As is noted from the equations, only a line-averaged velocity is measured in

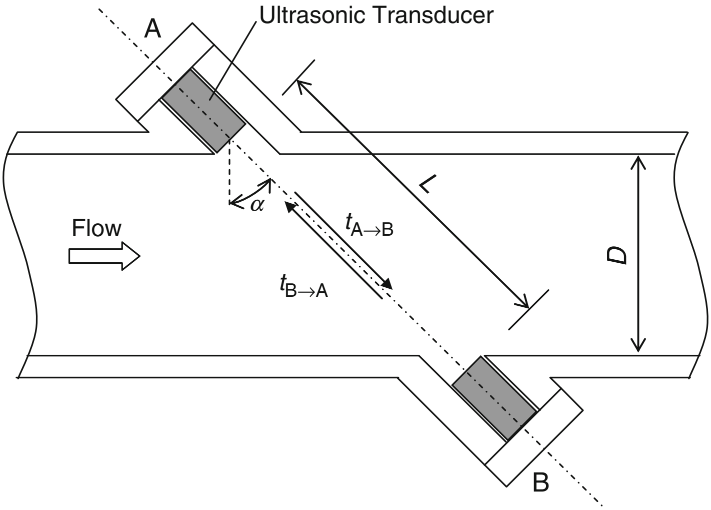

Fig. 6.1 Schematic of transit-time ultrasonic flow meter

the flow meter. Then, the flowrate estimation needs to use a correction factor k to compensate departure from the assumption on the velocity profile in a pipe. The use of this correction factor is a fundamental problem of the principle of this type of flow meter and makes it difficult to realize high accuracy for the results.

It is well known that a velocity profile in a pipe changes depending on upstream conditions such as straight pipe length and some obstacles. Moreover, a velocity profile depends on the Reynolds number of the flow. Therefore, the correction factor k has to be calibrated and adjusted by the flow condition, which induces regressively a degradation of the measurement accuracy of the flow meter. Manufacturers normally suggest and require keeping a sufficient upstream length from the installation point to realize a nominal high accuracy. In reality, this is difficult to do, and the condition depends on the site of installation. Moreover, the effect of the temperature and viscosity of the working fluid must be incorporated into an accuracy estimation. These difficulties are intrinsic disadvantages of the current ultrasonic flow meters.

6.1.2 Flowrate Measurement by the UVP Method

6.1.2.1 Principle

The development of an ultrasonic flow meter based on the velocity profile measurement was started in the 1990s for a pipe flow, and then development studies were made for a wide range of flow fields. The feature that no correction or calibration is needed is revolutionary because the measurement is not influenced by an upstream condition of the flow channel. Here we describe a flowrate measurement for a flow in a circular pipe.

Flowrate is defined as a volume of fluid passing a cross section of the pipe where a velocity is distributed. Using a cylindrical coordinate system, it is given as the following equation:

$$Q(t) = \iint V_z(r,\theta,t) r \,\mathrm{d}r \,\mathrm{d}\theta \tag{6.3}$$

Here we assume that a flow is axially symmetric and the axial component V_z is one dimensional, only neglecting the radial component V_r (=0). A flowrate can be estimated by measuring the velocity profile in pipe with measurement angle α:

$$Q(t) = 2\pi \int V_z(r,t) / \sin(\alpha) r \,\mathrm{d}r \tag{6.4}$$

This result indicates that a flowrate measurement based on velocity profile measurement is simplified to require only a single measurement line of UVP. It should be noted that, in most cases where a conventional flow meter is installed, flow condition for the assumption adopted here is realized because the assumption is also involved a priori for those instrumentations. It is therefore promising that this method might eliminate a problem of using k factor [correction factor in Eq. (6.1)]. This idea also implies that the flowrate measurement is not affected by upstream condition and Reynolds number.

Another advantage of the UVP method is its capability of clamp-on-type of installation on the existing pipe, which is a characteristic of conventional flow meters other than the ultrasonic flow meter.

6.1.2.2 Measurement Example

The confirmation experiment was performed [1] using a pipe flow where the valve installed downstream of the test section was switched on and off. The obtained flowrate was compared with data measured by an electromagnetic flow meter and an orifice flow meter operated simultaneously on the same line (Fig. 6.2). It is clearly shown that the temporal response of the flowrate measurement is as good as that of the orifice flow meter to show good agreement of even a small fluctuation of the flow. This result indicates that this type of flow meter might be suitable for measuring the transient behavior of flow loops in plants.

Regarding the accuracy of measured flowrate, a time-averaged value of such time-dependent results can only be studied in comparison with the data at any flow calibration standard of meteorological offices. One such typical comparison was performed by Mori et al. [1] at NIST, which shows an excellent result within a difference of about 0.1%. The accuracy of this method is discussed later in this section.

Application to a large pipe was tested by Tezuka et al. [2] for a pipe diameter of 2 m at a hydraulic electric power plant. The result was compared with Pitot tube measurement (Fig. 6.3). The detailed measurement method is described in Sect. 5.7.

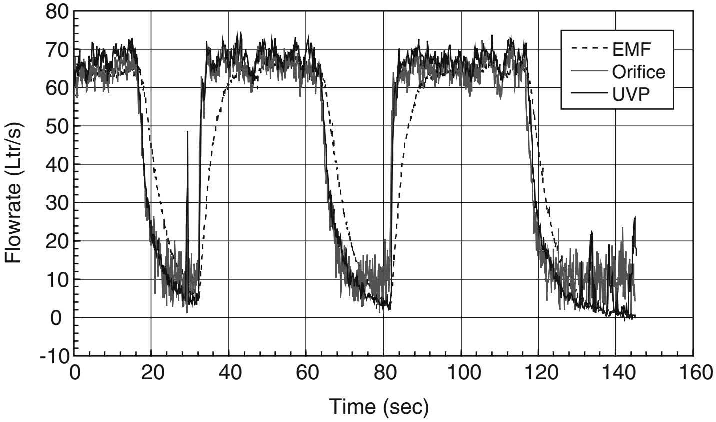

Fig. 6.2 Example of flowrate measurement by UVP method [1] (with kind permission from Springer Science+Business Media)

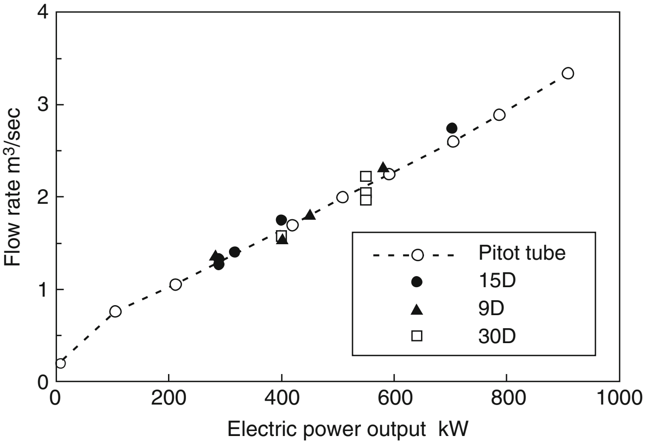

Fig. 6.3 Flowrate measurement in a large pipe at a hydraulic electric power plant (reprinted from [2] with permission from Elsevier)

Flowrate measurement in a very large pipe is difficult because the flow meter to be used cannot be easily calibrated and, on site, entry length upstream of the flow meter is not sufficiently long to fulfill the installation conditions. Flow metering using the UVP principle is promising in this application also because it does not require a long upstream length.

6.1.2.3 Application Example

Flowrate Measurement by Multi-line Method

Single-line flow metering assumes axisymmetry of the flow in a pipe, as was already given. However, it is well known that upstream pipe configuration such as

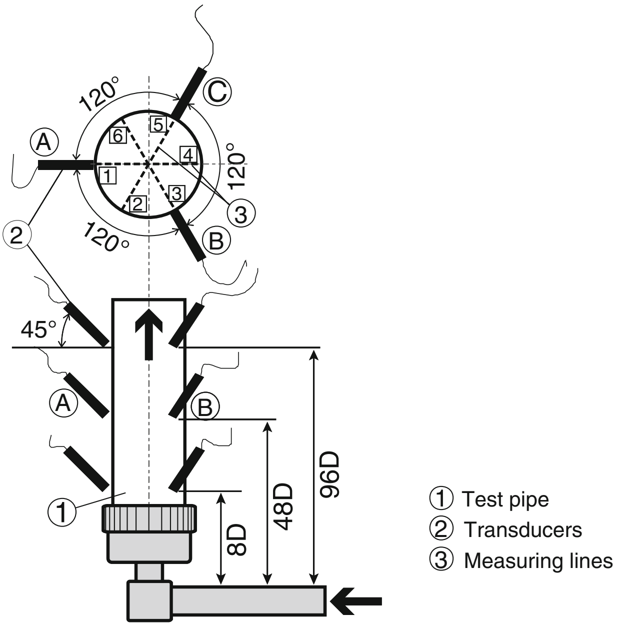

Fig. 6.4 Flowrate measurement by multiple lines [3] (reprinted by permission of the publisher (Taylor & Francis Ltd, http://www.tandf.co.uk/journals).)

T-branching or bends induces asymmetry of the velocity distribution, which remains even over a long distance of the flow channel. Use of a flow straightener or a flow rectifier such as a perforated plate hardly helps to compensate for this flow asymmetry. This configuration often degrades the accuracy of the measured results. To cover this discrepancy and to maintain high accuracy, multiple measurement lines are used. The method corresponds to performing integration on the azimuthal direction in the basic definition equation (6.1). The basic equation to calculate flowrate using N measuring lines is

$$Q(t) = \sum \left\{ \Delta\theta \int V_z(r,\theta,t) / \sin(\alpha) r \, \mathrm{d}r \right\} \tag{6.5}$$

Here, $\Delta\theta = 2\pi/N$, where N is the number of measurement lines. Multiple-line flow metering was studied by Wada et al. [3] on the effect of upstream bends in terms of measurement accuracy with respect to the number of measurement lines at various upstream distances (Figs. 6.4 and 6.5). At 8D, just after the bend, symmetry of the flow is broken, and single-line flowrate measurement gives a scattering of the results depending on the azimuthal position of the measurement line. Even at 96D, the accuracy cannot reach below 1%. However, with three measurement lines, accuracy has been improved significantly below 1%. They also concluded that three measurement lines on the diameter, that is, six radii ($N = 6$), can reduce the accuracy to the significant level and a larger number of measurement lines is not necessarily effective.

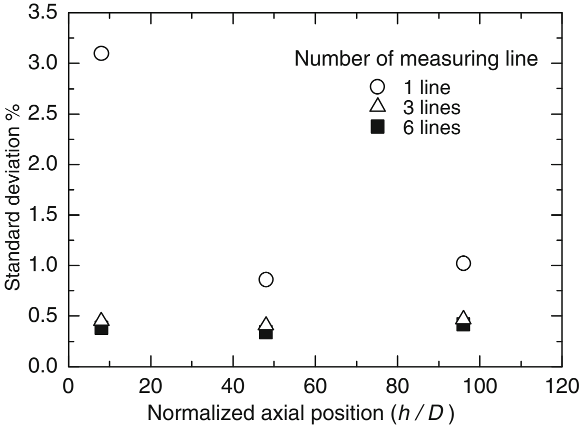

Fig. 6.5 Standard deviation for each measuring position with respect to the number of measuring lines [3] (reprinted by permission of the publisher (Taylor & Francis Ltd, http://www.tandf.co.uk/journals).)

Flowrate Measurement by Hybrid Method

In some industrial applications of flowrate measurement, it is not expected to have a sufficient amount of tracers in the fluid. To compensate for the weakness of the UVP method, which requires tracers, there is a hybrid system in which the UVP method can be used in combination with the TOF method [4]. This combination is complementary for both methods. Where the fluid includes too many bubbles, the TOF method does not work, whereas the UVP method works when there are too few bubbles. It is also possible to perform a simultaneous evaluation of *k* factor for the TOF-type flow meter when the UVP method can obtain a velocity profile and evaluate the flowrate on site. A commercial product using this concept has been developed and marketed by Fuji Electric [5].

Flowrate Measurement at an Open Channel

Flow with a free surface such as an open channel and partially filled pipe flow can be found in many places and situations in nature and industry, for instance, in rivers, agricultural canals, and water and sewer services. Flowrate measurements in these configurations are normally performed by using a weir flow meter, flume-type and transit-time ultrasonic flow meters, and others. All these flow meters require use of a correction factor that modifies the measured value in comparison with an ideal or theoretical flow situation. In some cases, this correction factor is based on calibration, although such calibration is difficult to perform with high accuracy. Moreover, the time-dependent variation of the surface condition affects the accuracy to a large degree, and in a natural environment the geometric condition of the flow channel changes with time. Therefore, it is implausible to be able to provide a flow meter with high accuracy for these configurations. Flowrate measurement using UVP can be adopted for such flow configurations because it is based on direct measurement of the velocity profile and does not rely on the use of a correction factor. It is also

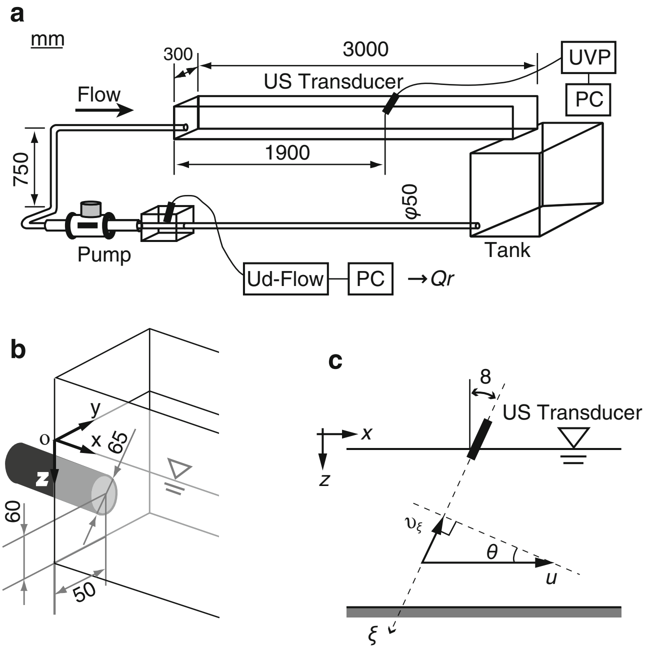

Fig. 6.6 Flowrate measurement at an open channel. (**a**) Schema of the facility. (**b**) Inlet section of the channel. (**c**) Configuration of the ultrasonic transducer

advantageous that change in geometry of the flow channel would hardly influence the measured results. Tasaka et al. [6] measured flowrate in an open channel and indicated that measurement accuracy can be obtained as high as 4% compared to a reference flowrate. Figure 6.6 shows an experimental apparatus for flowrate measurement at an open channel.

6.1.3 Measurement Accuracy of Flowrate by the UVP Method

Theoretical verification of measurement accuracy of flowrate using the UVP method was made by several researchers. Ohkubo et al. [7] discussed the error caused by discretization of the measuring point and by unsteadiness of the flow. They concluded that, with sufficient number of data points in the flow area and careful averaging time with respect to the temporal characteristics of the flow, total measurement accuracy of flowrate much less than 1% can be achieved. Yamanaka et al. [8] discussed the error caused by the measurement volume determined by beam size and pulse length. They concluded that this error is also about 1%.

A calibration using an actual flow was also performed to verify the accuracy of the UVP method. Before showing the results, an actual calibration method of a liquid flow meter is described here. A weighing method or a gravitational method is

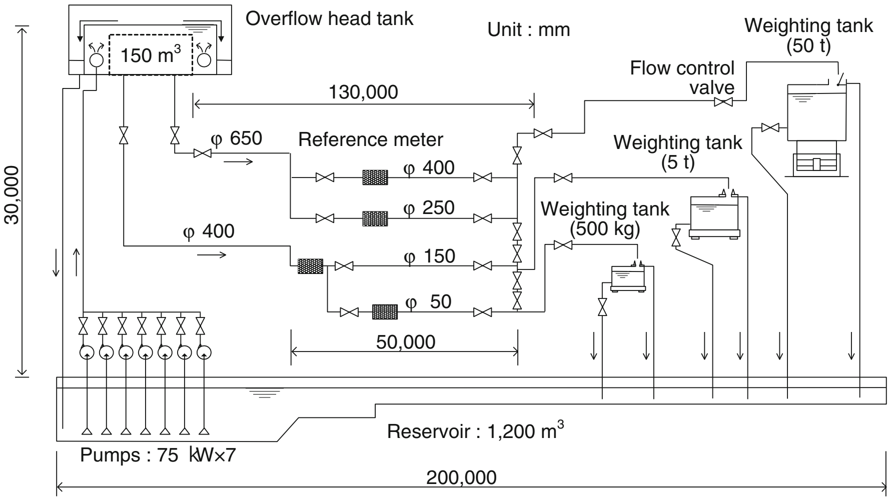

Fig. 6.7 Flowrate calibration facility

generally used for a liquid flow meter. These methods can calibrate an integrated value over some period of time but not an instantaneous value. In the weighing method, water fills a tank, normally called the weighing tank, for some time interval. The time-averaged flowrate is obtained by the volume converted from weight accumulated in the weighing tank divided by the measurement time. The actual flow calibration is carried out by a comparison between the flowrate by a meter under test and this standard flowrate.

The calibration facility of flowrate by weighing method at AIST, NMIJ in Japan, is described by Furuichi et al. [9]. Figure 6.7 shows a flow sheet of a flowrate calibration facility in NMIJ. From the overflow head tank, stable flow is supplied to the test section and the reference standard flowrate is obtained by the weighing system located downstream of the test section.

Regarding the accuracy of the meter under test, a deviation index E from a reference flowrate is defined as

$$E = (Q_{DUT} - Q_{Ref}) / Q_{Ref} \tag{6.6}$$

where the subscript DUT is the value indicated by the meter under test and Ref is the reference standard flowrate. The deviation means the difference between the flowrate indicated by the meter under test and the reference flowrate. A smaller deviation indicates higher accuracy of the meter. This index includes not only the error or inaccuracy by velocity profile but also other systematic errors caused by measurement of pipe diameter, measurement time, and other sources. On the other hand, the standard uncertainty of calibration is obtained by combining uncertainty

Table 6.1 Examples of calibration at national standard (reprinted from [11] with permission from Elsevier): *upper*, NIST; *lower*, NMIJ

Average flowrate of reference meter (l/min)	Average flowrate of UdFlow (l/min)	Deviation (%)	Combined standard uncertainty (%)	Expanded uncertainty (%)
69.611	69.634	0.032	0.1541	0.308

Average flowrate of reference meter (l/min)	Average flowrate of UdFlow (l/min)	Deviation (%)	Combined standard uncertainty (%)	Expanded uncertainty (%)
2,000.5	2,000.8	0.421	0.1442	0.288
1,512.7	1,508.2	–0.294	0.0390	0.078
986.1	984.6	–0.147	0.0890	0.178

of the calibration facility u_F and standard deviation of calibration σ according to GUM [10]:

$$u_{DUT} = \sqrt{u_F{}^2 + \sigma^2 / n} \tag{6.7}$$

This is, however, an uncertainty of the calibration coefficient but not an accuracy of the flow meter under test.

For estimating the uncertainty of a flow meter, not only uncertainty by calibration as expressed by Eq. (6.7) but also deviation from reference flowrate, as Eq. (6.6), must be combined. Furthermore, other factors such as repeatability and reproducibility that arise from the protocol of the calibration procedure must also be included. If necessary, the effects of upstream pipe condition such as elbows and valves, and the surface roughness of the pipe, effect of temperature, and pressure of working fluid should be included. It is recommended to use GUM in the detailed estimation of uncertainty of the flow meter.

The calibration results for flowrate measurement by the UVP method at the national standard are given by Tezuka et al. [11]. Examples of the calibration results are shown in Table 6.1. The calibration was made at NIST in the USA and NMIJ in Japan. They reported that a deviation from the reference flowrate is as low as –0.534% to 0.421%. This finding indicates that flowrate measurement by the UVP method can work well with high accuracy because this measurement method is a direct measurement of the volumetric flowrate and needs no correction factor to obtain the flowrate.

6.2 Food and Other Suspension Flow

6.2.1 Transient Flows and Process Monitoring

Technical advances in recent years in electronics but also optimized processing have enabled real-time process monitoring and control. The UVP+PD method can thus now be used to monitor changes in rheology, with respect to changes in profile shape and in rheological parameters, in industrial unit operations such as rapid startup or shutdown of the process, crystallization and liquid displacements during rinsing or product change, in-line mixing, and thermal processing.

6.2.1.1 Polymer Melt Flows and Effects of Thermal Processing

In in-line rheological measurements of a polymer melt were investigated in steady tube flow using the UVP+PD method [12]. Experimental results with a polydimethylsiloxane melt showed that the shear viscosity can be measured over nearly one and one-half decades of shear rate from a single velocity profile with decreasing shear viscosity over this range of shear rates. In another study, the flow of non-Newtonian solution of Carbopol EZ-1 with sodium hydroxide was studied by Pfund et al. [13]. The changes in rheology with respect to changes in profile shape and in rheological parameters during thermal processing have also been studied by a few groups. Choi et al. [14] measured tomato concentrate physical properties during evaporation and correlated these properties to ultrasound properties and to measured fluid viscosities, obtained using in-line UVP+PD. Rapid changes in velocity profile shape and in rheological properties of a tomato-based soup resulting from thermal processing were recently studied under true aseptic processing conditions by Wiklund and Stading [15]. The UVP+PD method was used to measure instantaneous radial velocity profiles and viscosity in-line at the 40°C, 95°C, 120–140°C, and 60°C measuring locations corresponding to different temperature zones. Figure 6.8 shows measured mean velocity profiles at each measuring location averaged over 30 profiles. The profile shape changed from a more parabolic profile at 40°C (inlet) toward a blunter profile shape (outlet) during the thermal treatment. The velocity profiles measured near the outlet thus indicate a shift toward more shear-thinning behavior.

6.2.1.2 Liquid Displacements

Liquid displacement of one miscible or immiscible fluid by another is a very common and important process in the fluids industry. Typical situation examples are startup or shutdown of operations where, for example, a transition from water to product or vice versa takes place, for intermediate rinsing to prepare for a product change, or the use of the same filler for different products. Obvious reasons for monitoring the displacement zone are to ensure product integrity and reduce product loss, waste load, and related costs. The possibility to accurately monitor the displacement process, the related mixing zone, and the real-time changes in rheology of both model and industrial non-Newtonian fluids using the UVP+PD method was demonstrated by Regner et al. [16] and Wiklund et al. [17]. The velocity profile development, related mixing zone, and real-time changes in rheology were monitored when one fluid was displaced by another with different rheological properties. Four sets of model systems, all well described by the power law model and relevant

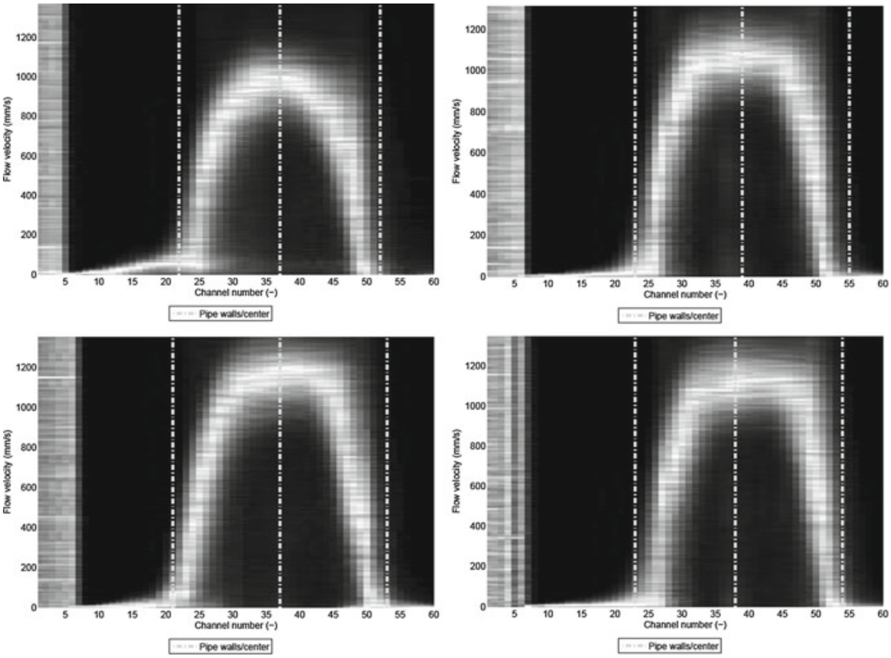

Fig. 6.8 Measured velocity profiles at the 40°C, 95°C, 120–140°C, and 60°C measuring locations corresponding to different temperature zones (replotted from the results of Wiklund and Stading [15])

for the food industry, were used to adequately cover different classes of fluids. In addition, two sets of industrially produced foods with similar flow characteristics were used to test the industrial applicability limitations of the UVP + PD method. Figure 6.9 shows an example of the measured temporal development and variation in the power law parameters: the consistency index, K, and flow index, n, over time for the displacement of a non-Newtonian Xanthan solution with Newtonian sunflower oil.

The results demonstrate that the in-line UVP + PD method is an attractive multipoint method for real-time process monitoring and control of non-Newtonian fluids.

6.2.1.3 Validation of CFD Simulation and Models

The UVP technique gives directly the one-dimensional (1-D) solution to the Navier–Stokes equations and has therefore recently been shown to be a promising new tool for validating, for example, computational fluid dynamics (CFD) simulations for predicting liquid displacement of one fluid by another in a pipe [16] and, recently, also heat transfer models for aseptic processing [15]. Detailed knowledge about the rheological flow properties of the product and how they change, for example, during

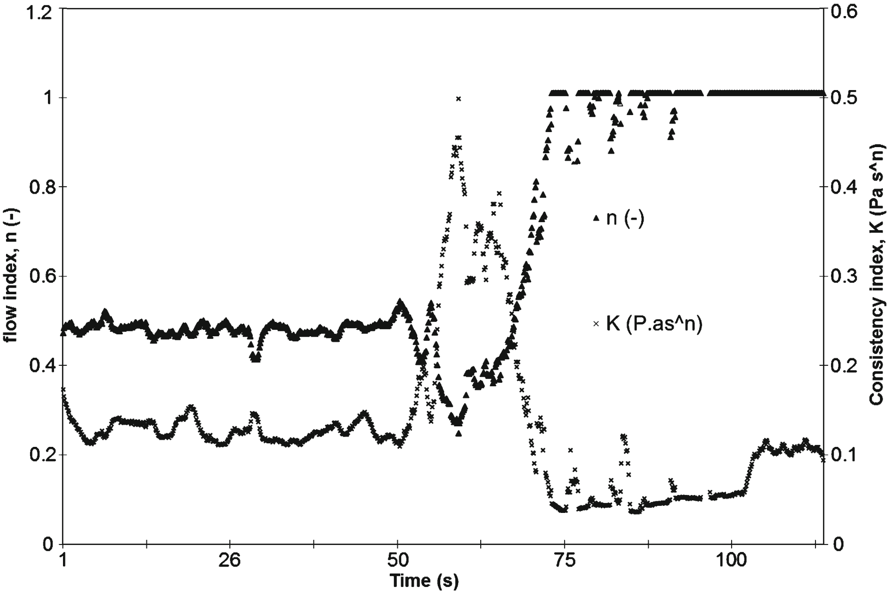

Fig. 6.9 Real-time development and variation in power law parameters: the consistency index, *K*, and flow index, *n*, over time for the displacement of Xanthan with sunflower oil (replotted from the results of Wiklund et al. [17])

thermal processing, is also of great interest for the design and operation of new and existing plants. A good example was presented by Regner et al. [16], who used the volume of fluid (VOF) method in CFD to predict the phase distribution, including the tailing effect, and velocity during the displacement of yogurt by water. The UVP+PD method was used to characterize the displacement, related mixing zone, and changes in rheology in real time, in-line, and it was demonstrated that results were in good agreement with CFD simulations. However, as shown in Fig. 6.10, the predicted velocity close to the wall was slightly higher than that measured using the UVP technique.

6.2.2 *Nucleation and Fat Crystallization*

The UVP+PD method combined with the measurement of sound velocity (related to crystal content) was shown, in several successive studies, to be an interesting approach for the in-line monitoring of nucleation and fat crystallization processes.

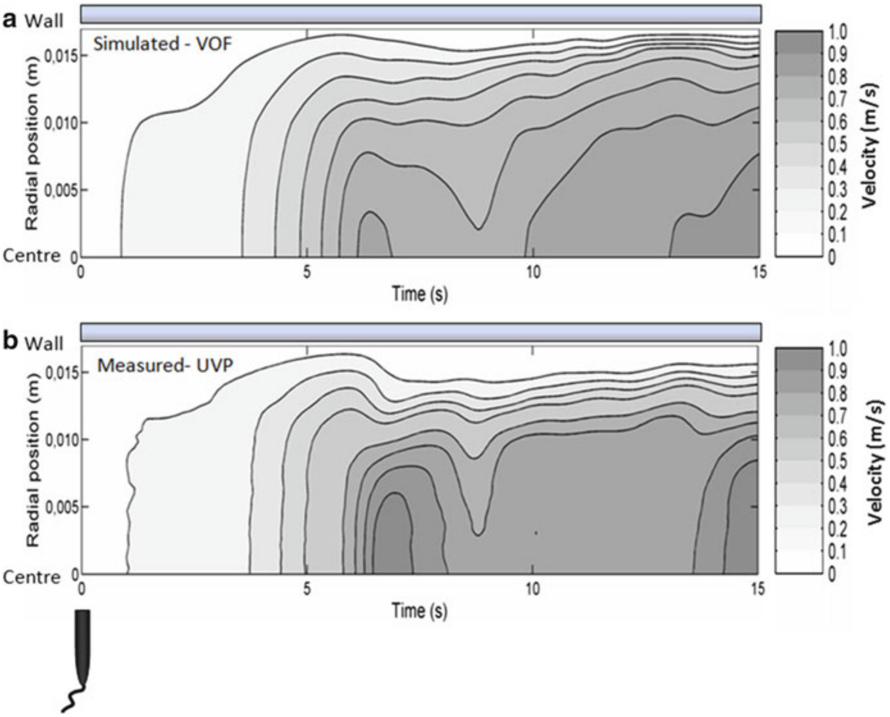

Fig. 6.10 (**a**) Velocity profile development with time during yogurt rinsing in a pipe measured horizontally using UVP. (**b**) Calculated using CFD. Each *gray level* indicates a change in velocity of 0.1 m/s between 0 and 1.0 m/s. The *dashed line* in (**b**) illustrates the interface between yogurt and water (replotted from the results of Regner et al. [16])

6.2.2.1 Fat Crystal Seeding of Chocolate

Ouriev [18] and Ouriev et al. [19] investigated concentrated chocolate suspension containing more than 60 wt% of solids. The measurement was performed at stable process conditions at temperatures between 29.5°C and 30.0°C. Two separate crystallization process cycles were carried out by injection of (1) 0.14 wt% and (2) 0.05 wt% additional solids, respectively, into two chocolate suspension mainstreams containing 60 wt% solids. A lower concentration of injected solids corresponds to a decrease of the flow velocity (Fig. 6.11a), where the calculation of the fit velocity profile was performed along the diameter distance *D* within the time delay between measurement and monitoring. The variation in viscosity with shear rate calculated using the power law model and the comparisons between off-line and in-line measurements [18, 19] are shown in Fig. 6.11b. The shear viscosity of precrystallized chocolate suspension with higher concentration (0.14 wt%) of injected solids is more than that with lower concentration (0.05 wt%) of injected solids into the liquid matrix. The positive offset and different slope of the curves can

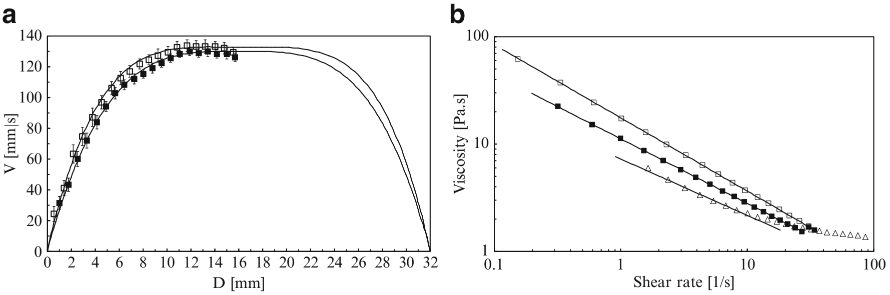

Fig. 6.11 (**a**) Experimental (*symbols*) and in-line fitted (*solid line*) velocity profiles during the injection of additional 0.14 wt% (*open squares*) and 0.05 wt% (*closed squares*) of solids into the chocolate suspension mainstream containing 60 wt% solids. *Vertical bars*, mean standard deviation. (**b**) Comparison of shear rate-dependent viscosity of the crystallized chocolate (*open and closed squares*) determined from in-line UVP measurements with those from off-line measurements (*triangles*) of molten chocolate suspension with less crystal concentration. *Solid lines*, calculated power law fit (replotted from the results of Ouriev [18] and Ouriev et al. [19])

be seen by the higher concentration of injected solids corresponding to an increased shear-thinning behavior. The shear rate-dependent viscosity of the molten chocolate measured using an off-line rheometer can be seen to be lower than those of the crystallized chocolates at two concentrations of the injected additional solids determined using an in-line UVP+PD method. The authors mentioned the difficulty of measurement of the shear rate-dependent viscosity of a highly concentrated crystallized chocolate suspension using an off-line rheometer.

6.2.2.2 Fat Crystallization in Cocoa Butter

The dynamic response of the cocoa butter shear crystallization process to a step reduction in temperature of a two-stage shear crystallizer was investigated using UVP+PD in another study by Birkhofer et al. [20]. The temporal variation in the velocity profile shape, the apparent viscosity at different shear rates, and the corresponding radial position in the pipe were determined by fitting the measured velocity profile and pressure drop to the power law rheological model. The liquid cocoa butter was found to be Newtonian with a parabolic profile shape, whereas the cocoa butter crystal suspension was found to be shear thinning, the value of the power law exponent decreasing with increase in solids (Fig. 6.12).

6.2.3 Concentration and Solid Fat Content

The UVP+PD method combined with the measurement of sound velocity and attenuation of ultrasound (related to crystal content) has been demonstrated to be

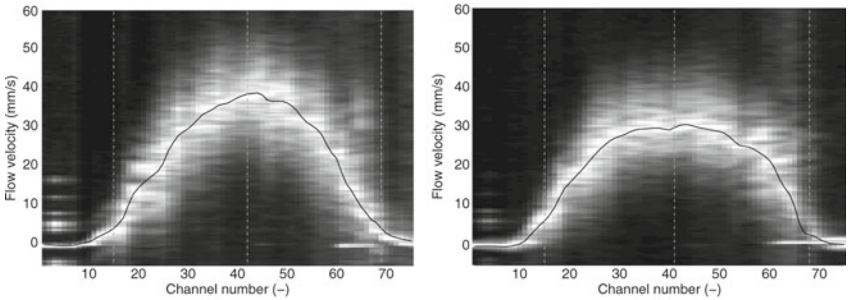

5 min 22.5 min

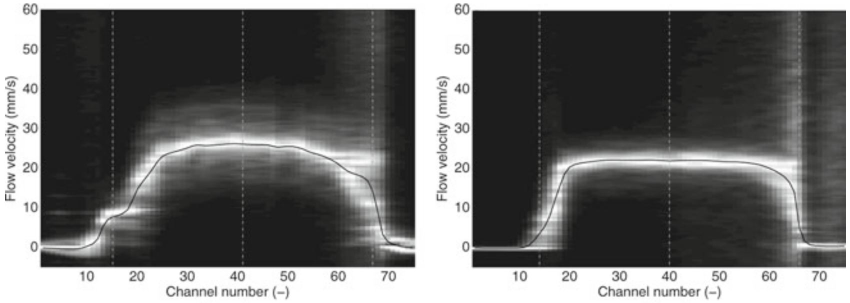

25 min 36 min

Fig. 6.12 Velocity profiles (average of 30 single profiles) in terms of channel-wise normalized baseband signal power spectra (gray-scale background). *Full lines*, estimated velocity profiles along the pipe diameter at different times after startup of shear crystallizer (reprinted from [20] with permission from Elsevier)

an interesting approach for the in-line determination of concentration of solids and solid fat content (SFC) in fat suspensions. Birkhofer et al. [20] determined SFC from sound velocity measurements using a calibration curve from ^{31}P-nuclear magnetic resonance (p-NMR) measurements. More recently, Young et al. [21] and Wassell et al. [22] developed the UVP + PD method further to enable determination of both SFC and rheological properties under true dynamic processing conditions directly in the processing line. It was demonstrated that the transient flow behavior from liquid to fully crystallized suspension could be monitored in real time and that SFC measurements in two-component systems demonstrate good agreement with the conventional p-NMR techniques; thus, it has good potential for replacing p-NMR as a standard method. The measurements can be made off-line, on the laboratory scale, or directly on the processing line [22]. An example of SFC values determined using both p-NMR and the ultrasonic method is shown in Fig. 6.13.

6.2.4 Flow Mapping in Complex Geometries

The UVP technique and the UVP + PD method have been shown to be promising new tools for flow mapping in complex geometries and possibly also for determining extensional viscosity of non-Newtonian fluids in line. A few examples are given next.

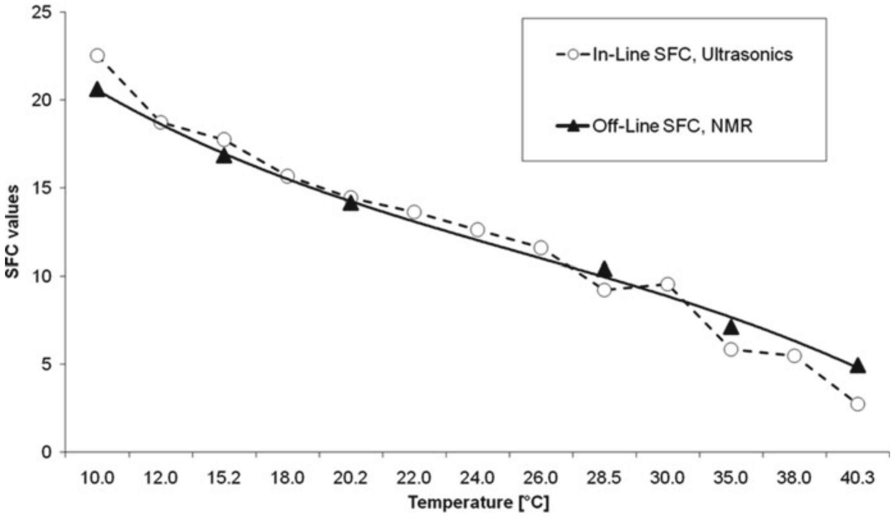

Fig. 6.13 Solid fat content (SFC) expressed as percentage values versus temperature for 30% palm strearin/70% rapeseed oil measured by standard p-NMR technique (*triangles*) and in-line dynamic conditions from UVP+PD (*circles*) (replotted from the results of Wassell et al. [22])

6.2.4.1 Abrupt Contraction: Die Entry

In an early study the UVP+PD method was used for die entry visualization in the flow of highly concentrated shear-thinning and shear-thickening suspensions [23]. A transducer pair was used to create a flow map in the narrow die but with limited spatial resolution because of limitations with the existing transducers.

6.2.4.2 Hyperbolic Contraction

Shear-thinning carboxymethyl cellulose (CMC) model fluids have been studied in hyperbolic contraction flow and in a diaphragm valve. The CMC was pumped through the hyperbolic nozzle, designed to give a constant extension rate. The radial velocities and profiles throughout the nozzle were determined using the UVP technique and were found to be in good agreement with the theoretical values. Axial velocity profiles confirmed the design criteria of constant extension rate throughout the nozzle, and that the UVP+PD method may be used to determine extensional viscosity in-line [24].

6.2.4.3 Diaphragm Valve

Velocity profiles were also measured at three different positions at the center (contraction) of a specially manufactured 50% open diaphragm valve. Experimental results obtained using UVP again showed good agreement with theoretical predictions. Results showed that the most important problem is that it is not possible to accurately measure from the transducer front, which is the result of the ultrasonic transducer near-field. This study confirmed that the problem may be eliminated by the introduction of a next-generation transducer, which is currently under development [25, 26].

6.3 Ship

The resistance of a moving ship is classified as wave resistance resulting from in-front wave generation and frictional resistance acting on the submerged surface caused by seawater. The wave resistance has been reduced considerably via a number of efforts in research and design made by ship builders, such as improvement of the bow shape. In contrast, frictional resistance has not been reduced, and it thus accounts for around 80% of the total drag for large vessels [27], which means simply that 80% of the fuel is consumed solely by the friction from seawater. The friction is governed by the dynamics in the turbulent boundary layer that is created at the ship surface submerged in seawater [28]. In this context, UVP is a potential tool for the assessment of the boundary layer structure [29]. In comparison with PIV and other velocimetry techniques, the advantages of UVP for seawater flow application are compact installation of the sensor on the surface of the ship body, toughness in a high-speed seawater flow environment, and real-time assessment of the unsteady flow field. In general, two types of velocity apply to a cruising ship. One is ground speed, which is the velocity of the ship relative to the Earth and can be measured with a Global Positioning System (GPS) device. The other is the velocity to current, which is the velocity of the ship relative to the local seawater current around the ship. The velocity to current is often measured for large vessels employing the time-of-flight method and low-frequency ultrasound. In comparison with the velocity to current, UVP is a more local measurement of the velocity profile such as inside the boundary layer or around the propeller.

6.3.1 Ark Test in a Pond

To determine potential technical problems in the field application of UVP to the seawater environment, a small ark (i.e., a box-type test float) was designed (Fig. 6.14a, b). The planar bottom plate was steel with thickness of 12 mm, which is the same as for a real ship including the chemical paint on the surface. An ultrasound transducer was attached beneath the plate, the front edge of which was inclined so that ultrasound pulse was emitted at an angle of 15° to the normal of the wall. The test was performed for multiple purposes, namely, assessment of the tracer concentration, stability of the electric power source in an isolated system,

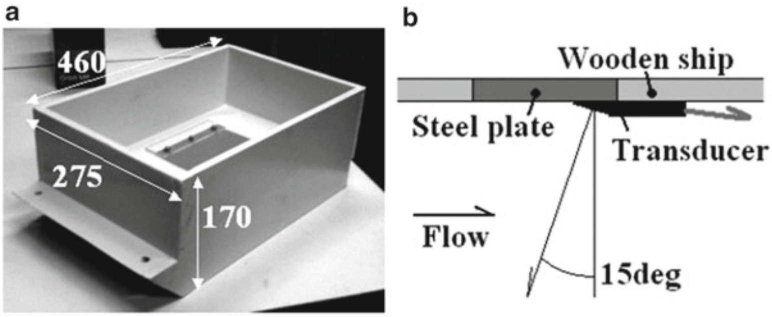

Ark for test transducer mount

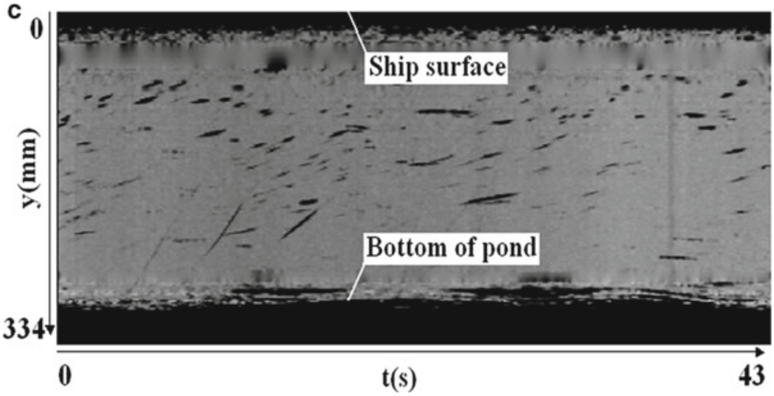

Fig. 6.14 Examination of velocity profiling with an ark in a pond. (**a**) Picture of the ark for the test. (**b**) Transducer mount and beam configuration. (**c**) Spatio-temporal velocity distribution beneath the ark

and effects of electromagnetic circumstance during wireless signal transport. Data quality, which changes with the type of oscillation of the ark's inclination, was also investigated. The basic frequency was 4 MHz, and the sampling interval was 27–43 ms in time and 1.48 mm in space. There was no artificial seeding for natural water.

In the UVP data, there was originally erroneous output near the wall from multiple reflections of the ultrasound pulse around the steel plate. Figure 6.14c presents the data after the erroneous layers were removed using spatiotemporal two-dimensional interpolation. The data have a basically uniform velocity distribution in the range above the bottom surface of the pond when the ark moves at a constant speed relative to stationary water in the pond. The data also show the bottom shape of the pond as a sudden change in velocity, which arises owing to a strong acoustic damping effect in the bottom soil. Furthermore, the moving-scanned distribution includes segment-like patterns that are caused by plants with long leaves and dot patterns that are caused by other suspensions.

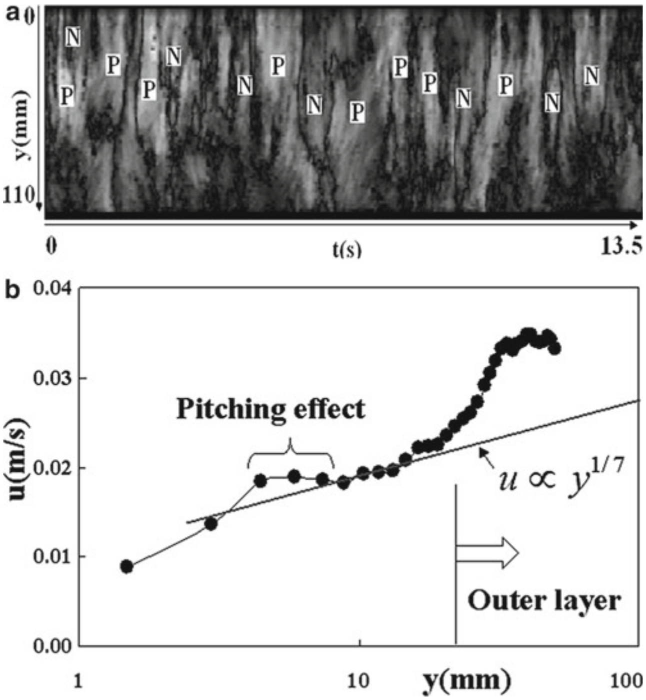

Fig. 6.15 (**a**) Velocity distribution obtained by ark in oscillatory state. (**b**) Semi-logarithmic profile of the time-averaged velocity

6.3.2 Influence of Ark's Oscillation

When the ark floats freely on the water surface, the velocity distribution has a striped pattern (Fig. 6.15a) owing to oscillation of the ark. In the figure, *P* and *N* represent positive and negative velocities, respectively. The stripe fluctuation appears because the emission angle of the pulse is nearly perpendicular to the bottom plane of the ark, and a slight inclination of the ark can thus be reflected as a change in the sign of the velocity. Such an effect is anticipated in a real ship application. The resonance frequency of the pitching mode for the test ark of simple rectangular shape is

$$f_n = \frac{\omega_n}{2\pi} = \frac{1}{4\pi}\sqrt{\frac{2g}{3h}} = 1.6\text{Hz} \tag{6.8}$$

where *h* is the submerged depth in water. The primary frequency estimated from the measured velocity distribution agrees with the theoretical frequency. The data also contain other types of oscillations from interaction between the ark's attitude and the flow field around the ark.

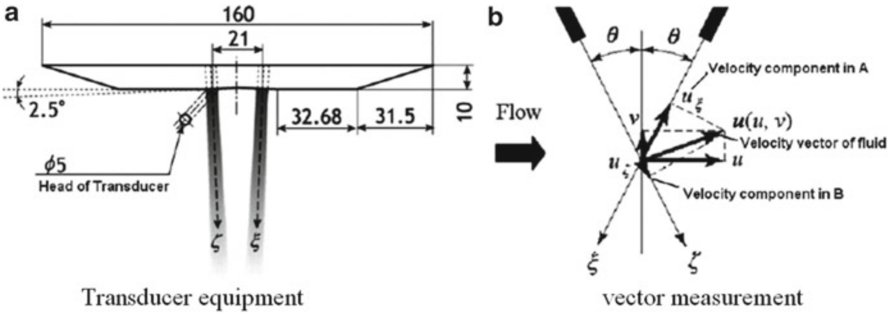

Fig. 6.16 Y-type angled-beam transducer (YABT) for ship application. (**a**) Schema of the transducer. (**b**) Beam configuration and vector formation

Figure 6.15b shows the semi-logarithmic profile of the time-averaged velocity as a function of the distance from the wall. The profile seems to obey the 1/7th law or standard logarithmic law in the short range within $10 < y < 30$ mm, but it deviates from the law in other ranges. In the layer at $y < 10$ mm, the upheaval of the profile means that the oscillation of the ark transports the momentum in the main flow direction. The velocity in the outer layer at $y > 30$ mm must be explained by considering the effect of the largely expanded effective beam diameter at a far distance.

6.3.3 Stereoscopic Transducer for Ship Application

Because the ark reveals the importance of reducing ultrasonic multiple reflections that arise around the thick steel plate, a series of acoustic damping tests are performed. The final design derived from the tests is the damper-built-in transducer, which has the additional merit of being tough in a seawater environment. Furthermore, a molecular coating is made to relax microbubble attachment to the head of the transducer and to electromagnetically shield long-distance signal cables up to 100 m in length and thus maintain a low signal-to-noise ratio. For the problem of oscillation of ship orientation relative to the horizontal plane, a stereoscopic transducer is designed and manufactured so that the velocity vector profile relative to ship attitude can be measured. The stereoscopic transducer, which is called a Y-type angled-beam transducer (YABT), Fig. 6.16a provides two measurement lines at a fixed angle (Fig. 6.16b). Several types of YABT are mounted at preferred positions on the ship, (see Fig. 6.17b) using different basic frequencies to consider the ambient flow conditions. Figure 6.16a shows one of the three designs, which has a basic frequency of 2.0 MHz. The YABT is designed to measure the velocity profile of the turbulent boundary layer beneath the bottom plate of the ship. The two measurement lines have a baseline of 21 mm, and the angle θ is 2.5° to the normal of the wall. With this configuration, the local average velocity vector distribution between the two measurement lines is measured as well as the Reynolds shear stress distribution [30].

Cement transporter for examination

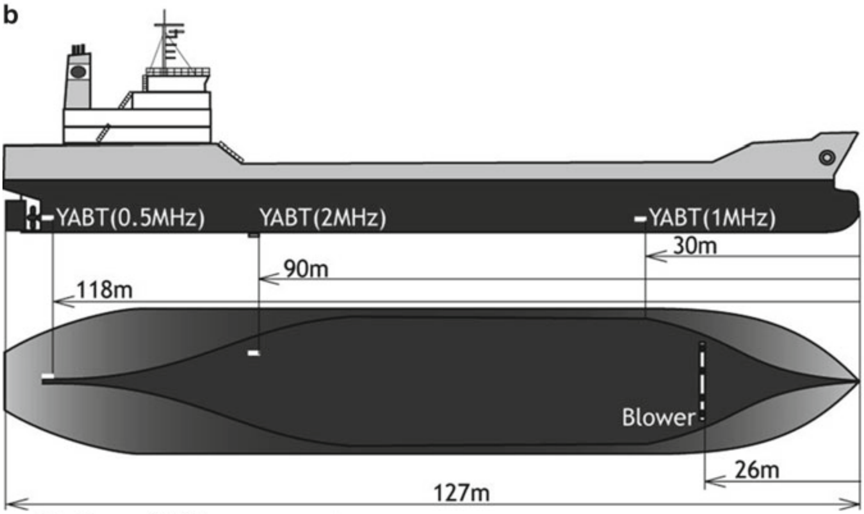

Poisitions of UVP measurement

Fig. 6.17 (**a**) Picture of cement transporter for examination. (**b**) Mounting of ultrasound transducers on ship

6.3.4 *Result of Ship Application*

The first application of UVP to a ship cruising on seawater was carried out around Japan in January 2008. The ship was the *Pacific Seagull*, which belongs to Azuma Kaiun Transport (Fig. 6.17a). It has a length of 127 m and power of 5,280 ps. YABT with different basic frequencies were attached three positions on the beneath of the ship as shown in Fig. 6.17b. The experiment was performed for two situations: full-load and ballast conditions. The routes in the experiment were from Yamaguchi to Tokyo and the return route, which are longer than 800 km. The ultrasonic reflector in deep seawater had insufficient concentration under the full-load condition. Therefore, data were analyzed only for the ballast condition.

Figure 6.18a presents the measurement results for the mean velocity profiles and Reynolds shear stress profiles under the ballast condition. Results are the velocity profiles 90 m from the bow or stern of the ship. It is confirmed that, for the mean velocity profile in the main flow direction, *U*, there was low velocity from the wall to 15 mm, indicating a boundary layer. However, the near-field effect of the YABT

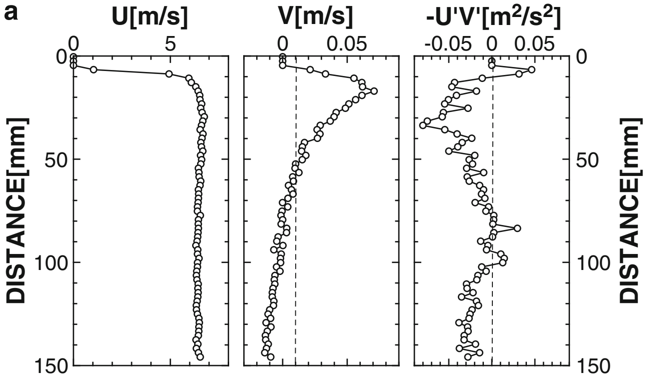

Without bubble injection

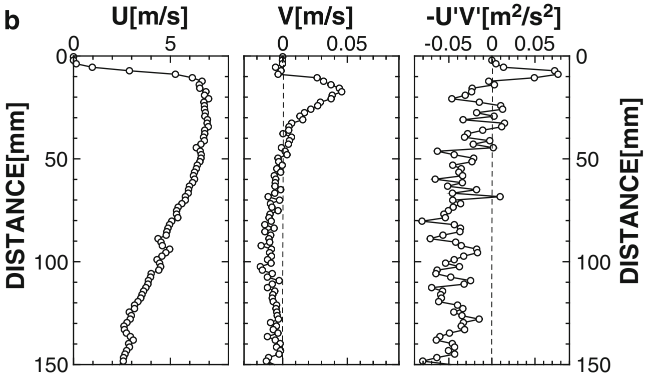

With bubble injection

Fig. 6.18 Time-averaged profiles of flow beneath the ship wall. (**a**) Without bubble injection. (**b**) With bubble injection

made the velocity unrealistically low in the layer within 10 mm. The wall-normal velocity, *V*, was measured to be around 1% of the main flow velocity at 20 mm from the wall, and the sign was positive. Thus, local downward flow, although being very small, was generated by the installation of the YABT. The Reynolds shear stress profile was obtained as 50 Pa (=0.05 $m^2/s^2 \times 10^3$ kg/m^3) near the wall and was in fairly good agreement with the wall shear stress at the wall of the planar boundary layer for the same Reynolds number of 6×10^6.

Data in Fig. 6.18b are the results for the case that bubbles are injected from the bow of the ship. The bubble injection was made to investigate how it modified the boundary layer structure while it reduced the frictional resistance of the ship. The main flow velocity, *U*, was measured as being remarkably low in the layer deeper than 40 mm from the wall, which is caused the lack of an ultrasonic echo returning to the transducer through the dense arrangement of large bubbles within the boundary layer. The Reynolds shear stress was measured at around 80 Pa, higher than in the case without bubble injection.

The reason for this trend is unclear, but it seems to originate from the fact that UVP mainly senses the velocity of bubbles when bubbles occupy the space around the measurement lines. Some appropriate post-processing may be required to separate the results for liquid and gas phases [29, 31].

When the local difference in the mean velocity profile is compared near the wall, it is found that bubble injection increased the velocity by around 10%. This result implies that there was a shear-thinning effect in the turbulent boundary layer during seawater cruising, which has phenomenological consistency with the drag reduction.

References

1. Mori M, Takeda Y, Taishi T, Furuichi N, Aritomi M, Kikura H (2002) Development of a novel flow metering system using ultrasonic velocity profile measurement. Exp Fluids 32:153–160
2. Tezuka K, Mori M, Suzuki T, Kanamine T (2008) Ultrasonic pulse Doppler flow meter application for hydraulic power plants. Flow Meas Instrum 19:155–162
3. Wada S, Kikura H, Aritomi M, Mori M, Takeda Y (2004) Development of pulse ultrasonic Doppler method for flow rate measurement in power plant: multilines flow rate measurement on metal pipe. J Nucl Sci Technol 41:339–346
4. Kikura H, Inoue Y, Wada S, Aritomi M, Mori M (2006) Development of pulse ultrasonic Doppler method for flow rate measurements of power plant (characteristics of sound pressure distribution and evaluation of the hybrid ultrasonic flowmetering system using TOF and UDM). In: Proceedings of the ICONE14:89695, Miami, 17–20 July 2006
5. Yao H, Ohmuro Y, Hagiwara, K, Kishiro M, Miyamoto A, Yamada K, Tadata N, Ohgawara G, Yamamoto T, Takeda Y (2004) Advanced hybrid type ultrasonic flow meter utilizing state-of-the-art pulsed-Doppler method along with traditional transit time method. In: Proceedings of the 4th international symposium on ultrasonic Doppler method for fluid mechanics and engineering, pp 89–93
6. Tasaka Y, Takeda Y, Yokoyama K, Kojima S (2007) Environmental flow field measurement by ultrasonic velocity profiling. Proc ASME-FEDSM 2007:37071
7. Ohkubo T, Takeda Y, Mori M (2006) Accuracy evaluation of high-accuracy flowmeter using UVP. Trans Jpn Soc Mech Eng Series B 72:81–89 (in Japanese)
8. Kikura H, Yamanaka G, Aritomi M (2004) Effect of measurement volume on turbulent flow measurement using ultrasonic Doppler method. Exp Fluids 36:187–196
9. Furuichi N, Terao Y, Takamoto M (2009) Calibration facilities for water flowrate in NMIJ. In: Proceedings of 7th international symposium on fluid flow measurement, CD-ROM, pp 1–7
10. Guide to the Expression of Uncertainty in Measurement (GUM) (1995) ISO
11. Tezuka K, Mori M, Suzuki T, Takeda Y (2008) Calibration tests of pulse-Doppler flow meter at national standards loops. Flow Meas Instrum 19:181–187
12. Dogan N, McCarthy MJ, Powell RL (2005) Measurement of polymer melt rheology using ultrasonics-based in-line rheometry. Meas Sci Technol 16:1684–1690
13. Pfund DM, Greenwood MS, Bamberger JA, Pappas RA (2006) Inline ultrasonic rheometry by pulsed Doppler. Ultrasonics 44:e477–e482
14. Choi YJ, Milczarek RR, Fleck CE, Garvey TC, McCarthy KL, McCarthy MJ (2006) In-line monitoring of tomato concentrate physical properties during evaporation. J Food Process Eng 29:615–632
15. Wiklund J, Stading M (2009) Application of ultrasound doppler based in-line rheometry method to complex process streams. In: Fischer P, Pollard M, Windhab EJ (eds) Proceedings of the 5th international symposium on food rheology and structure, pp 90–93

16. Regner M, Henningsson M, Wiklund J, Östergren K, Trägårdh C (2007) Predicting the displacement of yoghurt by water in a pipe using CFD. Chem Eng Technol 30:1–11
17. Wiklund J, Stading M, Trägårdh C (2010) Monitoring liquid displacement of model and industrial fluids in pipes by in-line ultrasonic rheometry. J Food Eng 99:330–337. doi:10.1016/j.jfoodeng.2010.03.011
18. Ouriev B (2000) Ultrasound Doppler based in-line rheometry of highly concentrated suspensions. PhD Thesis, ETH, Zürich
19. Ouriev B, Windhab E, Braun P, Zeng Y, Birkhofer B (2003) Industrial application of ultrasound based in-line rheometry: visualization of steady shear pipe flow of chocolate suspension in pre-crystallization process. Rev Sci Instrum 74:5255–5259
20. Birkhofer BH, Jeelani SAK, Windhab EJ, Ouriev B, Lisner K-J, Braun P, Zeng Y (2008) Monitoring of fat crystallization process using UVP-PD technique. Flow Meas Instrum 19:163–169. doi:10.1016/j.flowmeasinst.2007.08.008
21. Young NWG, Wassell P, Wiklund J, Stading M (2008) Monitoring struturants of fat blends with ultrasound based in-line rheometry (ultrasonic velocity profiling with pressure difference). Int J Food Sci Technol 43:2083–2089. doi:10.1111/j.1365-2621.2008.01826.x
22. Wassell P, Wiklund J, Stading M, Bonwick G, Smith C, Almiron-Roig E, Young NWG (2010) Ultrasound doppler based in-line viscosity and solid fat profile measurement of fat blends. Int J Food Sci Technol 45:877–883. doi:10.1111/j.1365-2621.2010.02204.x
23. Ouriev B, Windhab E (2003) Novel ultrasound based time averaged flow mapping method for die entry visualization in flow of highly concentrated shear-thinning and shear-thickening suspensions. Meas Sci Technol 14:140–147
24, Zatti D, Wiklund J, Vignali G, Stading M (2009) Determination of velocities profiles in hyperbolic contraction using ultrasound velocity profiling. In: Nevalainen K (ed) Annual transactions of the Nordic Rheology Society, vol 17. pp 277–281
25. Kotzé R, Wiklund J, Haldenwang R, Fester V (2010) Measurement and analysis of flow behaviour in complex geometries using ultrasonic velocity profiling (UVP) technique. In: Wiklund J, Bragd EL, Manneville S (eds) Proceedings of the 7th international symposium on ultrasonic Doppler methods for fluid mechanics and fluid engineering, pp 65–68
26. Kotze R, Wiklund J, Haldenwang R, Fester VG (2011) Measurement and analysis of flow behaviour in complex geometries using ultrasonic velocity profiling (uvp) technique. Flow Meas Sci J 22:110–119. doi:10.1016/j.flowmeasinst.2010.12.010
27. Murai Y, Fukuda H, Oishi Y, Kodama Y, Yamamoto F (2007) Skin friction reduction by large air bubbles in a horizontal channel flow. Int J Multiphase Flow 33:147–163
28. Huang J, Murai Y, Yamamoto F (2008) Shallow DOF-based particle tracking velocimetry applied to horizontal bubbly wall turbulence. Flow Meas Instrum 19:93–105
29. Murai Y, Fujii H, Tasaka Y, Takeda Y (2006) Turbulent bubbly channel flow investigated by ultrasound velocity profiler. J Fluid Sci Technol 1:12–23
30. Ohta S, Shigetomi A, Tasaka Y, Murai Y, Takeda Y, Hinatsu M, Kodama Y (2008) Boundary layer measurement of a vessel sailing over the sea. In: Proceedings of the 6th international symposium on ultrasound Doppler methods, pp 139–142
31. Murai Y, Oishi Y, Takeda Y, Yamamoto F (2006) Turbulent shear stress profiles in a bubbly channel flow assessed by particle tracking velocimetry. Exp Fluids 41:343–352

Chapter 7
Extended Techniques

Hideki Murakawa, Tatsuya Kawaguchi,
Hironari Obayashi, Yuichi Murai, and Yuji Tasaka

Abstract We have many demands to understand flow phenomena in many industrial applications. Detecting the gas–liquid interface is important when measuring velocities in two-phase flow or in an open channel. We want to obtain velocity distributions two dimensionally, also. To extend the applicability, many techniques utilizing the ultrasonic Doppler velocity profiler (UVP) have been recently developed. This chapter shows these extended techniques. Liquid and gas velocity distributions are obtained simultaneously using a multi-wave transducer are described in Sect. 7.1. Techniques detecting a gas–liquid interface depending on fluid interface relative to the ultrasonic wavelength are presented in Sect. 7.2. The UVP is utilized for measuring void fraction distributions in Sect. 7.3. Section 7.4 shows a technique measuring two-dimensional velocity components. A new approach for improving temporal resolution using the ultrasonic correlation method is presented in Sect. 7.5.

Keywords Correlation method • Free-surface • Multi-wave method • Vector profile • Void-fraction profiling

---

H. Murakawa (✉)
Graduate School of Engineering, Kobe University,
1-1 Rokkodai, Nada, Kobe 657-8501, Japan
e-mail: murakawa@mech.kobe-u.ac.jp

T. Kawaguchi
Tokyo Institute of Technology, Tokyo, Japan

H. Obayashi
Japan Atomic Energy Agency (JAEA), Ibaraki, Japan

Y. Murai • Y. Tasaka
Faculty of Engineering, Hokkaido University, Sapporo, Japan

Y. Takeda (ed.), *Ultrasonic Doppler Velocity Profiler for Fluid Flow*,
Fluid Mechanics and Its Applications 101, DOI 10.1007/978-4-431-54026-7_7,

7.1 Multi-wave Method

When UVP is applied for measuring two-phase bubbly flow, the obtained velocity data include both liquid and gas velocity information. Hence, the post-processing method described in Sect. 5.6 is proposed for separating the liquid and gas velocity data or detecting the gas–liquid interface. A multi-wave method is an idea for detecting gas–liquid interface using a multi-wave transducer equipped with two ultrasonic elements. This method makes it possible to obtain both liquid and gas velocity distributions simultaneously.

7.1.1 Background

Ultrasonic measurement volume is important for measuring flow velocity, especially for multiphase measurements. In bubbly-flow measurement, with an increase in void fraction, the probability of bubbles crossing the measuring line consequently increases. Furthermore, the correlation of bubble size to beam diameter of the ultrasonic transducer (TDX) is important as well. The probability of bubbles crossing the measuring line increases with an increase in the ultrasonic beam diameter. In general, ultrasonic directivity and the ultrasonic pressure distribution depend on two important ultrasonic parameters: basic frequency (f_0) and the ultrasonic sensor diameter (D_{US}). Taking into account the pressure field mentioned in Sect. 2.4, they are empirically chosen (Table 7.1) [1].

Figure 7.1 shows an example of velocity probability density function (PDF) at a channel measured by using different kinds of TDXs in two-phase bubbly flow. The channel was vertically rectangular, 20×100 mm^2, and liquid and gas flowed upward. The void fraction (α) was 1.8%, and bubble diameter range was 3–4 mm. Because the rising velocity of bubbles is higher than the liquid velocity, the velocity PDF of the bubbles is higher than that of the liquid. The probability of bubbles crossing the measuring line becomes higher with an increase in the D_{US}. At $D_{US} = 2.5$ mm, the velocity PDF peaks at the mean liquid velocity. However, at $D_{US} = 5$ mm, the maximum value of the PDF becomes higher than the liquid velocity, and the PDF has two peaks. Furthermore, the PDF has one maximum and one peak value at $D_{US} = 10$ mm. If the void fraction is low, these PDFs also change. Taking into account these characteristics, the selection of the TDX is related to the relative sizes between D_{US} and

Table 7.1 Relationship between basic frequency and sensor diameter (D_{US})

Basic frequency, f_0	Wavelength, λ (water at 20°C)	Sensor diameter, D_{US}
2.0 MHz	0.74 mm	10 mm
4.0 MHz	0.37 mm	5 mm
8.0 MHz	0.185 mm	2.5 mm

Fig. 7.1 Effect of measurement volume for velocity PDF

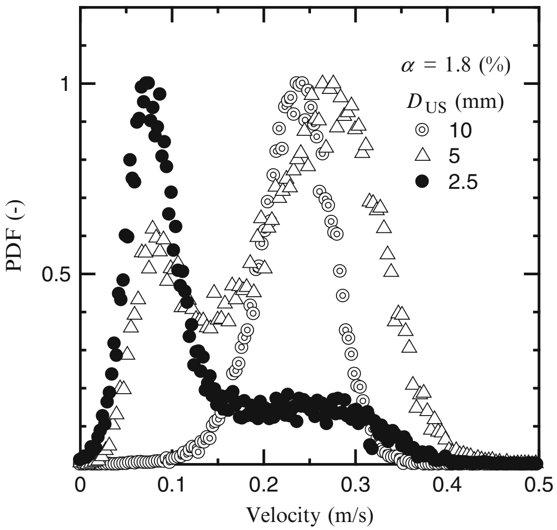

Fig. 7.2 Schematic diagram of a multi-wave TDX

the reflector. D_{US} of about 2.5 mm is suitable to obtain the liquid velocity under these conditions. Conversely, when D_{US} is 10 mm, the measured data primarily include the rising velocity of the bubbles. Therefore, if an appropriate ultrasonic transducer is selected, gas–liquid interface and liquid velocities can be measured selectively. Based on the selectivity of the reflector size, the multi-wave measurement method was developed. In this subsection, the multi-wave method and its application are introduced.

7.1.2 Multi-wave Transducer

Based on the foregoing concept, a unique ultrasonic transducer with two basic ultrasonic frequencies was developed. The TDX is referred to as a multi-wave TDX (Fig. 7.2). The TDX is covered by a cylindrical phenolic resin and has an outer diameter of 13 mm, a length of 60 mm, and a thickness of 0.2 mm. A piezoelectric element of 8-MHz basic ultrasonic frequency, 3 mm in diameter, is installed in the center of the TDX. Furthermore, a piezoelectric element at 2 MHz with a hollow shape is set along the central axis. The inner diameter is 3 mm and the outer diameter is 10 mm. Each element is connected with the BNC via lead wires. The piezoelectric elements are made of a composite oscillator with PZT (lead titanate zirconate)

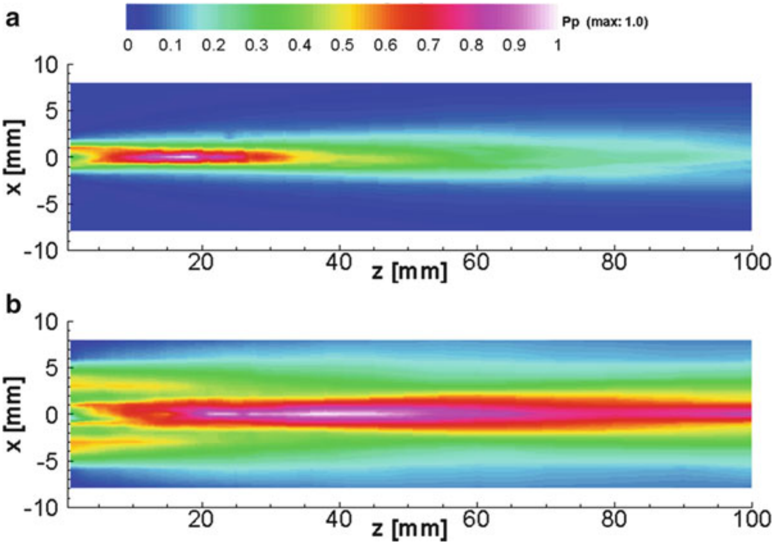

Fig. 7.3 Measurement results of ultrasonic pressure field in multi-wave TDX. (**a**) 8 MHz ($D_{US}=3$ mm). (**b**) 2 MHz with hollow shape ($D_{US}=10$ mm) (reprinted from [2] with permission from Elsevier)

and plastic. An epoxy resin half the thickness of the wavelength is used as the acoustic matching layer. Because the composite oscillator has low acoustic impedance, the energy loss is low at the acrylic wall surface compared with other materials. An epoxy damper is set behind the elements. The multi-wave TDX emits ultrasonic pulses independently for the two basic frequencies of 2 and 8 MHz, respectively. Using the multi-wave TDX, two types of ultrasonic measurement volumes can be obtained for multiphase flow measurements using a single ultrasonic probe.

Figure 7.3 shows sound pressure fields of the 2- and 8-MHz parts of the multi-wave TDX measured using a needle hydrophone. The color scale represents the pressure intensity normalized by the maximum value. It can be confirmed that the TDX can emit two ultrasonic frequencies of 2 and 8 MHz in a straight line. The pressure field in 2 MHz has a unique shape in the near-field, and it is expected that echo signals are difficult to obtain in the area. However, the effect of the hollow shape does not clearly appear in the far-field ($z>20$ mm), and the far-field region must be used for the measurement.

7.1.3 Application of the Multi-wave Transducer

The multi-wave TDX has two ultrasonic elements with different basic frequency, and these can emit and receive ultrasonic signals independently. If two UVP systems are connected with the elements, velocity measurements can be conducted in

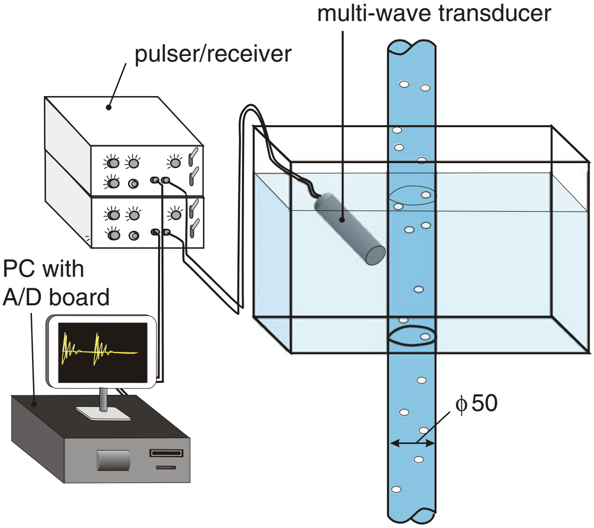

Fig. 7.4 Measurement system in bubbly flow using multi-wave TDX (reprinted from [2] with permission from Elsevier)

different measurement volumes. Although attention must be paid to the measurement volume in the outer element, there are some applications where the multi-wave TDX can be used. Here, an application using the cross-correlation method (see Sect. 7.5) is introduced.

Figure 7.4 shows a schematic diagram of the experimental apparatus. This system is applied for measuring both liquid and bubble-rising velocity distributions by using the ultrasonic time domain cross-correlation method (UTDC). The measurement system includes two ultrasonic pulser/receivers to emit and receive ultrasonic pulses. Both 2- and 8-MHz ultrasonic elements were connected to the pulser/receivers. The echo signals received in each pulser/receiver were recorded on an A/D board with the sampling resolution of 8 bits and a sampling rate of 100 MS/s at two channels. The A/D board and the pulser/receivers were connected to each other and synchronized. Therefore, both the 2- and 8-MHz ultrasonic echo signals were simultaneously recorded. The time resolution was 1 ms because the pulse repetition frequency (f_{prf}) was set at 1 kHz. The signals were stored in the memory of the A/D board. The recorded data were calculated by the PC using the correlation method, and the velocities were obtained. The spatial resolution was set at 0.74 mm along the measuring line. The working fluids were air and tap water seeded with nylon tracer particles with average diameter of 80 μm. The water temperature was kept at 20 ± 0.5°C.

An ultrasonic pulse is reflected on both nylon particles that are seeded in water and the gas–liquid interface. Hence, the original velocity profiles include both gas and liquid velocities. However, the ultrasonic echo signals from the gas–liquid interface are stronger than those from the microparticles. Therefore, signals smaller than a threshold level are omitted to eliminate the echo signals from the particles. Hence, it is comparatively easy to measure the bubble-rising velocity by using the correlation method. However, particles with echo signals of low intensity must be selected to obtain the liquid velocity.

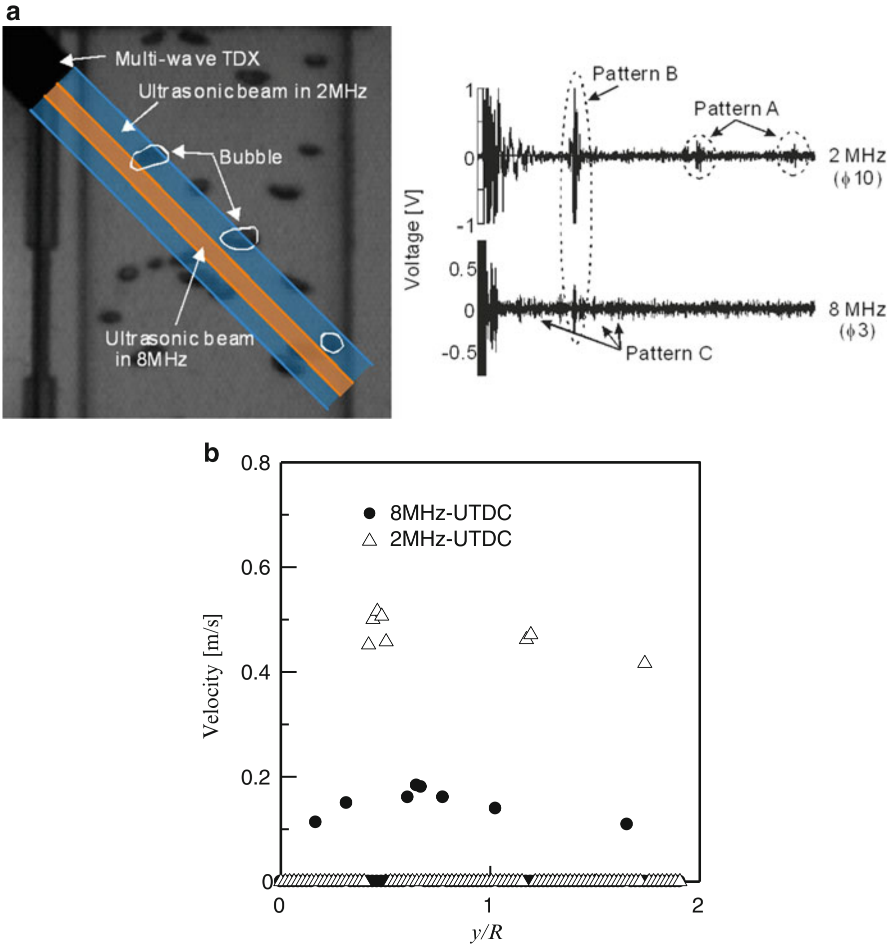

Fig. 7.5 Result of measuring gas–liquid velocity distributions. (**a**) Distributions: picture and reflected signals. (**b**) Instantaneous velocity distributions of bubbles (2 MHz) and liquid (8 MHz)

Because the echo signals reflected by the bubbles are stronger than those scattered from the particles, the particle signals can be easily eliminated from the recorded signals at 2 MHz, and bubble-rising velocity distributions are easily obtained. However, the bubble data must be eliminated from the measured data at 8 MHz to calculate the liquid velocity distribution. If signals at 8 MHz include echo signals reflected on bubbles, the signal can be recorded at 2 MHz as well. Based on this concept, it is possible to obtain only liquid data using 8-MHz signals [2].

A picture of bubbly flow and the reflected signals measured by the multi-wave TDX, and instantaneous velocity profiles in bubble and liquid, are shown in Fig. 7.5. The picture and the signals are synchronized, and the relationship between the bubble positions and the signals can be obtained. Measurement lines at 2 and 8 MHz are shown in the picture. Calculated velocities are converted into velocity component in

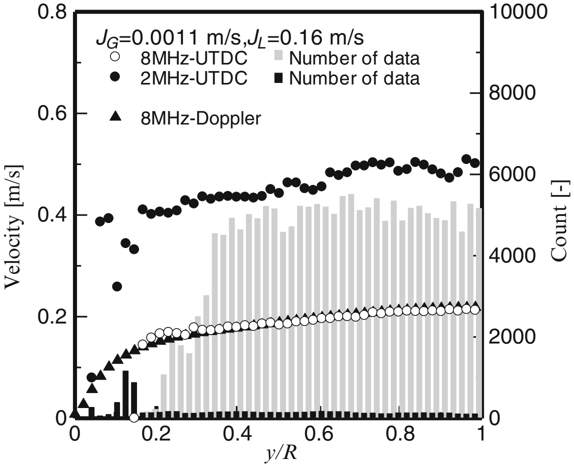

Fig. 7.6 Average velocity distributions in bubbly flow

the flow direction. *y* and *R* represent distance from the wall surface and the pipe radius. Signals of pattern A (echo signals appear at 2 MHz and no echo signal appear at 8 MHz) and pattern B (echo signals appear at both ultrasonic frequencies) can be considered as echo signals from bubbles, and pattern C (no echo signal at 2 MHz and echo signals appear at 8 MHz) is echo signals from the particles. Velocity separation between liquid and bubble were possible comparing the signals, and instantaneous velocities of both phases were obtained.

Figure 7.6 represents average velocity distributions. Velocities were simultaneously measured by the UTDC at 2 and 8 MHz: 8-MHz Doppler are data measured independently by using the Doppler method shown for a comparison. Count is the data count successfully obtained at the position. Using the technique, both liquid and bubble velocities could be measured at the same time and position, and we can obtain the local drift velocity between liquid and bubble. Uncertainty of the velocity data was increased by the noises caused by the frequency interaction, and the improvement of the signal-to-noise ratio is further investigation. The multi-wave method can be also applied for the Doppler method.

7.1.4 Summary

In this subsection, the multi-wave ultrasonic method, which employs two ultrasonic elements was introduced. The method is based on the difference of echo signal intensities. Applying a threshold based on the reflected signal, multiple measurement targets can be measured at the same time and position. Velocities of gas–liquid interface and liquid can be obtained simultaneously in case of bubbly flow, which means that the technique can give us the drift velocity. It is expected that the UVP is applied for many flow conditions and applications with developing other unique ultrasonic transducers.

7.2 Free Surface Detection

In cases in which moving free surfaces intersect a measurement line of UVP in measurements of open channel flows, e.g., rivers, detecting the surface position is difficult for usual measurements, and thus casts uncertainty on measurement accuracy. Synchronized recording of surface images by a video camera with UVP measurement may improve this problem, but of course such a measurement utilizing other equipment spoils the advantages of UVP measurement. Here we introduce some techniques to detect interfaces by information obtained only from UVP, namely, ultrasonic echo intensity, pseudo-velocity variation obtained around free surfaces, and statistical values of velocity fluctuation. Principles, applications, advantages, and remaining problems of the techniques are described. There are many measurement tools to detect interfaces, e.g., optical or ultrasonic displacement gauges. The techniques we introduce here are used for supporting flow field measurements by UVP and do not always have advantages compared to the proper measurement tools.

7.2.1 Reflection Patterns of Ultrasonic Waves at Free Surfaces

In contrast to moving solid interfaces, free surfaces have the following characteristics: (1) the free surface has large freedom on position and shape and thus is difficult to detect; (2) as most gas–liquid combinations have large differences in acoustic impedance, the amplitude of the reflected ultrasonic wave is maintained so long as the reflection is one dimensional; and (3) the phase of waves reflected at the free surface is inverted (see Sect. 2.1). Figure 7.7 illustrates the possible reflection patterns classified by the length scale of the fluid interface L relative to the ultrasonic wavelength λ. For bubbles smaller than the ultrasonic wavelength, $L < \lambda$, the reflected

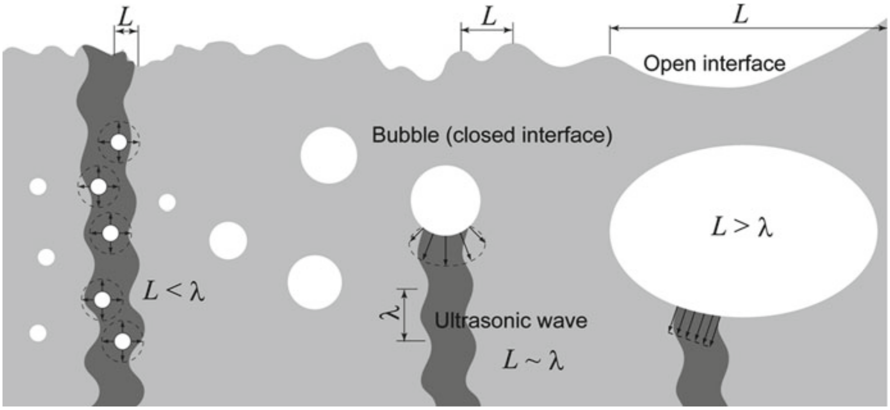

Fig. 7.7 Reflection patterns of ultrasonic pulse on gas–liquid interface with different scales (reprinted from [3] with permission from Elsevier)

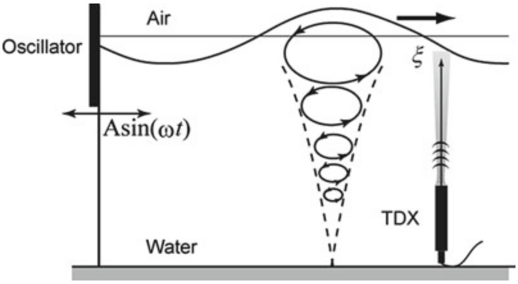

Fig. 7.8 Schematic diagram of free traveling wave measurement in an open channel; here the waves are generated by sinusoidal oscillation of the vertical plate mounted at the end of the channel (reprinted from [3] with permission from Elsevier)

wave radiates from individual bubbles. As the ultrasonic wave interferes with the resonant frequency of the bubbles, the bubbles start to produce intrinsic pulsation at frequencies different from that of the original ultrasonic wave. This phenomenon is exploited in ultrasonic spectroscopy to measure bubble size distributions. Doppler information detected from microbubbles yields fluid velocity because microbubbles accurately trace fluid flow. Thus, microbubbles are applicable to UVP as tracer particles. Other than from small spherical bubbles, ultrasonic waves also reflect diffusely from turbulent interfaces associated with waves shorter than the ultrasonic wavelength. When the interfacial length scale becomes comparable to the ultrasonic wavelength, $L \sim \lambda$, complex reflection patterns occur in a heterogeneous manner. This principle leads to the irregular flickering reflection of the ultrasonic wave on open interfaces subjected to surface waves. Bubbles and open interfaces with length scales larger than the ultrasonic wavelength, $L > \lambda$, produce total reflection of the ultrasonic wave. Simultaneously, the slope of the interface strongly influences the direction of the reflected wave, making it difficult when the interface migrates to detect the reflected wave using a single ultrasonic transducer.

According to the foregoing characteristics, we introduce some interface detection techniques that are applicable to each reflection pattern. The identification technique of tracer particles from a bubble–liquid mixture is also explained in the following subsections.

7.2.2 *Echo Intensity Technique*

Because a free surface satisfying $L > \lambda$ provides an extremely large reflection echo compared to tracer particles, its position can be detected by ultrasonic echo intensity. Here we introduce a flow field measurement under a free traveling wave as an application of the technique. Figure 7.8 shows a schematic of a free traveling wave measurement in a water container that is 1 m long, 300 mm wide, and filled with 170 mm tap water. One-dimensional waves are generated at the end of the container by horizontal oscillation of a flat vertical plate. The stroke and frequency of the oscillation are $A = 50$ mm and $f = 2$ Hz, respectively. The theoretical description of the wave amplitude ζ and the vertical velocity profile u_z is

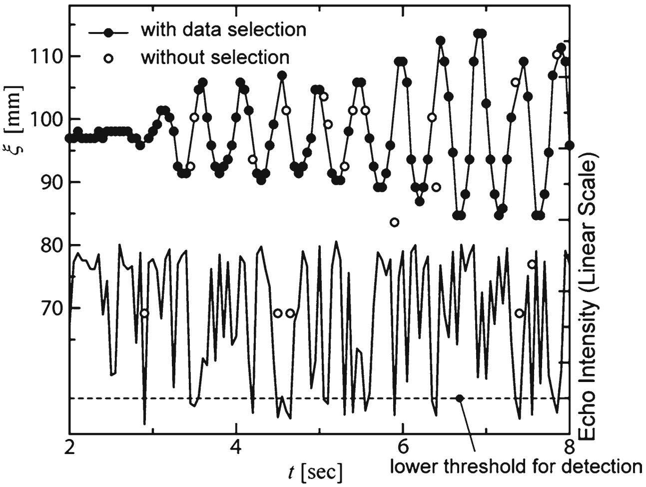

Fig. 7.9 Detected interface position and absolute value of the ultrasonic echo intensity. *Solid and open circles* indicate detected interface position from the echo intensity with or without initial data selection, respectively, by giving a lower threshold (*dashed line*) (reprinted from [3] with permission from Elsevier)

$$\begin{aligned} \varsigma &= A_w \cos(kx - 2\pi ft) \\ u_z &= -kB \sinh k(z+h) \cdot \sin(kx - 2\pi ft) \end{aligned} \tag{7.1}$$

where A_w, k, and f are the amplitude, wave number, and angular frequency of the wave, respectively. In Eq. (7.1), B, z, and h are velocity potential at the wave surface, vertical coordinate, and initial height of the surface. A 4-MHz four-cycle ultrasonic pulse is emitted from the bottom to measure the vertical velocity profile $u_z(\xi, t)$ and the echo intensity profile, using UVP; here ξ is the measurement coordinate of UVP as shown in Fig. 7.8. Porous polymer particles, 100 µm in mean diameter and 1.07 in specific density, are seeded in the water as tracers. The sampling rate and the spatial resolution of the velocity and echo profiling are 50 ms and 1.11 mm, respectively.

Figure 7.9 shows the water depth fluctuation (i.e., the interface position), which is obtained from the echo intensity profile by setting a threshold at half the maximum intensity. This threshold was empirically determined here, and thus it should be modified depending on the noise level of the echo information in general cases. Note that we also introduce a lower limit to separate the interface from noise. The solid or open circles in the figure indicate whether such a selection is made. The bottom graph in Fig. 7.9 presents the temporal fluctuations of the echo intensity, which are reflected from the interface. The echo intensity weakens in the region where the interface has a steep gradient. From the video images recorded synchronously with the ultrasonic measurement, we find that for an interface slope angle greater than 5° the echo intensity is smaller than the lower sensing limit. This phenomenon is attributed to the ultrasonic mirror effect at the gas–liquid interface, which occurs when the interface has a locally planar form from which the ultrasonic

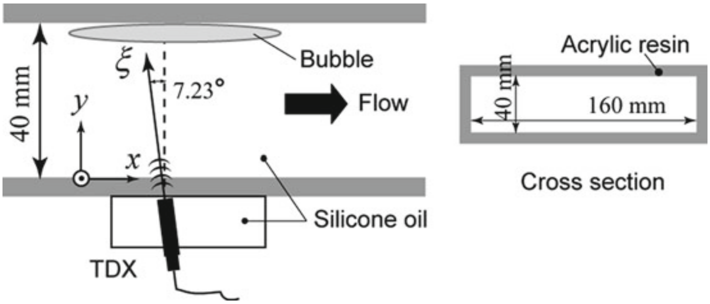

Fig. 7.10 Schematic of measurement setup for horizontal bubbly channel flow (reprinted from [3] with permission from Elsevier)

reflection occurs. A geometric estimation of the mirror-reflection state indicates that the maximum detectable interface inclination angle coincides with the ultrasonic beam divergence angle. The result obtained in this experiment is consistent with this theory. Using a wide angular radiation type of ultrasonic transducer will overcome this problem, but the spatial resolution for detecting the interface would decrease.

7.2.3 Local Doppler Technique [3, 4]

One or two measurement volumes around free surfaces in $L > \lambda$ give clearly different values in comparison with actual velocity, caused by a standing wave that is formed near the interface by interference between incident and reflected waves [4], or by detecting not particle motion but free surface motion. Detecting such local deformation of the velocity profile can tell us the interface position; this is called *local Doppler technique*.

When gas–liquid interfaces migrate with a base flow, interface detection must be done dynamically. In such a situation, the inclination angle of the interface changes rapidly with the passage of bubbles through the ultrasonic beam and thus the echo intensity technique is not applicable. In this section, we consider just such a bubbly channel flow to examine the ultrasonic interface detection technique. Figure 7.10 illustrates the measurement setup for a horizontal channel 6 m long, 40 mm high, and 160 mm wide in which bubbles larger than 100 mm in the flow direction migrate near the upper wall. Silicone oil, with kinematic viscosity of 10 cSt, 935 kg/m^3 density, and a speed of sound of 1,008 m/s, is used as a working liquid while air bubbles are mixed into the channel at room temperature. The mean liquid speed is set at 0.5 m/s. A 4-MHz ultrasonic transducer is mounted beneath the channel at 7.23° with respect to the vertical axis. Polyethylene particles of 180 μm mean diameter and 918 kg/m^3 density are seeded as ultrasonic reflectors. The temporal and spatial resolutions are 29 ms and 0.62 mm, respectively.

Figure 7.11a shows a sample of the spatiotemporal velocity distribution. The figure presents the layer between 34 and 40 mm to focus on the Doppler velocity near

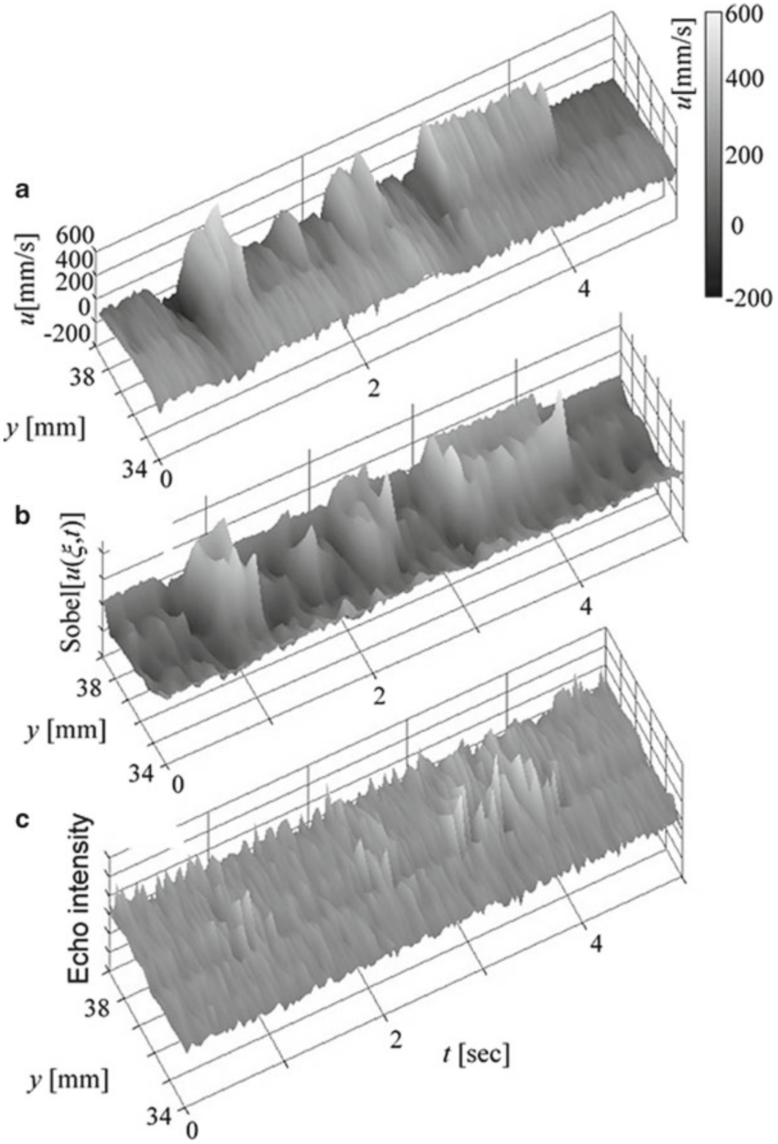

Fig. 7.11 Interface detection in bubbly channel flow. **(a)** Spatiotemporal velocity distribution. **(b)** Distribution of Sobel-filtered velocity. **(c)** Distribution of ultrasonic echo intensity (reprinted from [3] with permission from Elsevier)

the bubble interface. The measured velocity distribution consists of two parts: a monotonic decrease toward the wall and a steep increase near the wall. The latter part arises from ultrasonic reflection from the bubble interface, which does not indicate real flow velocity but does indicate the presence of bubbles. In each upstream bubble region, the velocity becomes negative because of the bubble wake. Figure 7.11b

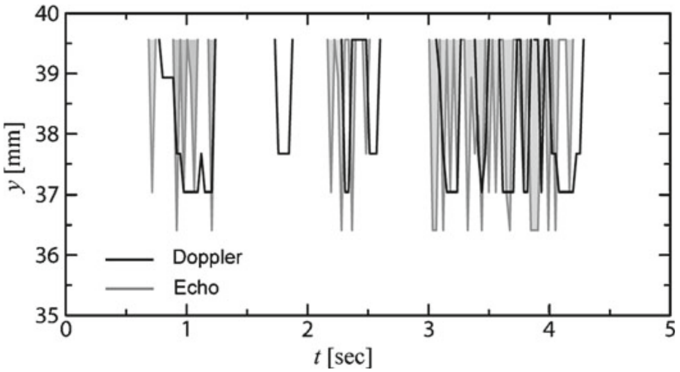

Fig. 7.12 Detected interface of bubbles in channel flow by local Doppler and echo intensity techniques (reprinted from [3] with permission from Elsevier)

shows a filtered distribution converted from the original Doppler velocity distribution and Fig. 7.11c shows echo intensity distribution. A Sobel filter is used to sharpen the signal to find the interface. Comparing these two distributions, the peak value emerges at almost the same position in both cases. However, the echo intensity has fewer peaks in time, which means that the echo intensity technique is often unavailable to moving interfaces.

Setting a threshold for each distribution allows us to determine the interface position along the measurement line (Fig. 7.12). The interfaces obtained from the two techniques roughly agree with each other, but in carefully analyzing the difference, we find that the interface positions calculated from the echo intensity correspond to the front part of the bubbles detected by Doppler technique. This observation implies that the bubbles reflect ultrasonic wave only in a very limited angular range, as we mentioned in the former test case. In contrast, the local Doppler technique is feasible for detecting moving interfaces more sensitively than the echo intensity technique.

7.2.4 *Velocity-Variance Technique*

When the interface is not directly detected by either of the two techniques just described because of very complex interfaces, using fluid flow kinematics provides a third technique. The following equation is the kinematic interface condition (e.g., [5]) and expresses the relationship among three factors: interface position S along the measurement line, flow velocity component v perpendicular to the measurement line, and flow velocity component u in the direction of the measurement line.

$$\frac{\partial S}{\partial t} + v\frac{\partial S}{\partial y} = u \tag{7.2}$$

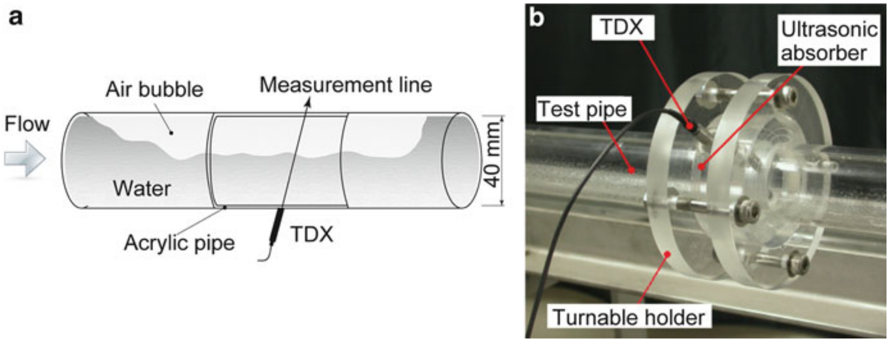

Fig. 7.13 Interface detection in gas–liquid two-phase slug flow in a horizontal tube. (**a**) Schematic diagram of measurement environment. (**b**) Photograph of the transducer holder, which can be rotated around the tube axis (reprinted from [3] with permission from Elsevier)

In Eq. (7.2), y represents the spatial coordinate in the direction perpendicular to the measurement line. In computational fluid dynamics simulation of free surface flows, this equation is used to calculate the interface position S given the two velocity components obtained from the Navier–Stokes equations. In the same way, the free surface position can be determined from the velocity components measured by ultrasonic Doppler velocimetry. If using a single ultrasonic transducer, Eq. (7.2) is insufficient to determine the interface position S because only a single velocity component profile u is obtained. One idea to overcome this problem is to use the variance of u in time; this may be understood by considering the interface position $S = S_0 \sin(\omega t + ky)$. Substituting this into Eq. (7.2) gives

$$u = S_0(\omega + kv)\cos(\omega t + ky) \leftrightarrow \overline{u'^2} = \frac{1}{2} S_0(\omega + kv) \tag{7.3}$$

In other words, the temporal change and the spatial form of the interface are reflected in the variance of the velocity component in the direction of the ultrasonic beam. As indicated by Eq. (7.3), the larger the temporal and spatial changes of the interface, the larger the velocity variance. Thus, this principle is applicable to periodic interfacial flow such as in plug and slug flows in pipes.

As an application of the velocity-variance technique, we introduce slug flow in pipe, which carries turbulent waves over large-scale interfaces [6]. Neither of the two techniques described in the last two sections can detect the interface of slug flows because of the complex interfaces. Figure 7.13 shows the measurement setup for air–water two-phase flow in a horizontal pipe 40 mm in inner diameter. The superficial velocities are set at 0.66 m/s for water and 0.44 m/s for air, which corresponds to a mean mixture velocity of 1.10 m/s, a Reynolds number of 4×10^4, and a mean void fraction of 40%. In this test, 4-MHz four-cycle ultrasonic pulses are emitted from the bottom at an angle of 5° with respect to the vertical axis.

To completely catch the slug flow interface, we introduce the velocity-variance technique, which facilitates the data processing of Doppler velocity distributions.

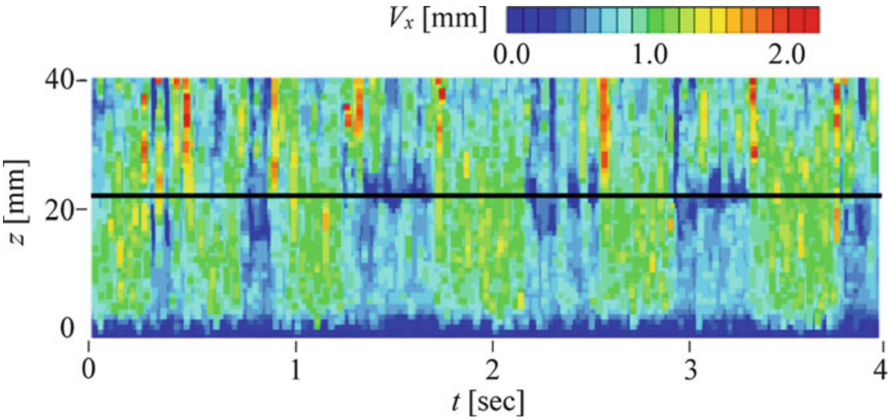

Fig. 7.14 A spatiotemporal velocity distribution of a slug flow in a pipe (reprinted from [3] with permission from Elsevier)

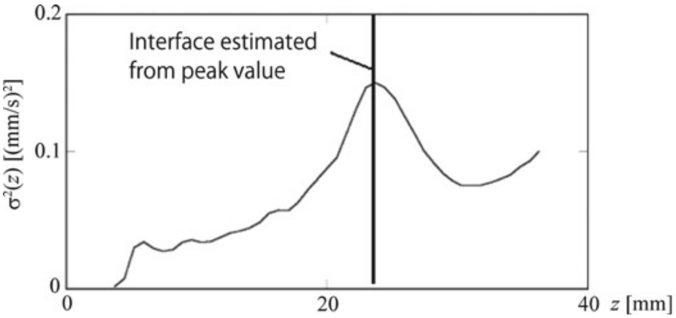

Fig. 7.15 Variation of the maximum value of co-variance between the classes (reprinted from [3] with permission from Elsevier)

A sample of the spatiotemporal Doppler velocity distribution $v_x(z, t)$ is shown in Fig. 7.14. The Doppler velocity decreases intermittently near the center of the pipe, indicating the presence of local standing waves at the gas–liquid interface. Sampling the Doppler velocity along the black line in the figure, a velocity fluctuation seems polarized into low-speed and high-speed regions. A velocity much lower than the bulk mean velocity of 1.1 m/s is obtained from the disappearance of the Doppler effect at the interface. Therefore, the statistical separation of the velocity histogram into real and pseudo-fluid velocities enables the detection of the interface. The separation can be made using the mutual deviation theorem proposed by Otsu [7]. We assume that the probability distribution at a point consists of high-speed and low-speed classes. The threshold to separate the classes is given as v_x, at which co-variance between the classes

$$\sigma^2(v_x) = \omega_1\omega_2(\mu_1 - \mu_2)^2 \tag{7.4}$$

becomes the maximum, where ω and μ are total probability and expected value in each class. Figure 7.15 shows a plot of the maximum of $\sigma^2(v_x)$ at each position,

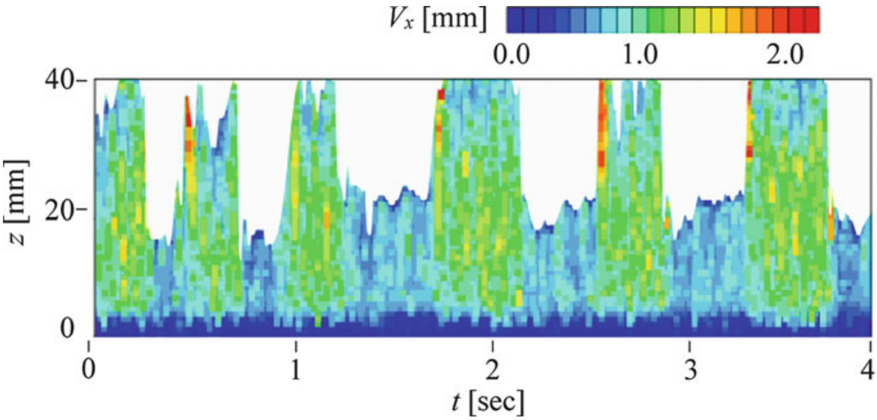

Fig. 7.16 Detected interface position and velocity field, where the gas phase is erased (reprinted from [3] with permission from Elsevier)

where the plot takes the maximum around $z = 23$ mm. This position corresponds to the position where the low-speed region clearly exists, and thus the obtained interface position seems reasonable. The interface position determined by this technique at each time is shown in Fig. 7.16, where the area corresponding to the gas phase is erased. The detected interface agrees with the actual interface position estimated from video images.

7.2.5 Interface Detection for $L \sim \lambda$

As mentioned in Sect. 7.2.1, because the reflection pattern of the ultrasonic wave greatly changes with the incident angle of the ultrasonic wave and interface shape in this condition, finding a universal technique to detect the interface position is difficult. Also, flows induced by motion of such interfaces are quite complex. Here we introduce detection free-rising bubbles as an example of this case.

Bubbles 3.5 mm in equivalent particle diameter were launched from a needle to stationary water layer. In this condition, bubble deformation is allowed and the bubble changes its shape with time. According to the deformation the bubbles take spiral or hobbling motions. A 8-MHz ultrasonic transducer was mounted, and velocity profile measurements were done with four-cycle ultrasonic bursts. Sampling period and spatial resolutions of the measurement are 20 ms and 0.37 mm.

Figure 7.17 shows instantaneous velocity profiles (top), echo intensity profiles (middle), and snapshot image of bubbles (bottom). In this figure the transducer is located at the left end, and thus the positive velocity indicates flows in the right direction. The velocity changes with bubbles passing the measurement line; however, the echo intensity does not show typical change. Then, we can use here only Doppler velocity information to detect interfaces. There is a peak at somewhat before the interface on the instantaneous velocity profiles. The peak value reaches the maximum when the bubble goes across the measurement line. To detect the interface

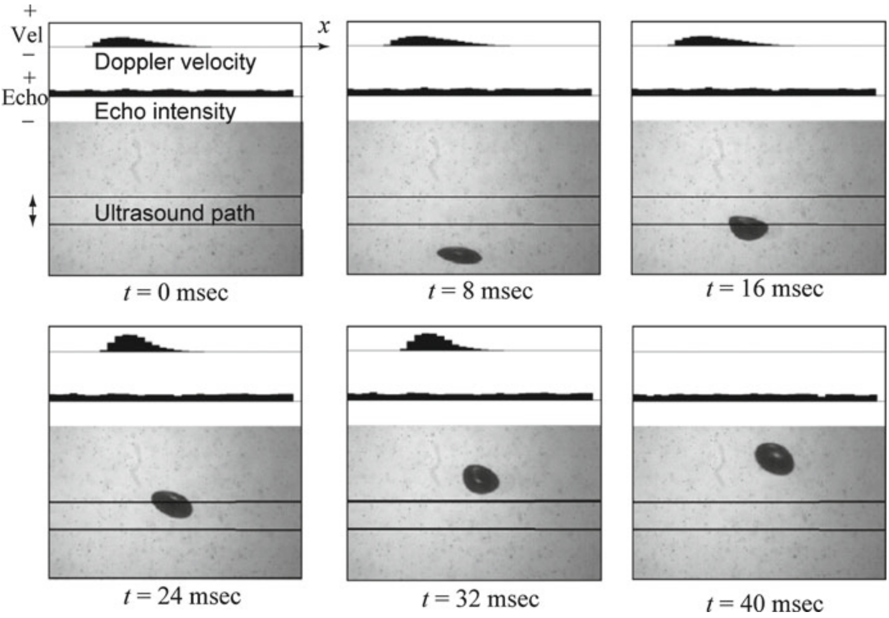

Fig. 7.17 Comparison of several filtering functions for spatiotemporal Doppler velocity distribution to detect bubbles where x and t denote horizontal coordinate and time (reprinted from [3] with permission from Elsevier)

position utilizing this characteristic of a Doppler velocity profile, we examined several numerical filters including the Sobel filter. Obtained results were compared with the correct interface position determined from high-speed video images. To evaluate the applicability of filters, success rate of the detection and following index

$$E = \sqrt{\left(\frac{\delta x}{\Delta x}\right)^2 + \left(\frac{\delta t}{\Delta t}\right)^2}, \tag{7.5}$$

were calculated for 500 samples at each filter, where Δx and Δt represent space and time intervals and δx and δt indicate detection error. The evaluation picks up a smoothing filter (Fig. 7.18), which smooths the data only in the space direction, as the best filter. The matrix in the figure represents actual calculation in the smoothing filter, where the average of the velocity at a point with adjacent four points is given. The filter introduced here cannot be universal. According to this procedure, however, we can design the best filter to detect interfaces in different systems.

7.2.6 Identification of Tracer Particles from a Bubbly Liquid

In cases of measurement of dispersed bubbly flows, we have to identify tracer particles from bubbly flows because the obtained spatiotemporal velocity distribution

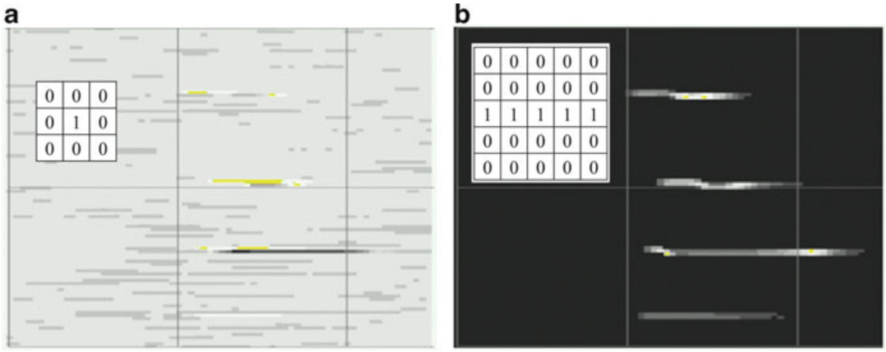

Fig. 7.18 (**a**) Spatiotemporal velocity distribution. (**b**) Distribution modified by the smoothing filter (reprinted from [3] with permission from Elsevier)

of liquid phase contains information about bubble advection. Scattering intensity of particles depends on the relative diameter of the particle *d* against the wavelength of the ultrasonic wave λ. Also, the reflection rate at the bubble interfaces is larger than that at particle surface because of the large gap in acoustic impedance between gas and liquid phase. A technique for identifying tracer particles from bubbly media utilizing these two characteristics has been proposed (see Sect. 7.1).

7.3 Void Fraction Profiling [8]

A method for measuring the spatial distribution of the void fraction in bubbly two-phase flow is discussed. The method is referred to as ultrasonic void fraction profiling because it is based on the signal processing of an ultrasonic pulse scattering at a bubble interface [1, 2, 8]. The technique can be compared with optical techniques [9–12] and electrical impedance-based techniques [13–16]. The ultrasonic method is established using two processes for the ultrasonic sensing of bubbles. One approach is to detect the bubble interface along a measurement line (i.e., the path of the ultrasonic pulse in the liquid), as mentioned in Sect. 7.2. The other approach is to reconstruct the void fraction profile from the number of bubble interfaces. A theoretical formula for the estimation is proposed by considering ultrasonic reflection in a suspension of bubbles. The validity of the formula is examined theoretically and numerically. Finally, the method is demonstrated for four flow configurations, in which the void fraction profile governs the modulation of the liquid flow field.

7.3.1 Principle of Void Fraction Measurement

The gas–liquid interface is detected with an ultrasound pulse as already described in Sect. 7.2. However, the approach only detects the bubbles closest to the ultrasonic

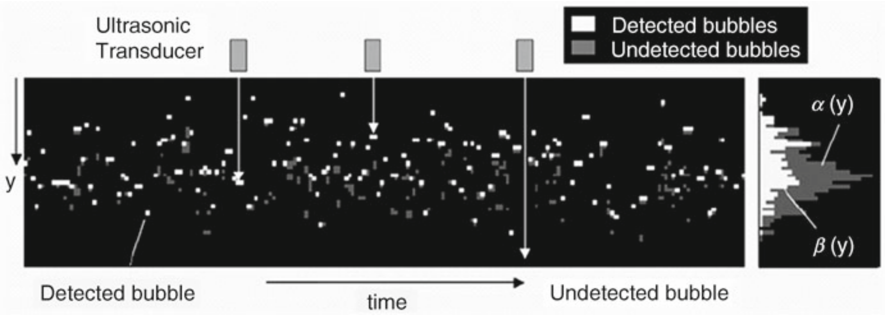

Fig 7.19 Reflection of ultrasound at bubbles closest to transducer for densely distributed bubbles. *Gray dots* are the existing bubbles; *white dots* are the bubbles detected by ultrasound pulse (reprinted from [8] with permission from IOPsciense)

transducer, as shown by the white plots in Fig. 7.19 (gray plots indicate existing bubbles). Because an ultrasonic pulse cannot propagate regularly beyond bubbles larger than the ultrasonic beam diameter, little information is obtained beyond those bubbles. A certain intensity of the ultrasonic pulse penetrates the bubbles; however, the pulse weakens extremely as it crosses those bubbles on its return to the transducer. Thus, we need to abandon the idea of using information of the far region. Only the distribution of the first-reflecting bubbles can be obtained with sufficient signal quality.

As shown on the right side of Fig. 7.19, the true void fraction profile, $\alpha(y)$, and the profile of detected bubbles, $\beta(y)$, are not identical. We refer to the quantity $\beta(y)$ as the detected void fraction in this chapter. In the following, the relationship between these two profiles is explained in detail.

Figure 7.20 explains the relationship in a digitized domain. The vertical axis gives the measurement distance from the transducer at a given spatial resolution and the horizontal axis gives the time for a given sampling rate. The gray cells are space–time cells inside the liquid phase and the dark cells are the first bubbles that reflect the ultrasound. White cells are cells unavailable for measurement, where no information is obtained by the ultrasound. The value AC (available cells) is the number of gray and dark cells at each depth from the ultrasonic transducer, the value DB (detected bubbles) is the number of dark cells at each depth, and the value VF (void fraction) is the void fraction at each depth, which is the ratio of DB to AC. Once DB is measured, AC is known because the cells before the first bubble should be liquid cells. Therefore, the relationship between the true void fraction α and the detected void fraction β in digitized form can be expressed as

$$\alpha_1 = \beta_1, \quad \alpha_2 = \frac{\beta_2}{1-\beta_1}, \quad \alpha_3 = \frac{\beta_3}{1-\beta_1-\beta_2}. \tag{7.6}$$

The first equation means that the two void fractions take the same value at the first position from the transducer. The next equation expresses that the true void fraction at the second position is estimated by the ratio of the detected void fraction,

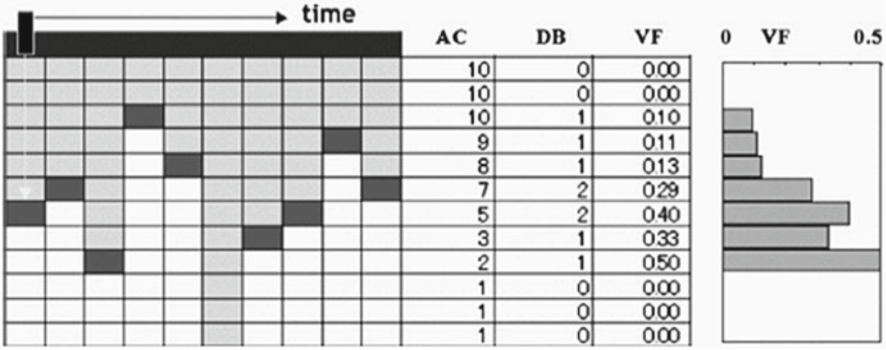

AC	DB	VF
10	0	0.00
10	0	0.00
10	1	0.10
9	1	0.11
8	1	0.13
7	2	0.29
5	2	0.40
3	1	0.33
2	1	0.50
1	0	0.00
1	0	0.00
1	0	0.00

Fig. 7.20 Digitalized representation of void fraction distributed in the space–time two-dimensional domain (reprinted from [8] with permission from IOPsciense)

β_2, to $1-\beta_1$. This denominator is smaller than unity because of the obstruction due to the bubbles located in the first position. In the same manner, the void fraction in the third and deeper layers is expressed as written. The description of these relationships between α and β implicitly assumes that the probability of finding a bubble behind a previously detected bubble is the same as in the bulk of the flow. Thus, the relationship at an arbitrary depth coordinate *i* is written as

$$\alpha_i = \beta_i \left(1 - \sum_{j}^{i-1} \beta_j\right)^{-1}. \tag{7.7}$$

The conversion of this equation to a continuous system with coordinate *y* yields

$$\alpha(y) = \beta(y)\left(1 - \frac{1}{\delta}\int_0^y \beta(y)\mathrm{d}y\right)^{-1}, \tag{7.8}$$

where δ is the interval between two data in the *y*-direction and corresponds to the spatial resolution of the measurement. The equation becomes a function of δ because of the definition of β. That is, the detected void fraction is defined as the ratio of the number of detected bubbles to the total sampling number within a given finite depth δ in the spatial direction. It is noted that this equation is derived in a deterministic manner without the introduction of any physical model or empirical assumption. For instance, the ultrasonic attenuation coefficient is not used in the equation. We do not invoke any probability theory in this derivation. Using Eq. (7.8), the true void fraction profile α(*y*) is calculated from the detected void fraction profile β(*y*). Because the range of integration in Eq. (7.8) is from zero to *y*, the true void fraction profile is explicitly determined by integrating the detected void fraction from the origin. This very light computational load allows us to realize real-time monitoring of the void fraction profile. The distance *y* is obtained from the time of flight of the ultrasonic pulse; $y = C \times t/2$, where *C* and *t* are the speed of sound and the time elapsed since the emission of the ultrasound pulse from the transducer. In the same manner, the inverse relationship at each depth is derived mathematically as

$$\begin{cases} \beta_1 = \alpha_1, \quad \beta_2 = \alpha_2(1-\beta_1) = \alpha_2(1-\alpha_1), \\ \beta_3 = \alpha_3(1-\beta_1-\beta_2) = \alpha_3(1-\alpha_2)(1-\alpha_1), \ldots \end{cases} \tag{7.9}$$

Therefore, the inverse relationship at arbitrary depth is written as

$$\beta_i = \alpha_i \prod_{j=1}^{i-1} (1-\alpha_i). \tag{7.10}$$

By conversion to a continuous function, Eq. (7.10) is rewritten as

$$\beta(y) = \alpha(y) \exp\left[\frac{1}{\delta} \int_0^y \log\{1-\alpha(y)\} \mathrm{d}y \right]. \tag{7.11}$$

In summary, Eq. (7.11) is used to estimate the detected void fraction from the true void fraction while Eq. (7.8) gives the true void fraction from the detected void fraction that is measured with the ultrasonic pulse. Obviously, these two equations are symmetric to one another, and the solutions are perfectly reversible so long as the detected void fraction satisfies the condition

$$\frac{1}{\delta} \int_0^y \beta(y) \mathrm{d}y \leq 1. \tag{7.12}$$

The foregoing condition is always satisfied if the function $\beta(y)$ is defined by the distribution of the first-detected bubbles, i.e., the ultrasound detects a single bubble located closest to the transducer. In other words, the function $\beta(y)/\delta$ is defined as the probability density distribution of the first-detected bubbles, the full-range integral of which is unity.

7.3.2 *Buoyancy-Driven Two-Phase Flow in Aeration*

There is a need in engineering to measure the void fraction inside a reactor, such as reactors used in water treatment, sedimentation, fermentation, and the refinement of metals. In such systems, media are highly contaminated with a variety of suspensions. The ultrasonic sensing of the void fraction is hence expected because optical techniques are often unavailable. As a basic examination, the bubbling behavior in a water tank is measured using the present method.

Figure 7.21a shows the flow configuration. Air bubbles are injected through three capillary needles connected to an air induction tube. Bubbles range from 1.0 to 2.5 mm in diameter. An ultrasonic transducer is placed on a sidewall of the tank to measure the bubbles in the horizontal direction. As the Weber number of bubbles is around 4, bubbles rise in zigzag and spiral modes, resulting in a diffused profile in

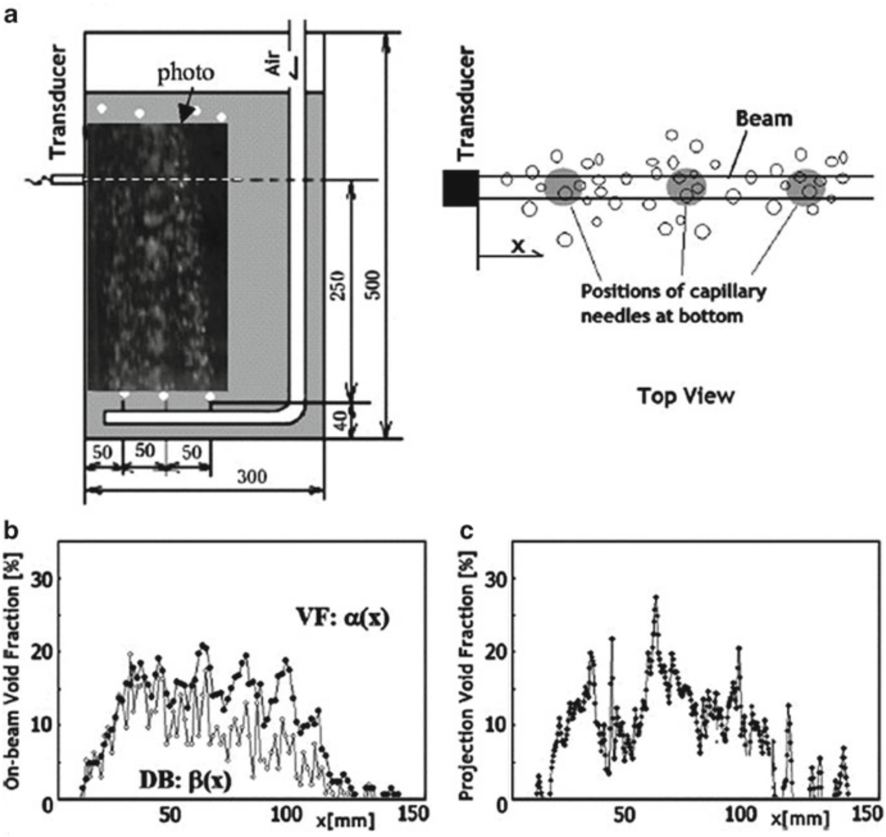

Fig. 7.21 Measurement of bubble distribution in buoyant bubble flow in a quiescent tank. (**a**) Flow and measurement configurations. (**b**) Void fraction measured by the present method. (**c**) Void fraction measured by image processing for the same condition as (**b**) (reprinted from [8] with permission from IOPsciense)

the upper part of the tank. The geometric relationship between the path of ultrasound and the three injection needles is shown on the right of the figure. Ultrasound detects only the bubbles that are inside the ultrasound beam. Hence, the void fraction is defined as the volume of these bubbles divided by the cylindrical volume of the beam. As shown in Fig. 7.21b, the first reflecting bubbles are distributed more frequently nearer the transducer. The void profile, $\beta(x)$, is thus biased on the left side. The transform using Eq. (7.8) gives the estimated profile of the real void fraction, $\alpha(x)$ (as shown by solid circles) and is flatter in the horizontal direction than $\beta(x)$. Figure 7.21c presents the time-averaged void fraction measured by image processing for 60 frames. The image processing originally measures the two-dimensional shadow area fraction of bubbles. Hence, it has been converted to the projection void fraction using the estimated thickness of the bubble distribution in the direction perpendicular to the image plane. The comparison with the result indicates that the mean values of the void fraction roughly match each other. The discrepancy is found to have a spiky distribution seen in the image processing, which is not detected by ultrasound. This discrepancy originates from the different volumes in defining the local volume-averaged void fraction. Image processing detects the pixel-by-pixel void fraction so that local chained bubbles in a row a few millimeters long are captured. Ultrasound does not detect such bubbles; however, it captures the profile smoothed in the beam direction. To increase the accuracy, one feasible idea is to mount another ultrasonic transducer on the opposite side of the tank; this will also guarantee a symmetric resolution about the beam direction.

7.3.3 Upward Jet Containing Small Bubbles

As another demonstration of upward bubbling flow, we measured the bubbly two-phase flow ejected from a nozzle with inner diameter of 13 mm. Bubbles were injected from eight capillary needles with inner diameter of 0.12 mm, which were mounted inside the nozzle. The bubble size observed in the downstream ranged from 0.5 to 3.0 mm when the initial jet velocity was set as 2 m/s (Fig. 7.22a). One objective of the demonstration was to determine how the small bubbles are maintained in the shear layer downstream [17], which is important for estimating the persistency of the jet-modifying effect of bubbles. The void fraction measured employing the ultrasonic method is shown in Fig. 7.22b. The individual bubble was measured using the echo intensity technique. Two gas flow rates were supplied at the nozzle: 2.5% in case 1 and 5.0% in case 2. We confirmed that the bubbles clearly tended to accumulate in an annular shear layer of the jet. This accumulation is explained by the distribution of enstrophy (i.e., the roll vortex beside the jet center), which keeps bubbles within the shear layer of the local pressure gradient in each vortex. The asymmetric profile of the void fraction seen along the path of the ultrasound pulse is related to the flow instability that occurs in the azimuthal direction. The source of the instability is similar to that seen in two parallel planar jets.

Figure 7.22c, d compares the void fraction profiles between ultrasonic and optical techniques. Because image processing is restricted for the cylindrical structure of the bubbly jet, the projection void fraction (i.e., void fraction integrated in the direction of the viewing axis) is obtained by converting the data of Fig. 7.22b to compare the two results in the same frame. The projection void fraction is derived by integrating the two-dimensional void fraction distribution in the viewing direction. The two-dimensional void fraction is given by projecting the on-beam void fraction in the azimuthal direction assuming axisymmetricity. The result shows significant differences between the two results, caused by the difference in spatial resolution as explained in the previous test case. However, the following two points are confirmed. Case 1 has a higher peak of the void fraction near the jet central axis, and case 2 has a more diffused profile far from the center. These points are consistent

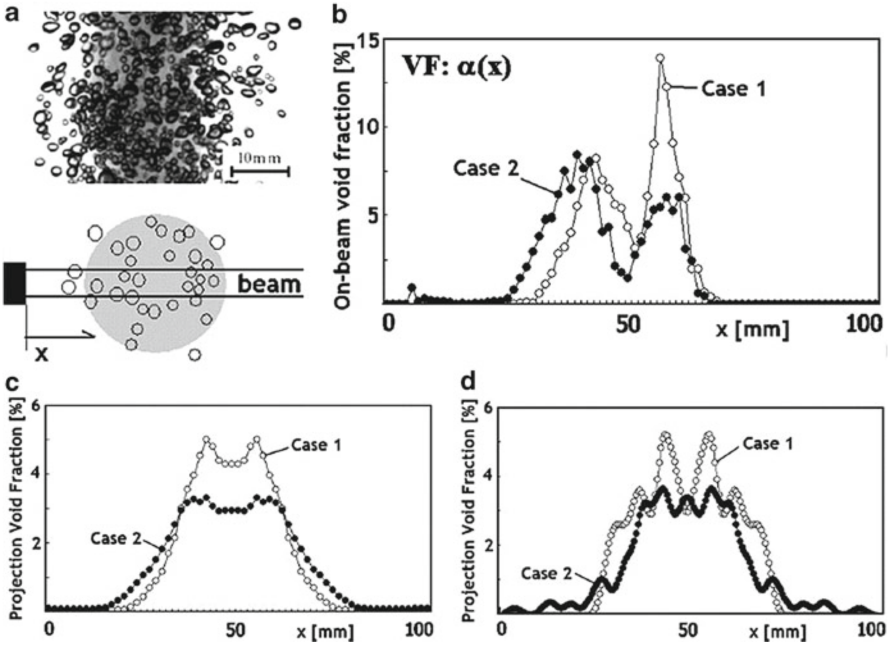

Fig. 7.22 Measurement of the upward bubbly two-phase jet ejected from the concentric nozzle. (**a**) Measurement target and bubble image. (**b**) On-beam void fraction measured by the present method. (**c**) Projection void fraction estimated from the ultrasonic data. (**d**) Projection void fraction measured by image processing (reprinted from [8] with permission from IOPsciense)

with the phenomenological understanding of a two-phase jet. Therefore, we could say that the functionality of the present ultrasonic technique has been confirmed.

7.3.4 High-Speed Two-Phase Turbulent Boundary Layer of a Model Ship

Figure 7.23 presents measurement data of the bubble distribution inside a turbulent boundary layer of a model ship. The ship was towed at two different speeds in a 400-m-long tank. The length of the ship was 50 m, and the ultrasonic transducer for measuring the void fraction at its base was located 27 m from the bow of the ship. The purpose of this experiment was to confirm and elucidate the frictional drag reduction of a ship by injecting small bubbles into the boundary layer. The drag was reduced to around 85% (i.e., 15% drag reduction) by injecting bubbles, which was determined from the towing force. We wished to determine the void fraction profile in the boundary layer, which is difficult to estimate theoretically because of the turbulent flow with a very high Reynolds number of around $Re = 108$ and bubbles

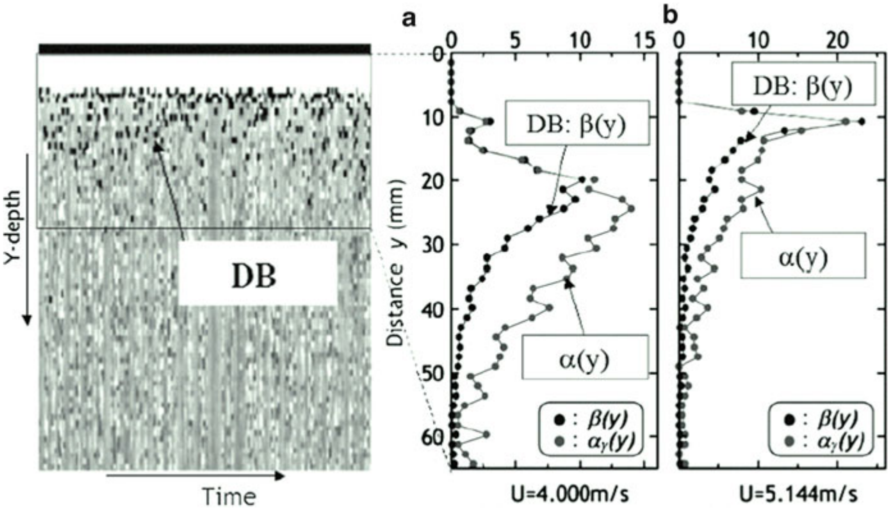

Fig. 7.23 Measurement of bubble distribution in the turbulent boundary layer of a towed ship. (**a**) Detected bubbles. (**b**) Void fraction profiles reconstructed (reprinted from [8] with permission from IOPsciense)

with a very high Weber number of *We* = 103. In addition, it is impossible to accurately simulate such a boundary layer for numerical analyses in any type of two-phase flow model. However, it is known that there is drag accumulated near the layer of the peak Reynolds shear stress. In short, it is desirable to have a void fraction profile similar to the Reynolds shear stress profile to maximize drag reduction. However, it has not been possible to measure and evaluate the void fraction profile for a bubbly turbulent boundary layer with such high *Re* and *We* numbers to date. As shown in Fig. 7.23a, the bubbles closest to the transducer are detected by ultrasound sensing. In this case, the Doppler technique is applied. The time-averaged profile of the first-reflecting bubbles, $\beta(y)$, is then obtained. The transform to the true void fraction leads to the profiles shown in Fig. 7.23b. From the results for the two different towing speeds, it is confirmed that the peak void fraction is 24 mm from the ship's bottom surface for the towing speed $U = 4.00$ m/s and 11 mm for $U = 5.14$ m/s. These results clearly indicate that the peak void fraction occurs considerably deeper than the location of the peak Reynolds shear stress. This finding implies that we can further improve drag reduction by optimizing the bubbling conditions. Moreover, using these new data, we can discuss why the peak approaches the ship hull in the high-speed condition; this is tightly connected to the following strategy for promoting drag reduction.

Providing an array of ultrasonic transducers, the void fraction distribution in higher dimensions can be measured in real time with the help of a computer tomography algorithm [18–20]. Such a technique is expected to be applied in the engineering application of a heterogeneous structure of two-phase flows.

7.4 Vector Profiling Method

7.4.1 Introduction

Essentially, a flow field is four dimensional, including time as represented as $\boldsymbol{v} = \boldsymbol{v}(\boldsymbol{x}, t)$; a full representation of a flow field requires the three functions of the velocity components (u, v, w) as spatial functions (x, y, z) and time (t). Therefore, in experimental study for fluid dynamics, the goal is to obtain such information. Recently, such ideal measurement may be realized by the dramatic progress of particle image velocimetry (PIV). However, PIV cannot be applied to opaque fluids and an opaque apparatus. On the other hand, UVP is a very effective tool for velocity profile measurement of opaque fluids [21, 22]. Present UVP systems, however, give only a one-directional velocity component on a measurement line, and it is less informative in comparison with the velocity vector field given by PIV. The purpose of this study is to overcome this disadvantage of the conventional UVP by expanding the dimension of the velocity vector. A concept of velocity vector profile measurement based on UVP that has been reported by Lemmin et al. [23–25] is apparently not suitable for fluid dynamic study because the measurement volume is too large. So, we advance this concept to be applied to the experiment of fluid dynamics. In this study, we developed a prototype system that enables us to obtain two-dimensional velocity vector profiles on a measurement line and applied this system to actual flow fields.

7.4.2 Measurement Principle

The measurement principle of the velocity vector profile measurement that was established by Lemmin et al. [23–25] is described in Fig. 7.24. This system consists of a central emitter of ultrasound and surrounding multiple receivers. An ultrasonic pulse is emitted into fluids from the emitter, and surrounding receivers receive the echo reflected from tracer particles suspended in the flowing medium. At least two receivers are required to obtain the three-directional velocity vectors when the emitter is utilized as the receiver (the figure shows a three-receiver configuration). By analyzing these received echo signals, three-directional velocity components can be obtained in the same process as in the conventional UVP for each receiver. Each velocity component v_i ($i = 1, 2, 3$) is determined by the following equation:

$$v_i = cf_{\mathrm{Di}} / 2f_0, (i = 1, 2, 3) \tag{7.13}$$

where c is the speed of sound in the medium and f_{Di} and f_0 are Doppler shift frequency to the direction i and the basic frequency of the ultrasonic beam, respectively. In this system, the Doppler shift frequency of each direction is acquired by the same method as the conventional UVP, and revision is not required [22].

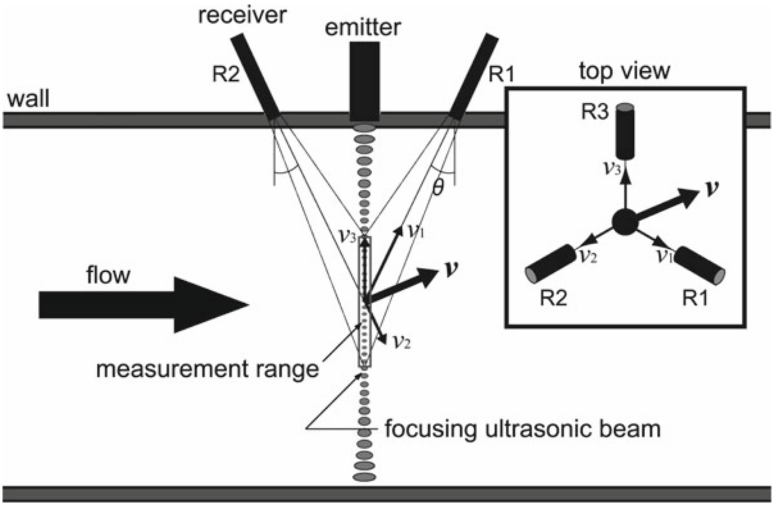

Fig. 7.24 Schematic illustration of concept of vector measurement using ultrasound (reprinted from [26] with permission from Elsevier)

Fig. 7.25 Configuration of ultrasonic transducers and vector formation where $\boldsymbol{v}_1$ and $\boldsymbol{v}_2$ are velocity components measured by each transducer (reprinted from [26] with permission from Elsevier)

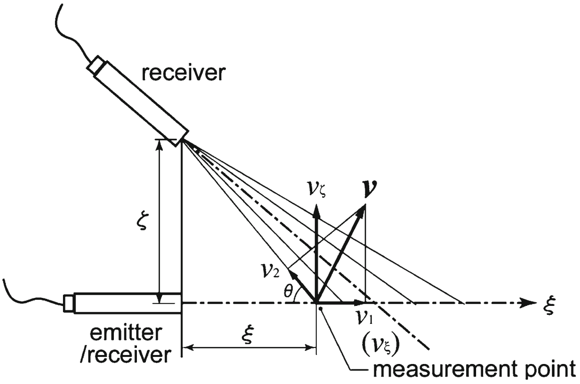

Because these receivers have a certain spatial range of receivable area (Fig. 7.24), it can receive the echo from each point on the ultrasonic beam in this range. Therefore, this system can obtain the profile of the three-dimensional velocity vector along the propagation direction of the ultrasonic beam. In the two-dimensional configuration shown in Fig. 7.25, the orthogonal velocity components v_ξ and v_ζ are determined from the measured velocity components v_1 and v_2 as in the following equations:

$$\begin{aligned} v_\xi &= v_1 \\ v_\zeta &= \frac{v_1}{\tan\theta} + \frac{v_2}{\sin\theta} \end{aligned} \tag{7.14}$$

where the angle formed by emitter, measurement point, and receiver, θ, is a function of the measurement position ξ, which follows if the distance between the emitter and receiver, ξ, is fixed:

$$\theta = \tan^{-1}\frac{\xi}{\zeta} \tag{7.15}$$

To reduce the spatial uncertainties of the measurement position, reducing the diameter of the ultrasonic beam is required. Lemmin and co-workers [23–25] achieved that by using a phased-array transducer that realized the quite linear beam. When a measurement medium is water, because the system can fix the diameter of an ultrasonic beam to a constant size to the depth of 0.5 m, it is an extremely effective technique. This adjustment is, however, quite complex, and enlarging the initial diameter of the beam is inevitable. In the simplified system, a focusing ultrasonic transducer (F-TDX) that is able to decrease the diameter of the beam by mounting an acoustic lens was employed as an emitter.

In UVP measurement, position on the measurement line, ξ, is obtained as time-of-flight of the ultrasonic pulse, τ, as

$$\xi = \frac{c\tau}{2} \tag{7.16}$$

and thus ξ is proportional to τ. This relationship is also satisfied to the receiver, which is also used as the emitter in the present system. However, in the receiver held with an opening angle to the measurement line (see Fig. 7.25), ξ is not proportional to τ as represented:

$$\xi + \sqrt{\xi^2 + \zeta^2} = c\tau \tag{7.17}$$

If the same sampling protocol is applied to both receivers, the measurement point would differ between the receivers. However, in the system proposed here, the difference appears to be much smaller than the limit of the sampling speed of the A/D board, and we neglected it in the present system.

7.4.3 Example of Measurement

The wake of a cylinder in a shallow channel filled with silicon oil was measured for demonstrating a developed system for a two-dimensional unsteady flow. The construction of the experimental setup is described next.

A cylinder with diameter $d = 10$ mm is mounted in a channel, 160 mm wide and 40 mm high, at 1,700 mm downstream of the inlet of the channel (Fig. 7.26). The working fluid is silicone oil. Ultrasonic transducers, an emitter and a receiver,

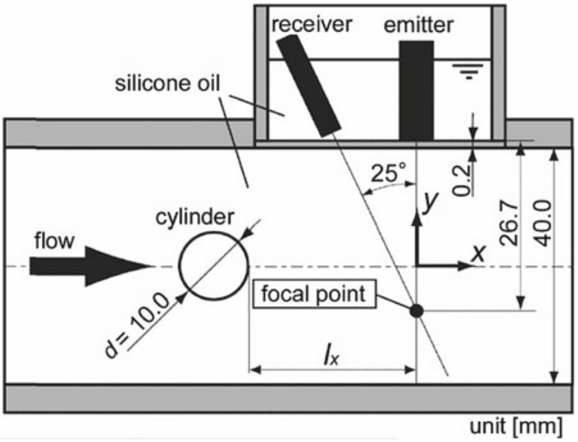

Fig. 7.26 Experimental setup for measurement of the wake of a cylinder in a shallow channel (reprinted from [26] with permission from Elsevier)

are mounted on the top of the channel behind the acrylic plate, which is 0.2 mm thick. Setting of the transducers is optimized based on the results of the numerical simulation for the ultrasonic beam (see Obayashi et al. [26]). An intersection of the axes of the transducers was chosen for being the focal point of the emitter at 26.7 mm from the front of the emitter. The receiver angle is fixed at 25°. Position of the measurement line, l_x, is chosen as 3.75 d from the cylinder.

Temporal variation of the obtained velocity vector profile is shown in Fig. 7.27. The sampling period is 30 ms, and the profiles are arranged inversely to measurement time (i.e., from right to left). In the area enclosed with a black line in the figure, two large vortices can be observed. Because the channel does not have enough height in comparison with the diameter of the cylinder, vortex shedding seems symmetric to the center of the channel, unlike the Bénard–Kármann vortex street (see visualized photograph shown in Fig. 7.28, where the white line corresponds to the measurement line in this case). It shows, however, that the shedding of vortex is periodic.

Two-dimensional velocity vector distribution behind the cylinder wake, $v(x, y)$, can be determined from the temporal variation of the obtained velocity vector profiles by applying Taylor's frozen hypothesis, where the spatial value x is determined as

$$x = u_m t \tag{7.18}$$

where u_m is mean stream velocity in the flow channel. Figure 7.27 expresses the measurement data displayed in space–time configuration and signified the general flow in total sampling time over 19 × 30 ms. And here, vorticity distribution, $\omega(x,y)$ ($= \partial v/\partial x - \partial u/\partial y$), can be computed from the velocity vector distribution shown in Fig. 7.29. The four islands (two gray and two white) represent two vortices with negative vorticity and two with positive vorticity. The position of each corresponds to the top and bottom edge of the cylinder; they appear in an alternating manner. Such alternate vortex

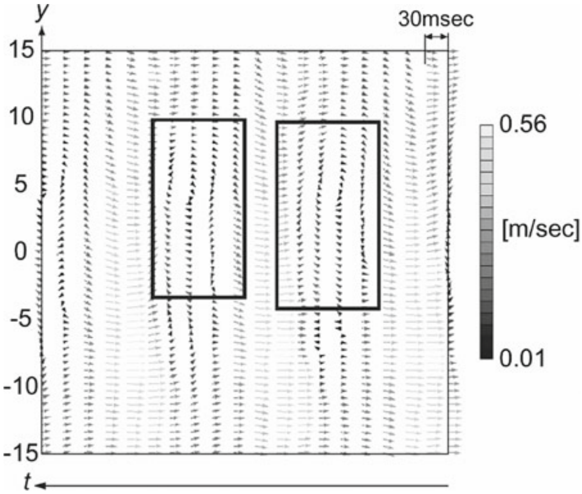

Fig. 7.27 Temporal variation of the velocity vector profile: the sampling period is 30 ms and the profiles are arranged inversely to measurement time (from *right* to *left*) (reprinted from [26] with permission from Elsevier)

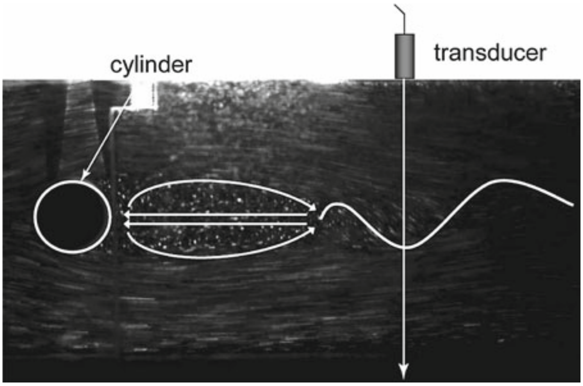

Fig. 7.28 Visualized photograph of the wake and supplemental illustration (reprinted from [26] with permission from Elsevier)

shedding is difficult to confirm in the temporal variation of the velocity vector profile (Fig. 7.27) because of the lesser temporal resolution of the obtained profile (30 ms in temporal resolution corresponds to 4.5 mm in spatial resolution, and this value is comparable with the size of the vortex). On the other hand, the measurement volume is defined as well as conventional UVP by the width of the burst signal and the diameter of an ultrasonic beam. By improvement of temporal resolution, this system would contribute to experiments in fluid dynamics.

7.4.4 *Summary*

In this section, the velocity vector profile measurement technique with multiple ultrasonic transducers is introduced. The active diameter of the ultrasonic beam is decreased by using a focusing transducer as an emitter, and it could reduce the spatial uncertainty. However, because the active diameter becomes large adversely in the

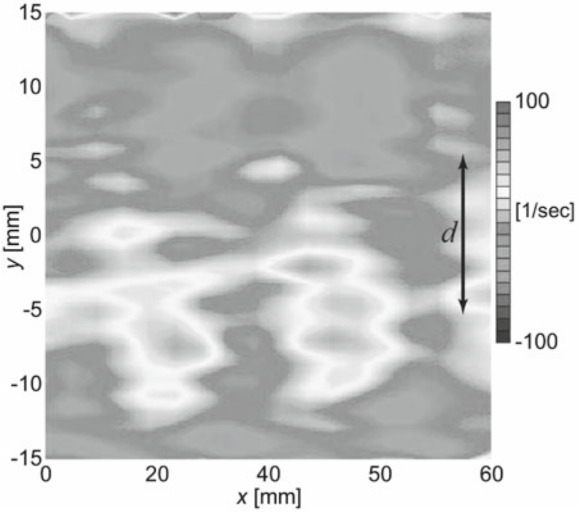

Fig. 7.29 Vorticity distribution computed from velocity vector distribution (reprinted from [26] with permission from Elsevier)

region except the focal region, it is necessary for the setting position of the emitter to be adjusted so that the target region is measured. In addition, because the focal regions are different in every measurement medium under the influence of sound velocity, it is important that the focal regions are grasped by preliminary calculations. The introduced technique is a measurement system to be composed of two ultrasonic transducers and realizes the two-dimensional velocity vector profile measurement on the measurement line. The system was also applied to measure two-directional velocity vector profile of unsteady flow, a wake behind a cylinder in a shallow channel. The obtained temporal variation of the velocity vector profile confirmed the applicability of the developed system to unsteady flow. The vortex shedding in the wake was well reproduced as in the vorticity distribution, which was computed from the temporal variation of the vector field using the Taylor frozen hypothesis. Although a temporal resolution is still not high, we conclude that applicability of the measurement system has been confirmed. This technique, which can measure locoregional multiple velocity vector profiles, is extremely effective in precision improvement of the predictive calculations and the grasp of the properties of the heat flux motion in the cooling system of a nuclear reactor that adopted liquid metal as a coolant.

7.5 Correlation Method

The correlation method is one of the novel signal processing techniques for the ultrasound velocity profiler. By the conventional pulse Doppler technique that was employed by the commercial ultrasound velocity profiler, multiple sets of ultrasound emission and data acquisition were required to determine the instantaneous velocity profile; i.e., a few hundred echo signals must be stored for the determination of the single velocity profile along the ultrasound beam. Therefore, the temporal resolution

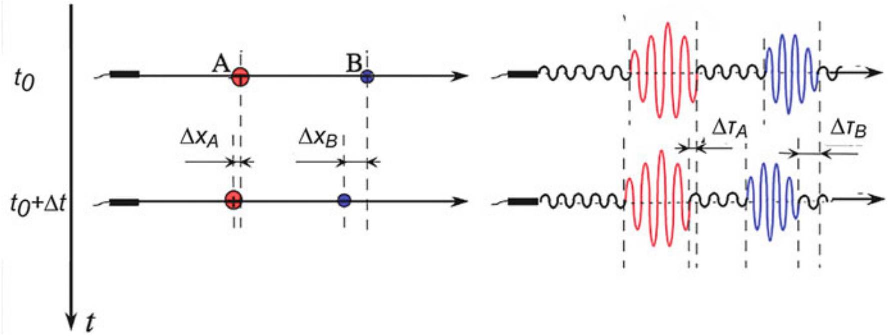

Fig. 7.30 Phase modulation of the echo signals resulting from the motion of a tracer particle

of the pulse Doppler technique was restricted to several tens of milliseconds to 100 ms. Ozaki et al. [27] has developed a novel signal acquisition and processing system of the ultrasound velocity profiler to improve the temporal resolution of the velocity measurement. The system consisted of the sinusoidal tone burst pulser-receiver as well as the synchronized high speed and high bit count analog-to-digital convertor (A/D convertor) with a faster storage memory. Because the system employs the cross-correlation method in software and could determine the instantaneous velocity profile from the two consecutive echo signals, the sampling frequency of the velocity profiling is beyond the kHz range.

Figure 7.30 illustrates an example of the reflected echo signals from tracer particles in fluid. By the ultrasound transducer, the pulsed sinusoidal ultrasound was introduced into fluid flows. The tracer particles in fluid reflect ultrasound as a consequence of the difference of acoustic impedance of the particles.

Now, the time τ represents time difference between ultrasound emission and echo detection of the reflected ultrasound, and c is defined as a sound velocity. Distance from the transducer and measurement point, x, is defined as $x = c\tau/2$, which is exactly the same as the pulse Doppler techniques. By acquiring the successive echo signals after the time interval of Δt, quite similar echo signals could be obtained. Assuming that the fluid flow as well as the tracer particle is moved, τ could be changed.

The temporal difference of τ is $\Delta\tau$; the velocity, $u(x)$, at location x is expressed as follows:

$$u(x) = \Delta x / \Delta t = \frac{c\Delta\tau}{2\Delta t} \tag{7.19}$$

where Δx represents the local displacement of the fluid flow within a certain time interval. When the tracer particle is homogeneously distributed in the fluid flow, Eq. (7.19) provides the velocity distribution along the ultrasound beams.

In general, the shape of the echo signal is not a simple sinusoidal function but is strongly affected by the solid wall, local impedance difference, and size distribution of the tracer particles. The characteristics of the echo signal such as amplitude, phase, and envelope profile were significant information for the correlation calculation. If the time interval between a pair of successive echoes, Δt, is quite small, the similarity of the echo signals is high. In other words, almost the same sinusoidal signal is observed with the phase modulation because of the velocity distribution in flow field. Consequently, the phase modulation between two echo signals corresponds to the local velocity distribution of fluid flow. By the signal processing technique, the phase modulation could be extracted by using a cross-correlation function.

The similarity of the two echo signals, $h(t)$ and $g(t)$, could be quantified by the cross-correlation coefficient as follows:

$$R = \frac{\sum_{t=1}^{n} h(t) \cdot g(t)}{\sqrt{\sum_{t=1}^{n} h^2(t)} \sqrt{\sum_{t=1}^{n} g^2(t)}} \tag{7.20}$$

The normalized cross-correlation coefficient, R, is the value that represents the similarity between the first and second echo signals. To determine the peak location of the correlation coefficient, the correlation value distribution must be calculated. Because the echo signal captured by the A/D convertor is not a continuous function but a set of discrete values, the calculated cross-correlation coefficient is the discrete function as well. Therefore, the function fitting was used to determine the accurate displacement of the echo signals between consecutive signals, which is used for the sub-pixel displacement of particle image velocimetry (PIV). The function fitting enables us to improve the resolution of the displacement determination of the echo signals as well as the velocity resolution.

Let the first and second echo signal be reference wave and interrogation wave, respectively. Figure 7.31 shows an example of the cross-correlation function between echo signals. The peak value of the function must first be determined. Then, the sub-pixel displacement could be calculated from the peak value of the cross-correlation coefficient and the neighboring coefficients. Following is the modification equation by the Gaussian curve fitting:

$$\Delta\tau = k + \frac{1}{2}\left(\frac{\ln R_{k-1} - \ln R_{k+1}}{\ln R_{k-1} - 2\ln R_k + \ln R_{k+1}} \right) \tag{7.21}$$

where R_k and k denote the discrete correlation coefficient and peak index of the coefficient, and R_{k-1} and R_{k+1} are the contiguous correlation coefficients.

For the correlation technique, the sampling frequency of the A/D convertor must be much faster than that of the fundamental frequency of the ultrasound. In contrast to the conventional pulse Doppler technique of an ultrasound velocity profiler, the entire echo signal must be continuously acquired to determine the displacement of the local sinusoid and to determine the local velocity along the ultrasound beam. The fundamental frequency of the ultrasound is 2–8 MHz by noting the spatial

Fig. 7.31 Function fitting for the discrete cross-correlation coefficients for the estimation of sub-pixel displacement

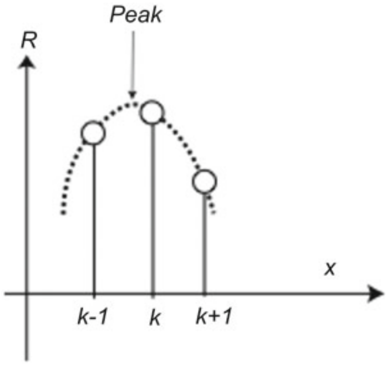

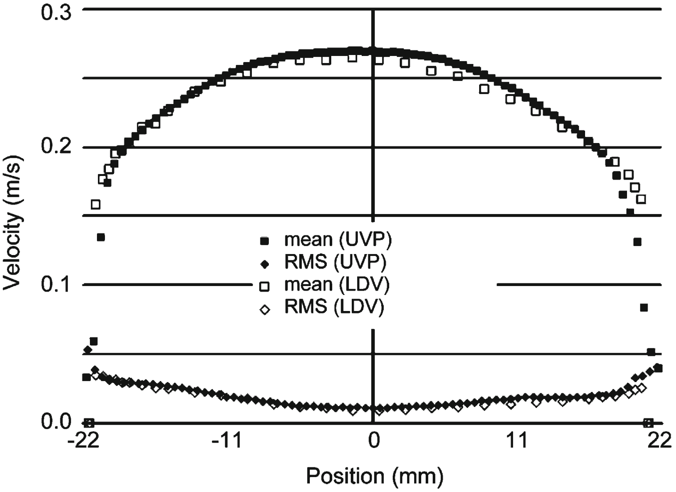

Fig. 7.32 Comparison of velocity distributions in a pipe between cross-correlation UVP and laser Doppler velocimetry. $Re = 10{,}000$

resolution of the velocity measurement as well as the diverging angle of the acoustic beam. Therefore, the representative sampling frequency and bit resolution of the A/D convertor are more than 100 MHz and 8 bits, respectively. For example, 200 kB of storage memory is necessary for the acquisition of a couple of echo signals with a 100 MHz analog to digital convertor, measurement depth of 70 cm, and pulse interval of 1 ms. For continuous 1 s acquisition, 100 MB of storage memory is required. Such faster and larger amounts of data acquisition are possible because of the recent development of the faster RAM of computer systems.

Figure 7.32 shows an example of the velocity distribution in a circular pipe by means of the novel correlational UVP technique [27]. In the study, the internal diameter of pipe was 44 mm and Reynolds number was ~10,000. The measured result by laser Doppler velocimetry (LDV) is also shown in Fig. 7.32. Inclined angle

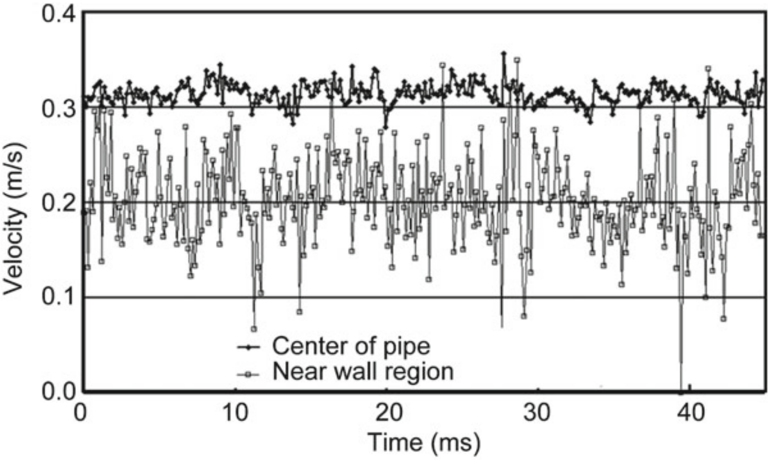

Fig. 7.33 Temporal profile of velocity at the center of a pipe and in the vicinity of the pipe wall

between pipe and transducer was 45°; the mean and root mean square (RMS) of absolute velocity was calculated from the 3,000 velocity profiles. As the LDV technique is a point-measurement technique, the entire optical system must be moved by means of the one-dimensional traverser to measure the profile of velocity in flow. The UVP system, in contrast, does not require the mechanical traverse of the measurement system.

Figure 7.33 depicts the temporal profile of the velocity at the center of pipe and in the vicinity of the wall of the pipe. Pulse repetition interval was 0.5 ms, which is equivalent to the sampling frequency of 2,000 Hz. By the results of the correlational UVP technique, the magnitude of velocity is larger and the fluctuation component is smaller at the center of the pipe. The technique enables us to measure flow fields with a higher Reynolds number, to analyze the high-frequency fluctuation of the fluid flow, and to investigate the spatial correlation of the velocities and other physical quantities between different positions in turbulence.

References

1. Murakawa H, Kikura H, Aritomi M (2005) Application of ultrasonic Doppler method for bubbly flow measurement using two ultrasonic frequencies. Exp Therm Fluid Sci 29:843–850
2. Murakawa H, Kikura H, Aritomi M (2008) Application of ultrasonic multi-wave method for two-phase bubbly and slug flows. Flow Meas Inst 19:205–213
3. Murai Y, Tasaka Y, Nambu Y, Takeda Y, Gonzalez ASR (2010) Ultrasonic detection of moving interfaces in gas-liquid two-phase flow. Flow Meas Inst 21:356–366
4. Murai Y, Fujii H, Tasaka Y, Takeda Y (2006) Turbulent bubbly channel flow investigated by ultrasound velocity profiler. J Fluid Sci Technol 1:12–23
5. Acheson DJ (1989) Elementary fluid dynamics. Oxford University Press, Oxford, pp 89–100

6. Gonzalez SR, Murai Y, Takeda Y (2009) Ultrasound based gas-liquid interface detection in gas-liquid two phase flows. Adv Chem Eng 37:1–27
7. Otsu N (1979) A threshold selection method from gray level. IEEE Trans Syst Man Cybern 9:62–66
8. Murai Y, Ohta S, Shigetomi A, Tasaka Y, Takeda Y (2009) Development of an ultrasonic void fraction profiler. Meas Sci Technol 20:114003
9. Julia JE, Harteveld WK, Muddle RF, Van Den Akker HEA (2005) On the accuracy of the void fraction measurements using optical probes. Rev Sci Instrum 76:035103
10. Schleicher E, da Silva MJ, Thiele S, Li A, Wollrab E, Hampel U (2008) Design of an optical tomograph for the investigation of single- and two-phase pipe flows. Meas Sci Technol 19:094006
11. Murai Y, Matsumoto Y, Yamamoto F (2001) Three dimensional measurement of void fraction in a bubble plume using statistic stereoscopic image processing. Exp Fluids 30:11–21
12. Murai Y, Oiwa H, Sasaki T, Kondou K, Yoshikawa S, Yamamoto F (2005) Backlight imaging tomography for gas–liquid two-phase flow in a helically coiled tube. Meas Sci Technol 16:1459–1468
13. Kim S, Fu XY, Wang X, Ishii M (2000) Development of the miniaturized four-sensor conductivity probe and the signal processing scheme. Int J Heat Mass Transfer 43:4101–4018
14. Neal LG, Bankoff SG (1963) High resolution resistivity probe for determination of local void properties in gas–liquid flow. AIChE J 9:490–494
15. Yang HC, Kim DK, Kim MH (2003) Void fraction measurement using impedance method. Flow Meas Inst 14:151–160
16. Warsito W, Fan LS (2001) Measurement of real-time flow structures in gas–liquid and gas–liquid–solid flow systems using electrical capacitance tomography. Chem Eng Sci 56: 6455–6462
17. Felton K, Loth E (2002) Diffusion of spherical bubbles in a turbulent boundary layer. Int J Multiphase Flow 28:69–92
18. Supardan MD, Masuda Y, Uchida SM (2007) The investigation of gas holdup distribution in a two-phase bubble column using ultrasonic computer tomography. Chem Eng J 130:125–133
19. Xu LJ, Xu LA (1997) Gas-liquid two-phase flow regime identification by ultrasonic tomography. Flow Meas Inst 8:145–155
20. Longo S (2006) The effects of air bubbles on ultrasound velocity measurements. Exp Fluids 41:593–602
21. Takeda Y (1987) Measurement of velocity profile of mercury flow by ultrasound Doppler shift method. Nucl Technol 79:120–124
22. Takeda Y (1995) Instantaneous velocity profile measurement by ultrasonic Doppler method. Invited paper. JSME Int J B 38:8–16
23. Shen C, Lemmin U (1996) Ultrasonic measurements of suspended sediments: a concentration profiling system with attenuation compensation. Meas Sci Technol 7:1191–1194
24. Lemmin U, Rolland T (1997) Acoustic velocity profiler for laboratory and field studies. J Hydraul Eng ASCE 123:1089–1098
25. Hurther D, Lemmin U (1998) A constant beam width transducer for 3D acoustic Doppler profile measurement in open-channel flows. Meas Sci Technol 9:1706–1714
26. Obayashi H, Tasaka Y, Kon S, Takeda Y (2008) Velocity vector profile measurement using multiple ultrasonic transducers. Flow Meas Inst 19:189–195
27. Ozaki Y, Kawaguchi T, Takeda Y, Hishida K, Maeda M (2002) High time resolution ultrasonic velocity profiler. Exp Therm Fluid Sci 26:253–258

Appendix

Yuji Tasaka

Acoustic Properties

Here we summarize the acoustic properties of liquids (Table A.1) and solids (Table A.2).

The speed of sound in water, c_w, depends on both temperature and pressure. The dependence is described as

$$\begin{aligned} c_w(T, p_0) = {} & 1402.39 + 5.03711T - 0.0580852T^2 + 3.33420 \times 10^{-4} T^3 \\ & - 1.47800 \times 10^{-6} T^4 + 3.14643 \times 10^{-9} T^5 + 1.6 \times 10^{-6} (p_0 - 10^5) \end{aligned} \tag{A.1}$$

where T is temperature in °C and p_0 is absolute pressure in Pascals. This equation was obtained as a fitting curve on experimental data taken between 0 and 99.9°C.

If you need further information about acoustic properties, please visit the appropriate websites [1, 2]. Povey [3] also provides the speed of sound in some solutions with different concentrations and the speed in bulk of some mixtures.

Ultrasonic Transducers

Figures A.1 and A.2 show ultrasonic transducers for ultrasonic Doppler velocity profiler (UVP) measurement that can be purchased commercially. Specifications of the transducer are summarized in Tables A.3 and A.4, respectively. Please read Sect. 2 to understand the details of the transducers and the content of the tables.

Y. Tasaka
Faculty of Engineering, Hokkaido University, Sapporo, Japan
e-mail: tasaka@eng.hokudai.ac.jp

Y. Takeda (ed.), *Ultrasonic Doppler Velocity Profiler for Fluid Flow*,
Fluid Mechanics and Its Applications 101, DOI 10.1007/978-4-431-54026-7,

Table A.1 Acoustic properties of liquids

Material	Speed of sound (m/s)	Density (10^3 kg/m^3)	Acoustic impedance [10^6 kg/(m^2 s)]	Temperature (°C)
Water	1,480	1.00	1.483	20
Seawater	1,531	1.025	1.569	25
Ethanol	1,207	0.79	0.95	25
Methanol	1,103	0.791	0.872	25
Silicone oil (1 cSt)[a]	960	0.818	0.74	
Silicone oil (10 cSt)[a]	968	0.94	0.91	
Silicone oil (1,000 cSt)[a]	990	0.972	0.96	
Gasoline	1,250	0.803	1.00	
Glycerin	1,904	1.26	2.34	25
Fluorinert FC-40	640	1.19	1.86	
Fluorinert FC-75	585	1.76	1.02	
Liquid gallium	2,870	6.09	17.5	30
Lead bismuth eutectic	1,750	10.2	N/A	125
Mercury	1,450	13.5	19.58	25
Sodium	2,420	8.81	21.31	300

[a] *cSt* centi-Stokes

Table A.2 Acoustic properties of solids

Material	Speed of sound (m/s)	Density (10^3 kg/m^3)	Acoustic impedance [10^6 kg/(m^2 s)]
Acrylic resin	2,730	1.18	3.2
Mild steel	5,900	7.8	46
Stainless steel (347)	5,790	7.89	45.7
Aluminum	6,320	2.7	17
Copper	4,700	8.9	42
Tin	3,320	7.3	24
Pyrex glass	5,640	2.24	13.1

All properties in the table are for longitudinal wave

Fig. A.1 Photograph of ultrasonic transducers provided by Met-flow S.A. [8]

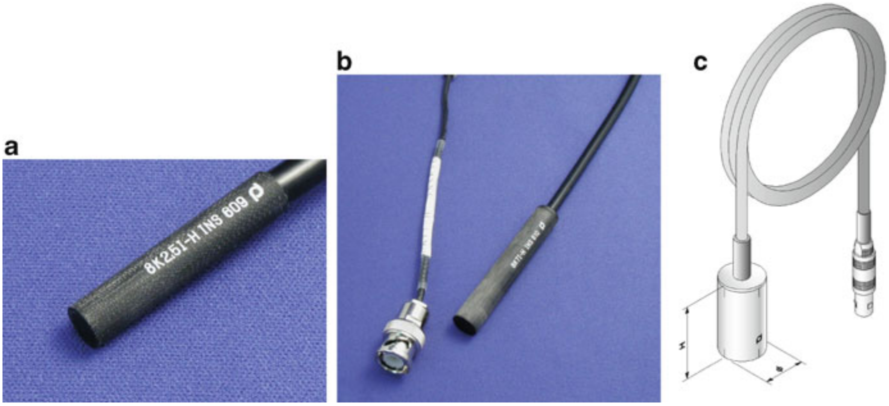

Fig. A.2 (**a**) Head. and (**b**) overview of a probe (8 K2.5-H (**c**) Central frequency 8 MHz, active diameter 2.5 mm). Schematic of standard transducers provided by Japan Probe Co. [9]

Table A.3 Lineup of ultrasonic transducers provided by Met-flow S.A. [8]

Central frequency (MHz)	Active diameter (mm)	Overall diameter (mm)	Focal distance (mm)	Divergence half-angle (degrees, °)
0.5	19	23	30.5	4.6
1	13	16	28.5	3.4
2	10	13	33.8	2.2
4	5	8	16.9	2.2
8	2.5	8	8.5	2.2

Table A.4 Conditions for producing ultrasonic transducers by Japan Probe Co. [9]

Central frequency	Active diameter	Operating temperature limit
0.1–10 MHz	2–50 mm	120°C

Couplants

One of the advantages of the UVP method is that a sensor (transducer) can be set outside the containing wall, which enables avoiding any disturbance to the flow, i.e., noninvasiveness. In such configurations, a gap between the transducer front surface and the wall surface has to be filled with any substance that eliminates the air layer to prepare a smooth transition of acoustic impedance from the transducer to the wall. This requirement is also true even when two surfaces make direct contact without inclination of the transducer, because the surface roughness of the materials inevitably holds an air layer between the two surfaces.

In a simple configuration water is used as it is for nondestructive testing. Or, an ultrasonic gel is widely used in medical applications. Both couplants are effective for our applications also. The latter is composed mainly of water, but the composition varies from product to product.

Table A.5 Specifications of seeding particles commercially available

Product name	Type	Material	Mean diameter (μm)	Density ($\mathrm{g/cm^3}$)	Supplier
Griltex 5P1	Sphere	Nylon	75	1.06	EMS Co. Ltd.
DIAION HP20SS	Porous sphere	Divinylbenzen	~100	1.02	Mitsubishi Chemical Co.
SEPABEADS SP20SS	Porous sphere	Divinylbenzen	~50	1.02	Mitsubishi Chemical Co.
Flobeas CL-2507	Sphere	Polyethylene	180	0.919	Sumitomo Seika Chemicals Co., Ltd.
HGS	Hollow sphere	Glass	10	1.1	Dantec Co.
Q-Cel	Hollow sphere	Glass	50–90	0.14–0.48	Potters Industries LLC
Spherical	Hollow sphere	Glass	12–47	0.25–1.10	Potters Industries LLC

It is important to know that gel dries, so that it should be refreshed from time to time, especially when the surface or surrounding temperature is high. Special products of high-temperature couplant are available; for example, Sono 600 is applicable for ultrasonic flaw inspections in high-temperature environments up to 260°C [acoustic impedance is $1.35\text{–}1.40 \times 10^6$ $\mathrm{kg/(m^2\,s)}$] [4].

Seeding Particles

Examples of tracer particles for UVP measurements that can be purchased on the market are specified in Table A.5. Please refer to Sect. 3.2.6 to know the requirements for tracer particles.

Particle motions in unsteady flows are described by equations of motion of a particle (Maxey–Riley equations [5, 6]), for example:

$$\begin{aligned}\frac{\pi d^3}{6}\rho_p\frac{\mathrm{d}\boldsymbol{u}_p}{\mathrm{d}t} &= 3\pi\upsilon\rho_f d\left(\boldsymbol{u}_f-\boldsymbol{u}_p\right)+\frac{\pi d^3}{6}\rho_f\frac{\mathrm{d}\boldsymbol{u}_f}{\mathrm{d}t}+\frac{1}{2}\frac{\pi d^3}{6}\rho_f\left(\frac{\mathrm{d}\boldsymbol{u}_f}{\mathrm{d}t}-\frac{\mathrm{d}\boldsymbol{u}_p}{\mathrm{d}t}\right)\\ &\quad+\frac{3}{2}d^2\rho_f\sqrt{\pi\upsilon}\int\frac{\mathrm{d}\xi\left(\mathrm{d}\boldsymbol{u}_f/\mathrm{d}t-\mathrm{d}\boldsymbol{u}_p/\mathrm{d}t\right)}{\sqrt{t-\xi}}\end{aligned} \tag{A.2}$$

where $\boldsymbol{u}_p$ and $\boldsymbol{u}_f$ are the velocity vector of the particle and the flow at a point, d, and ρ_p, ρ_f, and ν are the diameter and density of the particle and the density and kinetic viscosity of the fluid, respectively. The foregoing equation, Eq. (A.2), takes into account four forces, namely, viscous drag, pressure gradient force, added mass, and Basset history force (development of boundary layer). Further, lift force, buoyancy, or centrifugal force would not become negligible in some cases.

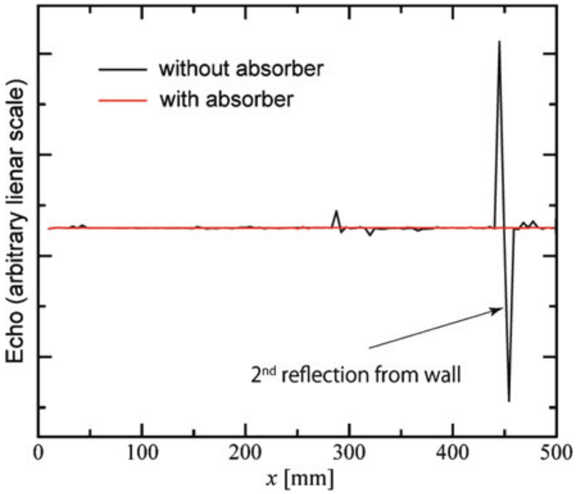

Fig. A.3 Averaged echo profile recorded in a 2,000-mm-long rectangular tank with or without an ultrasonic absorbing plate placed on the wall

Ultrasonic Absorbers

Detection of a spurious echo signal often cannot be avoided, depending on the geometric configurations and seeding conditions. Especially in the small contained configuration where there are many solid materials around the measurement volume, multiple scattering of the ultrasonic pulse bouncing from these solid walls causes time-frame aliasing, which deteriorates the velocity profile to an annoying extent. It is therefore important to design measurement configuration such that a pulse reflected on the wall shall not reach back to the transducer by arranging the beam line in an appropriate manner. A key practice for this is to use the oscilloscope to monitor the echo signal. This step is especially important where a reflection on the free surface is foreseen, because a reflection from the moving free surface will destroy the velocity profile from measurement frame to frame.

It is still often unavoidable to have echo reflected from the wall. In such cases a special ultrasonic absorbing material can be used to replace the wall material or to cover the wall surface by the absorber. Figure A.3 shows an example of eliminating echo reflected from the wall. The front face of a 2-MHz ultrasonic transducer is located at 1,500 mm from the wall of a rectangular tank 2,000 mm long. The tank is filled with water and the transducer is fully submerged in the water. The figure indicates the average echo profile with or without attaching an ultrasonic absorbing plate (EUA201A is shown in Fig. A.5a) on the wall of the tank. The wall position from the transducer is outside the range in this graph, and the large peak on the profile indicated by the arrow is the second reflection from the wall: the emitted ultrasonic pulse propagated between the walls in the tank twice before the transducer detected it. The profile utilizing the absorber seems smooth, and the echo of the second reflection is eliminated.

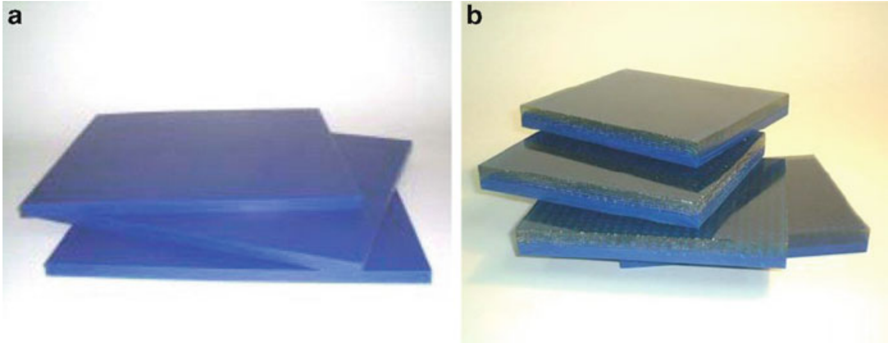

Fig. A.4 (**a**) Photographs of ultrasonic absorber EUA201A. and (**b**) EUA101A provided by EASTEC Co. (specifications of the materials are summarized in Table A.6)

Table A.6 Specifications of ultrasonic absorbers provided by EASTEC Co. [7]

	EUA201A	EUA101A	AptFlex
Material	Polyurethane	Polyurethane	Polyurethane
Range of frequency for US	> 0.5 MHz	> 0.7 MHz	> 0.4 MHz
Echo reduction at 1 MHz	25 dB	40 dB	2.29 dB/mm
Size (mm)	300 × 300 × 10	120 × 95 × 14 250 × 200 × 14	

Fig. A.5 Cylindrical test section made of ultrasonic absorbing material (AptFlex; see Table A.6)

Figure A.4 shows photographs of ultrasonic absorbing plates that can be purchased on the market [7]. Table A.6 specifies the characteristics of the plates. Using AptFlex makes possible to design a universal shape of test sections with the absorbing material. Figure A.5 shows a cylindrical test section made of AptFlex for flowrate measurement of bubbly flows (see Sects. 5.5 and 7.3).

References

1. Onda Corporation, Table of Acoustic Properties of Materials. http://www.ondacorp.com/tecref_acoustictable.shtml. Accessed 19 June 2012
2. NDT Resource Center, UT Material Properties. http://www.ndt-ed.org/EducationResources/CommunityCollege/Ultrasonics/Reference%20Information/matproperties.htm. Accessed 19 June 2012
3. Povey MJW (1997) Ultrasonic techniques for fluids characterization. Academic, London
4. Sonotech, ULTRASONIC NDT COUPLANTS. http://www.sonotech-inc.com/. Accessed 19 June 2012
5. Maxey MR, Riley JJ (1983) Equation of motion for a small rigid sphere in a nonuniform flow. Phys Fluids 26:883–889
6. Auton TR, Hunt JCR, Prud'homme M (1988) The force exerted on a body in inviscid unsteady non-uniform rotational flow. J Fluid Mech 197:241–257
7. EASTEK Co., Product Information(EUA201A, EUA101A, AptFlex), info@eastek.co.jp
8. MET-FLOW S.A., TRANSDUCERS, http://www.met-flow.com/. Accessed 19 June 2012
9. Japan Probe Co., Ltd., PROBE, http://www.jp-probe.com/jp-global/index.html. Accessed 19 June 2012

Index

Y. Takeda (ed.), *Ultrasonic Doppler Velocity Profiler for Fluid Flow*,
Fluid Mechanics and Its Applications 101, DOI 10.1007/978-4-431-54026-7,